2009

Investigation into the Hydrothermal Treatment of Sugarcane Bagasse under Near- and Supercritical Conditions

John E. White
Louisiana State University and Agricultural and Mechanical College

INVESTIGATION INTO THE HYDROTHERMAL TREATMENT OF SUGARCANE BAGASSE UNDER NEAR- AND SUPERCRITICAL CONDITIONS

A Dissertation

Submitted to the Graduate Faculty of the
Louisiana State University and
Agricultural and Mechanical College
in partial fulfillment of the
requirements for the degree of
Doctor of Philosophy

in

The Interdepartmental Program in Engineering Science

by
John E. White
B.S.E., University of Michigan, 1996
M.S.E., Johns Hopkins University, 2003
May 2010

Dedicated to the memory of Jim Catallo

Pioneer in the field of Hydrothermal Conversion Chemistry

Professor, Advisor, Mentor, Friend

ACKNOWLEDGMENTS

A complete list of those who have contributed along the tortuous and byzantine path culminating in this work would require another volume and still this would not be sufficient space to convey my gratitude or debt to them. In accordance with the historic principles of triage in such matters, I thank the following people while absolving them from any inferior work herein with a *mea culpa*.

Before his sudden, untimely death, Dr. Jim Catallo had served as my committee chair, professor, mentor, and friend. The encouragement, guidance, and pearls of wisdom he imparted to me were instrumental in the completion of this research effort. His compassion, insight, and levity have been, and continue to be, deeply missed.

I am grateful to Dr. Donal Day and Dr. William Constant for the leadership and technical direction they provided as committee co-chairs. Thanks are also extended to the rest of my committee, Dr. Robert Gambrell, Dr. Todd Shupe, and Dr. John Westra for their participation and constructive input regarding this work.

I would be remiss not to acknowledge the support of Dr. Michael Saska and Dr. Benito Stradi, who served as my previous committee chairs. Under their direction, I was privileged to acquire an invaluable understanding and appreciation of the fundamental thermochemical processes: pyrolysis, liquefaction, and gasification.

I am indebted to Mathew Monagle (AIC, Inc., Albuquerque, New Mexico) for his expertise and advice in gas phase gas chromatography. The successful restoration of the nearly defunct HP 5890 II GC could not have been performed without his assistance.

The staff of the Audubon Sugar Institute is hereby recognized for their support. I would also like acknowledge the support of previous Audubon employees, Victor Bazan, Raul Cortes,

and Michael Robert for their gracious assistance in the earlier gasification portion of this project.

I am grateful to Dr. Wei-Hsung Wang of the LSU Radiation Safety Office for prioritizing my sugarcane bagasse samples and irradiating them promptly.

I also acknowledge the assistance of Dr. Dandina Rao and his graduate student, Dayanand Saini, (Petroleum Engineering Dept., LSU, Baton Rouge, La.) for permitting me to use their dead-weight pressure testing unit.

Special thanks are accorded to the following persons and institutions for their assistance in various aspects of this project: Tonya Morgan (Center for Advanced Energy Research, University of Kentucky) for performing liquid density measurements; Dr. Robert Williams (Pharmaceutics Dept, University of Texas at Austin) for performing Karl Fischer titration analysis of the liquid samples; Russell Davis and Dr. Oladiran Fasina (Biosystems Engineering Dept. for permitting me to use their helium pycnometer for bagasse particle density measurements.

My long-suffering girlfriend, Sheilah Menard, endured the periodic episodes of frustration and temporary insanity during these past five years with remarkable aplomb and her support and devotion have been unflagging.

Equally important, I wish to recognize the indefatigable commitment of my parents, John W. and Barbara White, to ensure that their son and daughter both received the finest upbringing and education possible. I also thank my parents and sister, Kathy White, for their love and encouragement over the years.

Finally, I wish to thank the Providence of God for granting me the wherewithal to complete this work.

TABLE OF CONTENTS

LIST OF TABLES

LIST OF FIGURES

ABSTRACT

Processing biomass in near- and supercritical water has garnered increasing attention because of its ability to accept a variety of wet feedstocks, energy efficiency, and ability to regulate the solubility and separation of components. Very few studies of biomass hydrothermal conversion provide a comprehensive evaluation of multiple process parameters and various additives and their effects on a single product phase.

This research examined the influence of temperature, residence time, biomass concentration, and particle size on volatiles production from the hydrothermal conversion of sugarcane bagasse. Temperature had the greatest impact on volatile yields with the largest increase (23 wt %) occurring between 400 and 500 °C. The hydrogen mass yield increased 1000% between 300 and 600 °C.

Increasing the residence time from 1 to 60 min resulted in a 49% increase in the mass yield of volatiles and 12.1% increase in the overall conversion of bagasse. The heating value of the volatile products declined after 10 min. Thermal cracking reactions dominated the early gas phase chemistry through 10 min but may have been accompanied by oxygenolysis of intermediate compounds at extended reaction intervals.

In general, the use of Li/MgO and MnO_2 catalysts improved the hydrothermal conversion of bagasse by 10%. An increased selectivity toward propylene production by both catalysts suggests metal oxide catalysts may promote partial oxidation via hydroxyl radicals.

A side by side comparison of runs conducted in a Hastelloy X bomb and a titanium bomb revealed possible wall effects. The titanium bomb run produced 13 times more CO than the Hastelloy X bomb run along with at least 60 ppm of H_2S. Lower hydrocarbon yields from the

former run also support the theory that Ti is more catalytically active than Fe, Ni, and Cr in hydrothermal media.

Chromatographic analysis revealed that methane in the volatile product generated from an experiment conducted using D_2O instead of H_2O had been perdeuterated, implying that hydrogen from the water medium is a labile participant in hydrothermal reactions.

The Arrhenius parameters for bagasse hydrothermal conversion at 500 °C were determined as shown: $E_a = 101.4\ kJ \cdot mol^{-1}$ and $A = 1.28 \times 10^9\ min^{-1}$.

Chapter 1. INTRODUCTION

Recent concerns about the dramatic volatility in oil markets, anxiety regarding the longevity of existing petroleum reservoirs, worries over continued supply from politically unstable oil-producing nations, and continued fears over the contribution of fossil fuels to global climate change have all generated renewed consideration of alternative energy sources. Indeed, biomass is an appealing, viable alternative energy reserve that has gone largely untapped. Currently biomass ranks fourth internationally as an energy source, supplying about 14% of global energy requirements [1]. The use of biomass fuels as an energy source would likely result in net zero carbon dioxide emissions since carbon dioxide is removed from the air during plant growth [2]. Moreover, biomass is the sole renewable resource of carbonaceous matter, and it is available in abundant supply both nationally and globally.

The emergent biomass alternative energy sector has raised legitimate questions regarding the sustainability of current agricultural systems in light of increased biomass consumption [3]. It is generally assumed that both agricultural wastes and dedicated energy crops will be required to support the operational demands of biomass conversion processes. The possibility that agricultural acreage presently devoted to food production could be displaced in favor of energy crops has become a controversial issue. Fortunately, there are several other biomass resources, such as municipal solid waste, algae, aquatic biomass, sewage sludge, noxious weeds, etc., that are also readily available. Interestingly, the use of noxious weeds has received little attention in recent years despite their prolific abundance. For instance, kudzu, also known as the "scourge of the South", has now overspread nearly 10 million acres in the southeastern United States and advances at a rate of 150,000 acres annually[4]. It is estimated that kudzu exacts a $500 million toll each year in both eradication costs and lost agricultural and timber production [5].

Apprehension regarding the accessibility of fossil fuels during the midst of World War II, prompted a study by Berl [6] at the Carnegie Mellon Institute on the alternative production of oil from plant matter. It was already recognized that America's petroleum reserves would not last indefinitely and that the conversion of biomass carbohydrates to fuel would assist in eliminating wartime rival Germany's competitive edge in the production of synthesis gas via the Fischer-Tropsch process. Berl showed that biomass cooked in an alkaline aqueous solution at temperatures near 230 ºC formed a plastic product termed "proto-product". The proto-product contained 60% of the original carbon content found in the biomass substrate. Complete hydrogenation of the proto-product resulted in a mixture of aliphatic and aromatic hydrocarbons that was "very similar to natural oil". Heinemann [7] analyzed petroleum-type hydrocarbons that are produced from sugarcane pyrolyzed under pressure at approximately 400°C in an alkaline aqueous solution. The liquefied sugarcane yielded 33 wt % petroleum-type hydrocarbons, 10 wt % gasoline and 7 wt % lubricating oil on a dry, ash free basis.

In 1941, 30 million cars on U.S. highways burned 5.56×10^7 long tons of liquid fuel (i.e., 1 long ton = 1016.05 kg). Berl estimated that 9.7×10^6 acres of planted sugarcane in the continental United States would yield this value of transportation fuel, assuming average sugarcane yields of 18.55 long tons per acre from Louisiana fields. The significantly higher yields of sugarcane per acre in the present era (in 2008, 31.5 short tons = 28.13 long tons) per acre in Louisiana) [8] would require dramatically less acreage to achieve the same amount of liquid fuel. It was determined that 100 long tons of dry sugarcane would provide 2,980 gallons of gasoline, 3,430 gallons of middle weight oil, 1,210 gallons of lubrication oil, and 8.45 long tons of raw cane sugar. Furthermore, Berl suggested that 6.6×10^7 long tons of liquid fuel could

be generated each year in the U.S. simply if the 2.6×10^8 long tons of plant residue produced annually were converted to liquid fuels.

The ultimate objective of biomass conversion is to transform a substance having a relatively low calorific or economic value into gas or liquid products having either substantive calorific content for direct use as fuels or into economically valuable chemical commodities. The crude bio-oil resulting from biomass conversion is especially attractive because of its high energy density relative to unprocessed biomass, increased transportability, straightforward utilization, and compatibility with existing petroleum-based technology and infrastructure. The separation and isolation of individual components for the specialty chemicals market in an efficient, cost-effective manner is a challenge confronting the industrial utilization of biomass-derived liquids [9].

Biochemical and thermochemical conversion processes were not originally designed for refractory agricultural feedstocks, such as sugarcane bagasse, but rather for wood and coal. Bagasse has traditionally been regarded as a problematic fuel due to its fibrous nature, low bulk density, high moisture content, and moderate ash content [10]. The heterogeneous, voluminous nature of bagasse has been a crucial issue in its transition to becoming a feedstock for modern pyrolysis and gasification technologies. For instance, raw bagasse tends to float on top of the bed instead of mixing inside the bed material in fluidized bed reactors. Therefore, bagasse must typically be sieved, milled, and pelletized before it is capable of being utilized in energy applications. This achieves a higher density feed and reduces the amount of soil that goes into the operation, although it does incur additional processing costs. The substantial moisture content of sugarcane bagasse can be another troublesome issue in traditional pyrolysis and gasification processes, wherein the biomass substrate must be dried before being processed to

avoid system upsets resulting from bridging and clogging. Frequently, enzymes or acid are used to "pre-treat", or hydrolyze, lignocellulosic feedstocks. Enzymes are often incapable of sufficiently degrading recalcitrant biomass substrates and the isolation, purification, and maintenance of enzymes is expensive. Acids are able to disrupt the internal structure of lignocellulose but they are beset by their corrosiveness, which requires the use of costly corrosion-resistant materials.

The use of hydrothermal media in organic reactions has surged over the last two decades, largely because water under such conditions can effectively minimize the processing difficulties experienced with other biological or thermochemical techniques [11-19]. Hydrothermal media are nominally subdivided into two categories: supercritical water and subcritical water. Water above its critical point (374 ºC and 221 bar) is termed supercritical water, while water below its critical point is referred to as subcritical water. A third category called near-critical water is sometimes used to identify water in close proximity to the critical point. In this paper, near-critical water is defined to exist between 350-400 ºC at pressures above the critical pressure. Near-critical and supercritical water (NSCW) possess unique solvent abilities that are strongly influenced by changes in the temperature and pressure [20]. In this state, water behaves as a homogeneous, nonpolar solvent that is capable of solubilizing diverse organics and gases [21, 22]. The temperature and pressure in NSCW processes can be adjusted to favor either free-radical or aqueous phase reaction as desired [12]. The ability to tune the properties of NSCW allows users of biomass hydrothermal processes to control the rate of hydrolysis and the solubilization of components. Biomass treatment in NCSW is also advantageous because wet feedstocks can be processed as received without requiring separation of the water. In other

biomass processing techniques, such as pyrolysis, gasification, and combustion, water can only be removed via a phase change, which acts a parasitic energy sink [23].

The newfound interest in hot, compressed water, however, has a long historical antecedent in preparative chemistry [24]. In 1851, de Sénarmont introduced the field of geological sciences to the technique known as hydrothermal synthesis [25]. de Sénarmont discovered that he could prepare microscopic crystals from various mineral carbonates, sulfates, and sulfides using sealed glass ampoules in an autoclave. Since then, hydrothermal synthesis has been used to form a wide variety of materials, including single crystal elements, oxides, hydroxides, silicates, germanates, chalcogenides, and halides. Hydrothermal chemistry is also responsible for the conversion of biogenic marine and terrigeneous matter into petroleum and hydrocarbon gases near deep ocean volcanic vents [26-29], as pictured in Figure 1.

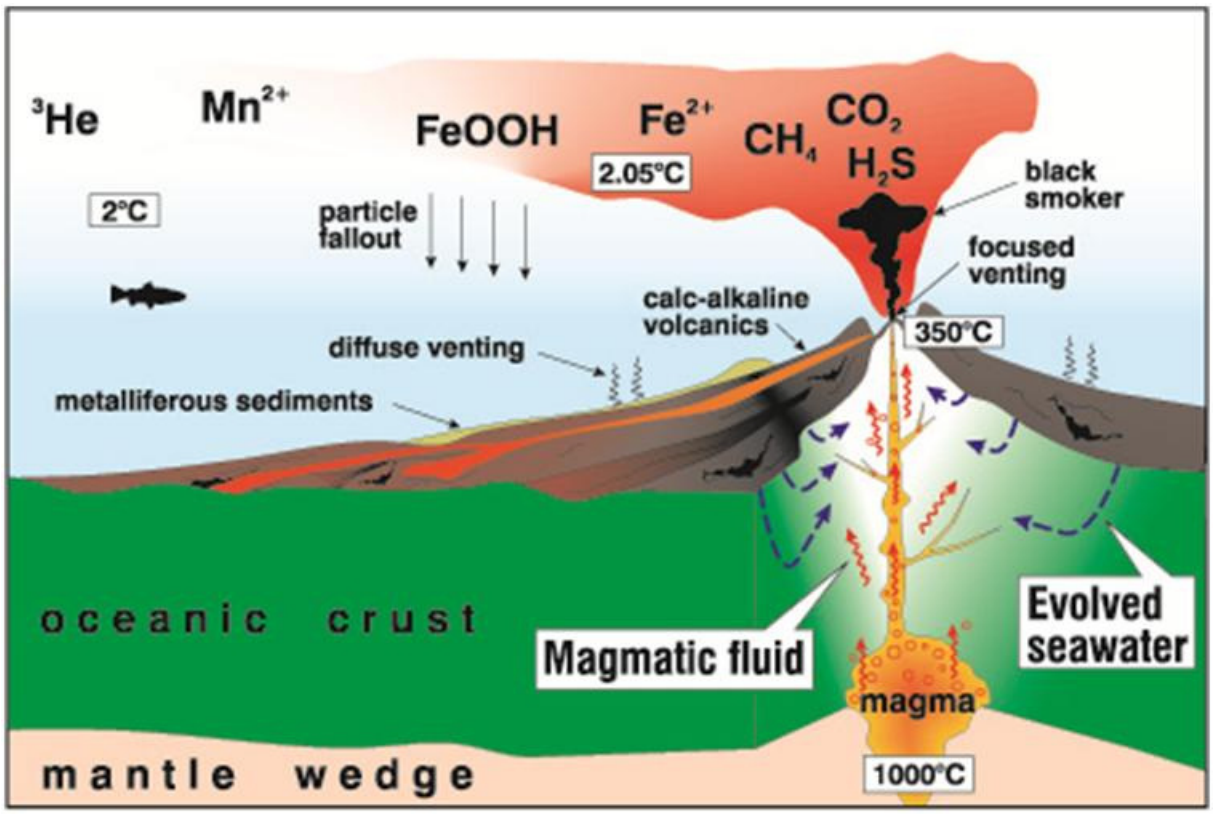

Figure 1. Hydrothermal subsea volcanic vent (provided courtesy of de Ronde [30]).

Numerous studies have explored the influence of temperature, pressure, heating rate, and water density on the hydrothermal gasification of both actual biomass and model biomass compounds [17, 31-39]. There have also been several kinetic studies performed on the hydrothermal conversion of model biomass compounds (e.g., glucose, fructose, sucrose, maltose, cellulose, cellobiose, etc.) [40-49] Far fewer studies have examined the importance of other processing parameters (i.e., residence time, particle size, substrate weight loading, atmosphere, etc.) on the rates, product distributions, and yields of hydrothermal reactions involving actual biomass. Although the severity parameter is commonly used to correlate time and temperature effects on biomass conversion in subcritical water [50-53], there is no evidence in the literature that a similar comparison is applied for biomass transformed in supercritical water. Moreover, there has been little attempt to discriminate differences that may arise by decomposing bagasse in near-critical water and in supercritical water. Aside from methane, published data on the production of volatile hydrocarbons from hydrothermally treated biomass is surprisingly scarce. Finally, it is frequently assumed that the hydrogen atoms in the volatile and semi-volatile products obtained from biomass hydrothermal conversion are derived from the biomass. This assumption belies the fact that nearly 60 atomic wt % of hydrogen gas formed the reaction of water with biomass theoretically comes from the water itself. Therefore, the research presented in this document represents an effort to address some of the unresolved issues surrounding biomass hydrothermal conversion that have been exposed here.

Chapter 2. LITERATURE SURVEY

2.1 Biomass Composition

Biomass is a complex material that is broadly defined as any non-fossil form of carbon of recent biological origin. It includes agricultural crops and residues, aquatic vegetation, forestry products and wastes, grasses, municipal solid refuse, and sewage [54, 55]. A more precise term for the organic matter that is derived from photosynthesis in green plants is phytomass [56]. It has been estimated that the global net primary production of phytomass equals 1.72×10^{11} metric tons per annum on a dry basis [57]. The net primary productivity of photosynthetic plants is defined as that fraction of organic matter that remains after a portion of the gross phytomass material has been expended in plant respiration. About 1% of the annual generation of phytomass is consumed in the construction, energy, and textile industries [56], and an additional 0.72% is harvested for food production, either directly from agricultural plants or indirectly from herbivorous livestock [58]. The composition and structure of phytomass vary depending on the type and species of plant selected. Most plant biomass consists of three primary organic building blocks, namely cellulose, hemicellulose, and lignin, along with additional minor constituents such as minerals and organic extractives (e.g., tannins, terpenes, waxes, fats, and flavonoids). The term lignocellulose is frequently used to designate the presence of these three main biomass fractions [59]. The lignocellulosic components of biomass are actually hydrolyzable polymers comprised of basic sugar units (e.g., glucosan, xylan, mannan, and galactan) and units with aromatic alcohols.

2.1.1 Cellulose

Cellulose comprises the largest component of the naturally occurring organic substances found on Earth (Figure 2). Fengel and Wegener [60] calculated that the total amount of cellulose in the biosphere is equal to 2.65×10^{11} metric tons, assuming that 40% of the carbon in plant matter is bound in cellulose.

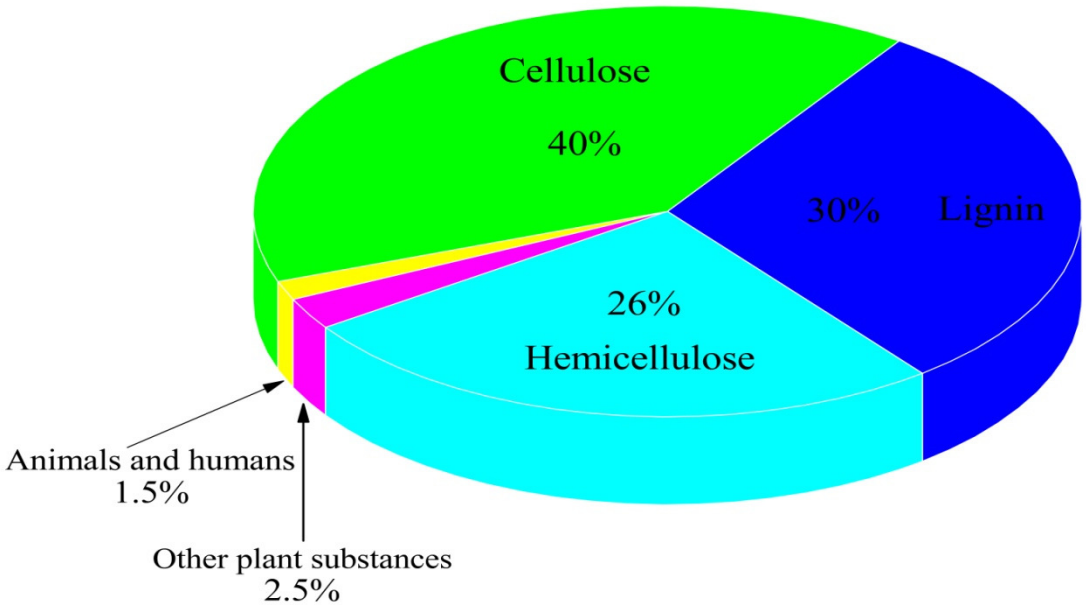

Figure 2. Distribution of carbon bound in biospheric organic matter. Adapted from Gruber [61].

The cellulosic component can be described by the gross chemical formula $(C_6H_{12}O_5)_n$. "Native cellulose" as it exists in plants can have an average molecular weight ranging from 5×10^4 to 2.5×10^6 g·(g·mol)$^{-1}$ [60]. Cellulose is a linear, non-branched macromolecule of variable length consisting of polymeric β-(1,4)-D-glucopyranose building blocks linked together by (1→4)-glycosidic bonds in the alpha configuration [62]. The β-glycosidic linkages between the anomeric carbons of cellulose produce linearity in the cellulose chains; the corresponding α-

glycosidic linkages in the glucose polymer forces starches to twist into a helical structure. The number of glucose monomer units in a given molecular chain determines its degree of polymerization (DP). Aside from its degree of polymerization (DP), cellulose is otherwise indistinguishable between different types of biomass. In contrast, the character of hemicellulose and lignin fluctuates significantly with respect to the type of biomass selected.

Typically, cellulose exhibits a high degree of crystallinity and has a relatively ordered structure that results in the formation of microfibrils having a high tensile strength. The microfibrils provide a rigid cellular matrix for plant cells that is extremely inert and very resilient against attack from chemical reagents. The chain rigidity and conformational stability observed in cellulose polymer chains is imparted largely by intramolecular hydrogen bonding [46]. Cellulose constitutes almost half of the cell wall material that provides the skeletal support structure of biomass. At standard ambient temperature and pressure (SATP), namely T = 25 °C and P = 1 bar, cellulose is insoluble in water. Cellulose undergoes significant thermal degradation in the temperature range of 280–320 °C [63, 64]. Pyrolysis of cellulose produces chiefly 1,6-anhydro-β-D-glucopyranose (levoglucosan) and 1,6-anhydro-β-D-glucofuranose, with minor amounts of furans, organics, and some volatiles (e.g., CO, CO_2, methanol, acetic acid, and hydroxyacetaldehyde).

2.1.2 Hemicellulose

Hemicelluloses are complex polysaccharides that are found in the cell walls of biomass along with cellulose. Unlike cellulose, hemicellulose is synthesized from several different polysaccharides, including glucose, xylose, arabinose, galactose, 4-*O*-methylglucuronic acid, and galacturonic acid residues. Hemicellulose has an average molecular weight that is less than 30,000 $g\cdot(g\cdot mol)^{-1}$. Hemicellulose has an amorphous, branched configuration with a relatively

low DP, usually on the order of 50–200. The hemicelluloses are located throughout the plant fiber and contribute to the development, growth, and structure of the cell walls of the plant [65]. Hemicelluloses can be segregated into three distinct groups, based upon the major sugar in their backbone chains: (1) xylans (e.g., xylan, 4-*O*-methylglucuronoxylan, 4-*O*-methylglucuronoarabinoxylan), (2) mannans (e.g., glucomannan, galactomannan), and (3) galactans (e.g., galactan, arabinogalactan) [56]. Xylan is the predominant polysaccharide found in wood hemicelluloses and it is also the principal hemicellulose found in hardwoods, while mannan is the major hemicellulose observed in softwoods. Xylan is also found in significant amounts in perennial C_4 plants, such as maize, sugarcane, and sugar beets.

Hemicellulose solubility depends greatly on the chain length and on the extent of branching and acetylation in the molecule. Although hemicelluloses can be readily solubilized in dilute alkali, difficulties in extraction and isolation are commonly encountered and have been ascribed to covalent bonding between hemicelluloses and lignin [65, 66]. Hemicellulose exhibits lower thermal stability than cellulose, decomposing in hot water at temperatures of 200–230 °C [67]. This is ostensibly due to the lack of crystallinity and order within the hemicellulose framework. Furan derivatives, acetic and formic acids, and some furanoses are formed in abundance during hemicellulose thermal degradation. Pyrolytic decomposition of hemicellulose also yields more gas and less liquid than for cellulose [68].

2.1.3 Lignin

The chemistry of lignin has garnered considerable scientific attention since 1838, when Anselme Payen ascertained that wood is essentially a matrix of cellulose fibers cemented together with a special material, which he coined *le matiérel incrustante*, or lignin [69]. Lignin is generally envisaged as an amorphous, highly-branched phenolic biopolymer. The lignin

structure contains three distinct substituted phenylpropanoid (C_9) monomers (i.e., coniferyl, *p*-coumaryl, and sinapyl alcohols) that are randomly assembled via connecting linkages to form a matrix. There are two different linkages that connect the repeating phenylpropane units, or "monolignols", with each other: alkyl ayrl ether (C-O-C) bonds and carbon-carbon (C-C) bonds. The most frequent linkage found in lignin polymers is the uncondensed β-alkyl-4-aryl ether (β-O-4): β-1 linkages connecting 1,2-diarylpropane units and β-5 linkages connecting *p*-phenylcoumaran units [70]. Less common are dialkyl and diaryl ether linkages. Lignin is formed when the various monolignol precursors undergo enzymatic oxidative polymerization. The precursors are obtained from phenylalanine by deamination, ensued by hydroxylation of the phenyl group, methylation, and decarboxylation of the terminal acetyl moiety [71]. Each phenylpropanoid compound has a hydroxyl group located in the *para* position and then anywhere from zero to two methoxy groups are located *ortho* to the *para* hydroxyl group, as shown in Figure 3.

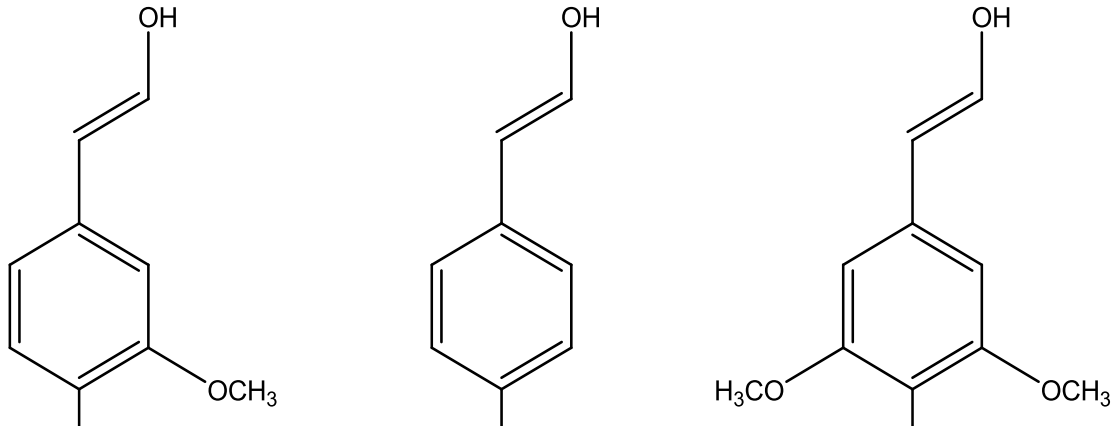

Coniferyl Alcohol *p*-Coumaryl Alcohol Sinapyl Alcohol

Figure 3. Structures of the three primary phenylpropane monomers.

The major phenyl propenols from lignin are the hydroxycinnamyl alcohols, coniferyl, p-coumaryl, and sinapyl alcohol. The hydroxycinnamyl alcohols are also commonly designated by their alternative names: guaiacol, *p*-hydroxyphenol, and syringol. The relative proportions of the three different monolignols will differ with respect to the botanical origin of the lignin, thereby affording a basis for the categorization of lignins.

A standard convention regarding the numbering of side chains in the monolignols has not yet been established. In fact, the observation by Pearl [72] in 1967 that "although many investigators have attempted to define lignin in terms of its chemical structure, none have succeeded in proposing an adequate definition" rings true even today because "lignin is a group of high molecular-weight amorphous materials that are chemically closely related." The complexity of the lignin polymeric structure is revealed in the schematic constitution for spruce lignin, as proposed by Freudenberg [73] and shown in Figure 4. The structural model was constructed using knowledge regarding the formation of lignin intermediates and data from lignin chemistry research (e.g., elemental composition of spruce lignin, mutual ratios of the 3 key monolignols, quantity and type of hydroxyl moieties, carbonyl group content, etc.) [72, 73]. It is worth noting that the schematic formulation, which contains 18 major structural units, is but a fragment of the entire lignin molecule. Freudenberg acknowledged that the scheme must be considered as an approximation and because of this he also included two variants to the main formulation for spruce lignin, as indicated by the structural units designated 13b/14b and 13c/14c, which are feasible alternatives to the cyclolignan units represented by 13a/14a.

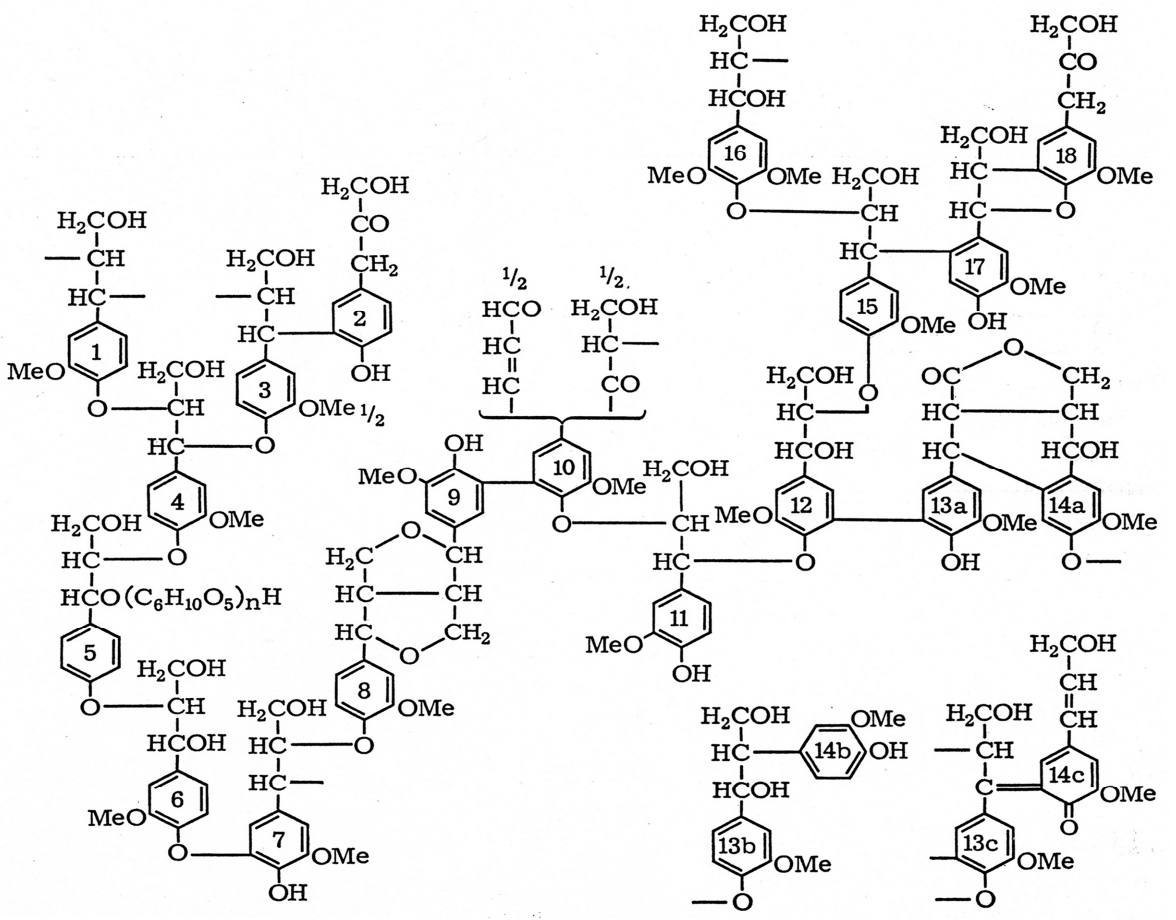

Figure 4. Spruce lignin structural scheme as proposed by Freudenberg [73]

There have been no fewer than 6 additional formulations for softwood lignins since Freudenberg's final spruce lignin formulation in 1968 [74-79]. Lignins exist as polymers in the cell wall structure, and are commonly attached to neighboring cellulose fibers to create a lignocellulosic complex. Although lignin is found in all plants, the degree of lignification is more extensive in highly-structured, vascular plants. Plants having a higher level of development contain more methoxy groups and fewer C-C bonds between the C_9 groups of the lignins [56]. Furthermore, there are reduced quantities of free phenol and carboxyl groups in the more advanced plants. Lignin is more plentiful in softwoods than in hardwoods or grasses. Table 1 displays the average distribution of hydroxycinnamyl alcohols in lignin derived from various biomass types.

In temperate locations, lignin tends to accumulate to a greater degree in softwoods (i.e., 25–35 wt %) than either hardwoods (i.e., 18–25 wt %) or grasses (i.e., 11–27 wt %) [80, 81]. Softwood lignin contains primarily guaiacols with a small amount of *p*-hydroxyphenols and a trace quantity of syringols. Hardwood lignin contains an almost equal proportion of guaiacols and syringols and a negligible quantity of *p*-hydroxyphenol. Hardwoods have a higher content of acetyl and methoxy groups making them suitable substrates for destructive distillation to produce acetic acid and methanol [82]. Grasses typically contain mostly guaiacols followed by respectively lower levels of syringols and *p*-hydroxyphenols. The relative ratio of syringyl to guaiacyl groups in lignin determines the frequency of the major bonds. Hardwoods contain approximately 60% β-O-4 ether linkages as compared to softwoods which contain about 48% β-O-4 ether linkages [70]. Softwood lignins are therefore more highly condensed and have a higher molecular weight than hardwoods, making them harder to delignify.

The distribution of hydroxycinnamyl alcohols can vary depending on the location within a specific plant. For instance, trees that are subjected to climatological and geological stresses (e.g., exposure to strong winds, heavy snows, unstable slopes, changing riverbanks, etc.) often feature trunks or main stems that are bent or displaced from the vertical [83]. Wood in the displacement region develops differently than wood growing in non-stressed regions and is referred to as reaction wood. In hardwoods reaction wood forms asymmetrically on the upper side of the displacement and is called tension wood, while in softwoods reaction wood forms on the underside of leaning trunks and branches and is termed compression wood. The vessels in tension wood are fewer and of smaller diameter than those in normal wood and consequently tension wood often exhibits longitudinal shrinkage. Tension wood also features a higher cellulosic content than normal wood. Compression wood is characterized as having a higher

density, hardness, and lignin content than normal wood. Lumber obtained from reaction wood has many undesirable physical properties, including a tendency to fail under load and to crack and split when being cut. Not surprisingly, there is a notable difference in the distribution of phenylpropane units in normal softwood tissues and those of compression wood as shown in Table 1 below. Guaiacol units are replaced with *p*-hydroxyphenol units in the stressed compression wood region.

Table 1. Distribution of hydroxycinnamyl alcohols in biomass. Adapted from Brunow [84].

Lignin Source	Guaiacol	Syringol	*p*-Hydroxyphenol
Grasses[1]	70%	25%	5%
Hardwoods	49%	49%	2%
Softwoods	95%	1%	4%
Compression wood	70%	0%	30%

Both lignins and lignocellulose are resilient to microbial decay and nearly impervious to chemical conversion via hydrolysis. Nevertheless, lignocellulose can be degraded and the lignin portion extracted upon treatment with concentrated sulfuric acid. Dehydration is the most common lignin degradation mechanism and is the reason nearly all low molecular weight products derived from lignin contain phenolic hydroxyl (OH^-) moieties. The primary pyrolytic decomposition products of lignin are phenols and aromatic hydrocarbons [63]. Although the thermal decomposition of lignins occurs over a broad temperature range [85], the main degradation zone and maximum recovery of phenols was found [63] to be in the temperature range of 275–350 °C. The formation of phenols occurred in the following sequence with increasing reaction temperature: methylguaiacol, ethylguaiacol, guaiacol, propenylsyringol, phenol, and catechol. Between 350–450 °C the phenols were transformed into catechols via demethylation of the dimethoxy groups.

2.2 Properties and Characterization of Sugarcane Bagasse

Sugarcane is an important agricultural commodity that is cultivated in over 100 countries with an annual worldwide production in 2007 of 1.56 billion metric tons [86]. It is grown commercially in a broad swath that extends roughly from a latitude 13.5° north of the Tropic of Cancer (i.e., Salobreña, Spain) [87, 88] to a latitude 8° south of the Tropic of Capricorn (Salto, Uruguay) [88]. Sugarcane is a perennial C_4 grass whose photosynthetic efficiency is virtually nonpareil in the plant kingdom [89]; only the giant sequoia tree (*Sequoia gigantea*) is capable of producing more biomass [90]. Despite the current excitement surrounding the efficacy of microalgal carbon dioxide fixation [91-96], sugarcane still appears superior to microalgae at converting incident solar radiation into carbohydrates (maximum recorded solar energy capture efficiency of 5.0% for sugarcane in Hawaii [97] and 5.1% for sugarcane in S. Africa [98] vs. 4.9% for green algae in Thailand [99]) [97-101][2]. Alexander [103] determined that the average annual energy output for a first-generation energy cane grown in Puerto Rico was 1138 $GJ\cdot(ha\cdot year)^{-1}$, while Huber *et al*. [104] reported a maximum annual energy productivity of 1460 $GJ\cdot(ha\cdot year)^{-1}$ for sugarcane. These values are 23% and 57% greater than the net annual energy yield for microalgae (928 $GJ\cdot(ha\cdot year)^{-1}$), respectively, as calculated by Christi [105].

The predominant components in sugarcane are water, soluble solids, of which sucrose is foremost, and lignocellulosic fiber, of which cellulose is the main constituent. The composition of sugarcane is influenced by numerous environmental determinants and cultural practices, *viz*. climatic factors, weather hazards, topography, soil type, sugarcane variety, planting practices,

---

[1] *p*-coumaric acid attached by ester linkages is not included

drainage, irrigation, diseases, pests, fertilization, and harvesting methods [88, 106-108]. Current practice for harvesting of sugarcane utilizes mechanical combines that cut whole cane stalk into sections called billets. The billeted sugarcane is then processed in a sugar mill where it is macerated and shredded using swing-hammer crushers. After this stage, the crushed cane is conveyed to a train of multiple-roller mills to be pressed. During this step, imbibition water is introduced to the system so as to increase the juice extraction efficiency at each successive mill. The shredded fibrous residue that exits the last mill is called bagasse.

Given its provenance from sugarcane, it is natural that bagasse also exhibits great compositional and morphological heterogeneity. On average, fresh bagasse consists of 44–56 wt % moisture, 43–52 wt % lignocellulosic fiber, and 2–6 wt % soluble solids, and 1–5 wt % inorganic matter [109-111]. The amount of ash in bagasse is largely dependent on the amount of soil brought in from the fields with the sugarcane [112]. Sugarcane bagasse contains three major structural components [110, 111, 113], *viz*.,

- Long, hard-walled cylindrical cells that compose the rind, known as true fiber, and fibrous vascular bundles composed of small phloem vessels in the interior and large xylem vessels on the exterior are known collectively as fiber
- Soft, thin-walled parenchyma and epithelial cells from the inner stalk that are known as pith and which contain most of the juice in cane
- A dense non-fibrous epidermis known as the wax

Dry bagasse typically contains about 50 wt % true fiber, 15 wt % fibrovascular bundles, 30 wt % pith, and 5 wt % wax [90, 110, 111]. The proportion of the major components in

---

[2] It bears mentioning that the debate regarding whether microalgae or sugarcane is the better synthesizer of sunlight is not new and dates back at least 60 years, when Ledón *et al*. [102] determined that sugarcane had a higher photosynthesis conversion efficiency (3.4%) than the microalgae Chlorella pyrenoidsa (2.5%).

bagasse depends largely on the aforementioned environmental factors that influence sugarcane, the variety of cane, its maturity at harvest, harvesting practices, and the milling efficiency [110]. Table 2 provides a compositional analysis of bagasse cultivated in various countries. Multiple listings for a single country indicate that the analyzed bagasse came from samples collected at different locations within the country, in different years, or possibly both. An indication of the compositional variation that arises because of varietal differences in sugarcane is given in Table 3. The danger of falsely assuming that bagasse samples collected from a sugar mill pile are uniformly homogeneous is clearly illustrated in Table 3 by examining the compositional differences that occur between "average" samples 1 and 2. The chemical composition of bagasse varies between 27–50% cellulose, 20–35% hemicellulose, 10–25% lignins, and 1–6% ash on a dry weight basis. A nominal composition of 40% cellulose, 32% hemicellulose, 20% lignin, 6% extractives, and 2% ash for dry bagasse is sometimes reported [114, 115].

The calorific values of most biomass materials and fossil fuels are commonly reported in terms of either the gross heating value (GHV) or the net heating value (NHV). The GHV is the amount of heat released from a specific quantity of fuel (initially at 20 °C) after it is combusted and the products cool back to 20 °C. The latent heat of vaporization of water is included in the GHV. The NHV is equal to the GHV less the latent heat of the vapor, and it is often used to denote the calorific value of moist biomass. In practice, the NHV is commonly used in European publications, whereas the GHV is routinely reported in North American publications [116]. Hugot [117] reported the average GHV of dry bagasse to be 19.25 $MJ \cdot kg^{-1}$ and the average NHV of dry bagasse to be 17.78 $MJ \cdot kg^{-1}$. Hugot also reported the average GHV and average NHV of wet bagasse (i.e., 50 wt % moisture) to be 9.62 $MJ \cdot kg^{-1}$ and 7.64 $MJ \cdot kg^{-1}$, respectively. Behne [118] analyzed eleven varieties of bagasse and found an average GHV of 19.52 $MJ \cdot kg^{-1}$ on a dry,

ash-free basis (dafb). Nicolai [119] reported that the GHV of bagasse samples collected from sugarcane in six different countries ranged from 19.13 to 23.97 $MJ \cdot kg^{-1}$ (dafb) with a mean value of 20.42 $MJ \cdot kg^{-1}$ (dafb).

Table 2. Composition of whole bagasse from various origins (dry wt % basis).

Origin	Cellulose	Hemicellulose	Lignin	Ash	Extractives
Australia [120]	41.3	30.3	10.0	6.1	12.3
China [121]	43.6	33.5	18.1	2.3	0.8[3]
Egypt [122]	41.8	27.5	17.9	2.0	NA[4]
Guadeloupe [112]	41.7	28.0	21.8	3.5	4.0
Mauritius [110]	26.6	29.7	14.3	2.4	NA[4]
Mexico [110]	34.9	31.8	22.3	2.3	2.8[5]
Mexico [110]	37.6	31.1	19.4	3.2	2.2[5]
Mexico [123]	40.0	32.0	20.0	2.0	6.0
Philippines [113]	34.9	31.8	22.3	2.3	NA[4]
South Africa [124]	38.5	31.4	22.2	3.1	NA[4]
Hawaii [110]	38.1	23.7	20.5	2.4	2.5[5]
Hawaii [125]	36.5[6]	25.0[6]	25.5	3.7	1.8[7]
Louisiana [110]	36.8	29.4	21.3	2.9	4.0[5]
Louisiana [126]	36.3	28.2	20.2	2.3	12.8
Louisiana [127]	50.4	28.5	14.9	2.0	4.2
Louisiana [128]	36.7[8]	24.7[8]	24.5	4.4	NA[4]
Puerto Rico [113]	30.1	29.6	18.1	3.9	NA[4]

[3] Alcohol – toluene extractives; represents wax fraction
[4] NA – Data not available
[5] Hot water extractives
[6] Calculated using the following formulas: % cellulose = 0.9(% glucose) and % hemicellulose = 0.9(% galactose + % mannose) + 0.88(% xylose + % arabinose + % uronic acids)
[7] Alcohol extractives

Table 3: Composition of whole bagasse from different sugarcane varieties (dry wt % basis).

Origin	Variety	Cellulose	Hemicellulose	Lignin	Ash	Extractives
Australia [129]	Badilla	28.2	22.2	24.4	4.1	3.0[9]
Australia [129]	1900	30.6	23.9	24.4	2.6	1.9[9]
Australia [129]	Mixed sample 1[10]	32.5	24.3	21.7	2.5	3.2[9]
Australia [129]	Mixed sample 2[10]	28.0	21.8	21.7	2.5	4.4[9]
Cuba [110]	Mecladas P. Noriega	46.6	25.2	20.7	2.6	4.1[11]
Mauritius [110]	M 134.32	40.6	28.4	19.6	6.3	3.1[11]
South Africa [110]	PO3 2878	45.3	24.1	22.1	1.6	4.7[11]
Florida [110]	CL-41-233	30.6	26.6	18.2	1.0	15.1[11]
Hawaii [110]	44-3098	38.7	27.1	21.6	4.6	2.6[11]
Hawaii [110]	37-1933	38.3	27.3	19.4	1.3	2.2[11]
Hawaii [130][12]	H65-7052	36.2[13]	22.5[13]	24.2	4.0	4.4[14]

For comparative purposes, the compositional characteristics and calorific content of sugarcane bagasse are provided in Table 4 along with those of municipal solid waste, lignite, and bituminous coal. It is immediately apparent that bagasse contains significantly higher moisture content than the other fuel types. Depending on the thermochemical conversion process that is chosen, the relatively high moisture content of sugarcane bagasse can be viewed either as an inherent liability or as an opportune benefit. In terms of inorganic content, bagasse is clearly a

[8] An amount equivalent to the detected level of arabinose (2.4 wt%) was deducted from the total glucan content (39.1 wt%) and attributed to the hemicellulose complex
[9] Alcohol – benzene extractives
[10] Samples were collected from a bagasse pile containing different varieties and thus represent an "average" variety
[11] Hot water extractives
[12] NIST reference material 8491
[13] Calculated using the following formulas: % cellulose = 0.9(% glucose) and % hemicellulose = 0.9(% galactose + % mannose) + 0.88(% xylose + % arabinose + % uronic acids)
[14] Alcohol extractives

superior feedstock. The lower levels of ash in bagasse are translated into greater economic savings during post-processing clean-up of volatile and semi-volatile products.

Table 4. Ultimate analysis of bagasse compared with other fuels. Reprinted from Nathan [131].

	Bagasse	Municipal Solid Waste	Lignite	Bituminous Coal[15]
Moisture, wt %	49	21	35	6
Ash, wt %	2	25	7	8
Combustible matter, wt %	49	54	58	86
Carbon[16]	48	52	45	79
Hydrogen[15]	7	6	7	6
Oxygen[15]	45	41	47	8
Nitrogen[15]		> 1	> 1	2
Sulfur[15]		> 1	> 1	5
GHV, $MJ \cdot kg^{-1}$				
As received	9.53	11.44	16.21	28.71
Moisture and ash free	19.46	21.05	28.05	33.59
NHV, $MJ \cdot kg^{-1}$				
As received	7.62	10.19	14.48	27.57

There are nearly 1200 sugar mills in 80 nations that process almost 1.2 metric GT of sugarcane annually [132]. About 280 kg of wet bagasse (i.e., 50 wt% moisture) is generated per metric ton of milled sugarcane. Up to 90% of this quantity is combusted in furnaces to supply the heat and steam requirements for the sugar mill, while the remainder is simply discarded by either burning, composting, stockpiling, or landfilling [133]. Bagasse is often intentionally burned at low efficiencies to avoid disposal issues. The extravagant intake of raw bagasse as a principal fuel source at sugar mills could be deemed "wasteful", considering its low NHV [134].

[15] High volatile B fraction
[16] Given as percent of combustible matter

Upgrades to aging sugar mill boiler units and ancillary infrastructure could decrease overall sugar mill energy demand to 50% of the bagasse generated [135]. The thermochemical conversion of sugarcane bagasse into a gaseous or liquid fuel would enhance the overall energy value of this residue and solve a substantial biomass disposal dilemma.

Typically, freshly processed bagasse is stored in piles that can be located either inside or outside the sugar mill. Bagasse stored under ambient environmental conditions is readily susceptible to microbial decay [109, 113, 136-142]. Bagasse deterioration studies have shown that degraded bagasse contains anywhere from 2 to 5×10^8 live microbes per gram of bone dry bagasse [138, 139]. The microbial distribution was categorized as follows: 74% bacteria, 13% yeasts, 7% fungi, and 6% actinomycetes. The general degradation mechanism experienced by stored bagasse is outlined in Figure 5. Microbiological activity in bagasse piles is maximized when bagasse moisture contents are above 60 wt % (wet basis) [109]. Activity is greatly diminished below 40 wt % moisture content and ceases almost entirely below 25 wt % moisture.

The residual sucrose in the bagasse pith ferments to yield both glucose and fructose. Yeast supplies the invertase necessary for the inversion of sucrose, which occurs most rapidly at 60 °C. The next step in the biological breakdown of the bagasse occurs when bacteria invade the storage pile. Glucose isomerase and hexokinase act to partially hydrolyze cellulose and hemicellulose. The fermentation of cellulose and hemicellulose produces additional heat and acidity within the pile. At this stage, the bagasse pile has had time to become infested with a broad assortment of bacteria and fungi. Black and brown rot fungi supply ligninase, laccase, and peroxidase enzymes, which hydrolyze the bagasse causing discoloration of the bagasse fibers. White rot fungi provide cellulase and hemicellulase enzymes, which cause moderate bagasse

deterioration resulting in reduced fiber length and strength. Actinomycetes will further feed on the degraded bagasse and cause severe damage and discoloration to the remaining bagasse fibers.

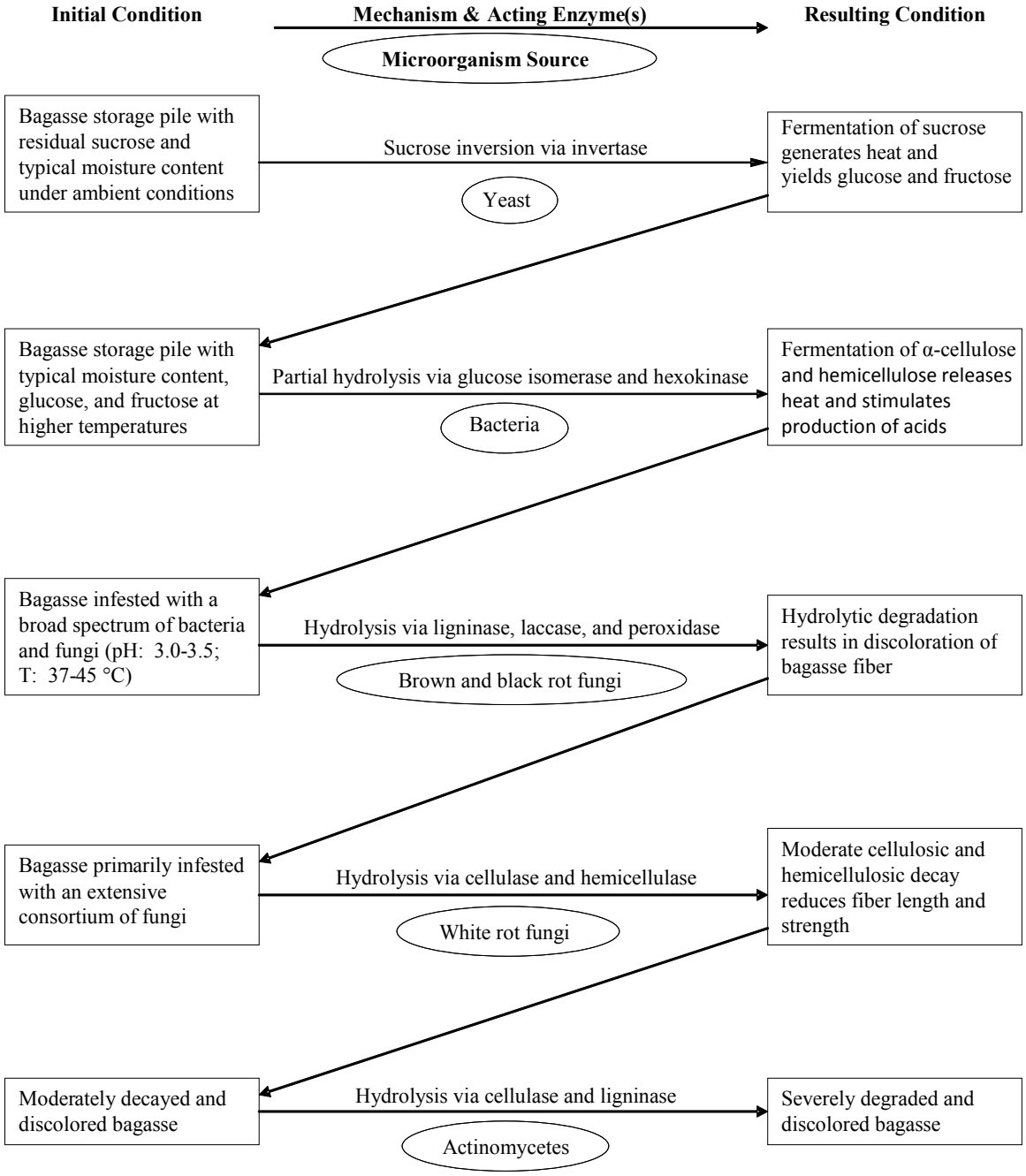

Figure 5. Routes for microbial decay in sugarcane bagasse. Adapted from Sharma *et al.* [140].

2.3 Unique Properties of Near- and Supercritical Water (NSCW)

Water is a prevalent and readily accessible compound occurring in nature. Water has the added benefit of being the most environmentally friendly material available, making it the consummate 'green solvent' [143]. Liquid water at standard ambient temperature and pressure (SATP), defined as T = 25 °C and P = 1 bar, exhibits marginal miscibility with non-polar substances and gases. Nevertheless, it is an effective solvent for salts at SATP because of its high relative dielectric constant of 78 and a correspondingly high density of 0.997 $g \cdot cm^{-3}$.

The critical point of water occurs at 373.946 °C (T_c) and 220.64 bar (P_c). Water at temperatures above its critical point is designated supercritical water (SCW). The distinction between gases and liquids vanishes beyond the critical point. Water that exists both above the critical temperature and pressure is normally termed as a supercritical fluid, whereas water that is above the critical temperature but below the critical temperature is generally referred to as superheated vapor. Traditionally, water in an environment at or below its critical point has been termed near-critical or subcritical water, depending on its relative proximity to the critical point [144]. The physical boundaries that separate the near-critical water regime from those of the subcritical and supercritical regions are vaguely defined and often are incongruent between different studies [12, 145-147]. In this study, subcritical temperatures are defined as those below 350 °C. The near-critical temperature region is demarcated between 350–400 °C. Supercritical conditions are considered to exist above 400 °C. The phase diagram for water is depicted in Figure 6. At the triple point, labeled TP, all three phases – gas, liquid, and solid – exist in equilibrium. The gas and solid phases exist in equilibrium along the blue curve below TP, which is known as the sublimation pressure curve of the solid. Along the vapor pressure curve (between TP and CP) the gas and liquid phases are in equilibrium. The solid and liquid phases

are in equilibrium along the green curve above TP. The negative slope up to 2 kbar indicates that the melting temperature decreases as the pressure is increased. This interesting phenomenon is linked to the decrease in the volume of H_2O that occurs upon melting as the very open structure of ice partially collapses

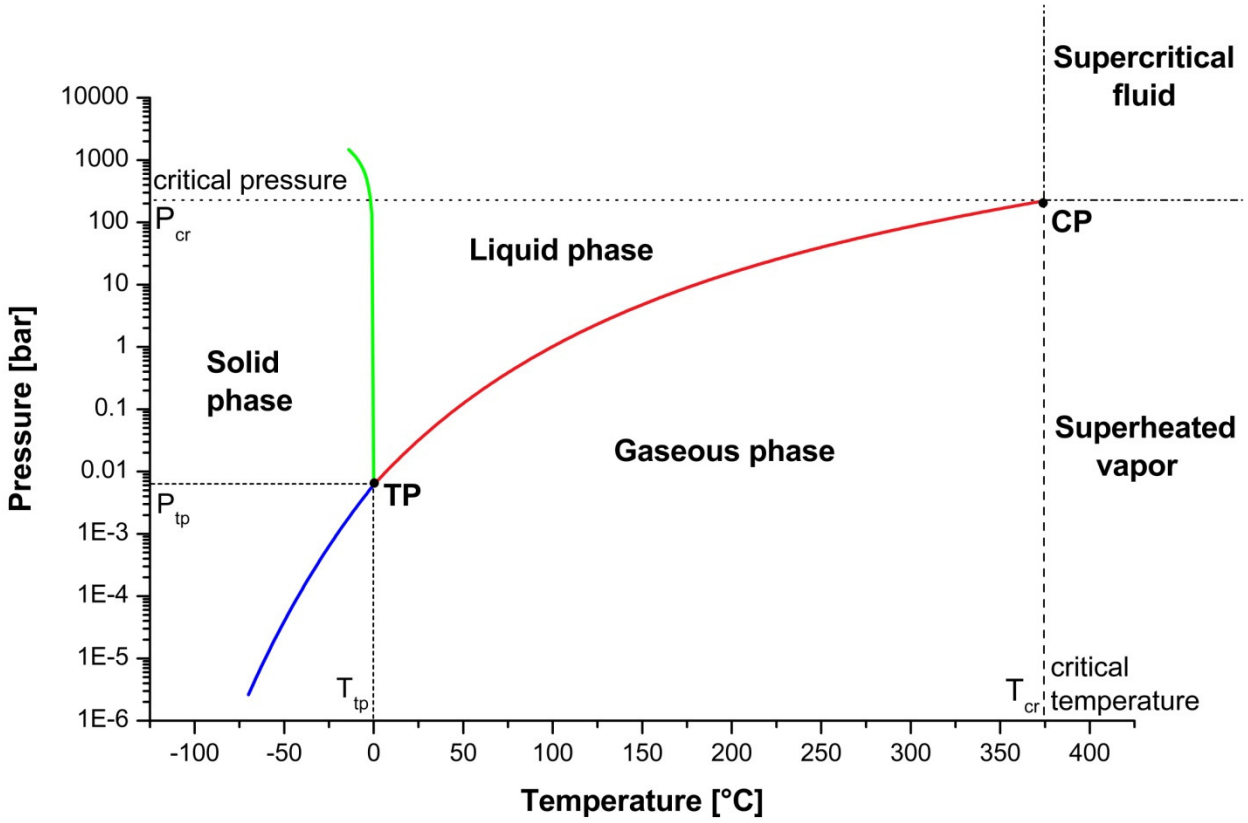

Figure 6. Phase diagram for water. Plotted using reference data from NIST [148].

At the supercritical point, the boundary between liquid and gaseous phases for water becomes blurred resulting in a single, homogeneous state of matter. Salient properties of water, such as the dielectric constant and ionization, can be altered simply by adjusting the density of water, which, as a state function, is closely dependent upon pressure and temperature. The surface diagram illustrated in Figure 7 represents the isobaric heat capacity (C_p) of water plotted as a function of temperature and pressure. The heat capacity approaches infinity at the critical point of water [20]. Even at 400 °C and 250 bar, the heat capacity remains an order of

magnitude greater than its asymptotic value of roughly 4 $kJ \cdot °C^{-1}$ at regions far from the critical point. The phase transition between a liquid and a supercritical fluid is classified as a first-order phase transition. A first-order phase transition is one in which the first derivatives of the chemical potentials with respect to pressure and temperature are discontinuous. The isobaric heat capacity is defined as the enthalpy of a substance divided by its temperature at a constant pressure. In a first-order phase transition, the enthalpy changes by a finite quantity for a marginal change in the temperature. Thus, as summed by Atkins [149], "first-order phase transitions are characterized by an infinite heat capacity at the transition temperature."

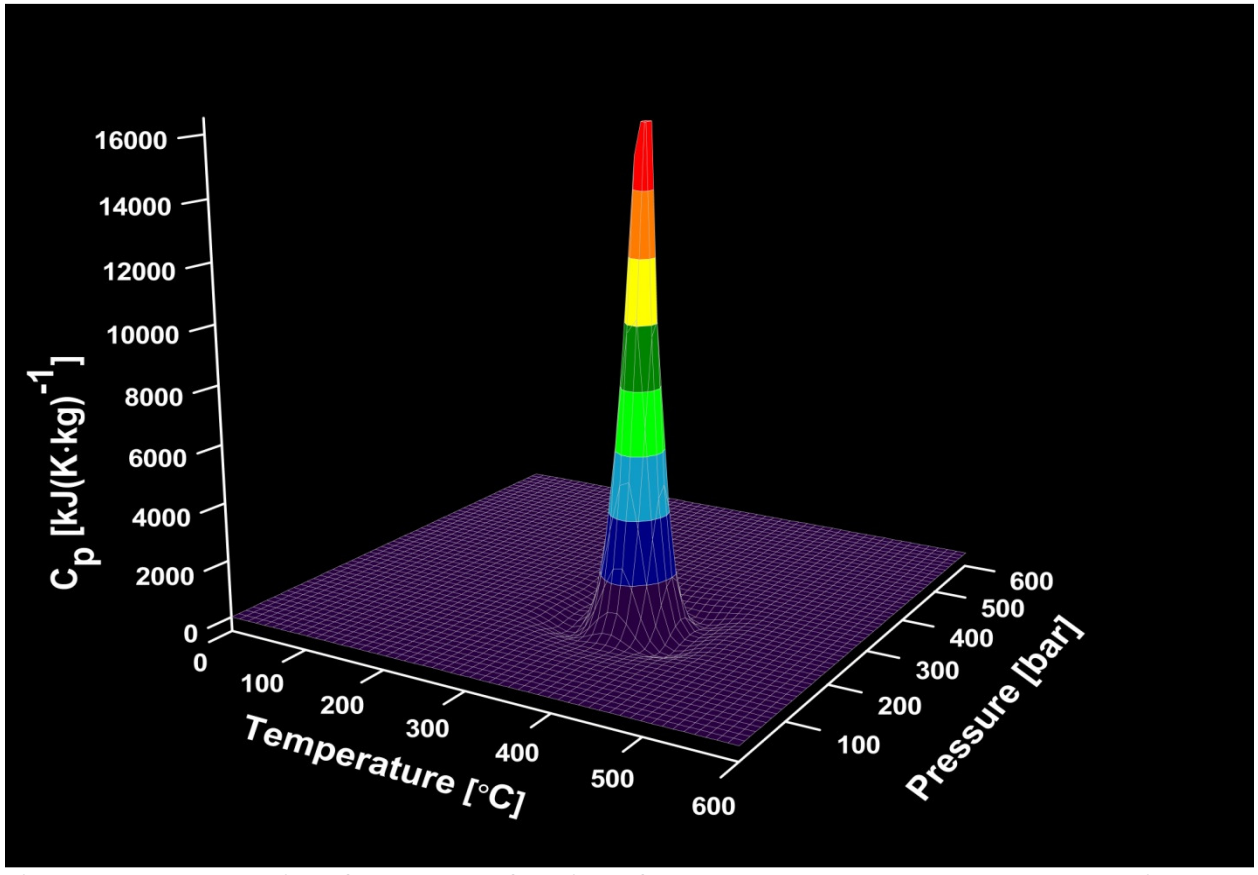

Figure 7. Heat capacity of water as a function of temperature and pressure. Plotted using data from NIST [148].

The density of water at SATP is 0.997 $g \cdot cm^{-3}$. As can be seen in Figure 8, the water density decreases slowly until about 100 °C, at which point the rate of decrease accelerates until

the density plummets to a minimum of about 0.068 g·cm^{-3} at 500 °C and 200 bar. At the critical point of water, the density of water, known as the critical density (ρ_c), is 0.325 g·cm^{-3}. The density of water has a considerable impact on reaction kinetics and dynamics under supercritical conditions. In the critical region, the density of the solvent can have a large influence on free radical chemistry because the solvent molecules are often collision partners in free radical reactions [13]. Free radical reactions tend to predominate in lower pressure and less dense SCW, while ionic reactions prevail in high pressure and dense SCW.

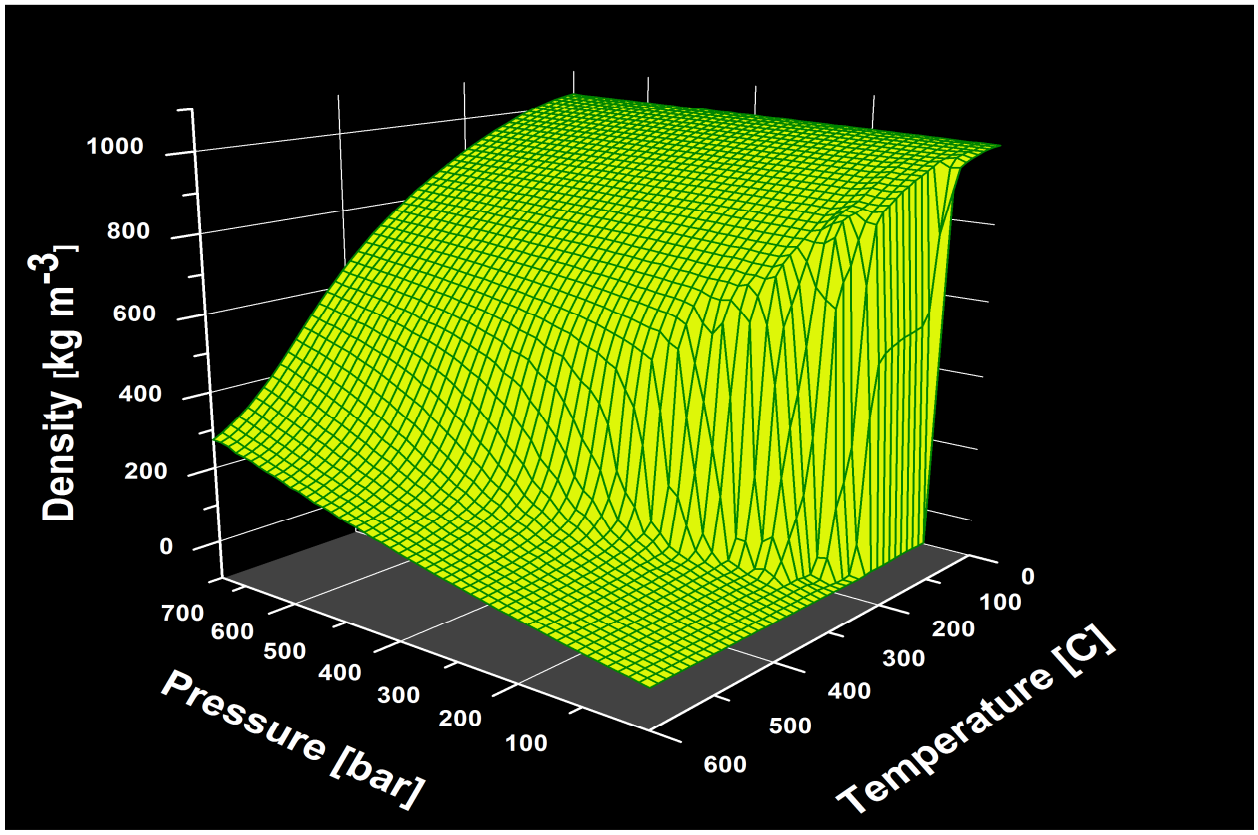

Figure 8. Density of water as a function of temperature and pressure. Plotted using data from NIST [148].

A distinctive feature of supercritical water is its ability to be concomitantly used as both a reactant and a solvent. Water in the critical region has a unique status as a solvent; it is an inferior solvent for ionic compounds, such as mineral salts, yet it is entirely miscible with numerous gases and organic compounds. In SCW, the density (ρ_w), dielectric constant (ε),

hydrogen bonding, ion product of water (K_w), and dynamic viscosity (η) are modified to an extent that the behavior of the water is comparable to that of a mildly polar organic solvent at SATP [150]. The dielectric constant for water at SATP is 78.5 but at the critical point this value plunges to just 6 [148]. The high dielectric constant of water at SATP, which is afforded by the strong, cohesive hydrogen bonding under these conditions, allows ionic and polar compounds to readily solvate. The sudden decrease in the dielectric constant of water at high temperatures and pressures diminishes the ability of water to buffer the electrostatic potential between ions at these temperatures, and thus dissolved ions can exist as contact ion pairs in SCW [20]. The very low dielectric constant of water in the critical region reveals that the water has lost much of its polarity, which is why supercritical water exhibits an enhanced solubility toward nonpolar organic compounds. Hence, typically insoluble nonpolar hydrocarbons, such as benzene, toluene, and heptane, become miscible at their respective critical solution conditions [151].

Several studies have even demonstrated that wood can be entirely liquefied in SCW. Conversely, the ability of water to ionize and solvate inorganic salts is markedly diminished under supercritical conditions. For instance, sodium chloride (NaCl) has a solubility of 101 ppm and calcium chloride ($CaCl_2$) has a solubility of just 3 ppm in supercritical water at 500 °C and 250 bar; in subcritical water at 300 °C the corresponding solubilities of these salts are 370,000 and 700,000 ppm, respectively [152-154]. The inability of near-critical and supercritical water (NSCW) to dissolve inorganic electrolytes that were previously solvated in liquid water at SATP is ascribable to the weakening and eventual disappearance of hydrogen bonding at high temperatures. The destabilized hydrogen bonding in NSCW results from the breakage of many hydrogen bonds under the energetic conditions at high temperatures and also from a reduction in hydrogen bond donating ability by about 10% for every 100 °C rise in temperature [155]. In

fact, Hoffman and Conradi [156] measured the proton NMR chemical shift for water from ambient to supercritical conditions and determined that the extent of hydrogen bonding at 400 °C and 400 bar is only 29% of that in ordinary water at SATP.

At SATP, the self-dissociation of water into hydronium (H_3O^+) and hydroxyl (OH^-) ions is almost negligible because the concentrations of these ions is extremely low at 10^{-7} mol·L^{-1}, which corresponds to an ion product (K_w) for water of 10^{-14} [mol·L^{-1}]^2. Here K_w is defined as the product of $[H_3O^+][OH^-] = 1.008 \times 10^{-14}$ at SATP. It has been determined that it requires approximately 10 h for a randomly selected water molecule to dissociate at SATP [157]. The ionization constant for water rises sharply near its critical point, and thus, water can hydrolyze compounds that are catalyzed by H^+ and OH^- ions. Aqueous phase chemistry prevails when the $K_w \geq 10^{-14}$ and heterolytic mechanisms are common. Free radical chemistry dominates when $K_w << 10^{-14}$ and homolytic reactions become the norm. Typically, the K_w is greater than 10^{-14} when the density of water, $\rho_w > 0.3$ [158]. Selectivity toward heterolytic mechanisms increases with increasing water density under isothermal conditions. Klein *et al*. [159] used kinetics and solvent effects to probe whether S_N1 or S_N2 mechanisms prevail during the hydrolysis of model compounds (i.e., dibenzyl ether, phenethyl phenyl ether, and guaiacol) in SCW. It was established that the S_N2 mechanism using water as a nucleophile represents the most probable hydrolysis reaction pathway.

Both near-critical and supercritical water have shown remarkable promise in facilitating hydrothermal reactions because of their unique physicochemical properties. The unique solvent strength associated with NSCW provides an inherent advantage over conventional processes for the devolution of biomass. Biomass contains lignocellulosic materials that are intractable. The use of NSCW as a reaction medium is environmentally benign because it precludes the need for

acids and harmful solvents. Moreover, traditional biomass decomposition methods, such as gasification and pyrolysis, often require the comminution of the biomass solids to promote efficient heat and mass transfer between the particle and the surrounding gas. A smaller particle size helps minimize the time required to transfer heat to the center of the particle and leads to higher conversion yields. The extensive solids comminution necessitated by other biomass conversion processes is substantially lessened in supercritical water treatment.

Traditional biomass conversion processes, such as pyrolysis and gasification, require sizable energy input relative to the overall biomass energy content in order to remove the latent moisture within the biomass. Hydrothermal techniques that utilize NSCW, however, are not hindered by the presence of moisture. On the contrary, water is beneficial because it serves as a reactant in the hydrothermal process. The energy requirements in a biomass liquefaction operation are substantially lowered because the drying stage can be eliminated. It is important to emphasize that the energy requirements needed to heat water at pressures greater than the saturation pressure (P_{sat}) or P_c are not prohibitive because it is possible to avoid an explicit phase transition in the system [23]. In fact, slightly more enthalpy (i.e., 3700 $kJ \cdot kg^{-1}$) is required to heat water up to 600 ºC in a system operating at atmospheric pressure (1.01 bar) than the enthalpy (i.e., 3440 $kJ \cdot kg^{-1}$) required to heat water up to 600 ºC in a system at 300 bar [160]. Systems operating at or below P_{sat} entail higher enthalpies because the liquid water must first be entirely evaporated at 100 ºC before proceeding to higher temperatures.

Treating biomass in hydrothermal processes is also advantageous because such systems allow the user to manipulate, or "tune", the solvation energy of the solute by adjusting the density of the solvent as necessary. Careful control of the density in a compressible medium, such as supercritical water, can make it possible to significantly vary the mean interparticle

distance between solute species and solvent molecules such that the intermolecular pair potential can be shifted to favor attractive forces at low densities and repulsive forces at high densities [161]. Selective separation and purification of intermediates and products can be achieved via phase partitioning. Similarly, various components can be retained in solution or precipitated out by tuning the water appropriately. By affording control over the solubility of biomass components, hydrothermal methods provide a means of regulating the rate of hydrolysis.

2.4 Thermochemical Conversion Processes

Biomass hydrothermal conversion, or hydrothermolysis, is the convergence of flash pyrolysis, liquefaction, and gasification processes. By controlling the operating parameters, such as temperature, pressure, residence time, and biomass loading, thermolysis processes in NSCW can be optimized for either gas or liquid production. A brief overview of each of these traditional thermochemical processes is provided for better comprehension of the wide variety of reactive processes that are possible in both sub- and supercritical water.

2.4.1 Pyrolysis

Thermogravimetric analysis of various types of biomass has revealed that biomass pyrolysis occurs in three stages, corresponding to three distinct temperature regimes: (1) evaporation of moisture occurs at temperatures less than 130 ºC; (2) primary devolatilization occurs at temperatures between 200 to 400 ºC with extensive depolymerization starting at about 300 °C; (3) substantially reduced volatilization occurs at temperature above 400 ºC [162, 163]. The primary devolatilization reactions involve a reduction in molecular weight, or degree of polymerization via bond cleavage, at a temperature in the range of 150–190 °C [82]. These initial reactions are accompanied by the formation of free radicals, scission of carbonyl,

carboxyl, and hydroperoxide groups, release of carbon monoxide and carbon dioxide, and ultimately creation of a charred residue. The solid char residue can undergo further chemical and physical conversions at temperatures in excess of 400 °C, albeit product formation occurs more slowly than during primary pyrolysis [163]. Cellulose and hemicellulose are the main sources of the volatiles in biomass feedstocks, such as bagasse, but they yield only 8 to 15% of their weight as charcoal under slow pyrolysis conditions [54]. Lignins yield almost 50% of their weight as charcoal in conventional slow pyrolysis processes. Fisher *et al.* [163] demonstrated that at low heating rates ($\leq$ 60 °C·min^{-1}) the mechanical integrity and structure of the cellulose particles in the biomass is retained, notwithstanding a slight contraction in size due to the heating. However, at rapid heating rates (> 1000 °C·s^{-1}) cellulose particles present evidence of softening and melting, seen under scanning electron microscopy (SEM), and the primary decomposition step no longer occurs directly through vaporization of the particles.

For biomass that contains mainly oxygenated cellulose and hemicellulose, pyrolysis is endothermic at temperatures under 400 to 450 °C and exothermic above those temperatures [54]. The primary exothermic reactions that result in the devolatilization and carbonization of the biomass are categorized according to their function, *viz*:

Pyrolysis Methanation Reactions

$$2CO + 2H_2 \rightarrow CH_4 + CO_2 \qquad \Delta H_{25°C} = -247 \text{ kJ/g·mol} \qquad (1)$$

$$CO + 3H_2 \rightarrow CH_4 + H_2O(g) \qquad \Delta H_{25°C} = -206 \text{ kJ/g·mol} \qquad (2)$$

$$CO_2 + 4H_2 \rightarrow CH_4 + 2H_2O(g) \qquad \Delta H_{25°C} = -165 \text{ kJ/g·mol} \qquad (3)$$

Methanol Formation

$$CO + 2H_2 \rightarrow CH_3OH \qquad \Delta H_{25°C} = -128 \text{ kJ/g·mol} \qquad (4)$$

$$CO_2 + 3H_2 \rightarrow CH_3OH + H_2O \qquad \Delta H_{25°C} = -87 \text{ kJ/g·mol} \qquad (5)$$

Pyrolysis (Char Formation)

$$C_6H_{10}O_5 \rightarrow 3C + CO + 5H_2 + 2CO_2 \qquad \Delta H_{25°C} = \text{-81 kJ/g·mol} \qquad (6)$$

Water-Gas Shift Reaction

$$CO + H_2O(g) \rightarrow CO_2 + H_2 \qquad \Delta H_{25°C} = \text{-41 kJ/g·mol} \qquad (7)$$

At higher temperatures the pyrolytic process is governed by the rate of heat and mass transfer rather than by chemical reaction kinetics. Rapid heating rates at temperatures below 650 °C followed by immediate quenching have been shown to favor the production of liquids and curtail char and gas formation [164]. Rapid heating rates, to temperatures in excess of 650 °C, tend to support the formation of gaseous products at the expense of liquid and char yields. The reduction in char formation at high heating rates is attributable to the cleavage of higher molecular weight compounds into smaller species [165]. Finally, slow heating rates at low reaction temperatures favors char production. The produced gas obtained from conventional biomass pyrolysis at slow heating rates typically has a net heating value (NHV) that is on the order of 3.5–8.9 $MJ\cdot(N\cdot m^3)^{-1}$, where '$N\cdot m^3$' indicates normalized volumetric flow at SATP [166]. As a comparison, gases produced from rapid pyrolysis of sugarcane bagasse have an average LHV that ranges between 15–20 $MJ\cdot(N\cdot m^3)^{-1}$ [167].

Fast, or rapid pyrolysis, has received considerable attention because it remains the only technique that has been commercially validated [168]. Rapid pyrolysis is performed using high heating rates on the order of 10–200 $°C\cdot s^{-1}$ at moderate temperatures between 400–600 °C under an inert atmosphere. Vapor residence times are generally under 2 s. Immediate quenching of products is necessary to eliminate conversion reactions resulting in gas or char formation. Flash pyrolysis is distinguished from fast pyrolysis by its use of exceptionally rapid heating rates (~ 10^4-10^5 $°C\cdot s^{-1}$), high temperatures (> 600°C), and brief vapor contact times (< 0.5 s) [169].

The rapid heating rate in fast pyrolysis causes bond scission of the polymeric units in the biomass leading to the formation of chiefly gaseous products. The duration of the vapor residence time has a significant impact upon the pyrolysis oil yield. It is known that secondary condensation reactions take place at temperatures below 400°C, resulting in a decreased average molecular-weight of the organic liquid product [170]. The extent of these secondary reactions is dictated by both the vessel temperature and the residence time. The collection of the liquid product requires prompt cooling and coalescence of the aerosolized vapors.

Pyrolysis oils usually contain a high oxygen and water content and thus have a calorific heating value (20–25 $MJ \cdot kg^{-1}$) less than half that of fuels derived from petroleum [171]. The low pH (2-3) of pyrolysis liquids caused by the high presence of acetic and formic acids poses corrosion concerns in any subsequent applications of the bio-oil [172]. Furthermore, pyrolytic oils have low thermal and chemical stability, which is attributed both to high oxygen content and the presence of many unsaturated double bonds (e.g., olefins, aldehydes, ketones, esters) [173].

2.4.2 Liquefaction

Liquefaction is the process of directly converting biomass, in a single step, into liquid fuels or chemicals. Although liquefaction is sometimes regarded as the "poor relation" in terms of the thermochemical processing triumvirate and as such has received limited focus [174], it should be noted that the use of liquefaction is economically advantageous for those feedstocks containing high levels of moisture, because unlike other processes the excess water in the biomass is a reactive asset. Direct liquefaction has the potential to produce liquid oils with high calorific content containing a broad spectrum of industrially important chemicals, *viz*. alcohols, aldehydes, condensed aromatics, ethers, furans, phenols, organic acids, etc. [175-178]. Friederich Bergius is credited with developing the coal liquefaction process, for which he

received a Nobel Prize in 1932 [179]. Liquefaction typically is performed under a low temperature (i.e., 300–400 °C), high pressure (i.e., 50–300 bar) environment and can be carried out either in the presence of absence of liquid media [169, 180-182].

Traditionally, biomass liquefaction has taken place in the presence of a reducing atmosphere (e.g., H_2, CO, or H_2 + CO) or in the presence of alkaline catalysts (e.g., Na_2CO_3, K_2CO_3, etc.). In fact, direct thermochemical liquefaction was previously defined as a process that "essentially consists of heating biomass particles in water with a mild alkali" [176]. Conventional direct liquefaction is frequently described as a process that exposes an aqueous slurry of wood chips or sawdust powder in the presence of sodium carbonate catalyst to a hydrogen and/or carbon monoxide atmosphere at 300–370 °C and 140–280 bar for a period of 20–90 minutes [183]. An overview regarding the status of not only technical advancements in direct thermochemical liquefaction, but also applied processes in pyrolysis and bio-oil upgrading, during the period 1983 to 1990 was provided by Elliot *et al*. [184]. Further information regarding historical developments in the catalytic hydrotreatment of thermochemically derived bio-oils is offered in a comprehensive review by Elliot [185]

The differences in operating conditions can have a dramatic impact on product yields and compositions. It is generally accepted that the solvent plays a critical role in the liquefaction of biomass. Liquefaction systems that have an aqueous solvent are known as hydrolysis processes, while those liquefaction methods whose active solvent is non-aqueous are called solvolysis processes. The solvent prevents the recondensation of intermediate compounds, circumventing the production of higher molecular weight condensates, which give rise to unwanted char. A French study by Bouvier *et al*. [180] revealed that biomass feedstock can be completely converted within 10 min at 240 °C with no char formation when phenol was used as a solvent.

Thermal efficiency is defined as the ratio between the calorific heat values of the bio-oil product and the biomass feedstock plus any external heat input. The theoretical thermal efficiency for any industrial process is 79%. The HTU biomass liquefaction process developed by the Shell Research Laboratory in the Netherlands has achieved a thermal efficiency of 75% [186-189]. The HTU process liquefies all types of biomass in liquid water at temperatures between 300–350 °C, pressures between 120–180 bar, and residence times ranging from 5 to 30 min. Liquefaction removes oxygen from the biomass primarily in the form of CO_2 and H_2O. The product consists of 45 wt % biocrude, 25 wt % gas (> 90% CO_2 and remainder CO), 20 wt % H_2O, and 10 wt % solubilized organics (e.g., acetic acid and methanol). The loss of oxygen lowers the overall O_2 content of the resulting biocrude to between 10–18 wt %. This confers a relatively high net calorific value (NHV) in the range of 30–35 $MJ \cdot kg^{-1}$ to the biocrude product.

During the OPEC oil embargo of the 1970s, the Pittsburgh Energy Research Center (PERC) went to great lengths to find the lowest possible liquefaction operating temperatures for a variety of organic substances and wastes (e.g., wood, cornstalks, rice hulls, pine bark, cellulose, softwood sawdust, newsprint, *mycelia* solids, and bovine and chicken manure), to minimize the costs associated with high steam pressure. Appell *et al*. [190, 191] at PERC examined the conversion of assorted cellulosic wastes to heavy oil. The rationale behind their study was to identify the extent of the hydrothermal reaction and the chemical mechanisms in this type of reaction. Cellulosic waste conversions were above 90%, often approaching 99%, with oil yields ranging from 40 to 60%, for temperatures between 250–425 °C, pressures between 100–275 bar abs., and a residence time of 10 to 30 min. They noted that liquefaction below 250 °C is not practical because of the slow rate of reaction that governs the conversion of carbohydrates to bio-oil at these temperatures. Appell's group also noted that operating above 400 °C was of little

economic value because of the high pressures involved. The PERC researchers determined that operating in the 300–350 °C temperature span provided the optimal compromise between product yield and quality versus carbon monoxide consumption and operating pressure costs.

Ogi *et al*. [192] observed that the maximum yield of heavy bio-oil (28.4 wt %) occurred at 300 °C. Above 300 °C the heavy oil yield and the oxygen content of the oil both declined, and by 400 °C the gas content rose to roughly 40 wt %. The calorific content of the fuels obtained at the higher temperatures was higher due to the removal of the oxygen. All of the heavy oils, except the oil obtained at 375 °C, tended to congeal and become viscous after prolonged exposure to air, suggesting repolymerization.

An early liquefaction study conducted by Modell [193] on glucose at subcritical and supercritical conditions is routinely cited among scientific reviews of biomass liquefaction. A remarkable discovery at near-critical conditions of 374 °C and 218 bar was observed, which became the foundation for three future U.S. patents [194-196]. There was absolutely no formation of solid char product; the products consisted only of liquid organics and a gaseous mixture of H_2, CO, CO_2, CH_4, and light, volatile hydrocarbons. The gaseous effluent contained hydrogen, carbon monoxide, carbon dioxide, methane, ethane, and ethylene. Acetylene was not observed and no higher molecular-weight gases were expressly sought, although their potential presence should have been as specious peaks during successive chromatographic sample analyses. The absence of such peaks and carbon mass balance closures approaching 97% or higher where the glucose was entirely converted to a gaseous product suggested that C_3 and higher gases were a nominal component under the experimental conditions.

A Canadian study [197] on the liquefaction of a hybrid poplar (*Populus Euramericana* clone I-45/51) at 350 °C and 103 bar for 2 h under a hydrogen atmosphere in the presence of

Raney nickel revealed complete conversion of the wood to oil and gas. The bio-oil product contained 10 wt % oxygen and had a calorific value of 41.8 $MJ \cdot kg^{-1}$. Longer reaction times resulted in lowered oil viscosities and higher heating values.

The compositional and physical properties of liquid bio-oils generated from wood chips using liquefaction (e.g., LBL oil and BOM oil) and pyrolysis are compared with standard No. 6 residual fuel oil in Table 5 below. The oils derived from biomass have substantially higher moisture and ash contents than traditional bunker fuel oil. The higher moisture levels also contribute to the higher oxygen content observed in the bio-oils. The increased oxygenation of the bio-oils causes a large decrease in their HHVs when compared to that of No. 6 fuel oil.

Table 5. Liquid bio-oil characterization and comparison with No. 6 fuel oil [198, 199].

Type of Oil	C	H	N	O	S	Moisture	Ash	Specific Gravity[17]	HHV [MJ kg^{-1}]
	Weight Percent								
No. 6 Fuel Oil	85.7	10.5	2.0	0-3.5	0-3.5[18]	< 0.05	0.20	0.98	42.3
BOM Wood Oil	82.0	8.8	0.6	9.2	—	0.66	3.1	—	36.8
LBL Wood Oil	72.3	8.6	0.2	17.6	0.006	0.78	8.5	1.19	33.7
Pyrolysis Oil	57.5	7.6	0.9	33.4	0.2	0.5-1.0	14	1.30	24.4

A comparative product analysis of bio-oils derived from liquefaction and flash pyrolysis processes is presented in Table 6. The consistently higher carbon content in the bio-oil product obtained from the liquefaction tests indicates that the treatment method may play an integral role in determining the overall product composition. It is speculated that the char from the flash pyrolysis processes contains predominantly carbon, whereas the solid residues from the liquefaction processes may contain more heteroatomic and inorganic content. It is also important to observe that the flash pyrolysis bio-oils are as a whole more highly oxygenated than the

[17]Where specific gravity of H_2O is equal to 1.00

liquefaction bio-oils. This observation simply reaffirms the aforementioned propensity for biomass oxygen to be removed in the form of CO_2 or H_2O during liquefaction processes. The relatively low hydrogen to carbon atomic ratios imply that a large proportion of the oil product is comprised of highly unsaturated compounds, including aromatics. The type of feedstock also has a large influence on the product oil composition as noted in a study by Elliot *et al*. [200]. Bio-oil from the flash pyrolysis of poplar wood was composed mainly of phenols, ketones, aldehydes, and organic acids; bio-oil from the flash pyrolysis of peat contained primarily straight chain olefins and phenols with minor quantities of ketones.

Table 6. Product analysis of bio-oils obtained from liquefaction and flash pyrolysis processes [181].

Feedstock	Temp. [°C]	Pressure [bar]	C	H	N	O	S	H/C
			Weight percent					
High-Pressure Processes								
Newsprint	250	138	71.7	7.3	< 0.3	~20.6	< 0.1	1.21
Pine needles and twigs	250	138	72.2	8.7	1.05	18.0	0.10	1.43
Sewage sludge	250	138	77.0	10.7	2.80	8.8	0.64	1.65
Cellulose	250	138	72.4	7.0	0.004	20.4	0.2	1.15
Sucrose	350	277	75.2	9.1	—	15.7	—	1.44
Municipal refuse	380	346	79.8	10.4	3.0	6.8	0.05	1.55
Manure	380	311	80.4	9.4	3.0	6.9	0.26	1.39
Microalgae	400	277[19]	81.2[20]	8.6	5.4	3.5	—	1.26
Flash Pyrolysis								
Aspen	450	0	53.8	6.7	—	39.3	—	1.48
Sewage Sludge	450	0	69.4	10.2	5.8	14.5	—	1.75
Poplar	500	0	49.8	7.3	0.0	42.8	0.0	1.74
Peat	520	0	67.1	9.0	3.4	20.3	0.1	1.59

[18]Legal sulfur limit determined by process site, e.g., 0.35% maximum in Los Angeles County
[19] Estimated
[20] Microalgae analysis was calculated from the analysis of product fractions (oil and asphaltenes) and the product distribution

2.4.3 Gasification

Gasification can be broadly classified as the thermal transformation of any carbonaceous fuel into a gaseous product with an exploitable heating value. This definition of gasification encompasses the processes of pyrolysis, partial oxidation, and hydrogenation, but omits combustion since the off-gas has no heating value. The partial oxidation of biomass to form a combustible gas is the hallmark that characterizes the gasification process; gasification usually requires about 30% of the oxygen required for complete, ideal combustion [201, 202]. Typically, gasification occurs at high temperatures (600–1000 °C) in three distinct steps, in which the biomass feedstock undergoes a thermal decomposition to produce a synthesis gas (also known as syngas) comprised primarily of carbon monoxide and hydrogen in various ratios. Other gas-phase products obtained from biomass gasification include carbon dioxide, methane, and water.

The gasification process involves an initial rapid pyrolysis of the biomass feedstock at high temperature followed by partial oxidation to form primarily gas products with varying quantities of char and tar, both of which can foul surfaces and plug pipes in the cooler sections of the system. The last stage of gasification involves the removal of char and tars from the gas product stream. Complete removal of the char can be effected with the use of filters since it is a solid particulate. Unfortunately, even the most sophisticated filtration devices can remove only 90% of the tar in the gas stream [203]. The final volatile product composition are contingent upon both the reactor type and the reaction conditions, which entail the heating rate, residence time, temperature, and internal atmosphere [204]. Figure 9 presents a simplified model describing the steps involved in biomass pyrolysis and gasification. The reactions in this

mechanism can be influenced by the reaction temperature, heating rate, residence time, particle size, atmosphere, pressure, and media composition [163].

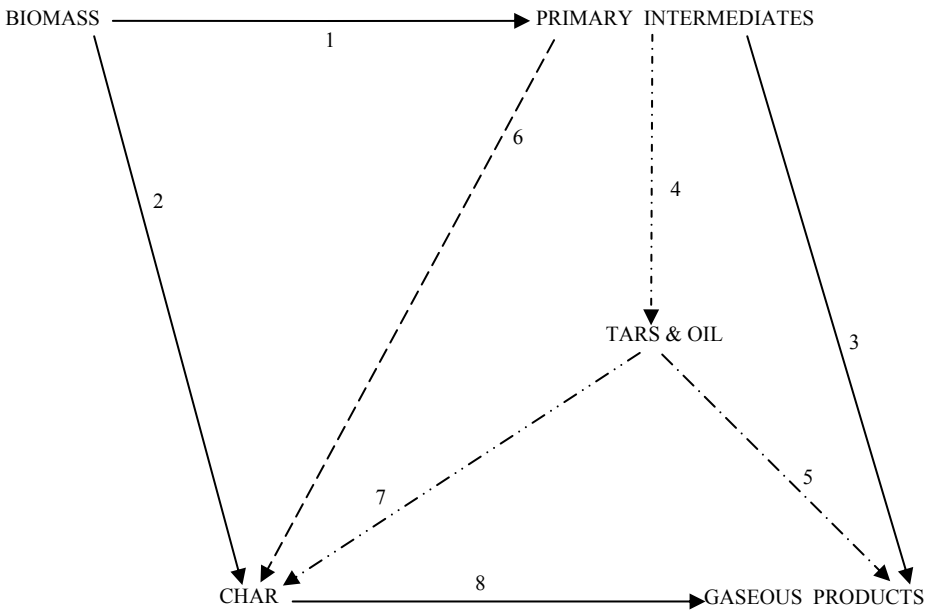

Figure 9. Simplified model for biomass pyrolysis and gasification. Reprinted from Rei *et al*. [205].

Rapid pyrolysis (step 1) involves a "complex thermal degradation" [206] of the biomass structure that is subsequently followed by a conveyance of the primary intermediates from the internal framework to gaseous products (step 3) [205]. The primary intermediates are the volatile components produced from the biomass during reaction step 1 and that can undergo further reaction in the gas phase or on the catalyst surface. The main transitional compounds from biomass are anhydrosugars, aromatics (including phenols and PAHs), water, carbon oxides, light oxygenates (e.g., methanol, acetaldehyde, acetone, furan, etc.), and weak acids (e.g., acetic and formic acids) [82, 207-213]. These intermediates can be steam reformed to provide gaseous products, as depicted in reaction step 3, or they can recombine to give rise to semi-volatiles, such as tars and oil, as shown in reaction step 4. A small quantity of solid char may arise from the condensation and exhaustive dehydration and dehydrogenation of the primary intermediates from step 1 or the tars and oil from step 4 via reaction steps 6 and 7, respectively [205]. Incidentally,

steps 3, 4, 5, 6, and 7 all represent secondary reactions in biomass gasification. Steps 3 and 5 play a predominant role in the evolution of gaseous products in rapid pyrolysis processes and their reaction rates and product selectivities can be profoundly affected by altering various process parameters (e.g., temperature, residence time, heating rate, etc.) or by the addition of a catalyst. The optimization of the process parameters and the selection of an appropriate catalyst can augment gaseous product yields of these two reactions by sacrificing the amount of semi-volatiles and char that are produced from steps 4, 6, and 7. Conventional slow pyrolysis, or carbonization, is represented by reaction step 2 in which char is the major product. Reaction step 8 signifies the gasification of char and it has been experimentally verified that higher gas yields can be achieved by increasing heating rates [214] or soaking the char in a catalyst solution [215, 216]. The combination of steps 2 and 8 signifies the typical gasification sequence for biomass.

The most important gasification reactions for both wet and dry gasification are provided below. For anoxic environments the oxygenolysis reaction can be ignored.

Carbon-Water Gasification Reactions (Steam Reforming Reactions)

$$C + H_2O\ (g) \rightarrow CO + H_2 \qquad \Delta H_{25^\circ C} = +\ 131\ kJ/g{\cdot}mol \qquad (8)$$

$$C + 2H_2O\ (g) \rightarrow CO_2 + 2H_2 \qquad \Delta H_{25^\circ C} = +\ 90\ kJ/g{\cdot}mol \qquad (9)$$

Boudouard Reaction

$$C + CO_2 \rightarrow 2CO \qquad \Delta H_{25^\circ C} = +\ 173\ kJ/g{\cdot}mol \qquad (10)$$

Oxygenolysis

$$C + O_2 \rightarrow CO_2 \qquad \Delta H_{25^\circ C} = -\ 394\ kJ/g{\cdot}mol \qquad (11)$$

Water-Gas Shift Reaction

$$CO + H_2O\ (g) \rightarrow H_2 + CO_2 \qquad \Delta H_{25^\circ C} = -\ 41\ kJ/g{\cdot}mol \qquad (12)$$

Gasification Methanation Reactions

Hydrogasification

$$2C + 2H_2O\ (g) \rightarrow CH_4 + CO_2 \qquad \Delta H_{25^\circ C} = +\ 15\ kJ/g{\cdot}mol \qquad (13)$$

Hydrogenation

$$C + 2H_2 \rightarrow CH_4 \qquad \Delta H_{25^\circ C} = -\ 75\ kJ/g{\cdot}mol \qquad (14)$$

Methane Dissociation Reaction

$$CH_4 + H_2O\ (g) \rightarrow CO + 3H_2 \qquad \Delta H_{25^\circ C} = +\ 206\ kJ/g{\cdot}mol \qquad (15)$$

Hydrothermal gasification of biomass is an endothermic process that requires substantial calorific input in order to propel the chemical reaction forward. Although external heat sources are normally used to furnish the requisite heat to HT systems, they are often incapable of delivering heat fast enough to overcome energy losses incurred by heat transfer and, consequently, the heating rates are often too slow for efficient gasification of biomass. Relying upon thermochemical fundamentals, some researchers have rectified this situation by adding oxygen to their hydrothermal reactors. Under NSCW conditions and an oxygen-rich environment, biomass undergoes an oxidative reaction that liberates heat and forms CO_2 and H_2O [217]. Its addition as a cheap, effective internal heat source notwithstanding, oxygen can prove to be a bane for HTG because the generation of H_2 and CH_4 declines with increasing concentration of reactant oxygen.

2.5 Terminology

A bewildering assortment of terms has been used to describe the treatment of biomass with water at an elevated temperature and pressure, including hot compressed water treatment [218], hot liquid water treatment [219, 220], hydropyrolysis [32], hydrothermal conversion [221, 222], hydrothermal gasification [34, 223], liquefaction [224], sub- and supercritical water

hydrolysis [225, 226], supercritical water gasification [227, 228], supercritical water treatment [229, 230], and thermochemical liquefaction [231]. The terms "liquefaction" and "gasification" are frequently used to denote the predominant products (i.e., liquid and gas, respectively) formed from the thermochemical conversion of biomass in an aqueous medium. The usage of these terms in technical parlance, however, is not exclusively restricted to hydrothermal reactions but also encompasses any reaction in which the reacting substrate is wholly converted to either a liquid or a gas, respectively, without regard to the actual medium or process involved. For instance, liquefaction is also used to designate many other processes, including those in which condensed gases form liquids, direct conversion of coal to liquid fuels either through the Bergius process (hydrogenation) or the Karrick process (carbonization).

2.6 Decomposition of Model Biomass Compounds

2.6.1 Hydrothermal Decomposition of Saccharides

Over the last two decades a concerted effort has been undertaken to acquire a better understanding of the mechanisms surrounding the oxidation and consequent decomposition of simple sugars and polysaccharides in sub- and supercritical water. The hydrothermolysis of simple monosaccharides in hot, aqueous media is often viewed as a paradigm for the hydrothermal conversion of more complex, heterogeneous lignocellulosic materials. Because of its simpler structure and availability at high purity levels, glucose, in particular, is commonly utilized in laboratories as an archetypical compound that emulates the reaction chemistry of the numerous carbohydrates found in biomass [160, 232-234]. It has been noted that previous studies on glucose pyrolysis and hydrolysis may not be entirely germane with reactions involving near- and supercritical water because of the significantly different processing environment [235]. Glucose pyrolysis tests are devoid of the SCW water that functions as a

reactive medium. Typical glucose hydrolysis studies are performed in liquid water, usually with the aid of an acidic agent, so that ionic chemistry is paramount. In SCW thermolysis, with temperatures at or above 374 °C and pressures of at least 220 bar, ionic chemistry is likely to exert only a minimal influence on the process. Nonetheless, Holgate *et al*. [235] acknowledged that earlier studies on glucose pyrolysis and hydrolysis do "provide a framework within which to develop an expectation of the types and identities of products that may be formed during the reactions of glucose (hydrolysis and oxidation) in supercritical water."

A comprehensive global scheme for the thermolytic decomposition of glucose and fructose is portrayed in Figure 10, where individual reaction pathways have been culled from several sources. Both glucose and fructose can undergo reversible isomerization via the Lobry de Bruyn-Alberda van Eckenstein (LBAE) transformation. According to a seminal work by Antal *et al*. [236, 237] the LBAE isomerization between glucose and fructose is very slow under hydrothermal conditions. Hydrothermal decomposition rate data for glucose was extracted from various studies and then plotted in the Arrhenius graph shown in Figure 11. Hydrothermally treated glucose can degrade via two primary routes: (1) retro-aldol condensation (i.e., C-C bond cleavage) to form aldehydes and ketones (e.g., glyceraldehyde, glycoaldehyde, dihydroxyacetone, erythrose, etc.) and (2) dehydration to form 1,6-anhydroglucose.

Kabyemela *et al*. [40] studied the hydrothermal decomposition kinetics of glucose at temperatures of 300, 350, and 400 ºC, pressures between 250-400 bar, and residence times between 0.02 to 2 s. They determined that the kinetic rate of glucose degradation increases as the conditions are shifted from subcritical to supercritical. It was also observed that pressure has no significant impact on glucose decay rates in the subcritical region, while in the supercritical region increasing pressure was found to retard the rate of glucose epimerization to fructose.

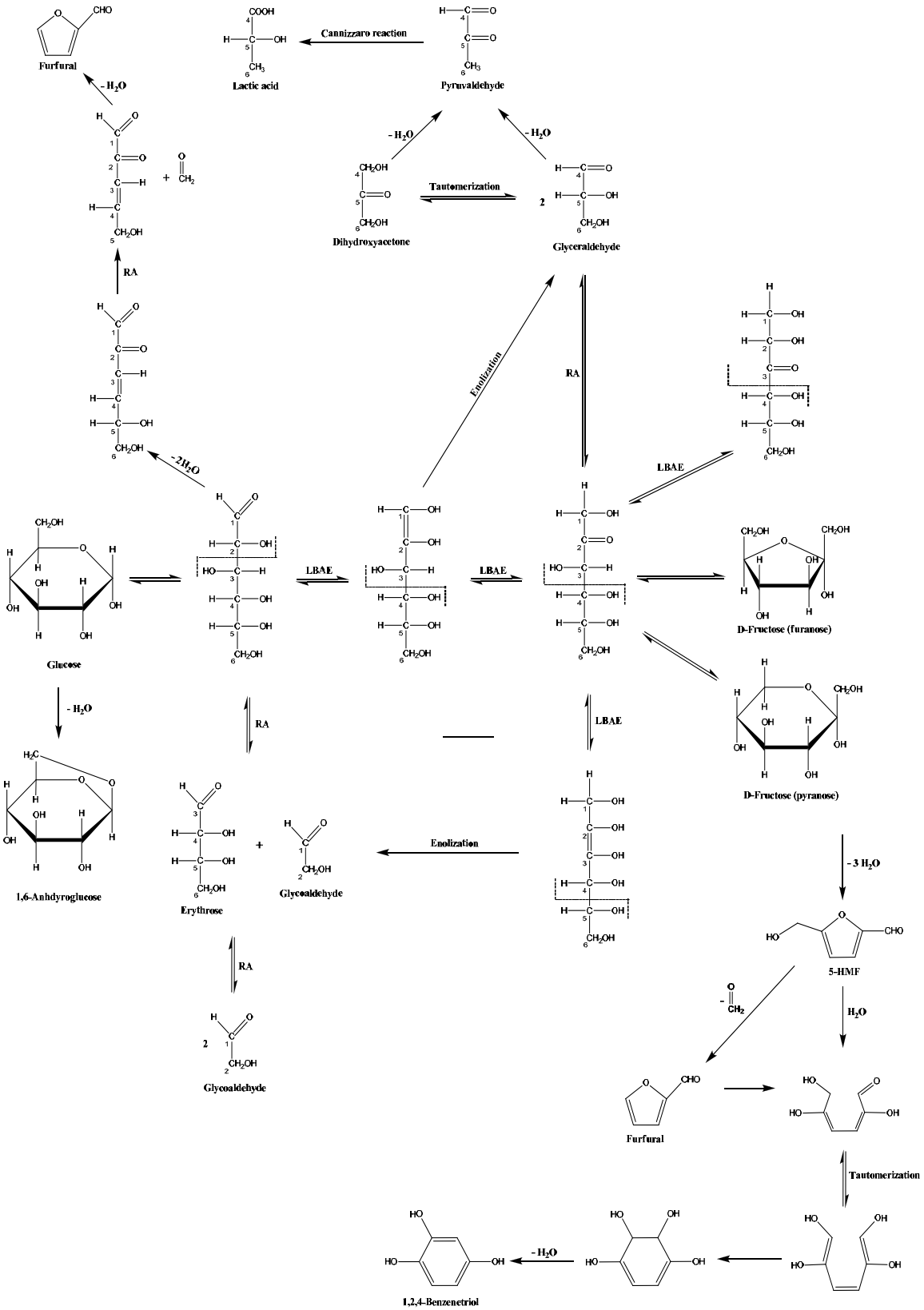

Figure 10. Reaction pathways for the decomposition of glucose and fructose based on literature [35, 43, 222, 227, 236, 238-246].

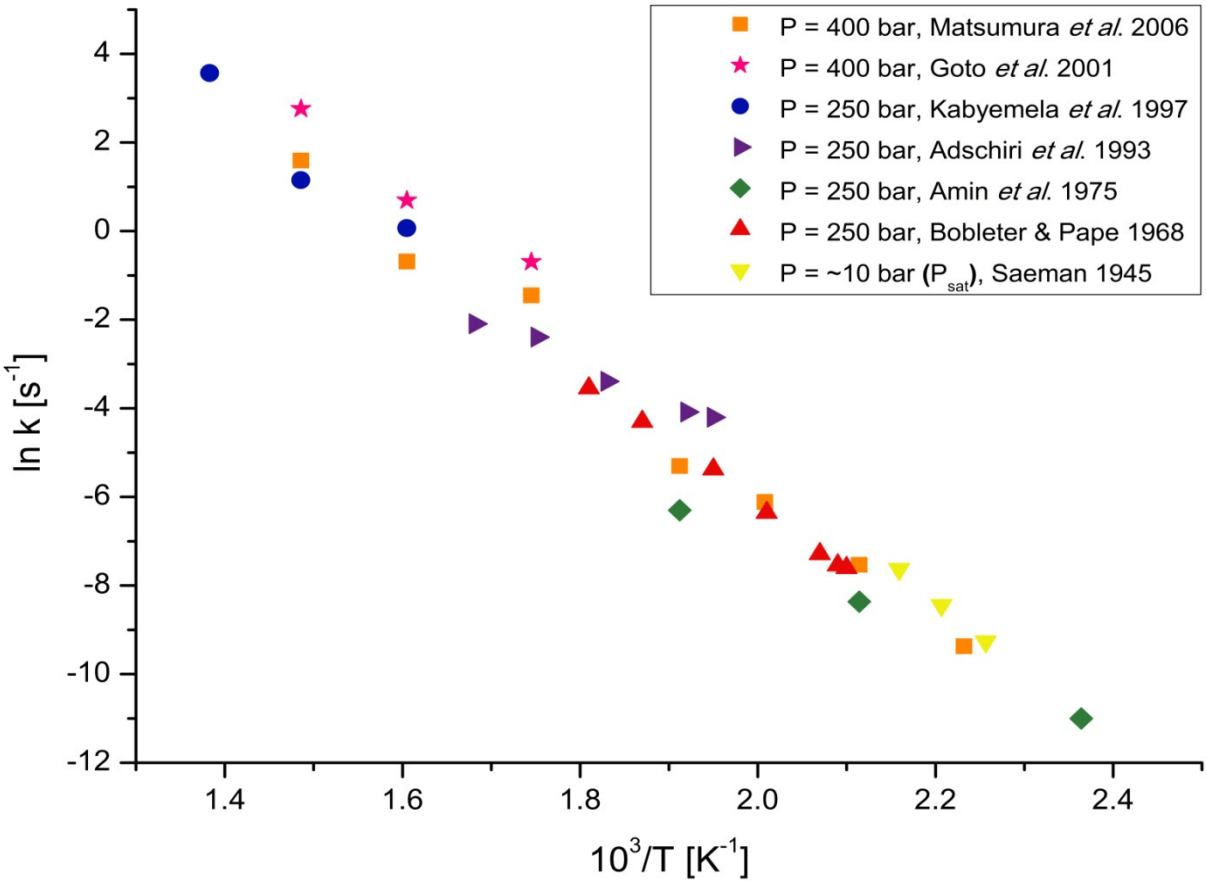

Figure 11. Arrhenius plot of kinetic rate data for the hydrothermal decomposition of glucose at various operating pressures. Data obtained from Matsumura *et al.* [41], Goto *et al.* [247], Kabyemela *et al.* [40], Adschiri *et al.* [248], Amin *et al.* [193], Bobleter and Pape [249], and Saeman [250].

Recent studies have shown that the thermolytic destruction of fructose is much faster than that of glucose in SCW, but in subcritical water the decomposition rate of glucose is somewhat faster than that of fructose. Aida *et al*. [245] obtained 67% conversion of fructose after 0.59 s at 350 °C and 80 bar and 99% conversion after 0.75 s at 400 °C and 100 bar; they obtained 80.1% conversion of glucose after 0.4 s at 350 °C and 80 bar and 98.9% conversion after 1.5 s at 400 °C and 80 bar. The change in degradation rate suggests that the predominant reaction pathways for both glucose and fructose are altered near the critical point of water. Notwithstanding variations in production distribution caused by different reaction operating parameters, the main product types obtained from the degradation of glucose and fructose are not identical. Although glucose

can lose water to form 1,6-anhydroglucose, it is more common for glucose to decompose via retro-aldol condensation pathways and form fragmentation compounds (e.g., glyceraldehyde, erythrose, dihyroxyacetone, etc). In contrast, the principal degradation routes of fructose involve loss of water molecules to form chiefly dehydration products, such as 5-hydroxymethylfurfural (5-HMF) and 1,2,4-benzenetriol [40, 43, 236, 245, 246].

Certain reaction pathways in the glucose and fructose decomposition network are highly influenced by the pH of the aqueous media. Asghari and Yoshida [251] investigated the production of 5-HMF from fructose in acidic media and discovered that not only the pH, but also the type of acid, can manipulate the degradation route. They observed that at a pH of 1.5 in 0.03 M hydrochloric acid 5-HMF experienced substantial rehydration to form levulinic and formic acids, yet at a pH of 1.5 in 0.1 M phosphoric acid the rehydration of 5-HMF to levulinic and formic acids was curtailed by 85% and 74%, respectively.

2.6.2 Hydrothermolytic Degradation of Cellulose

Cellulose can undergo rapid conversion without the use of catalysts in subcritical and supercritical water [248]. Cellulose can undergo depolymerization via two competitive reaction pathways to form oligosaccharides: (1) dehydration of the terminal glucose group via thermal cleavage of the (1→4)-glycosidic bond in cellulose and (2) hydrolysis of the (1→4)-glycosidic bond via cellulosic dissolution [47, 252, 253]. Under subcritical conditions the dehydration pathway takes precedence, whereas hydrolytic and fragmentation mechanisms prevail in the near- and supercritical water regime [230, 247, 254]. The oligosaccharides can then undergo further hydrolysis to generate monosaccharides, which degrade according to the mechanistic pathways described previously. Alternatively, the oligosaccharides can be converted by retro-aldol condensation to form pyrolysis products.

Kruse and Gawlik [31] proposed a simplified reaction scheme for the hydrothermal decomposition of cellulose as presented in Figure 12. Cellulose is initially hydrolyzed to form glucose and fructose. The glucose and fructose can then be converted via two competing pathways. Under subcritical conditions, dehydration reactions forming furfurals are favored presumably because of the high ion product of water. The furfurals can undergo further dehydration to form phenols and/or higher molecular-weight compounds, such as tars. In supercritical water, free radical reactions characterized by bond cleavage predominate because ot the lower relative density of water. Acids and aldehydes are the first products formed by bond cleavage reactions. The acids and aldehydes can then be converted to gaseous products.

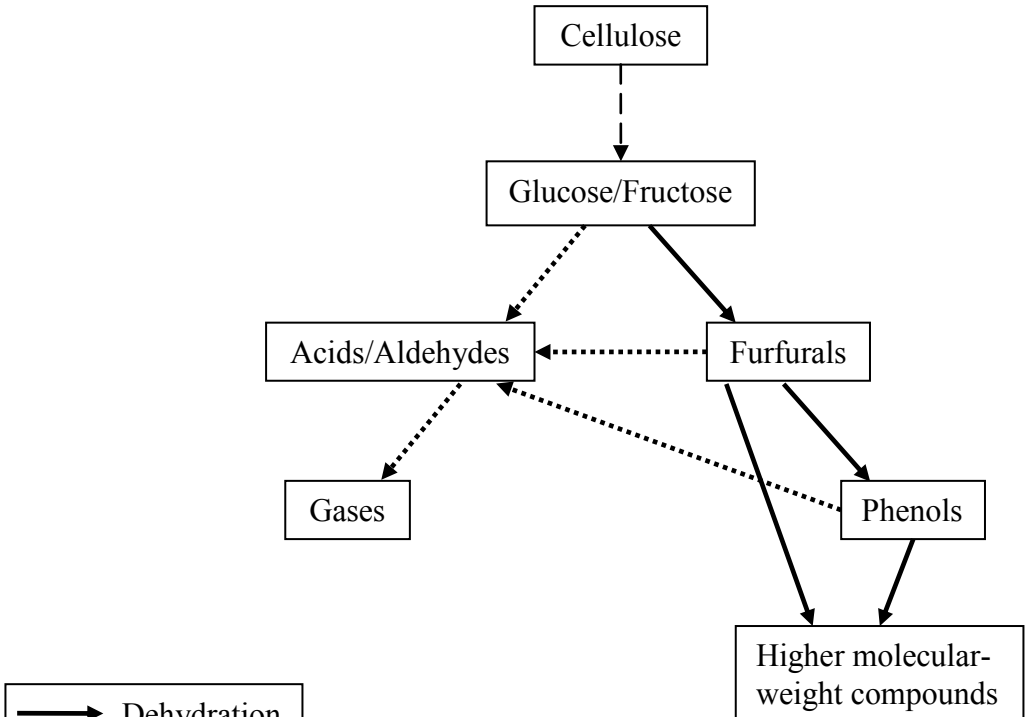

Figure 12. Simplified reaction scheme for hydrothermal conversion of cellulose. Adapted from Kruse and Gawlik [31] and Watanabe *et al*. [243].

It has been hypothesized that integrity of the rigid cellulosic crystalline structure may be compromised when hydrogen bonds in cellulose are cleaved under critical conditions in water [255]. Ehara *et al*. [230] theorized that the low viscosity and high diffusivity of NSCW facilitate its access to the internal framework of the cellulose macromolecule. They also asserted that cellulose microfibrils undergo dissolution because the free water that surrounds them behaves similarly to supercritical water. Accordingly, the cellulosic polymer is subjected to both an internal and external degradative assault in NSCW. Sasaki *et al*. [226] observed a softening of cellulose in hydrothermal water at 280 °C. Product yields from subsequent cellulosic HT experiments by Sasaki's group [256] revealed that at temperatures above 280 °C non-aqueous phase products were converted to aqueous phase products, whereas at temperatures below 280 °C the ratio between aqueous and non-aqueous phase products remained nearly constant. Further corroboration of the conversion of non-aqueous to aqueous products was provided by a mass spectrometry (MS) analysis which demonstrated that the distribution of polymeric species in the non-aqueous phase fraction swung to a lower molecular weight range when the HT water temperature was increased from 295 to 310 °C.

Sakaki *et al*. [257] studied the saccharification of cellulose in a flow reactor using 10 $mL \cdot min^{-1}$ of water at 295 °C with a total on-flow reaction time of 12 min. It was discovered that 99 wt % of the starting cellulose could be converted to oligosaccharides (81 wt %) having 2–5 glucose units and polysaccharides (18 wt %) having more than 5 glucose units. These findings are corroborated by those of Ehara and Saka [258], who studied the decomposition of cellulose in a flow reactor using both subcritical water (280 °C, 400 bar) and supercritical water (400 °C, 400 bar). In subcritical water, 49.5 wt % of the cellulose was converted to water-soluble products (i.e., monosaccharides, oligosaccharides, dehydrated and fragmented monosaccharides,

and organic acids) after 2 min; the amount of cellulose converted to aqueous-phase compounds increased to 82.7% after a reaction time of 4 min. In supercritical water the cellulose conversion to aqueous products was found to be 41.2 wt % after 0.1 s, increasing to 93.9 wt % after 0.3 s. These results taken in conjunction with those from Sakaki's laboratory suggest that use of longer residence times can be used to achieve higher substrate conversion efficiencies.

High-resolution mass spectra from Ehara and Saka [258] revealed that the water-soluble oligosaccharides obtained from subcritical water treatment had a maximum DP of 7, whereas those produced from the supercritical water treatment had a DP up to 12 (cellododecaose). Unlike the cellulose treated in NSCW, which experienced a 49.0 wt % conversion of cellulose to polysaccharide precipitates, there were no polysaccharide precipitates (i.e., defined here as having a DP range from 13 to 100) formed in the subcritical water treatment. The polysaccharide precipitates are insoluble in water under ordinary conditions but are soluble in supercritical water. The authors concluded that the presence of polysaccharides and large oligosaccharides in SCW treatment and their absence in subcritical water treatment suggests that cleavage of glucosidic bonds in cellulose must occur more often in SCW. The degradation of glucosidic bonds is a direct consequence of hydrogen bond cleavage in cellulose macromolecules under supercritical conditions [255].

Sasaki *et al*. [46] discovered an increase in the conversion rate of microcrystalline cellulose as water approaches near-critical conditions, which is readily discernable in the apparent activation energy ascent from 145.9 $kJ \cdot mol^{-1}$ to 547.9 $kJ \cdot mol^{-1}$ when the system is heated above 370 °C. In fact, the reaction rate at 400 °C was determined to be more than 1 order of magnitude higher than the rate at 350 °C. This evidence is consistent with an earlier observation by Malaluan [259] that the rate of cellulose decomposition in NSCW (i.e., 400 °C) is

1 to 2 orders of magnitude higher than that in subcritical water (i.e., 300–350 °C). The dramatic acceleration in the conversion rate kinetics is attributed to a fundamental difference, or "break point", in the reaction mechanism for cellulose decomposition that occurs in the vicinity of the critical point for water. It was posited that at higher temperatures the intra- and intermolecular hydrogen linkage present in the cellulose crystal are weakened and eventually broken so that the cellulose crystal may disperse into the aqueous media and form a homogeneous cellulose-water reaction environment. The kinetic rate data for three independent studies on cellulose hydrothermal conversion are presented in the Arrhenius plot shown in Figure 13.

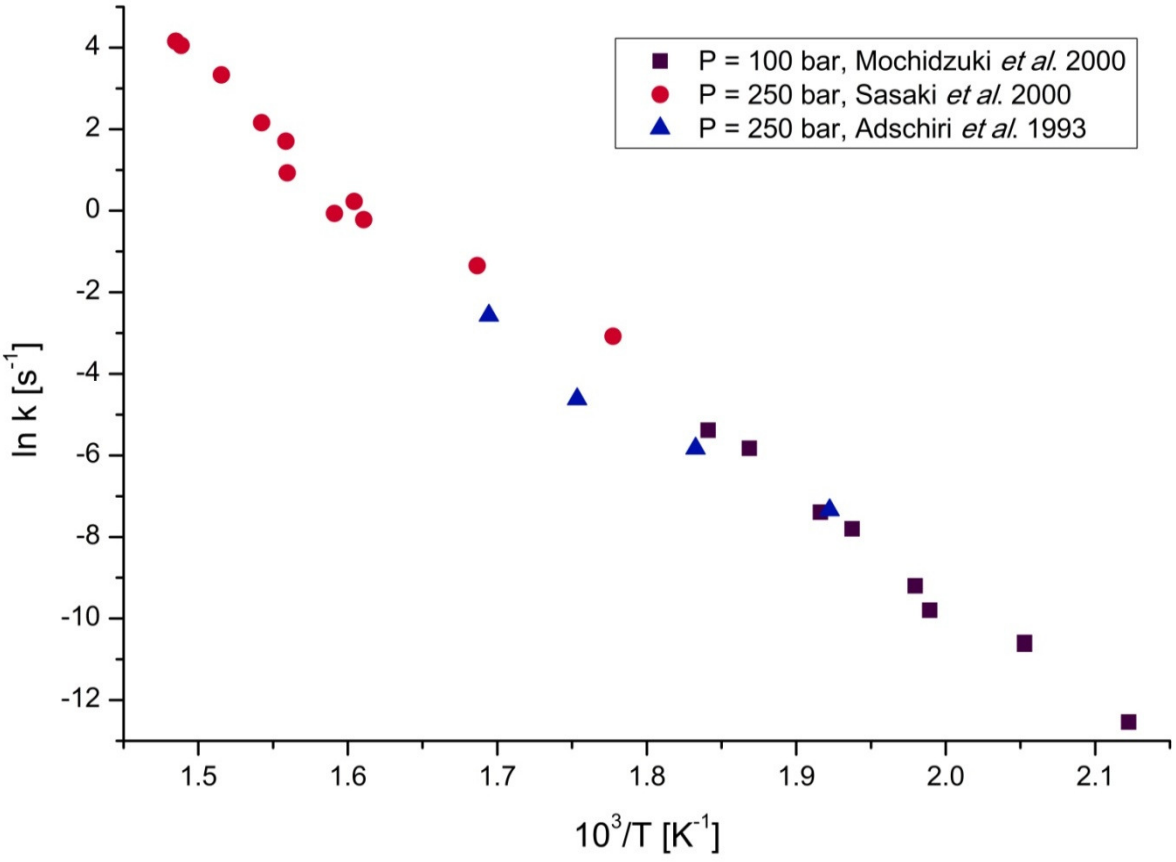

Figure 13. Arrhenius plot of first-order cellulose decomposition data at various operating pressures. Data obtained from Mochidzuki *et al.* [121], Sasaki *et al.* [116], and Adschiri *et al.* [109].

Cross-polarized optical microscopy is a technique commonly employed to detect the degree of birefringence in anisotropic materials. Crystalline substances are anisotropic and exhibit double refraction, or birefringence, whereby an intersecting ray of light will be decomposed into two rays. It is important to note that the birefringence measured in samples is a function not only of the intrinsic crystallinity of the material but also of the alignment of non-crystalline polypeptide chains [260]. Deguchi *et al*. [261] used *in situ* polarized optical microscopy to monitor the loss of birefringence in fibrous cellulose specimens during hydrothermal treatment under isobaric conditions (250 bar) at a heating rate of 11–14 °C·min^{-1}. Figure 14 provides a series of polarized microscope images illustrating the loss of crystallinity in a single cellulose fiber with increasing temperature. The birefringence of the cellulose samples remained constant up to 310 °C, implying that the crystallinity of cellulose is preserved through this temperature in subcritical water. A considerable loss of birefringence occurred between 310 and 320 °C, corresponding with a rise of more than 10% in image brightness. By 330 °C, the cellulose samples were no longer birefringent. The loss of crystallinity in a single cellulose fiber was examined in a sequence of images taken at 1 °C intervals between 324–329 °C. Between 324–326 °C there is continued loss of birefringence, but the structure of the cellulose fiber remains nearly intact. The cellulose fiber begins to deform at 327 °C when almost all of the birefringence in the sample has disappeared. At 329 °C, the shape of the cellulose fiber has become completely distorted. It is relevant that the advent of the collapse in the structural integrity of the cellulose fiber coincided exactly with the nearly complete loss of crystallinity in the cellulose sample. This result suggests that the dissolution of crystalline materials in hydrothermal environments proceeds almost instantaneously after the crystallinity of such substances is lost.

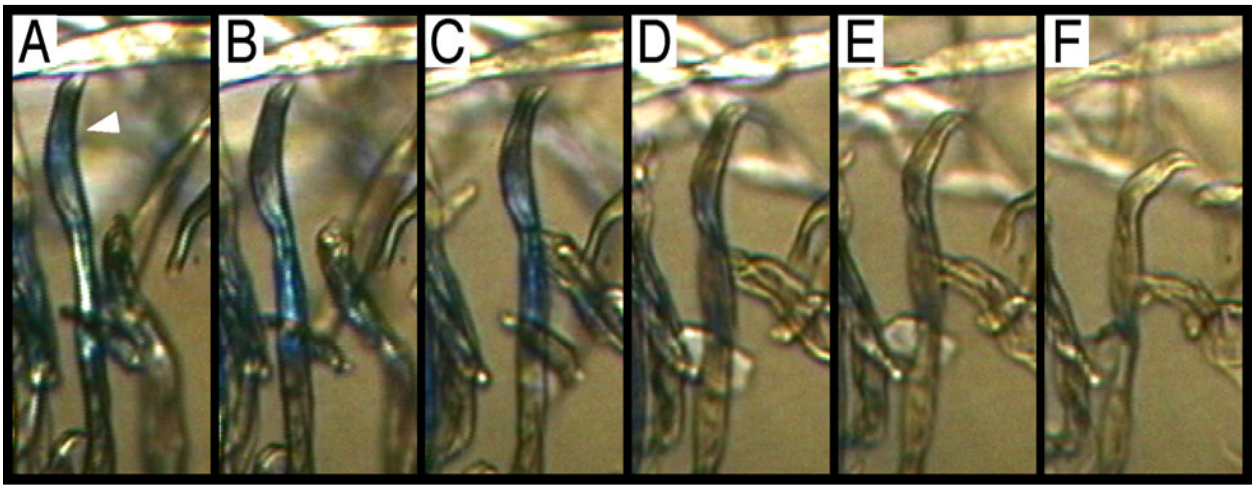

Figure 14. Sequence of cross-polarized micrographic images depicting the crystalline to amorphous transition for a single cellulose fiber (shown by the white triangle in A) undergoing hydrothermal treatment at increasing temperatures. Temperature (A) 324 °C, (B) 325 °C, (C) 326 °C, (D) 327 °C, (E) 328 °C, (F) 329 °C. Reprinted with permission from Deguchi *et al*. [261].

2.7 Effect of Process Parameters

Disagreement exists in the literature regarding the degree of influence that various process parameters have upon the product yields and reaction kinetics for biomass hydrothermal conversion. Ogi *et al*. [192] reported that heavy oil yields from biomass liquefaction were highly influenced by several reaction parameters, including temperature, pressure, residence time, and catalyst loading. Xiang *et al*. [262] concluded that temperature, reaction medium, and reactor configuration were the most important parameters governing the reaction kinetics of glucose hydrothermal decomposition. Yu *et al*. [263] indicate in a review of biomass hydrolysis in hot compressed water that the feedstock properties, water properties, reactor configuration, time-temperature history of the reacting particles, and the presence of additives may all impact the hydrothermal conversion of biomass. Shoji *et al*. [264] studied the decomposition of a wood block in sub- and supercritical water and determined that the apparent rate kinetics surrounding the decay of wood are strongly affected by the reaction temperature and the ionic product of the water. Kabyemela *et al*. [40] conducted extensive kinetic investigations on glucose

decomposition in subcritical and supercritical water. Their findings indicate that the role of pressure depends upon the state of water. In subcritical water the rate of glucose destruction was not affected by pressure but in supercritical water the kinetic rate of glucose conversion decreased with increasing pressure. D'Jesus *et al*. [265] gasified corn silage in supercritical water at various temperatures (300-700 °C), pressures (250-400 bar) and residence times (0.6-10 min). Their experimental data revealed that effects of pressure on biomass gasification were negligible. The effect of temperature was found to have the greatest impact upon the gasification efficiency of corn silage in SCW. Increased residence times improved gasification efficiencies until a maximum conversion was attained at 1.71 min. Increasing the residence time beyond 1.71 min did not enhance product yields further.

2.8 Catalysts

There are conflicting reports regarding the gasification efficacy of hydrothermal biomass conversion with the use of catalysts. An early study by Yokoyama *et al*. [266] demonstrated the effectiveness of potassium (K_2CO_3) and nickel carbonate (Ni_2CO_3) in wood liquefaction. Dried, ground wood (*Quercus serrata Thunb.*) and a 20 wt % loading of catalyst were stirred together in an autoclave pressurized with argon to 20 bar and subsequently heated to 350 °C in 36 minutes followed by a 30 minute hold. Without any catalyst, the yield of heavy oil was just 7.6 wt %, yet in the presence of a catalyst the yield jumped to 18.9 wt % or higher. It was also determined that K_2CO_3 is slightly more catalytically active than Ni_2CO_3 because the yield of heavy oil produced by K_2CO_3 was 2–6 wt % higher than that produced by Ni_2CO_3. The heavy oil produced with the K_2CO_3 had approximately 16 wt % oxygen and its heat of combustion was 33.4 $MJ \cdot kg^{-1}$, whereas the initial wood had an oxygen content of 47.4 wt % and a heat of combustion of 18.8 $MJ \cdot kg^{-1}$. In essence, the transfer of oxygen from the wood to the heavy oil product was largely blocked.

In the absence of any catalyst, the amount of carbon solubilized in the aqueous phase was found to be 62.1 wt %, roughly three times higher than the carbon level in the catalyzed liquid product. This suggests that the catalysts may have promoted secondary polymerization reactions among the products. The evolved gas for each run was found to contain a mixture of CO, CO_2, CH_4, and H_2, of which CO_2 was the principal constituent, comprising more than 90 wt % of the gas. The quantity of H_2 produced was negligible in the case of the uncatalyzed liquefaction experiment.

Minowa *et al*. [267] gasified a water slurry of cellulose with and without reduced Ni catalysts at 400 °C and 130 bar for 1 h. The overall gas yield increased from 20 to 80 wt % as the loading of reduced nickel was increased from 0 to 20 wt %, respectively. The yield of CH_4 also increased nearly 30 wt % over the same nickel loading range. Fang *et al*. [37] gasified cellulose at 350 °C and 165 bar in an autoclave for soak durations ranging from 0 to 60 min. The highest gas yield, obtained at 60 min, accounted for less than 10% of the overall product yield on a carbon basis. When a Ni/Si-Al_2O_3 catalyst was added and mixed well with the system, the gas yield reached 70% on a carbon basis after a residence time of 60 min and 96 wt % of the starting cellulose was gasified. A Chinese group compared supercritical liquefaction of corn stalks in a semi-continuous flow reactor (3 $mL \cdot min^{-1}$) at 410 °C and 250 bar both with and without addition of 1.0 wt % Na_2CO_3 catalyst [268]. The overall biomass conversion for the liquefaction process was 94.4 wt % without catalyst and 95.7 wt % with the Na_2CO_3 catalyst. The yields of total liquid product and bio-oil were substantially enhanced by the presence of a catalyst; with the addition of catalyst the total liquid product yield climbed from 77.6 to 88.9 wt % and the bio-oil yield rose from 33.4 to 47.2 wt %. An elemental analysis of the bio-oil products illustrated that the distribution of elements from catalytic liquefaction differed appreciably from that of

uncatalyzed liquefaction. When a catalyst was utilized the following trend was observed: carbon, hydrogen, and nitrogen content decreased, while the oxygen content and the H:C and O:C atomic ratios increased in relation to the same parameters for the uncatalyzed liquefaction bio-oil.

Even with the use of catalysts there is no guarantee that volatile yields from hydrothermal biomass gasification will increase. Yoshida *et al*. [269] gasified five different mixtures containing cellulose and lignin with a Ni catalyst at 450 °C and 250 bar for 20 min. At 3:1 cellulose to lignin loadings, all the mixtures exhibited methane insoluble carbon yields below 10% and very low hydrogen production rates. The diminished hydrogen gas returns were rationalized by concluding that the lignin structure was incorporating hydrogen atoms during the depolymerization. Yoshida *et al*. [270] examined the interactions among the three primary biomass constituents (i.e., cellulose, hemicellulose, and lignin) They noted that those mixtures containing a large proportion of lignin exhibited lower hydrogen concentrations than those with lesser amounts of lignin or no lignin at all.

2.9 Residence Time Effect

The effect of residence time on product yields and distributions from hydrothermal biomass treatment in NCSW is not entirely clear from the literature. Some studies suggest that increased heating times promote additional gasification and liquefaction of either biomass or the tar and char derivatives. A German group [265, 271] reported that gasification yields from corn and clover grass in SCW increased linearly with residence time until a maximum was reached. Wahyudiono *et al*. [272] examined the decomposition of guaiacol in NSCW at temperatures between 380-400 °C and residence times from 5-180 min. Increasing residence time resulted in increasing formation of guaiacol derivatives (i.e., catechol, phenol, and *o*-cresol). At prolonged

residence times, polymerization and condensation reactions resulting in increased char production became important. Even if biomass substrate conversion can be increased by extending residence time, there is also a possibility that longer reaction times will permit substantial degradation of bio-oil products to gases [224]. Some studies indicate that gasification product yields from hydrothermal glucose conversion are largely independent of residence time, except at the shortest reaction times (e.g., anywhere from 10.4 s to 1.7 min) where gas yields are reduced [234, 273]. It is also conceivable that the highest quantities of gas and liquid organics from biomass are generated at exceedingly short residence times. Holgate *et al*. [235] completely gasified glucose within 6 s in SCW at 600 °C and 246 bar.

2.10 Difficulty Posed by Use of Inconsistent Residence Time Definitions

Part of the uncertainty stems from the lack of a uniform definition regarding the duration of an experimental run. Some research groups consider residence time to begin the moment a substrate-filled reactor is first heated and to end the instant heat is no longer supplied to the reactor. Other laboratories extend this definition to include the time it takes for the reactor contents to cool down to SATP. Still other laboratories define residence time as only the actual hold time, or the time that a substrate material was held at a specified soak temperature. The disparity in these definitions is especially problematic when trying to evaluate the impact of heating duration on the overall hydrothermal process. For instance, an experiment conducted using a slow heating rate might take 30 min to reach the soak temperature. If the researcher then holds the temperature at the soak temperature for an additional 30 min before rapidly quenching, then the total run time is already at 60 min and it is very likely that the material within the reactor began to experience degradative attack by both the heat and water long before the 30 min soak began. Depending on the laboratory the reaction time for this hypothetical experiment would be

recorded as either 30 min or 60 min (and possibly the quench time). Without proper identification of the exact heating protocol employed, the results from the former scenario will then pose difficulties when they are compared with other experiments of "identical duration" by the scientific community.

2.11 Biomass Hydrothermal Conversion

A wide variety of biomass materials have been used to validate the hydrothermal conversion process for biomass. An early study [178] at the University of Saskatchewan in Canada investigated the bio-oil products obtained from the hydrothermal conversion of aspen poplar wood (*Populus tremuloides*) with an alkaline catalyst in a reductive environment. The materials consisted of 100 g of air-dried wood (i.e., 30 mesh, 5.4 wt % moisture) added to a solution of 500 g of water containing 10 g of sodium carbonate (Na_2CO_3). The materials were then added to a reactor that was charged to a pressure of 340 bar with carbon monoxide. The contents of the reactor were then heated in 2.5 hr to 360 °C and held at this temperature for 1 hr after which time the run was terminated and the reactor was cooled overnight. Similar runs were conducted in the reactor with polymeric cellulose, cellobiose, D-glucose, D-fructose, D-xylose, D-sorbitol, glycerol, and an isolated lignin. It is noteworthy that the gas chromatogram of the liquid oil product from polymeric cellulose reveals virtually the identical elutriated species as in the gas chromatogram for the oil obtained from the whole wood. Equally important, the liquid oils derived from polymeric cellulose and the smaller carbohydrate units all have a carbon content that is within an average of 0.95 wt % of that of the oil from the whole aspen (i.e., 72.8 wt % C). This would imply that all of the lignocellulosic components of the wood were transformed into a closely related product. However, hydrothermal conversion of the isolated lignin produced a startling difference; the proportional yield of oil product was much higher than

for the other carbohydrates or the whole wood and the oil also exhibited a charred disposition. The authors indicate that this probably occurs on the level of whole wood hydrothermal conversion but that the char in the oil from the lesser lignin fraction is solubilized in the major oil fraction from the other carbohydrates. It was observed that bio-oil was only produced from the available aldoses, which led the team to suggest a mechanism, whereby cellulose, and possibly hemicellulose, are depolymerized into smaller units more analogous to the dimer and monomer precursors. The smaller fragments are then converted to the bio-oil product.

A Canadian group [147] investigated the dissolution of willow wood in the 200–350 °C temperature span at 10 MPa using both batch and semi-continuous flow reactors. Using a batch-type diamond-anvil cell, it was observed that willow begins to dissolve at about 200 °C, as revealed by both a contraction of the willow particles and their transformation in color to yellow. The rate of dissolution was unaffected by a rise in temperature, which did, however, trigger pyrolysis of the willow. A second set of experiments was conducted in the semi-continuous flow reactor, where willow particles were dissolved at 215 °C and 230 °C. The amount of time required for the willow particles to dissolve was shown to be a function of the water flow rate, which suggested that the dissolution of willow in the semi-continuous flow process is governed by diffusion. Interestingly, the dissolution time was again unchanged by an increase in the process temperature which would suggest that the biomass reaction kinetics do not exhibit a standard Arrhenius dependence. Incomplete decomposition of cellulose is a potentially undesirable outcome that must be considered in batch hydrothermal treatment of lignocellulosic materials.

A research team [274] at the University of Minnesota examined the influence of heating and cooling rates on hydrothermal biomass liquefaction. Ground corn stover (d_p < 2 mm) and

aspen wood chips (0.5 in < d_p < 1.0 in) were reacted separately for 10 min in subcritical water at 350 ºC. Experiments were performed at three distinct heating rates of 5, 14, and 140 ºC·min and two different cooling rates of 5.5 and 66 ºC·min. Variations in the heating or cooling rates did not have a discernible impact on the composition of the liquid products for either substrate. There was also no significant change in the product yield when using the different cooling rates. The heating rate, however, did have a demonstrable effect on the product yield from both biomass substrates. In the case of the corn stover, there was a 35% increase (18 wt % gain) in liquid product yield and a 50-55% decrease (9-11 wt % loss) in solid residue when the heating rate was increased from 5 to 140 ºC·min. In the case of the aspen wood, there was a 46% increase (23 wt % gain) in the liquid product yield and a 73% decrease (18 wt % loss) when the heating rate was increased from 5 to 140 ºC·min.

2.12 Impact of Reactor Wall on Reactions

High temperature and pressure autoclaves are typically constructed of specialty alloys containing significant quantities of chromium, iron, nickel, and molybdenum. It has been hypothesized that the exposed metal on the inner surface of the autoclave could serve as a catalyst, particularly at the high temperatures experienced in NSCW reactions. However, published data offers contradictory results regarding the catalytic impact of reactor walls on the hydrothermal gasification process. A Dutch group [275] from the University of Twente added Inconel powder having a diameter of 100–200 μm to 5 wt % glycerol and placed the solution in an inert quartz capillary reactor. Hydrothermal gasification tests were conducted at 600 °C and 300 bar for a duration of 60 sec. Comparison of the Inconel powder tests with a blank run containing only 5 wt % glycerol demonstrated that the Inconel powder affected carbon conversion efficiency (CE) and product gas distribution. The addition of Inconel powder caused

a surge in the CE and the yields of H_2 and CO; but only a modest increase in the yields of CO_2 and CH_4 and appeared to have no discernible bearing upon the yield of C_2 gases. Unfortunately, there is no apparent correlation between the amount of Inconel powder that was added in these tests and the catalytic activity inside a metal reactor, yet the tests did highlight the pronounced catalytic effect Inconel has upon glucose supercritical gasification.

A study by Xiang *et al*. [262] explored the catalytic impact of four different metals, *viz*. copper, stainless steel, iron, and Hastelloy C-276, during glucose hydrothermal runs conducted at temperatures between 180–230 °C and pH values of 1.5–2.2. Under these conditions copper and Hastelloy C-276 exhibited negligible effects on glucose decomposition, whereas stainless steel and, especially, iron had a large impact. The presence of iron was shown to result in an 85% drop in the initial glucose charge in 10 minutes, while the same run conducted instead with stainless steel had a glucose conversion of only 50%. These findings, however, are contradictory to results obtained by Catallo [276] for runs conducted with biomass at 400 °C for 5 min. Iron and nickel powder were separately tested for their ability to catalyze the biomass substrate. Use of the iron powder had no demonstrable effect on biomass conversion with respect to a control run having no catalyst. The nickel catalyst, however, resulted in a biomass conversion efficiency approaching 99%.

Boukis *et al*. [277] discovered that oxidative treatment of the reactor walls can promote the water-gas shift reaction and enhance gasification rates. Methanol was reformed in an Inconel reactor using supercritical water at 600 ºC and 250 bar. One treatment was performed in a new Inconel reactor, while another treatment was conducted in an Inconel reactor that had been accidentally oxidized with a 3 wt % H_2O_2 solution for 50 h at 600 ºC and 250 bar. Secondary neutral mass spectrometry (SNMS) of the oxidized metal surface revealed that Cr and Mo had

leached out of the walls leaving behind a thick layer of nickel oxides. The Ni concentration at the surface was calculated to have increased by 1 order of magnitude, while the O concentration increased nearly threefold. The gasification efficiency in the new Inconel reactor was 86.5% versus 99.8% for the oxidatively "seasoned" Inconel reactor. The production of CO dropped from 10.2 vol % in the new reactor to 0.8 vol % in the oxidized reactor, supporting the author's argument that oxidative treatment of the metal walls can stimulate the water-gas shift reaction.

A study by Antal's group [232] demonstrated an important difference in the catalytic effect of new and used metal reactor walls. Glucose was gasified in supercritical water at 600 °C and 345 bar for 30 s residence time. Glucose gasified in a "corroded" Hastelloy C-276 tube reactor experienced complete conversion, whereas glucose reacted in a new Hastelloy reactor only achieved 85% conversion. Finally, glucose reacted in an Inconel reactor only attained a conversion level of 68%. Clearly, the metal compositions in the Hastelloy alloy are more conducive to gasification than those in the Inconel alloy.

It was also shown independently by Lira and McCrackin [278] that aging of metal reactor walls has an influence on product yields from hydrothermal reactions. They studied the conversion of lactic acid to acrylic acid in near-critical water (i.e., 360 ºC and 310 bar). Under hydrothermal conditions, lactic acid can be degraded via decarbonylation in the presence of a strong acid catalyst (e.g., H_2SO_4) to produce acetaldehyde, CO, and water or via decarboxylation at higher pH levels to produce acetaldehyde, CO_2, and H_2. Alternatively, lactic acid can be dehydrated to form acrylic acid and propionic acid, the yields of which reach a peak when a small quantity of base is used. Measurements were collected in a new Hastelloy C-276 reactor during the first 4 h of use and again after 70 h of use. The results indicated that the yield of CO_2 declined considerably with aging, whereas the yield of CO was relatively stable. No enhanced

selectivity toward the lactic acid dehydration route was observed using the aged reactor. Nonetheless, the absolute yield of acrylic acid increased when the aged reactor was employed because of the curtailment in the decarboxylation pathway conversion. The authors speculated that reactive wall sites may have been passivated in the aged reactor causing a negative influence on decarboxylation reactions.

Kruse [160] (cited in [279]) notes that the observed decline in catalytic activity with operation time in new reactors may be the result of surface carburization found inside aged reactors. The carbon coating may act to inhibit the catalytic properties of the metal walls.

2.13 Ambiguity of Yield Data Presented in Literature

Interpretation of product gas yields reported for NCSW gasification in the extant literature is beset by considerable ambiguity surrounding the yield basis. There are numerous instances wherein the reader is burdened with the responsibility of "inferring" the appropriate basis (i.e., gravimetric, molar, volumetric) for gasification quantities that are reported only as percentages or, even worse, as just raw numbers. The gasification scientist, however, can find solace in the low relative density of permanent gases and light hydrocarbon volatiles, which allows dismal mass gas yields to be "magically transformed" into remarkably high volumetric yields. Regardless of the cause, it is an inherently perilous practice to compel the readership into making "educated deductions" about the possible basis for gas yields reported in this manner. Anyone seeking to mine hydrothermal gasification literature reviews for data is strongly cautioned to treat such quantities circumspectly because much of this information has been culled from several sources of variable quality and transcription errors or data interpretation gaffes often abound.

Chapter 3. MATERIALS AND METHODS

3.1 Materials

3.1.1 Bagasse

Sugarcane bagasse was collected annually from 2005–2008. Bagasse samples were obtained from various storage piles located at either the Cora-Texas Mfg. Co. sugar factory (White Castle, La.) or the Raceland Raw Sugar Corp. sugar mill (Raceland, La.). In order to ensure representative sampling, bagasse was taken from the top, interior, and sides of these piles. All of the hydrothermal experiments described in the remainder of this document were conducted with bagasse that was obtained from the Cora-Texas sugar factory.

3.1.2 Chemicals and Reagents

The solvents used in this study were acetone (ACS, Fisher Scientific, Fair Lawn, N.J.), dichloromethane (HPLC, J.T. Baker, Phillipsburg, N.J.), diethyl ether (Pesticide, J.T. Baker, Phillipsburg, N.J.), methyl alcohol, (anhydrous, ChromAR®, Mallinckrodt Chemicals, Phillipsburg, N.J.), and tetrahydrofuran (HPLC, OmniSolv®, EMD Chemicals Inc., Gibbstown, N.J.). Other reagents used were ethyl acetate (HPLC, Chempure® brand, Curtin Matheson Inc., Houston, Texas), ethyl alcohol (200 proof, USP, Pharmco-Aaper, Shelbyville, Ky.), hexane (ACS, Fisher Scientific, Fair Lawn, N.J.), and toluene (ACS/HPLC, Burdick & Jackson, Muskegon, Mich.). Model compounds used to represent the lignocellulosic components in sugarcane bagasse, included long, fibrous cellulose and oat spelts xylan, both provided by Sigma Chemical Co., St. Louis, Mo., and alkali lignin supplied by Sigma-Aldrich, St. Louis, Mo. Experiments in deuterated water used deuterium oxide (Aldrich Chemical Co., Milwaukee, Wis.)

having 100.0 atom % D and a minimum isotopic purity of 99.96 % D. Reductants used in the hydrothermal reactions included sodium borohydride, Venpure® SF (Sigma-Aldrich, St. Louis, Mo.) and carbon monoxide, (Tech., Matheson Tri-Gas Inc., Basking Ridge, N.J.). Compounds used in catalyst development and testing were comprised of the following: purified lithium hydroxide hydrate and magnesium oxide, ACS grade (Fisher Scientific, Fair Lawn, N.J.), manganese dioxide (Mallinckrodt Inc., Paris, Ky.), and demineralized water (Mallinckrodt Baker Inc., Phillipsburg, N.J.). High purity gases used to supply the gas chromatograph (GC) included air, helium, and hydrogen (all Capital Welding Supply, Baton Rouge, La.).

3.1.3 Standards for Volatiles Analysis

The external calibration standards used for the GC analysis of permanent gases and hydrocarbon volatiles through C_6 consisted of two certified grade gas mixtures (Matheson Tri-Gas Inc., Joliet, Ill.), whose molar compositions are provided in Table 7 and Table 8 at the specified purity levels. In both mixtures, the blend tolerance for every analyte was within ± 10 % and the certified accuracy for each gas was within ± 2 %. Methane was included in both mixtures at nearly the same concentration to permit comparisons between the chromatographic response of the flame ionization detector (FID) and the helium ionization detector (HID). Because its use in the field of gas chromatography is not particularly widespread, additional details describing the operational theory and configuration of an HID are presented in Appendix A. Additionally, three mixtures of UHP grade hydrogen in balance UHP grade helium (Matheson Tri-Gas Inc., Joliet, Ill.) were delivered at certified concentrations of 10,379, 1054, and 99.0 ppm, respectively.

Table 7. Permanent gas and light hydrocarbon mixture.

Component	Concentration [mol %]	Purity Grade
Hydrogen	4.003	UHP
Oxygen	3.066	UHP
Nitrogen	5.011	UHP
Carbon monoxide	5.001	Tech
Carbon dioxide	5.001	BD
Methane	4.028	CP
Ethane	4.998	CP
Helium	68.892	UHP

Table 8. Hydrocarbon mixture excluding ethane.

Component	Concentration [mol %]	Purity Grade
Methane	4.0032	CP
Ethylene	2.0009	Tech
Propylene	1.0018	CP
Propane	2.0017	CP
Isobutane	0.7508	CP
1-Butene	0.2499	CP
1,3-Butadiene	0.5002	CP
n-Butane	1.0006	CP
Isopentane	0.1499	CP
n-Pentane	0.3001	CP
Hexane	0.1001	CP
Helium	87.9408	UHP

3.2 Materials Preparation

3.2.1 Bagasse Sample Preparation

Fresh bagasse is extremely moist and typically laden with microorganisms. Generally, the raw bagasse must either be dried or refrigerated quickly to prevent extensive microbial degradation. Size reduction of the bagasse fibers facilitates the subsequent processing of bagasse by ensuring a more uniform particle size distribution and eliminating the threat of clod formation. Irradiation of the bagasse helps to further reduce microbial populations and guarantees that all samples from the same batch should have identical carbon content. Sieving the ground bagasse provides an efficient method for establishing the effect of particle size on hydrothermal conversion product distributions and yields. After the raw bagasse was collected from the sugar mill it was prepared according to the procedures outlined in the succeeding sections.

3.2.2 Comminution, Drying, and Storage

After the bagasse samples had been collected, they were transferred into 30-gallon plastic bags and placed in a walk-in freezer operating at -7 °C to minimize deterioration. The frozen bagasse was subsequently comminuted with a Jeffco shredder (Jeffress Bros., Brisbane, Australia). The moist, shredded bagasse was then placed in large, stainless steel baking pans and dried at 45 °C for 72 h to give a final moisture content of 5.20 wt %. A 1 kg quantity of the dried, shredded bagasse was further heated at 70 °C until it became bone dry, defined here as having a moisture content at or below 0.10 wt %. A 25 kg portion of the processed bagasse underwent additional size reduction in a Wiley mill (Arthur Thomas, Philadelphia, Pa.) fitted with a 2.00 mm mesh screen, followed by further drying at 45 °C for 48 h to reach a final

moisture content of 3.25 wt %. The dry, ground bagasse was then poured into clean, 5-gallon high-density polyethylene pails that were stored at 6 °C.

3.2.3 Irradiation

To mitigate the possibility of microbiological activity during extended storage, the refrigerated bagasse used in the hydrothermal experiments was subjected to doses of ionizing gamma radiation, ranging from 0.25 to 2 MR. Bagasse used in the hydrothermolysis experiments was taken from a batch of bagasse that had received a 2 MR dose of gamma radiation. The 2 MR dose was selected based on several studies [280-283] of various grains, nuts, and fruits which indicate that a level of 1 MR is sufficient to destroy most microorganisms and that a level of 2 MR is enough to render innocuous even the most resilient fungi. The bagasse was irradiated at the LSU Nuclear Science Center field laboratory according to the following procedure. A Shepherd Model 484R cobalt-60 irradiator (J. L. Shepherd & Associates, San Fernando, Calif.) was used to irradiate the sample. The irradiator had a NIST traceable exposure rate of 1,743 $R \cdot min^{-1}$ (accuracy ± 5%) on November 5, 2003. Dried, shredded samples of bagasse were sealed in Mason jars that were then placed inside the irradiator. Given a half-life of 5.271 years for cobalt-60 [284] the decay-corrected exposure rate was 986.0 $R \cdot min^{-1}$ at a point 5 inches above the center of the Mason jar lid. The samples were subjected to an absorbed dose rate of 910.8 $R \cdot min^{-1}$. Irradiation treatment times varied depending on the desired absorbed dose.

3.2.4 Sieving

The shredded bagasse samples were separated by particle size into 13 fractions using a Retsch AS 200 control vibratory sieve shaker (Haan, Germany). The vibratory sieve shaker is

classified as a throwing-type sieving machine, which utilizes an electromagnetic drive to impart motion to a spring-mass system that transfers oscillations to a sieve stack [285]. Particles in throwing-type sieve shakers are subjected to 3-dimensional movement that is uniformly distributed across the entire sieving surface. Throwing-type sieve shakers permit both the amplitude, or vibration height, and the sieve bottom acceleration to be specified. The latter parameter is the most important in throwing-type sieve analyses. Both parameters are determined primarily by the natural frequency of the vibratory oscillations from the sieve shaker [286]. The 14 Retsch sieves used to partition the shredded bagasse particles all had a height of 50 mm and an outside diameter of 200 mm. The mesh opening sizes for the sieves are listed in Table 9. Shredded bagasse samples were sieved in 50 g batches on the vibratory sieve shaker for 30 minutes each using a vibratory height setting of 2.50 mm, a sieve bottom acceleration of 1 "g" (i.e., 1 "g" = 9.81 $m^2 \cdot s^{-1}$), and a vibration interval of 10 s.

Table 9. Chart of test sieve sizes and their corresponding mesh openings.

US Sieve Size	Mesh Opening [mm]	US Sieve Size	Mesh Opening [mm]
3/8 in.	9.50	No. 35	0.500
No. 3½	5.66	No. 45	0.355
No. 7	2.83	No. 60	0.250
No. 10	2.00	No. 80	0.180
No. 14	1.41	No. 120	0.125
No. 18	1.00	No. 140	0.106
No. 25	0.710	No. 230	0.063

3.3 Hydrothermolysis Experimental Method

Whereas numerous studies exist on the supercritical water gasification of model biomass compounds, comparatively fewer results are available on the SCW gasification of actual biomass. There is a small amount of data available on the conversion of sugarcane bagasse in subcritical water but this quickly drops to a nonexistent level for supercritical water.

Furthermore, there is a critical shortage of detailed information regarding the volatile products in the available biomass gasification literature. Therefore, this study was undertaken to closely examine the effects of temperature, residence time, biomass concentration, and particle size in relation to the composition and yields of volatile products.

3.3.1 Apparatus

Experimental runs were conducted inside a seasoned (> 50 operational hours) 65 mL reaction cell specially fabricated from Hastelloy X (Haynes Int'l., Kokomo, Ind.) stainless steel bar stock. Hastelloy X was selected because of its excellent high-temperature strength and oxidation resistance. A common criterion for evaluating oxidation strength of metals involves measuring the average corrosion depth after exposure to dry, hot air for extended periods. The average corrosion depth in Hastelloy X exposed to dry flowing air for 1008 h at 980 °C was shown to be 0.038 μm (1.5 mils) [287]. It is claimed that the formation of a tenacious oxide film at high temperatures shields Hastelloy X from oxidative attack [288]. Exceptional carburization resistance is also afforded by Hastelloy X. Tests in a carburizing atmosphere (i.e., 5 vol % each of H_2, CO, and CH_4 with balance Ar) at 980 °C for 55 h revealed that Hastelloy X picked up 2.5 mg C per cm^2 of surface area [287]. Hastelloy X plate stock that was heat treated at 1177 °C and then quenched has an average Rockwell B hardness of 89 at room temperature. The nominal chemical composition of Hastelloy X is given in Table 10 below:

Table 10. Nominal chemical composition of Hastelloy X bar stock in weight percent [287].

Ni	Cr	Fe	Mo	Co	W	C	Mn	Si	B
47[21]	22	18	9	1.5	0.6	0.10	1[22]	1[21]	0.008[21]

[21] As balance
[22] Maximum

Because of its exceptional ability to withstand the extreme processing conditions associated with supercritical fluid regimes, the reaction cell was appropriately termed "the bomb", which will be the designation used henceforth. The cylindrical bomb had a 6 in. (15.24 cm) height, a 1 in. (2.54 cm) internal diameter, and 1 in. (2.54 cm) thick walls. The bomb is sealed using a bored-through, tapered plug and a screw cap with a center porthole that is secured using a pipe wrench. Six ½ in. (1.27 cm) diameter Bumax® 88 stainless steel socket head cap screws are tightened to 80 $ft \cdot lb^{-1}$ (108.5 N·m) of torque to ensure that the plug is sufficiently cinched. Access to the interior of the sealed bomb is through a single port atop the screw cap. Thick-walled ¼ in. (0.635 cm) 316L stainless steel tubing (Swagelok, Cleveland, Ohio) was used to connect the bomb port to a 15 kpsi (1034 bar) pressure transducer (NOSHOK, Akron, Ohio) and a 20 kpsi (1379 bar) medium pressure valve (High Pressure Equipment Co., Erie, Pa.).

The pressure transducer was calibrated using an industrial dead-weight tester (Smiths Industries Ltd., Birmingham, England) from 2 to 10,000 psi (0.138 to 690 bar). A simple linear regression of the calibration data revealed that the pressure transducer measurement was accurate to within 0.76% of the true pressure value at pressures as high as 10,000 psi (690 bar), as shown in Figure 15. Given the remarkable consistency between the pressure transducer readings and the true pressure values it was felt that the linear regression relationship could be safely applied on pressure transducer measurements up 12,000 psi (827 bar), thereby permitting working pressures slightly in excess of 10,000 psi (690 bar). A Yokogawa DX104 data recorder (Tokyo, Japan) was used to convert a 4–20 mA output signal from the pressure transducer into a corresponding digital pressure reading. Pressure measurements were acquired every 0.5 s throughout the duration of experimental runs.

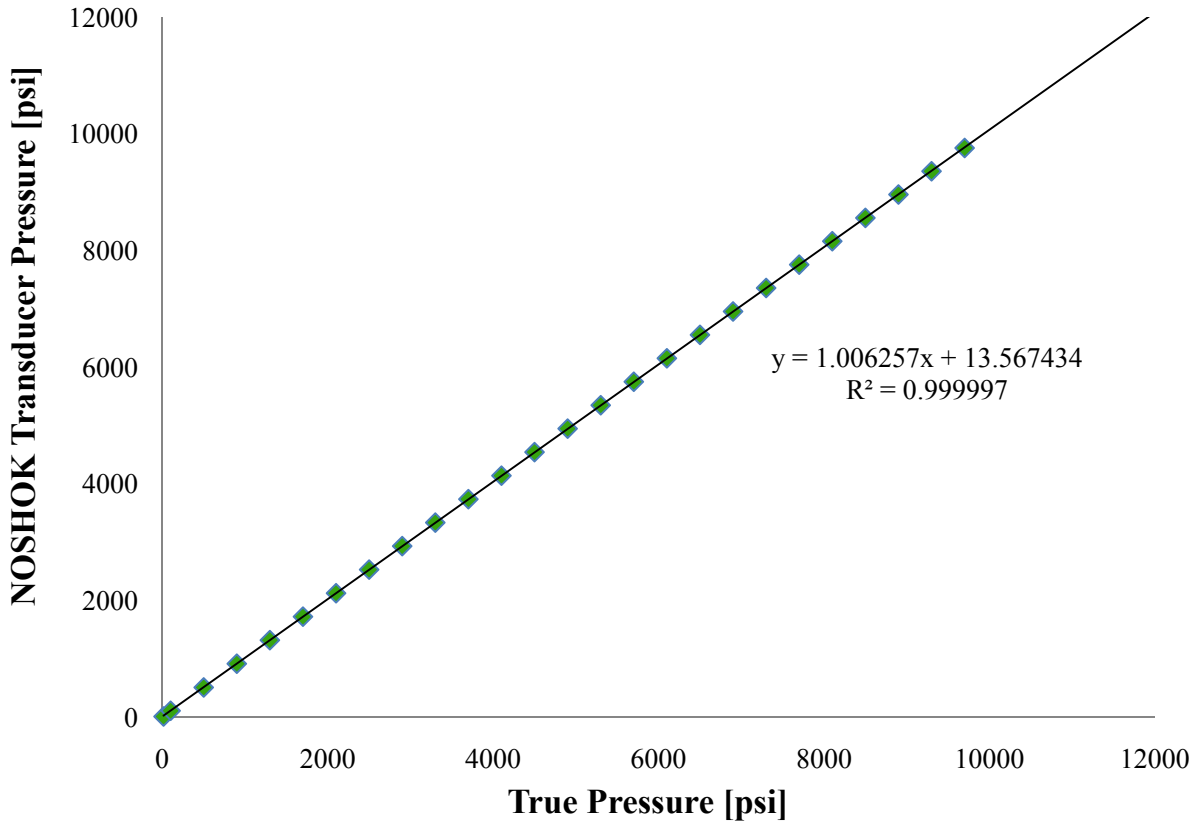

Figure 15. Pressure transducer calibration curve.

The bomb was heated to temperature in a molten tin-bismuth alloy (i.e., 99% Sn–1% Bi) bath using a Buzzer Model 172-HT furnace (Charles A. Hones, Inc., North Amityville, NY). The molten Sn-Bi bath was heated in a No. 183 cast iron melting pot (14 in. [35.6 cm] internal depth, 10 in. [25.4 cm] I.D., and 13 in. [33.0 cm] outside flange diameter) having an approximate working capacity of 260 lbs (118 kg) for tin. The furnace was powered using propane and its "full-tilt" heating output capacity was rated at 115,000 Btu·hr^{-1} (33.7 kW). A single-loop on-off controller (Watlow Electric Mfg. Co., St. Louis, Mo.) was used to regulate the furnace temperature. For any given set point temperature, the maximum positive hysteresis value was no more than 2% above the set point, while the minimum negative hysteresis value was always an no more than 0.05% below the set point. A photograph of the furnace is shown in Figure 16.

Figure 16. Molten metal furnace.

3.3.2 Experimental Testing Procedure

The experimental testing procedure used in every hydrothermal run is detailed below. The bomb was initially loaded with a specified amount of irradiated, shredded bagasse (refer to Section 2.2 for further details regarding bagasse sample preparation) or other biomass type. DI H_2O was then added to the biomass in such quantity calculated to give a prescribed biomass concentration. The pH of the DI H_2O was consistently in the range of 5.40 to 5.90. The bagasse (or other biomass) and the DI H_2O were then stirred with a glass rod until all of the bagasse had been visibly moistened. After the biomass slurry was sufficiently mixed, the bomb was immediately sealed according to the procedure described in Section 3.3.1.

In order to eliminate the presence of oxygen, every hydrothermal run was subjected to a purging cycle. The loaded, air-tight bomb was filled with He until the pressure reached equilibrium with that of the helium cylinder used. The helium cylinder valve was then closed and the bomb was vented in a water-filled bucket to slightly above atmospheric pressure. This routine was repeated 5 times, but it should be noted that on the fifth vent, unlike the previous ventings, the bomb pressure was lowered to between 15 and 95 psig (1.034 and 6.550 bar abs.).

A braided stainless steel rope was fastened to the bomb by securing S-hooks to the Bumax bolts. The braided steel rope was affixed to a latching hook that was used to attach the entire bomb assembly to a Clevis slip hook. The slip hook was connected via a stainless steel cable to a moveable pulley on a sliding track. The end of the cable was used to hoist and lower the bomb, while a secondary pulley cable was used to move the hoisted bomb between the furnace and an ice bath. A picture of the hoisted bomb assembly and the connecting pulley cables can be seen in Figure 17.

The bomb was then lowered into the molten metal bath until only the bomb cap remained above the molten tin, as pictured in Figure 18. Bomb height inside the furnace was controlled by restraining the pulley cables with a tieback clasp to prevent total submersion of the bomb in the molten tin bath. Submersion of the bomb cap was undesirable because the liquid tin was able to seep into the threaded grooves of the cap, creating enormous difficulties for post-run access to the bomb contents. The duration of the submersion ranged anywhere from 1 to 60 min, not including the 5 min that was required for the bomb to reach temperature. The bomb was quenched in an adjacent ice bath, as shown in Figure 19. Generally it took less than 60 s to drop the internal pressure in the bomb from 10,000 psi (690 bar) to below 1,000 psi (69 bar). Slightly longer times were required if the bomb cap became temporarily jammed on an ice floe.

Figure 17. Hoisted bomb shown before the start of a hydrothermal run.

Figure 18. Immersion of bomb in molten metal bath.

Figure 19. Quenching of bomb.

Special precautions and safety gear were employed to minimize operational hazards. Nevertheless, severe service environments, such as those encountered here, can lead to sudden, premature equipment failure. The high pressure valve shown in Figure 20 was operating within its designed specification limits when the seal inside ruptured unexpectedly.

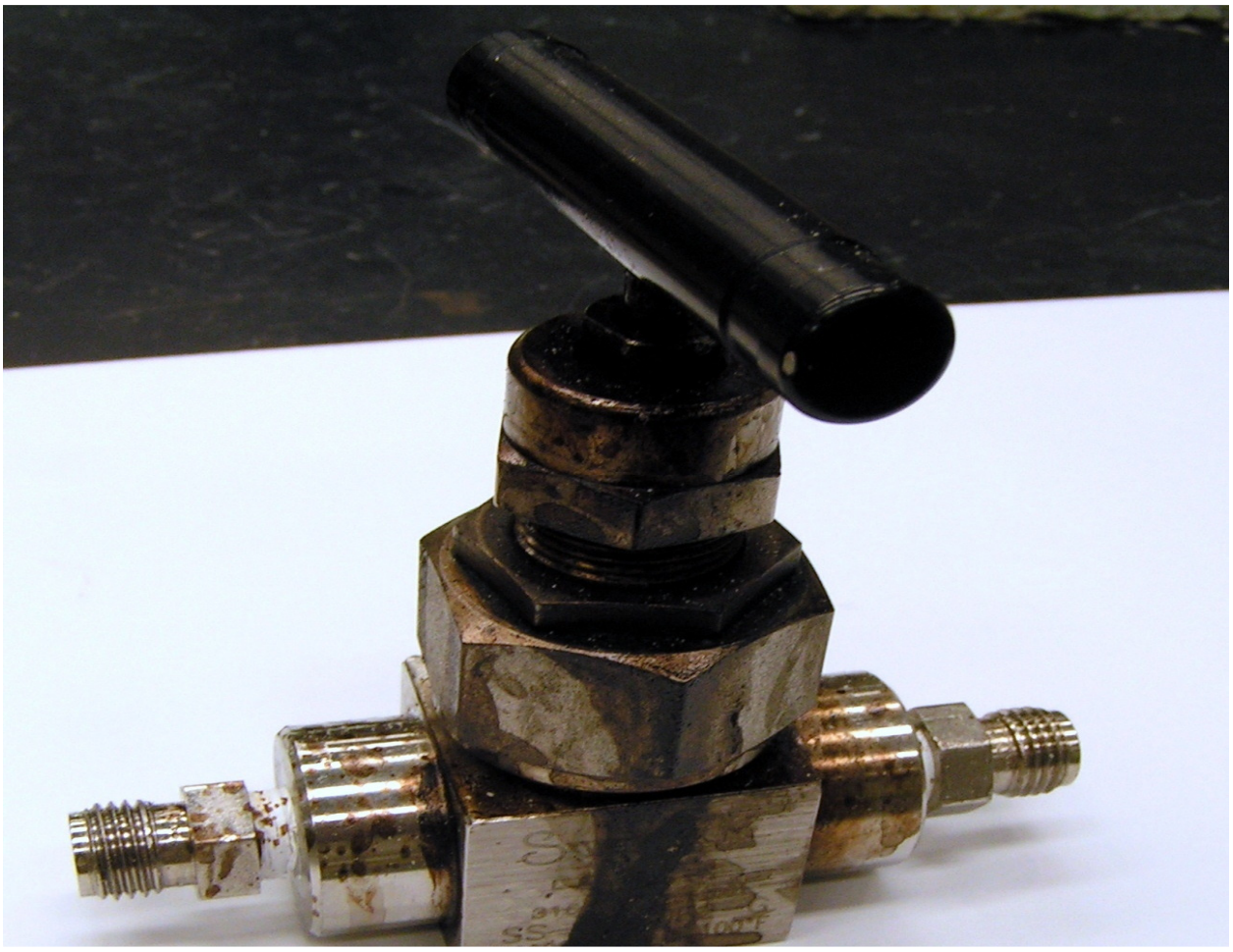

Figure 20. High pressure valve (10,000 psi) with ruptured internal seal.

Another example of the damage that can be caused when operating at high pressures is depicted in Figure 21. Here an in-line filter assembly used to remove aerosols and fine particulate matter from the bomb headspace is pictured. In this case, the filter assembly was rated to 20,000 psi (1379 bar), far in excess of the customary working pressures near 10,000 psi (690 bar). Similarly, the ¼ in. (0.635 cm) OD heavy-wall (0.095 in. [0.241 cm] wall thickness)

stainless steel tubing was designed to accommodate pressures up to 15,000 psi (1034 bar). The minimum bend radius for ¼ in. (0.635 cm) OD tubing is ¾ in. (1.905 bar), which is the radius that was used to create the 90° bend shown in Figure 21. A straight tube length of at least $^{13}/_{16}$ in. (2.064 cm) is required after a bend in ¼ in. (0.635 cm) OD tubing to provide ample space for seating compression tube fittings [289]. A straight tube length of 1 in. (2.54 cm) was used for the 90° bend between the in-line filter and the high pressure valve. The damage shown in Figure 21 happened during a preliminary trial run at 600 °C. There were no warning signs that presaged the explosion, which occurred just after the system pressure hit 11,767 psi (811 bar). The force of the explosion stripped the compression fitting from the tube as highlighted in the photograph. The explosion also bent back the straight tube between the in-line filter and the 90° bend by 30°.

Figure 21. High pressure in-line gas filter rated to 20,000 psi (1379 bar) shown with bent tube.

The dramatic pressure drop resulting from this explosion can be seen in Figure 22. The breach created in the system between the in-line filter and the high pressure valve posed another safety hazard. The dangling, top-heavy bomb had to be gingerly raised using the pulley guide cables to avoid upsetting the aqueous contents in the bomb. Spillage of the aqueous media into the molten metal bath could have caused the hot liquid tin to spray out of the furnace violently.

The cursory synopsis of major incidents that took place during operation of the hydrothermal experimental apparatus is not intended to serve as a comprehensive catalogue of

potential hazards associated with supercritical water systems. Instead these mishaps were included to emphasize the dangers that are inherently present when working with high pressure processes. Explosions can result in the loss of life or limb and the author strongly encourages aspiring readers to exercise the utmost caution and utilize common sense when designing, constructing, and operating hydrothermal systems. Please be aware that the author assumes no liability for those who are injured or die when following the experimental procedures listed in this dissertation.

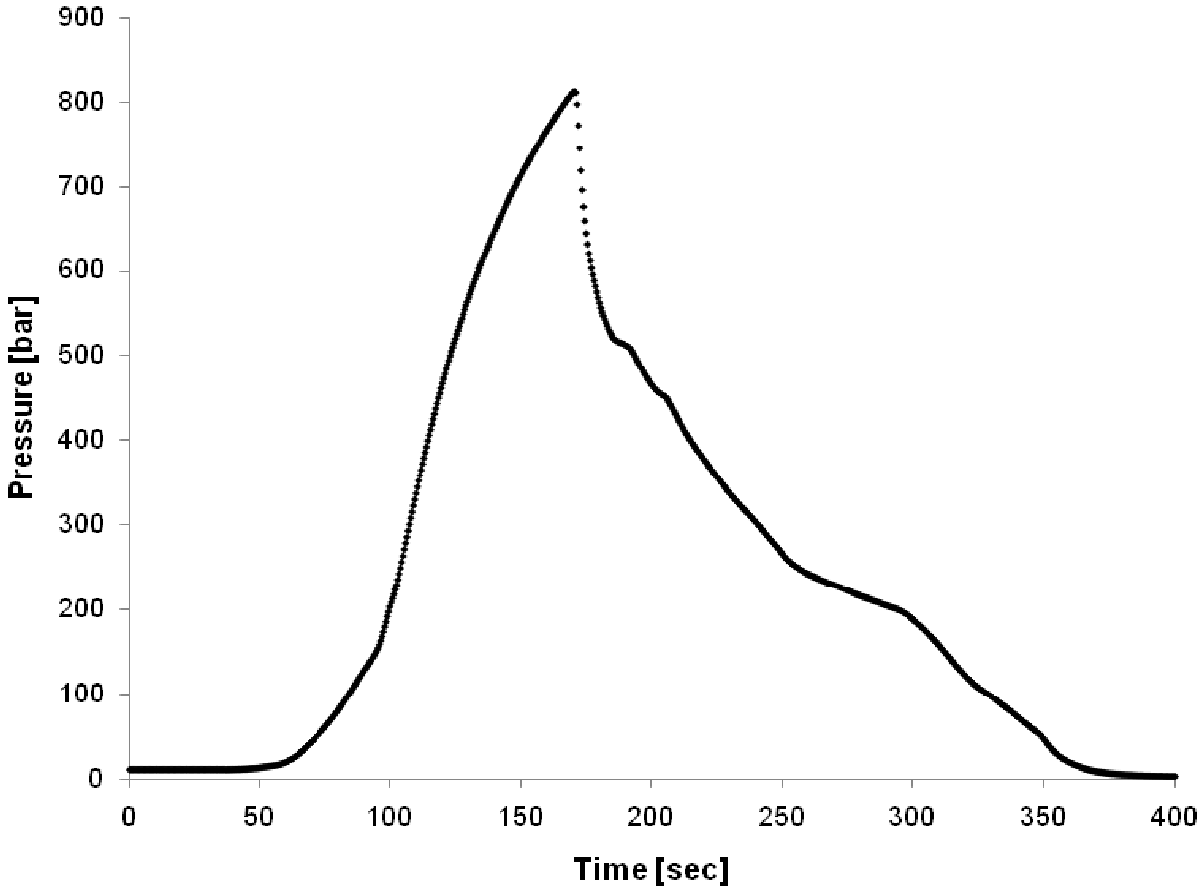

Figure 22. Pressure drop resulting from bomb explosion.

3.3.3 Experimental Run Design

A series of experiments was designed to explore the individual impact of temperature, residence time, biomass loading, and particle size on the hydrothermal decomposition of

bagasse. The selection of the former two variables is transparent because both temperature [17, 47, 226, 227, 257, 258, 265, 290-294] and residence time [257, 258, 265, 291, 292, 295, 296] are known for their influential role in biomass hydrothermal conversion. The effects of biomass loading and particle size on biomass hydrothermolysis have been studied in far less detail than either temperature or residence time, so it was deemed apropos to include them in this study.

Hydrothermal treatment with irradiated, unsieved bagasse particles (2 MR) less than 2 mm in diameter at 500 °C, 5 min residence time, and a 4.0 wt % biomass was arbitrarily designated as the standard baseline condition for the following experimental design. The baseline condition was used as an origin from which operational parameters were adjusted individually to assess their influence on the composition and yields of volatiles.

3.3.3.1 Temperature

Due to the significance of temperature in previous near-critical and supercritical water studies, a concerted effort was made to fully characterize this operational parameter before beginning the planned temperature study measurements. Hysteresis in the single-loop controller for the furnace at various reaction temperatures was investigated. The ramp time to the temperature was experimentally determined using a bomb fitted with a thermocouple connected to a digital temperature logger. The experiments used to evaluate the heating rate of the loaded bomb were conducted under air because the thermocouple precluded purging of the bomb with an inert gas. The volatile products from these tests were not captured for characterization. The heating rate experiments were conducted using either a 4.0 or 8.0 wt % loading of bagasse in water. Heating rate trials were performed at reaction temperatures of 300, 400, and 500 °C. The temperature curves for the trials at 400 and 500 °C are plotted in Figure 23a and Figure 23b, respectively. The time required to reach 5 and 10% of set point temperature is shown for each

plot. It took 5 min for the internal bomb temperature to come within 2.0% of the set point at 500 °C and 1.0% of the set point at 400 °C. It took only 3.75 min for the bomb temperature to reach the set point at 300 °C. The nominal ramp time to set point temperature was taken to be 5 min for every reaction temperature except for that of 300 °C, which was taken to be 3.75 min. Therefore, the heating rates for the experiments performed at 300, 400, and 500 °C were calculated to be 73, 75, and 95 °C·min^{-1}, respectively. The heating rate for the experiments at 600 °C was estimated to be 115 °C·min^{-1} based on theoretical heating curves obtained from finite element analysis modeling and empirical pressure data obtained from experiments performed at 600 °C. It can also be ascertained from Figure 23 that the quenching process required approximately 90 to 120 s to lower the system temperature from the set point temperature to less than 100 ºC. Upon reaching the target temperature, the single-loop feedback controller ensured that the system temperature did not deviate more than 2% above or 0.5% below the set point.

The actual temperature study experiments were carried out at 300, 400, 500, and 600 °C. The temperature tests were performed using DI H_2O with a 4.0 wt % bagasse loading. The bagasse weight loading refers to the weight of dry bagasse used in the preparation of the bagasse slurry. An effective residence time of 5 min was employed for all of the temperature runs. The effective residence time is defined here as the amount of time that the reaction spent at the target temperature and does not include the heating ramp time or the quench time.

3.3.3.2 Residence Time

The effect of residence time on bagasse hydrothermolysis was investigated by performing experiments at 5 different reaction times (i.e., 1, 5, 10, 30, and 60 min), while holding the reaction temperature (500 °C), biomass loading (4.0 wt %), and particle size (< 2 mm) constant.

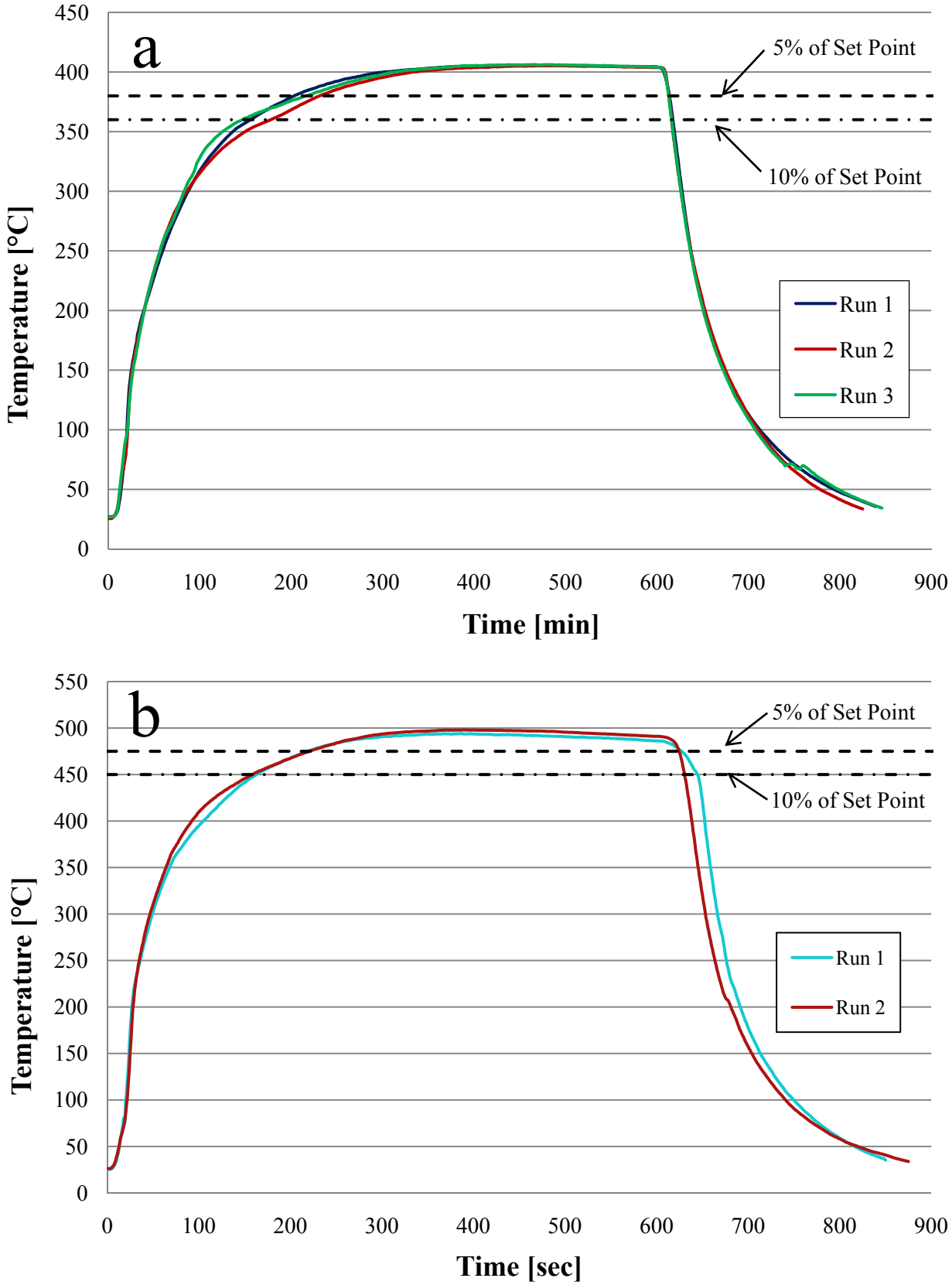

Figure 23. Temperature curves for hydrothermal reactions at a) 400 °C b) 500 °C.

3.3.3.3 Biomass Weight Loading

The effect of biomass weight loading on product distribution and yields was investigated using three different biomass concentrations, *viz*.: 2.7, 4.0, and 8.0 wt %. Biomass concentration is defined here as the total amount of dry biomass contained in the biomass slurry. The preceding biomass concentrations correspond with biomass to water ratios of 1:12.5, 1:25.0, and 1:37.5, respectively. The biomass weight loading runs were conducted using the baseline conditions of 500 °C, 5 min effective residence time, and particle size less than 2 mm.

3.3.3.4 Particle Size

Three different particle size fractions were employed to determine whether particle size is a factor in hydrothermal biomass treatment. The three sieve cuts of bagasse included particles sized between mesh numbers 18/25, 45/60, and 140/230. The results from the various sieved bagasse fractions were subsequently compared with baseline runs using unsieved bagasse having a particle size less than 2 mm. The particle size studies employed a uniform temperature (500 °C), biomass loading (4.0 wt %), and effective residence time (5 min).

3.3.4 Catalysis

The selection of hydrothermal gasification catalysts is dictated largely by the stability of a given catalyst in hot liquid water for extended periods of time [297]. Traditionally, the use of catalysts in supercritical water treatment of biomass has been restricted to activated carbons, certain alkali salts (e.g. potassium and sodium carbonates and hydroxides), noble metals (e.g., Pd, Pt, Ru, Rh), and a few base metals, most notably Ni, Co, and Fe. The reasons for the limitation of catalyst choice to this select handful of materials are not abundantly clear, except that it appears to be a matter of habit more than anything else. The only critical assessments

regarding the catalytic activity of various transition metals during hydrothermal gasification have come from Elliott's research group [297-299] at Pacific Northwest National Laboratory. Elliot *et al*. studied more than a dozen different transition metal elements on various supports and in different formulations. The volumetric amount of CH_4 formed was used as the criterion for measuring catalytic activity. It was determined that nickel, ruthenium, and rhodium have the highest level of catalytic activities. Catalysts having lower activity, include iridium, platinum, palladium, molybdenum sulfide, and copper on zinc oxide. It is theorized that cheaper catalysts proven effective in the petroleum hydrocarbon industry may also work in a supercritical water environment. Additionally, the use of standard hydrocarbon processing catalysts allows a facile comparison of the catalyst behavior in petrochemical systems versus that in biomass hydrothermal processes.

3.3.4.1 Catalyst Preparation

Lithium doped magnesium oxide (Li/MgO) was prepared via wet impregnation of MgO with an aqueous solution of lithium hydroxide hydrate ($LiOH{\cdot}H_2O$). Crystalline $LiOH{\cdot}H_2O$ was dissolved in demineralized water at 75 °C. MgO was added to this solution forming a slurry. The slurry was then stirred and maintained at 75 °C until the excess water had evaporated leaving behind a thick paste. The paste was then calcined in a crucible for 12 h at 500 °C and subsequently crushed and sieved. The particle size fraction between 30 and 60 mesh (250–600 μm) was retained.

3.3.4.2 Catalyst Runs

Manganese dioxide (MnO_2) was used as a catalyst to determine if oxidative coupling of methane (OCM) could occur under NCSW conditions. A report by Sofranko *et al*. [300]

indicated that between 15–20 wt % manganese loading is the optimal amount for the highest conversion of methane to C_2 hydrocarbons, including ethane (C_2H_6) and ethylene (C_2H_4). Lithium-doped magnesium dioxide (Li/MgO) was used as a catalyst to investigate whether traditional catalytic oxidation mechanisms that are exploited by the petroleum industry to convert ethane to ethylene proceed in a similar manner under supercritical conditions. The conditions used in the current catalyst runs are described in detail in Table 11.

Table 11. Experimental conditions for catalyst runs.

Catalyst	Loading [mg]	Catalyst : Substrate [wt %]	Temperature [C]	Pressure [bar]	Water Density [g·cm^{-3}]
Li/MgO[23]	299	21.0	500	729	0.422
MnO_2[24]	398	28.0	500	703	0.408
MnO_2[25]	398	27.8	500	730	0.423

3.3.5 Reductant Runs

Two runs were performed adding sodium borohydride ($NaBH_4$) as a reducing agent. The first run used 1.0 g $NaBH_4$ and the second run used 0.1 g $NaBH_4$. The H_2 content from the first run grossly exceeded the linear operating range of the HID and, thus, further analysis of this run was halted. The incorporation of 0.1 g $NaBH_4$ in the second run provided an additional 10.7 mg of hydrogen to the amount of atomic hydrogen available to react. In both instances, the $NaBH_4$ was placed inside borosilicate ampoules that were then flame-sealed to ensure that the reductive hydride would not react prematurely with the liquid water until near-critical conditions had been attained. A separate run utilized carbon monoxide (CO) as a reductant. The bomb underwent an identical purging procedure as previously described for the inert gas runs except that CO was

[23] 3 wt % Li loading
[24] 1st run
[25] 2nd run

used. After the fifth purge, the bomb was charged with CO to a pressure of about 105 psi, so that the total amount of CO in the bomb prior to the hydrothermal reaction was equal to 6.2 mmol.

Table 12. Experimental conditions for reductant runs.

Catalyst	Loading [mg]	Reductant : Substrate [wt %]	Temperature [C]	Pressure [bar]	Water Density [g·cm^{-3}]
$NaBH_4$	100	7.0	500	788	0.452
CO	174	12.2	500	713	0.413

3.3.6 Titanium Bomb

A run was conducted using the baseline experimental conditions inside an aged (> 20 operational hours) titanium bomb to determine the impact that the reactor walls may have on the hydrothermal reaction. Titanium Grade 5 alloy (Corrosion Materials, Baker, La.) was used in the fabrication of the bomb. The nominal chemical composition of the titanium bar stock is provided in Table 13.

Table 13. Nominal chemical composition of titanium bar stock in weight percent [301].

Ti	Al	V	Fe	O	C	N	H
90.3[26]	5.5	3.5	0.25	0.20	0.08	0.05	.0125

3.4 Analytical Test Procedures

3.4.1 Instrumentation for Volatiles Product Analysis

A Hewlett-Packard 5890 Series II gas chromatograph equipped with both a flame ionization detector (FID) and a hydrogen ionization detector (HID) was used to analyze the volatile contents in the bomb headspace. An aerosol removal system was devised to prevent water vapor in the moisture-laden volatile gas stream from condensing and plugging transfer tubing lines leading to the gas chromatograph. A train of three filter traps (Parker Finite Filter,

Oxford, Mich.) was used to capture 99.97% of particulate and aerosol matter larger than or equal to 0.01 µm. The initial trap, pictured in Figure 24, was used to eliminate excess quantities of liquids in the gas stream and contained a rolled stainless steel mesh that served as a water separator filter for droplets larger than 100 µm.

Figure 24. Initial moisture trap in aerosol removal system.

The second and third traps consisted of coalescing filter media designed for liquid and particulate elimination, with the second trap acting as a prefilter for the final trap by removing water,

---

[26] As balance

tenacious aerosols, and particulates having a diameter of 1.0 μm or greater. These latter two traps are shown in Figure 25.

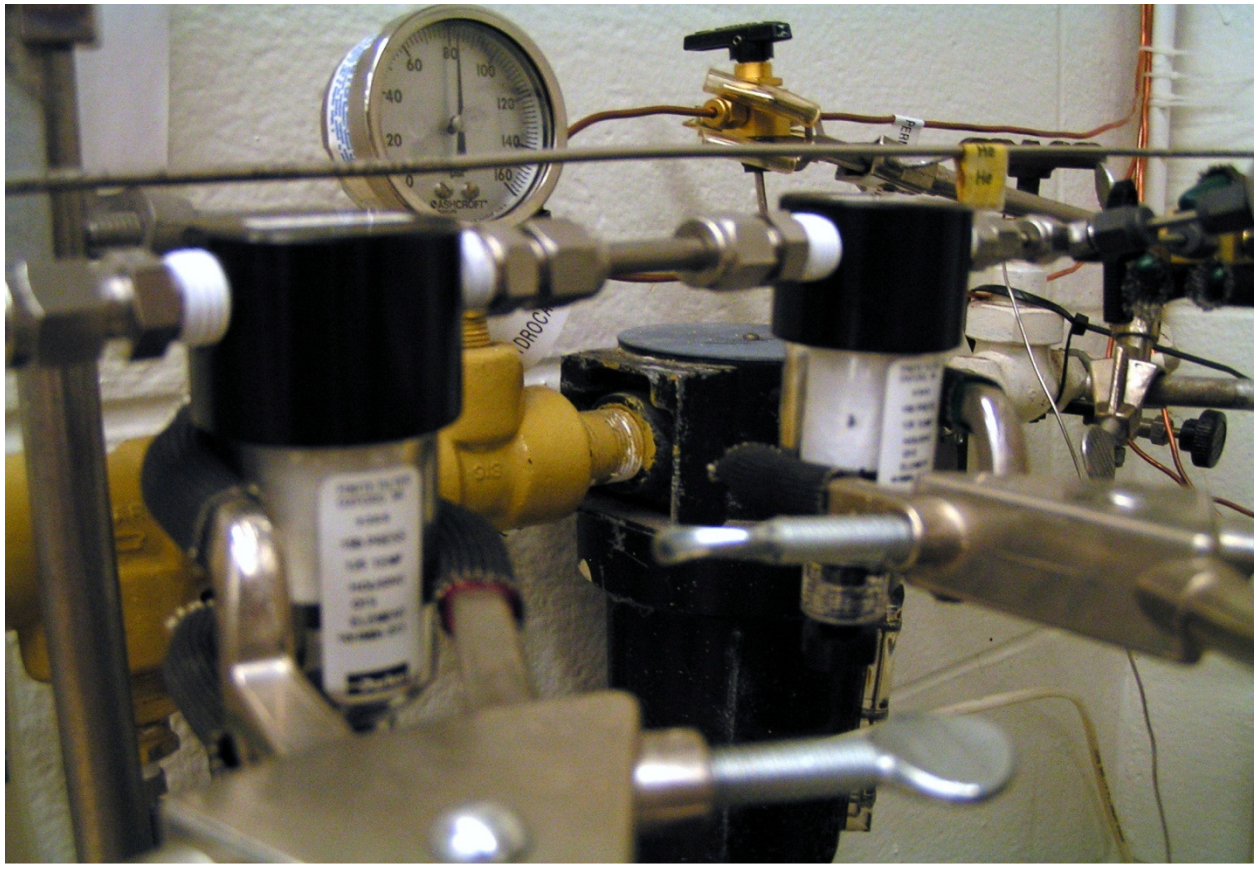

Figure 25. Coalescing filter moisture traps.

Two parallel micropacked columns were employed to perform the gas analysis. A Hayesep D (Hayes Separations, Bandera, Texas) column (2 m x 1.0 mm I.D.) micropacked with 100/120 mesh divinylbenzene particles followed by a FID detector was used in the detection of all hydrocarbons from C_1 to C_6. The permanent gases and light hydrocarbons through C_2 were measured using a ShinCarb ST (Restek, Bellefonte, Pa.) column (2 m x 1.0 mm I.D.) micropacked with 100/120 mesh carbon molecular sieve particles followed by an HID detector. The HID detector is a specialized dielectric barrier discharge (DBD) detector designed for permanent gas analysis and, in particular, hydrogen detection. The HID plasma reaction cell was powered by a 12 V, 0.5 A power supply. The plasma cell operated at 6 V and 270 mA. A photo

of the HID detector assembly is shown in Figure 26. The FID detector can be seen in the foreground.

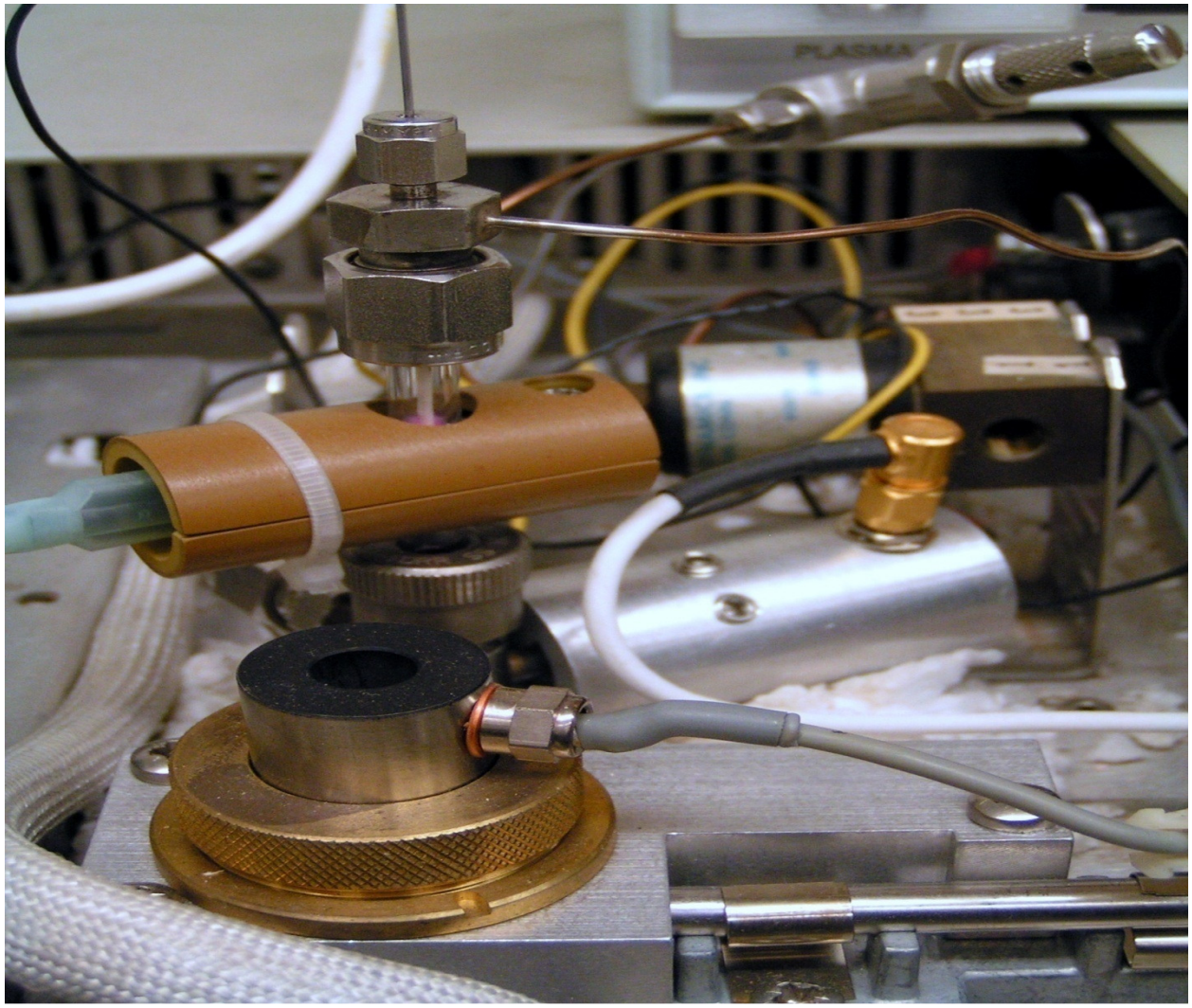

Figure 26. HID and FID detectors used in GC analysis of volatile products.

3.4.2 GC Method

The conditions employed in the GC analysis of the volatile products are expounded below. Both detectors were maintained at a uniform temperature of 150 °C to inhibit moisture adsorption. A stream of H_2 at 28 mL·min^{-1} and air at 280 mL·min^{-1} was supplied to the FID detector. The HID detector was supplied by a 75 mL·min^{-1} flow of He. A 34 mL·min^{-1} flow of He was directed to a pre-guard column located before a tee that separated carrier flow to the two

micropacked columns. The He flow to the Hayesep D micropacked column was 21 $mL \cdot min^{-1}$, while the He flow to the Shincarb ST micropacked column was 13 $mL \cdot min^{-1}$.

Introduction of standards and sample gases was controlled using a combination of 3-way valves and a Vernier metering valve. Gas samples were allowed to flow through a 250 μL GC gas sampling loop for approximately 2 min to ensure that a representative aliquot of the sample headspace had been obtained. Gas injection from the gas sampling loop occurred via a 6-port automated sampling valve as shown in the schematic given in Figure 27. After 2 min, the flow of gas sample was turned off at the 3-way valve and the gas sample in the loop was allowed to equilibrate to atmospheric pressure before injection. Atmospheric pressure sampling was verified by observing bubbling from the exhaust line of the gas sampling valve, which was vented into a beaker filled with water. When the bubbling from the exhaust line subsided the sample was injected into the GC system. There was no compensation for different atmospheric pressures on different days.

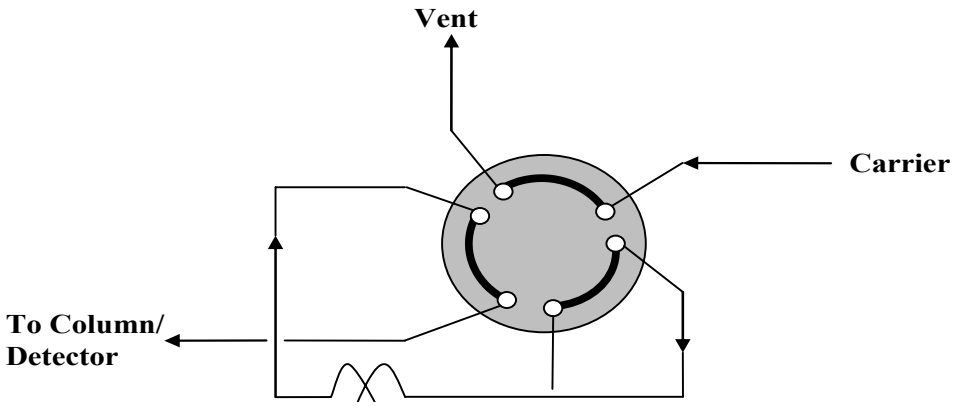

Figure 27. Automated 6-port GC sampling valve.

The complete GC analytical system used in the evaluation of the volatile products is illustrated in Figure 28.

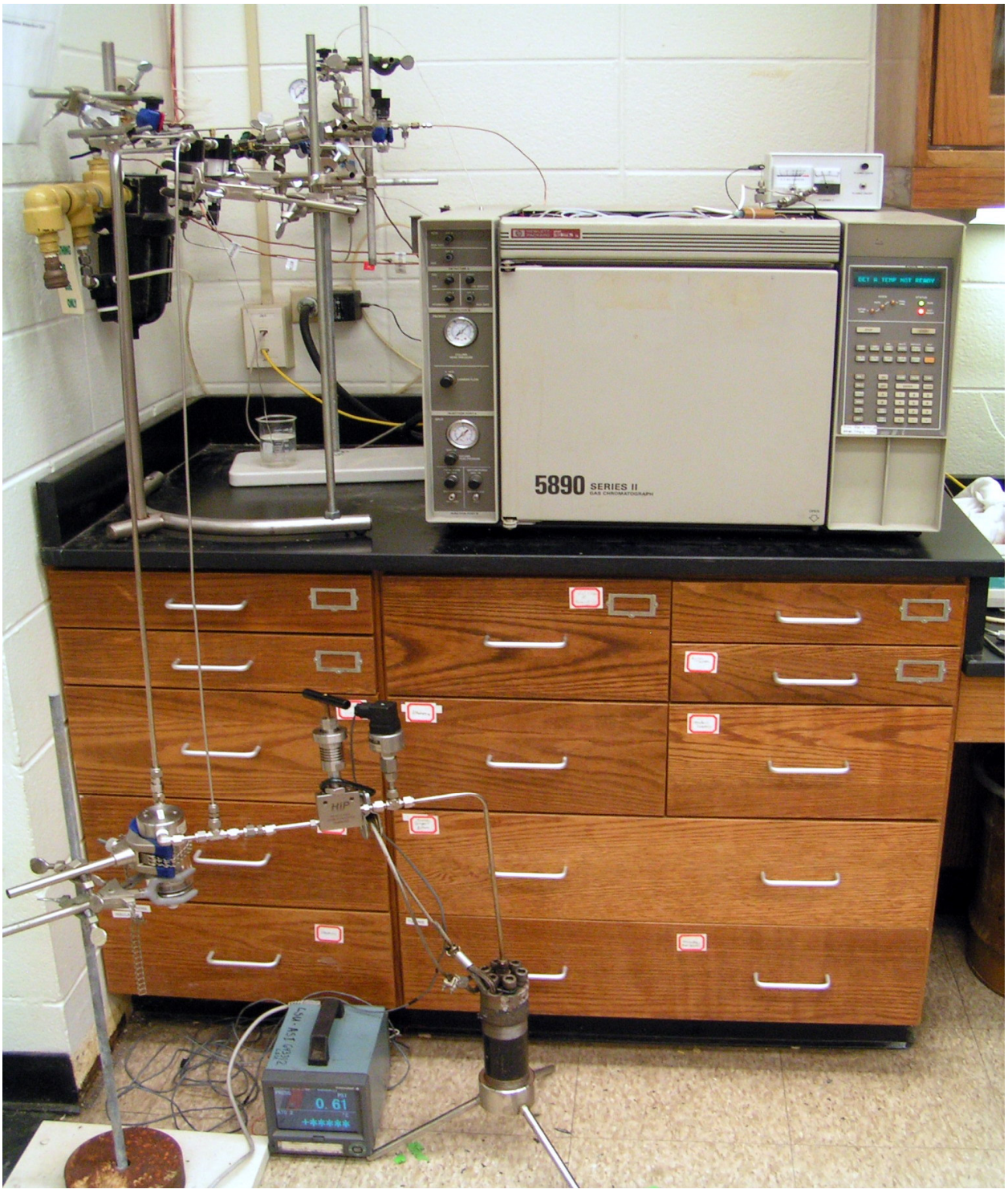

Figure 28. Complete GC analytical system used to evaluate volatile products from bagasse.

The GC oven was held isothermally at 40 °C for 5 minutes, after which time the oven temperature was heated at a ramp rate of 12.5 °C·min^{-1} until it reached a final temperature of 240

°C, which was maintained for 12 minutes before concluding the run. The total GC analysis run time was 33 minutes. The ramp rate and maximum temperature set point were deliberately selected to not only generate sharp, resolved peaks, but also to avoid the manifestation of ghost peaks on successive chromatograms from late eluting compounds.

A calibration curve, shown in Figure 29, was established for 0–10,000 ppm of H_2 in He for the HID detector. Three of the H_2 gas standards were purchased pre-mixed with nominal H_2 concentrations of 10,000, 1,000, and 100 ppm, as mentioned previously. The remaining mixtures were formulated in-house by diluting a given flow of H_2 standard with a prescribed flow of He to give the desired H_2 concentration. The lower detectable limit (LDL) of the HID was calculated by using a factor of 3 times the signal to noise ratio. Accordingly, the LDL of the HID for H_2 was 30 ppm.

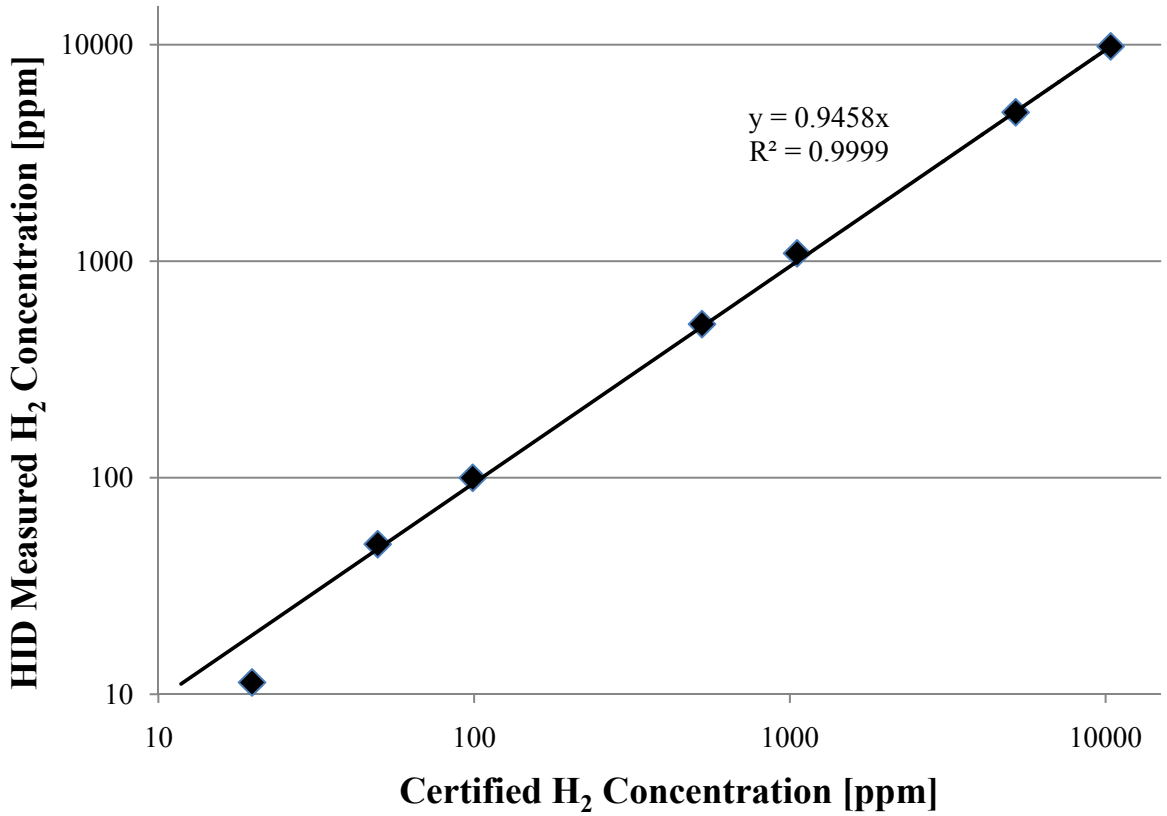

Figure 29. Calibration curve for 0-10000 ppm hydrogen in helium for the HID.

3.4.3 Access and Removal of Bomb Products

After the gas analysis was completed, the residual gas remaining in the bomb was vented until the bomb was depressurized. Accessing the bomb contents was occasionally complicated by the fact that some tin would seep into the first few grooves of the threaded bomb cap. The hardened tin was quite malleable and thus it required a concerted effort to wrench the cap free within a reasonable time frame to prevent evaporative losses from the aqueous phase. The liquid and solid contents of the bomb were scrupulously removed and weighed. Condensate that had deposited onto the internal bomb threads and inside the screw cap was absorbed onto previously tared Kimwipes® and then weighed. The recovery procedure for slurries located on the bomb floor depended upon their rheology and viscosity. Viscous slurries whose flowability resembled that of toothpaste or fresh asphalt were reclaimed using previously tared Kimwipes®. Thinner suspensions resembling sludges were removed by adding a known volume of DI water, followed by vigorously stirring the sediment at the bottom, and then quickly inverting the bomb and pouring the remnants into an aluminum weigh boat. An illustration of the separation procedure for the products from the hydrothermal conversion of bagasse is displayed in Figure 30. The aqueous fraction was filtered using a 1.2 μm type RA, mixed cellulose esters membrane filter (Millipore, Billerica, Mass.). The water-soluble filtrate from each sample was then extracted with diethyl ether using a 1:1 volumetric ratio. The ether soluble and aqueous phase fractions were both stored in a refrigerator at 5 °C for subsequent semi-volatiles analysis. The solid residue resulting from the aqueous phase filtration was washed with THF and then filtered using a 0.45 μm PTFE membrane filter (PALL Corp., Port Washington, N.Y.). The THF soluble fraction was also reserved for subsequent semi-volatiles analysis and stored in a refrigerator at 5 °C. The THF insoluble fraction was evaporated in a fume hood at SATP.

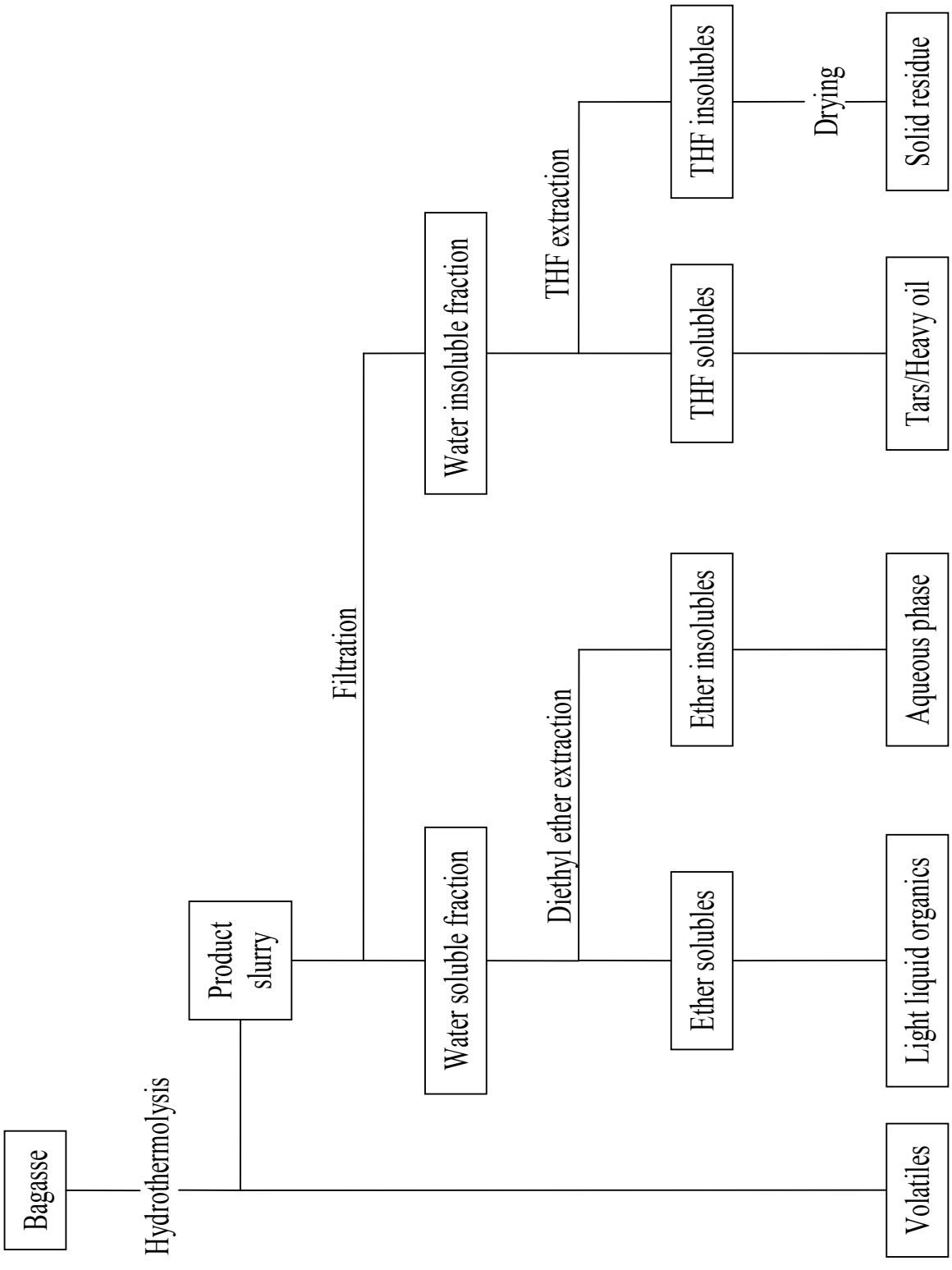

Figure 30. Procedure for separation of hydrothermal conversion products.

3.5 Biomass Characterization

The bagasse samples were characterized by determining their moisture, inorganic, and compositional content and by performing an ultimate analysis as outlined in the following sections. Absolute density measurements were taken of various particle size fractions of the dried, irradiated bagasse. Additionally, the calorific values of both irradiated and nonirradiated bagasse samples were also measured.

3.5.1 Moisture Analysis

Moisture determination for the freshly received, raw bagasse was performed using a Sartorius Mark 3 moisture analyzer, whereas moisture measurements for the dried, processed bagasse were performed using either the aforementioned analyzer or a Denver Instrument IR-35 moisture analyzer. Additionally, a traditional moisture analytical test established by NREL [302] was performed on the 2007 bagasse used in all NCSW experimentation. Moisture analyses of the representative lignocellulosic components (i.e., cellulose, hemicellulose, and lignin) found in sugarcane bagasse were conducted on the Denver Instrument IR-35 moisture analyzer.

3.5.2 Ash Test

Samples of dried, shredded bagasse were analyzed for ash according to a procedure developed by NREL [303]. There was an average of 4.0 wt % (± 0.3) inorganic content in the bagasse samples on a dry basis.

3.5.3 Compositional Content

The compositional content of the sugarcane bagasse used was previously determined [304]. The compositional content of bagasse is given on a dry weight basis in Table 14.

Table 14. Compositional content of bagasse.

Biomass Constituent	Percent (Total Dry Mass)
Ash	4.0
Extractives	2.1
Glucan	41.6
Lignin	21.4
Xylan	23.8
Arabinan	2.0
Mannan	ND

3.5.4 Ultimate Analysis

Ultimate analysis was performed on pulverized bagasse samples (60/120 mesh size) according to ASTM method 5373-02 on a Perkin Elmer CHNS Analyzer by the Coastal Ecology Laboratory (Dept. of Oceanography and Coastal Sciences, LSU, Baton Rouge, La.). The elemental analysis results for bagasse samples from different harvest years and sugar mills are shown in Table 15. The extremely heterogeneous nature of sugarcane bagasse is clearly manifest in the significant differences in carbon and oxygen content that transpire over different growing seasons or that occur as a result of geographic variability even within the confines of south Louisiana. Interestingly, the bagasse from the 2007 season had the highest carbon and hydrogen content and lowest oxygen content. However, it should be noted that the bagasse samples from 2007 were selected for the hydrothermolysis tests in this study long before the elemental analysis was conducted. It should also be emphasized that the bagasse samples used to perform the elemental analysis very likely included an amalgamation of different sugarcane varieties because each raw sugar mill processes sugarcane from a number of growers, each of whom may plant several different varietal breeds of sugarcane.

Table 15. Bagasse elemental analysis for different harvest years and sugar mills on a dry, ash free basis (wt %).

Year	Location	C	H	O[27]	N	S
2005	Cora Texas	34.40	5.09	56.22	1.46	0.49
2006	Cora Texas	33.64	5.19	56.86	1.44	0.50
2006	Raceland	36.73	5.35	53.56	1.60	0.52
2007	Cora Texas	42.96	6.14	46.75	1.62	0.57
2008	Cora Texas	25.90	3.65	66.59	0.72	0.36

3.5.5 Density

The true density of the bagasse was established using a Micromeritics Accupyc II 1340 gas pycnometer located at Auburn University (Auburn, Ala.). The true density of a material, sometimes called the skeletal density, is defined as the mass of the material divided by its skeletal volume [305]. Here the skeletal volume of the bagasse powder is rigorously defined to include both the solid bagasse particle volume and the volume of closed, interior voids within the bagasse particles. The skeletal volume does not the volume of open pores that are accessible from the particle surface or the volume of interstitial voids between particles. Several different particle size fractions of bagasse were analyzed and the results are shown in Table 16. The true densities were adjusted for the moisture content of each fraction and are therefore reported on a dry basis. It is believed that the collation of results in Table 16 represents the first time that the true densities of sugarcane bagasse have been published.

The bulk density of moist bagasse was evaluated using a 1 qt O'Haus iron canister. Moist, unground bagasse had a bulk density of 0.180 $g \cdot cm^3$, while dried ground bagasse (< 2 mm) had an average bulk density of 0.153 $g \cdot cm^{-3}$ ($\sigma = \pm 0.0093$).

[27] Oxgyen by difference

Table 16. **True densities for various bagasse particle size fractions.**

Bagasse Particle Size	Moisture Content [wt %]	True Dry Density [g·cm^{-3}]
Dried Unground	2.98	1.49
Moist Unground	69.48	2.87
Dried Shredded (< 9.51 mm)	4.70	1.66
Moist Shredded (< 9.51 mm)	54.16	2.07
Dried Ground (< 2 mm)	3.24	1.58
1.410 – 2.000 mm	4.94	1.97
1.000 – 1.410 mm	7.01	1.81
0.710 – 1.000 mm	7.08	1.84
0.500 – 0.710 mm	6.50	1.74
0.355 - 0.500 mm	6.86	1.72
0.250 – 0.355 mm	6.23	1.73
0.125 - 0.250 mm	6.83	1.78
< 0.125 mm	5.57	1.85

3.5.6 Calorific Value

The gross calorific value (GCV) for dried, shredded bagasse samples was measured using a Parr 6200 LE isoperibol calorimeter (Moline, Ill.) with 2 Parr 1103 adiabatic oxygen bombs. Measurements were obtained for both nonirradiated and irradiated (i.e., 2 MR absorbed dose) samples. The average GCV for the nonirradiated bagasse sample was 16.19 MJ·kg^{-1} ($\sigma = \pm$ 0.09), whereas the average GCV for the 2 MR irradiated bagasse sample was 16.48 MJ·kg^{-1} ($\sigma = \pm$ 0.05). An analysis of variance was conducted on the above means to determine whether they were equal. The null hypothesis that the means were equal was rejected because the F statistic was significant. A pairwise comparison of the means was made using the Bonferroni adjustment to the Fisher least significant difference (LSD) test. The Bonferroni pairwise comparison is the most conservative LSD test available and the minimum significant difference was calculated to

be 0.28. Thus, the results indicated that there is indeed a significant difference in the calorific values of the irradiated and nonirradiated bagasse samples.

3.5.7 Semi-Volatiles Density

The density of the semi-volatiles was recorded using an Anton Paar A420 automated density meter. The density analysis was performed by the Center for Applied Energy Research at the University of Kentucky, Lexington, Ky. The density of the semi-volatiles was used in the subsequent calculations to determine the volume of gas produced.

3.5.8 Semi-Volatiles pH

The pH of the DI water used at the beginning of each run and the pH of the aqueous bio-oil fraction produced at the end of each run were measured using a calibrated Orion model 520A pH meter.

3.6 Mass Balance and Volatile Molar Yield Calculations

Although the bagasse hydrothermal system can be considered as an isochoric process, the volume of the various phases is not constant because gases are condensed, liquids are dissociated, and solids undergo dissolution via liquefaction and gasification. The following procedure was employed to experimentally determine the amount of product gas generated during the hydrothermal conversion process. For the current work, the mass of reactants used was readily established. A complete mass balance for every run described in this document is presented in Appendix B.

After the volatile phase from each test run had been characterized using GC-FID/HID, the bomb was opened and the liquid contents were quickly transferred into a tared glass beaker

that was then weighed. An accurate measurement of the liquid volume was rendered impossible because a dense layer of particulate matter floated on top of the liquid and another layer of dark solids settled on the beaker bottom. The liquid product was subsequently filtered and an automated density measurement was performed on a 5 mL aliquot of each sample. The resulting liquid product density for the standard hydrothermal bagasse run (i.e., 500 °C, 4 wt % loading, 5 min residence time) was 0.9991 g·cm^{-3} at 20.05 °C. The corresponding volume of liquid product was then calculated from the previously determined mass of filtered liquid product and the liquid density. The liquid product determined from this calculation consists of both the aqueous fraction and the light organic semi-volatiles, as shown in the schematic given by Figure 30. The mass of the solid product was taken after the solid had been dried for 48 h in a fume hood at ambient temperature. Here, the solid portion was taken as the water insoluble fraction shown in Figure 30, which incorporates tars, waxes, char, and minor inorganic content. It was assumed that the dried, solid residue was comprised primarily of carbon; this allowed the volume of the solid residue to be approximated using an average carbon density of 2.23 g·cm^{-3}. The additive volumes of the individual solid, liquid, and gas phases (i.e., V_s, V_l, V_g, respectively) must equal the total bomb volume as written in Eqn 16.

$$V_{bomb} = V_s + V_l + V_g \tag{16}$$

The volume of gas produced was determined by difference as shown in Eqn. 17:

$$V_g = V_{bomb} - V_s - V_l \tag{17}$$

The ideal gas law (IGL) can be used to calculate the number of moles of gas (n) produced from the hydrothermal conversion process, as shown in Eqn. 18.

(18)

The IGL approximation works suitably for pure gases at low pressures but begins to break down for gases at elevated pressures or gases that exist in mixtures. At low pressures, molecules typically occupy a large volume and are therefore separated relatively far apart. The intermolecular separation distance decreases to a few molecular diameters at moderate pressures and attractive forces begin to pull the molecules closer together resulting in compression. At high pressures, gas molecules are nearly in contact with one another and molecular interactions tend to be highly repulsive resulting in expansion. The Lennard-Jones (12, 6) potential is often used to describe the sum of the repulsive and attractive interactions between neutral molecules as shown in Eqn. 19:

$$E = 4\varepsilon\left[\left(\frac{r_0}{r}\right)^{12} - \left(\frac{r_0}{r}\right)^{6}\right] \tag{19}$$

where E denotes the potential energy shared between two molecules, ε represents the minimum energy (i.e., potential well) corresponding to the equilibrium separation, r is the separation distance between the molecules, and r_0 signifies the separation at which the intermolecular potential energy is zero [149].

Cubic equations of state (EOS) are frequently used in the chemical industry to model the vapor-liquid phase equilibria of multicomponent systems at elevated pressures [306].

$$\ln f_i = \ln Px_i + \int_0^P \left(\frac{v_i}{RT} - \frac{1}{P}\right) dP \tag{20}$$

where f_i is the fugacity of component i, x_i is the molar fraction of component i, and v_i represents the molar volume of component i. The fugacity provides a measure of the chemical potential for any component in any system in terms of a "corrected pressure" [307]. The Soave-Redlich-

Kwong (SRK) EOS provides acceptable vapor pressure predictions at moderate to high temperatures for nonpolar compounds [308]:

$$P = \frac{RT}{v-b} - \frac{a(T)}{v(v+b)} \tag{21}$$

The two parameters a(T) and b are expressed for pure components as:

$$a(T) = \alpha(T)a(T_c) \tag{22}$$

$$a(T_c) = 0.42748\frac{(RT_c)^2}{P_c} \tag{23}$$

$$b = 0.08664\frac{RT_c}{P_c} \tag{24}$$

where $\alpha(T)$ is a function representing the temperature dependence of the attractive forces between molecules and T_c represents the critical temperature of the substance. The value of $\alpha(T)$ equals unity when T reaches T_c. For normal fluids, $\alpha(T)$ is given by the following relation:

$$\alpha(T) = \left[1 + m_i\left(1 - \left(\frac{T}{T_c}\right)^{1/2}\right)\right]^2 \tag{25}$$

where m_i is a constant that is unique to each substance, i:

$$m_i = 0.480 + 1.574\omega_i - 0.176\omega_i^2 \tag{26}$$

with ω denoting the acentricity of the respective species.

The Peng-Robinson (PR) relation is another EOS that is frequently used to estimate vapor liquid equilibrium in hydrocarbon systems [309]. The PR formulation is essentially a variation of the SRK EOS. The equilibrium vapor pressure in the PR EOS is given as:

(27)

The parameters $a(T_c)$, b, m_i, are modified slightly, as shown below:

$$a(T_c) = 0.45724 \frac{(RT_c)^2}{P_c} \tag{28}$$

$$b = 0.07780 \frac{RT_c}{P_c} \tag{29}$$

$$m_i = 0.37464 + 1.54226\omega_i - 0.26992\omega_i^2 \tag{30}$$

A one-fluid theory of mixtures is usually assumed, whereby the EOS for the mixture is presumed to be equivalent to that for a theoretical "pure" fluid having constants $a(T)$ and b that depend on composition. The manner in which $a(T)$ and b depend on composition must be specified using mixing rules. The quadratic mixing rule is commonly applied to hydrocarbon and petroleum mixtures [310]:

$$a_{\mathrm{m}} = \sum_i \sum_j x_i x_j a_{ij} \tag{31}$$

$$b_{\mathrm{m}} = \sum_i x_i b_i \tag{32}$$

where x_i and x_j are the molar fractions for components i and j, respectively. The quantity a_{ij} is given by the relation below:

$$a_{ij} = (a_i a_j)^{1/2}(1 - k_{ij}) \tag{33}$$

The term, k_{ij}, is a binary interaction parameter which characterizes the binary formed by the interaction of species i and j. Occasionally the binary interaction parameter is determined empirically, although a modified PR equation [311] defines k_{ij} as follows:

(34)

where $T_{c,i}$ and $T_{i,j}$ are the critical temperatures for the two components and $Z_{c,ij}$ is given by:

$$Z_{c,ij} = \frac{\left(Z_{c,i} + Z_{c,j}\right)}{2} \tag{35}$$

where $Z_{c,i}$ and $Z_{c,j}$ are the critical compressibility factors for the two components. Successful correlation of vapor-liquid equilibrium data is strongly affected by the selection of two parameters: the α function and the mixing rules that are employed.

The predictive capability of cubic EOS has been shown to be unreliable in binary mixtures where hydrogen is present in low molar concentrations. When the Soave-Redlich-Kwong (SRK) equation of state was applied to mixtures containing hydrogen, the accuracy of predicting the mixture vapor pressure declined substantially [308]. It was also noted by Soave that "for systems containing carbon dioxide, hydrogen sulfide and polar compounds […] large deviations were obtained," thereby, necessitating the use of an empirical correction factor, k_{ij}, for each binary present in the mixture. Bruno and Hume [312] measured the fugacity coefficients of hydrogen in binary mixtures with carbon dioxide at various temperatures using a constant pressure of 34.5 bar. At 80 °C and a 20% mole fraction of H_2, they observed that the Redlich-Kwang equation underpredicted the actual fugacity coefficient by at least 10%, while the PR equation underestimated the true value of the fugacity coefficient by about 8%. The failure of density cubic EOS to properly predict the thermodynamic behavior of mixtures containing hydrogen may be symptomatic of an inadequate description of the hydrogen bonding forces in such models. Hydrogen-bonding interactions are generally more cohesive and robust than van der Waal interactions [313]. Hydrogen-bonding is often characterized by the formation of association complexes that are referred to simply as "associates" [314]. Additionally, the use of an EOS presumes that the user is aware of the compositional content of both the gas and liquid products. Given the extremely complex nature of semi-volatile products derived the

hydrothermal treatment of biomass, a complete characterization of the semi-volatiles obtained from the bagasse was beyond the scope of this research effort.

The modified PR EOS was used to estimate the number of moles of gas produced from a baseline hydrothermal run at 500 °C. The number of moles of gas predicted from the PR EOS was 5.8% higher than that calculated from the IGL. Although there is little deviation in these values, the result from the PR EOS was treated with a healthy sense of skepticism because it could be seen from the spreadsheet of binary interaction parameters between the various gases that atypically low values were being generated from the binary interactions in which H_2 was a participant. Given the general untrustworthiness of such cubic EOS in the presence of H_2 it was deemed appropriate to utilize the IGL despite the fact that the complex mixture of volatile products existed at moderate pressures when the gas analysis was performed. The number of moles of gas produced was then finally able to be calculated as shown below:

$$n_{\mathrm{g}} = \frac{P_{\mathrm{f}} V_{\mathrm{f}}}{R T_{\mathrm{f}}} \tag{36}$$

$$n_{\mathrm{He}} = \frac{P_{\mathrm{ic}} V_{\mathrm{ic}}}{R T_{\mathrm{ic}}} \tag{37}$$

$$n_{\mathrm{g}^*} = n_{\mathrm{g}} - n_{\mathrm{He}} \tag{38}$$

A question also arose concerning the validity of the IGL given the compressibility difference in the aqueous media arising between the GC bomb pressure at which the volatiles were analyzed and atmospheric pressure when the volume of the liquids was actually measured. Consultation of compressibility tables for water [315] indicate that such fears were unwarranted. The pressure of the bomb contents during GC testing was between 13.5 to 18.0 bar. At 18.0 bar and 75 °C, the specific volume of water is 1.026633 $cm^3 \cdot g^{-1}$, whereas the specific volume of water at atmospheric pressure and 75 °C is 1.025805 $cm^3 \cdot g^{-1}$. The margin of error caused by the

0.08% difference in specific volume was considered acceptable for the preceding volume calculations. The mass and molar distributions of the volatile products from each run are presented in Appendix C, along with their respective heating values.

Chapter 4. RESULTS

4.1 Evaluation of Experimental Parameters

Before beginning the actual hydrothermal studies, several steps were taken to eliminate uncertainties in the experimental process and to identify any lurking variables that could jeopardize the validity of future calculations. A detailed understanding of the particle size distribution (PSD) is needed before any appraisals can be made regarding the effect of particle size on the product distribution and yields from biomass hydrothermal processes. The results of a particle size distribution analysis can be expressed in several different forms, *viz*:

- Histogram of the particle density function or percentage weight of particles binned between various mesh sizes
- Differential distribution of the particle size fractions expressed in terms of a cumulative undersize mass percentage (i.e., total mass percentage of particles passing through a given mesh size)
- Differential distribution of the particle size fractions expressed in terms of a cumulative oversize mass percentage (i.e., total mass percentage of particles retained by a given mesh size).

Histograms of the PSD for dried, unground bagasse and dried, shredded bagasse are portrayed in Figure 31. The "devil's staircase" appearance of the cumulative distribution function for dried, unground bagasse suggests that the PSD for unground bagasse follows a Cantor function. Slightly more than half (51%) of the cumulative mass percentage of particles is comprised of particles having a diameter greater than 1.0 mm. Apart from industrial furnaces that are used to combust unground bagasse at sugar mills, relatively few commercial or

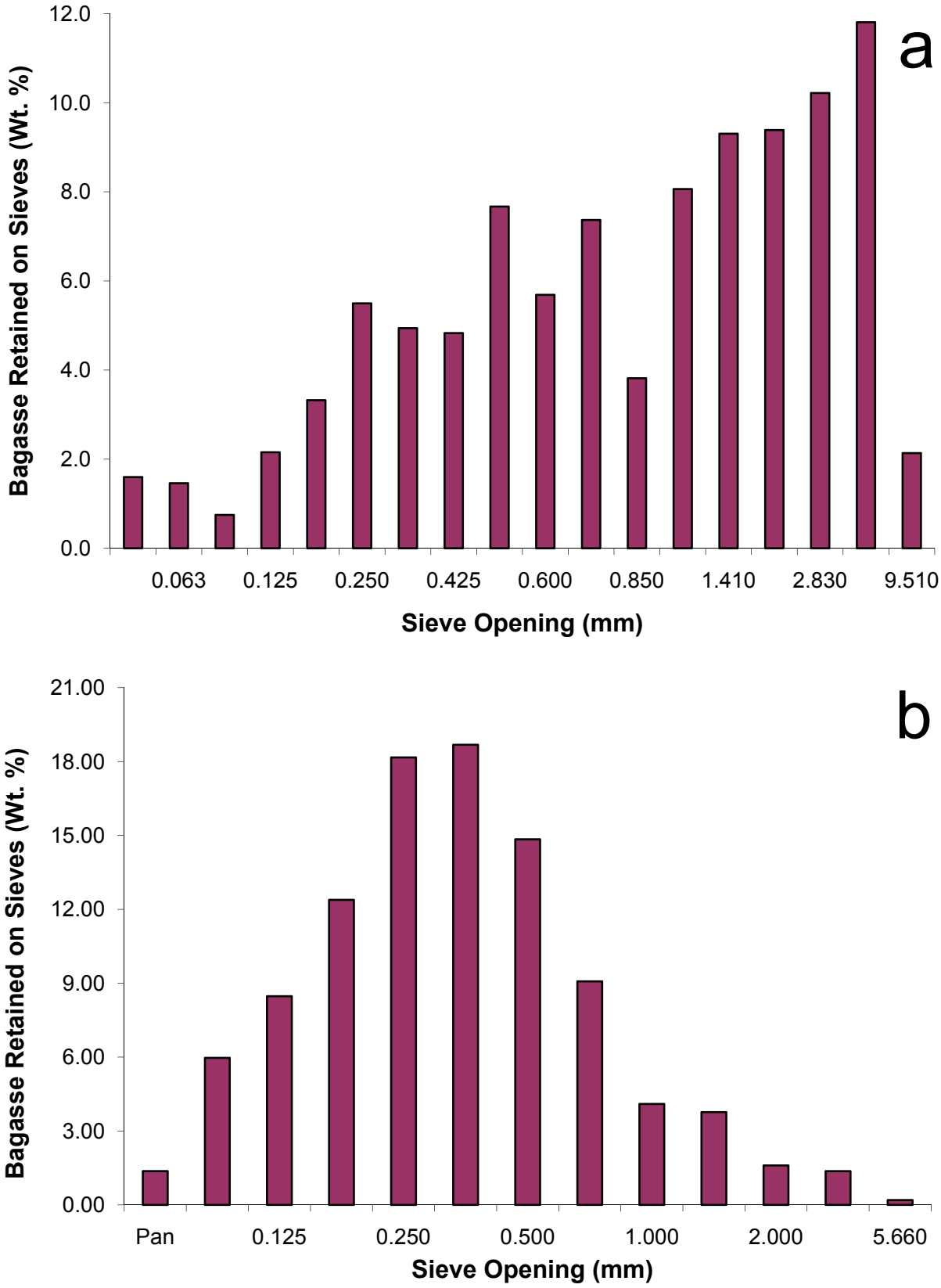

Figure 31. Particle size distribution for a) Dried, unground bagasse; b) Dried, shredded bagasse.

laboratory applications will be equipped to handle such particle sizes *in situ* without first making special accomodations to comminute the bagasse. The PSD for the dried, shredded bagasse has an almost classic normal distribution. The lower mass percentages of the particle size fractions between 1.0 and 2.0 mm are culpable for the minor deviation from ideal Gaussian behavior. More than a third (37%) of the overall mass percentage of shredded bagasse particles fall in a narrow region between 0.25–0.50 mm. The data presented in Figure 31 is an invaluable resource for anyone attempting to improve process efficiency by controlling particle size. Ideally, operators would be able to select from among various PSDs for a given material and choose the one that most accurately reflects the actual distribution behavior of the material depending upon their application. Several mathematical models can be employed to evaluate the PSD and particle density functions from experimental data.

The Rosin-Rammler (RR) model has been used extensively to describe the PSDs for a broad spectrum of powder materials and particle sizes. The RR model was developed in the 1930's to characterized pulverized coal fractions. The Rosin-Rammler function can be expressed using the following equation:

$$F(\phi) = 1 - \exp\left[-\left(\frac{\phi}{d_{\mathrm{m}}} \right)^{\mathrm{n}} \right] \tag{39}$$

where ϕ is the given particle diameter (mm), d_{m} denotes the mean particle diameter (mm), $F(\phi)$ represents the particle size distribution function on a mass basis, and n is a measure of the particle size spread. Both d_{m} and n are tuneable parameters that are unique to a given distribution.

Figure 32 depicts the fit of particle size data for both unground bagasse and shredded bagasse to the RR model. A linear regression analysis was used to fit the individual data points

from both bagasse fractions. It was impossible to obtain a single reasonable fit for all of the data points and, therefore, the data set for each fraction was divided into two portions. The location of each split was determined on the basis of an optimization routine that was used to identify the split resulting in the highest correlation coefficient for each linear fit. The broken linear fit in each plot indicates that the aspect ratio is an important variable that must be considered when evaluating the particle size distribution in fibrous materials, such as bagasse. The aspect ratio is defined here as the ratio of fiber's length to its diameter.

The lower linear fit for each bagasse fraction represents the particle size range where the particle diameter is the controlling parameter in the particle size distribution. The upper linear fit for each bagasse fraction denotes the particle size range where the fiber length is the governing parameter in the particle size distribution. In the case of unground bagasse, the lower linear fit corresponds to particles with a size less than 0.850 mm and the upper linear fit corresponds to particles having sizes between 0.850 to 9.51 mm. In the case of shredded bagasse, the lower linear fit corresponds to particles with a size less than 0.5 mm and the upper linear fit corresponds to particles having sizes between 0.500 to 2.00 mm.

Approximately 49 wt % of the unground bagasse particles are below 0.500 mm in size. Nearly 80 wt % of the shredded bagasse particles are less than 0.850 mm in size. The RR model is a suitable candidate for representing the particle size distribution of bagasse at has undergone comminution. Application of the RR model to unground bagasse exposes a bimodality in the particle distribution that was not readily apparent from the conventional cumulative distribution histogram in Figure 31a. The particle size distribution analysis of unground bagasse particles may require the use of a truncated log-normal distribution, which is bounded by minimum and maximum particle sizes that correspond approximately with the extents of linear fits above.

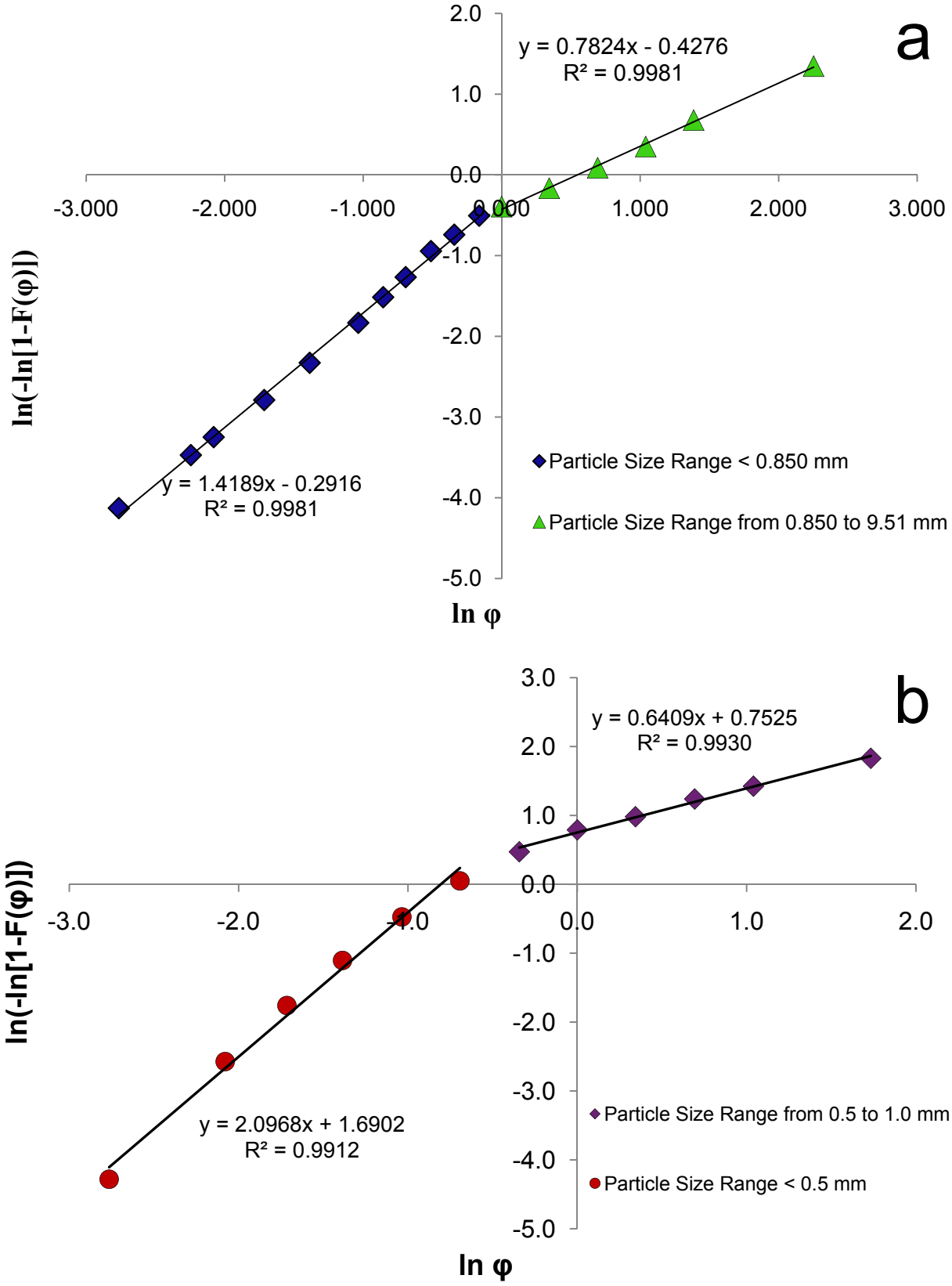

Figure 32. Fit of particle size data to the RR model for a) Unground bagasse; b) Shredded bagasse.

An important operational parameter that had to be evaluated and defined was the heating rate experienced by the bomb contents. Experimental heating rate studies were conducted as previously described. At steady-state, the overall heat transfer rate, q, into the hollow cylinder can be solved analytically using a simplified thermal circuit relationship [316]:

$$q = \frac{T_o - T_i}{R_i + R_w + R_o} \tag{40}$$

where T_o and T_i signify the interior cylinder temperature and the exterior bulk temperature, respectively, and Ri, Rw, and Ro represent the thermal resistances from internal convection, wall conduction, and outside convection, respectively. When the temperature within a body varies significantly only with time it is possible to perform a lumped-parameter transient conduction analysis on the system [317]. The nonlinearity introduced by the temperature-dependent properties of the system necessitates the use of finite element methods.

A finite element analysis model of the transient heating period was constructed using COMSOL Multiphysics software (COMSOL Inc., Burlington, Mass.). A general heat transfer application mode was applied that includes both conduction and convective heat transport terms. The model assumed that the inside of the bomb was filled halfway with water. The water was treated as a "solid", whose outer surface temperature was set equal to that of the inner wall of the bomb cylinder in order to facilitate calculations of the heat transfer to the water. The headspace above the water was modeled using the thermal properties of He. Both conduction and free convection were included as possible heat transfer modes during the heating of the bomb. It was assumed that the temperature of the exterior bomb wall was equal to that of the molten tin alloy bath and the heat transfer between the surrounding molten tin alloy and the outer wall of the bomb was instantaneous. The justification for this assumption was predicated on the calculation of the resistances to heat transfer, which showed that the largest heat transfer resistance in the

system occurred between the interior bomb wall and the water inside. The heating profile of the bomb as a function of time as calculated by the finite element analysis model is shown in Figure 33. It is visible from the different heating profile time snapshots that the water inside the bomb is indeed the last portion to reach temperature. Moreover, it can be seen from the temperature profile at T = 300 s that the temperature of the water inside the bomb is very near to the set point value, thereby validating the earlier decision to use 5 min as the nominal heating ramp time. Figure 34 also reveals that the conduction of heat is slower through the solid reactor plug, which is composed of a generic 316L stainless steel alloy, than the rest of the Hastelloy X reactor body.

The finite element analysis model, however, does not adequately reflect the true heating profile experienced by the wet bagasse mixture during experimental runs, as shown in Figure 34. In Figure 34, the temperature at a point 3.0 cm above the inside floor of the bomb is monitored throughout the duration of the heating ramp, corresponding to the actual location of the thermocouple during the experimental heating ramp trials. The difference in the heating profiles occurs because the finite element analysis model failed to properly account for the nearly vertical initial temperature rise. The profile of the experimental temperature curve provides an intriguing facet of information. The temperature inside the bomb at the interface between the biomass slurry and the headspace increases rapidly until the critical point temperature is approached. The heating rate experienced inside the bomb from 27 to 374 ºC is 4.95 ºC·min^{-1}. The heating rate slows to 0.55 ºC·min^{-1} from 374 to 500 ºC. The very high heat capacity of water in the vicinity of the critical point requires the expenditure of a substantial amount of additional heat energy to nudge the internal fluid temperature higher. Although the molten metal furnace is clearly able to furnish the extra heat to the bomb, the additional energy requirements exact a time penalty on the heating process.

Figure 33. Heating profile for the bomb as a function of time as determined by finite element analysis.

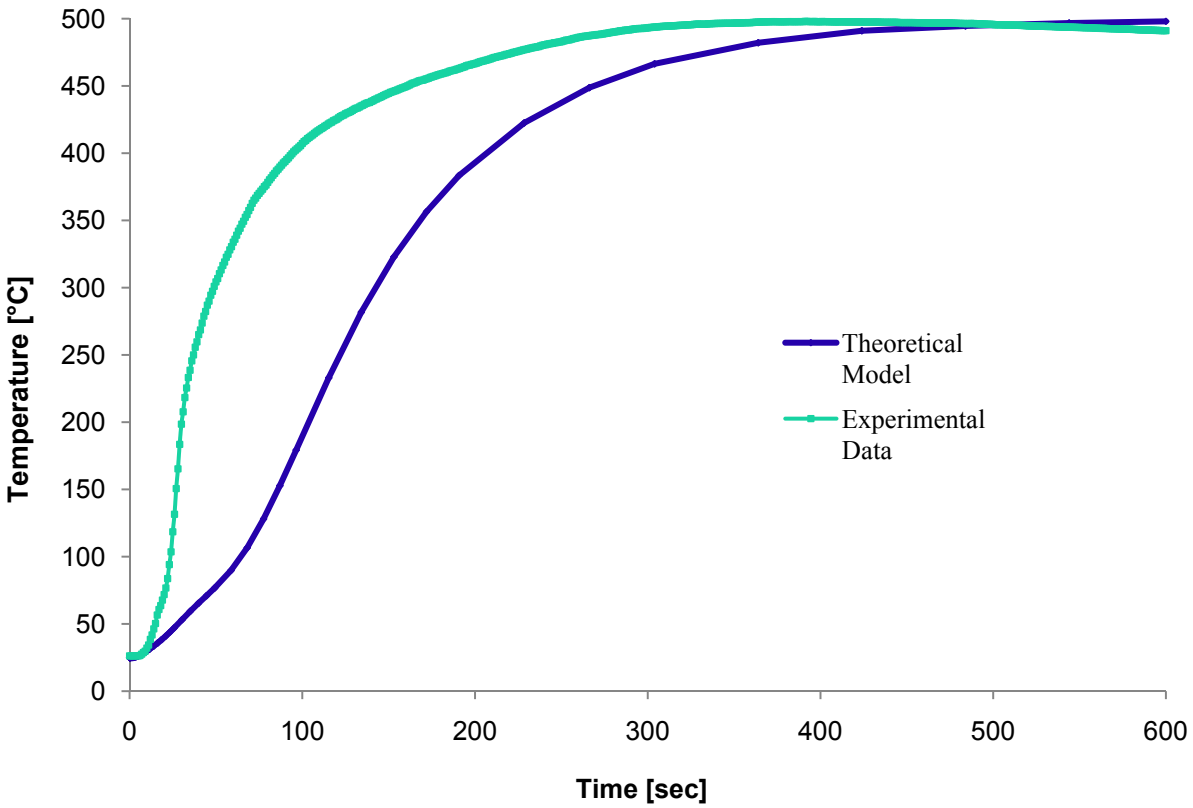

Figure 34. Comparison of theoretical and experimental heating curves during heating ramp at a point located 3.00 cm above the interior floor of the bomb.

Typical pressure curves for various operating temperatures are depicted in Figure 35. For process temperatures of 400 °C and above, it can be seen that the pressure stabilizes after 300 sec., which is the same amount of time required for the internal bomb temperature to reach the target process temperature. The spike in pressure that occurs at 600 sec in the curve obtained at 600 °C may reflect a shift in reaction chemistry at this temperature such that more volatiles are evolved, thereby, elevating the system pressure. Substantially reduced formation of char from the runs conducted at 500 and 600 °C, as shown in Table 19, also supports the notion that gasification behavior begins to become important in supercritical water systems at lower temperatures than traditional gasification processes. The pressure curve plot further reveals that it took approximately 90 sec to reduce system pressures from the maximum operating pressure to less than 50 bar. To demonstrate the repeatability of the hydrothermal tests, four runs were

conducted under identical conditions. The experimental parameters for the duplicate runs were selected so as to correspond with those used in the conventional baseline runs, namely 500 °C, 5 min residence time, and a 4.0 wt % loading of sugarcane bagasse. One gauge for measuring the repeatability of the testing procedures is the maximum system pressure attained. An average peak pressure of 734.7 bar with a standard deviation of 19.9 bar (i.e., 2.71%) was calculated from the data provided in Table 17.

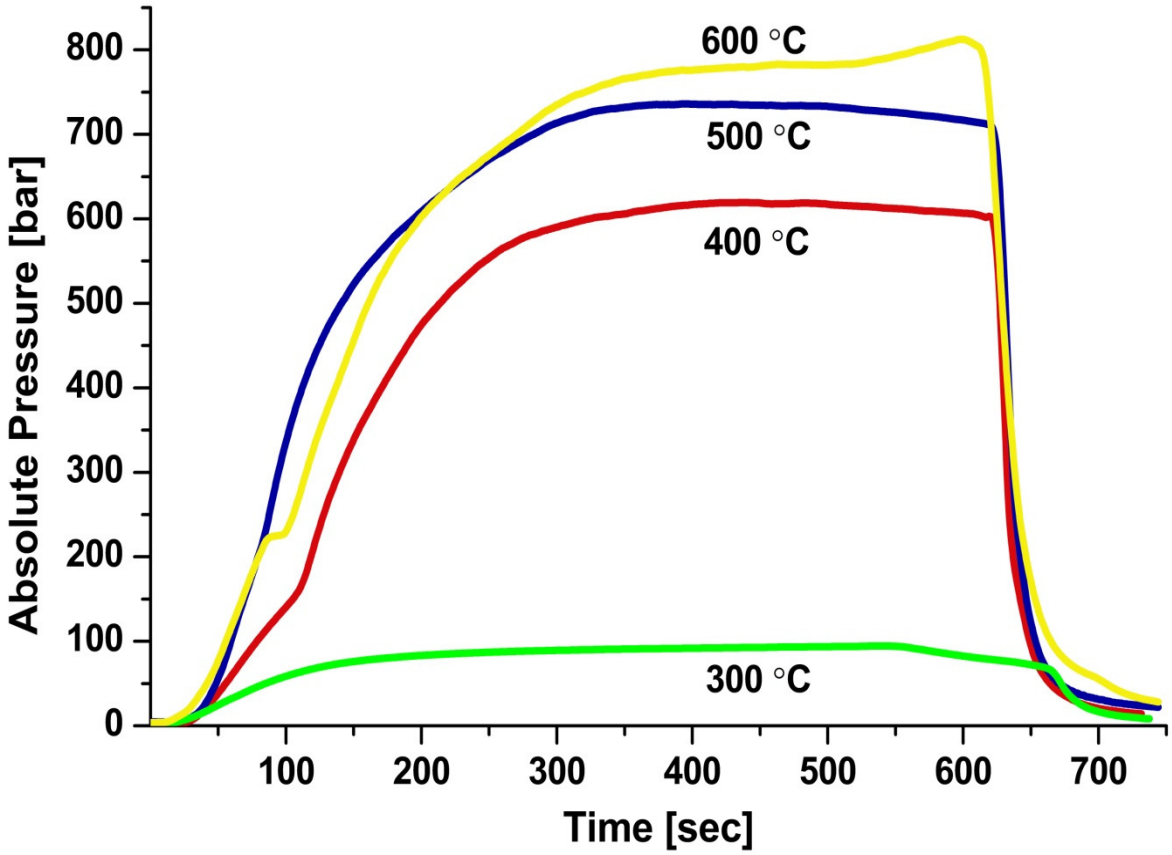

Figure 35. Pressure curves for various process temperatures.

Another benchmark for establishing the repeatability of hydrothermal experiments is to measure the overall volatile product yields from tests performed under identical conditions. A brief survey of the volatile yields for the hydrothermal runs listed in Table 17 reveals that the

average amount of gas produced on a dry biomass basis using the standard baseline conditions is equal to 35.13 wt % with a standard deviation of 0.12 wt %.

Table 17. Maximum system pressure and overall volatiles yield at 500 °C.

Run ID	Absolute Peak Pressure [bar]	Total Volatiles Yield [wt %]
5PB3	754.02	35.15
5PB4	736.05	35.42
5PB5	706.98	35.13
5PB6	741.60	34.83

Figure 36 depicts a representative chromatogram of the volatile products obtained from bagasse that was hydrothermally treated under standard, baseline conditions (i.e., 500 ºC, 5 min residence time, 4 wt % biomass loading, and irradiated, unsieved bagasse with particle size < 2 mm). Permanent gases and light hydrocarbons up to C_2 were measured by the HID detector, while the FID detector was capable of measuring all C_1-C_6 hydrocarbons. Throughout the remainder of this document the terms "permanent gases" and "fixed gases" are used interchangeably and refer to the following volatile species: H_2, CO, CO_2, and CH_4. Although these terms are normally defined to include both O_2 and N_2, these species are omitted here because the runs were purged of air and conducted under an inert helium blanket. Furthermore, the minor amounts of O_2 and N_2 that appeared in the gas chromatograms are a consequence of residual air remaining in the transfer lines between the bomb and the GC. All data contained herein is presented on an oxygen- and nitrogen-free basis. Ensuing gas yield data for permanent gases relies on results obtained from the HID detector, whereas subsequent gas yield data for C_1-C_6 hydrocarbons is drawn from the FID detectors. For the sake of completeness, it is noted that the C_4 olefins elute at the same time on the Hayesep D column and, thus, they were lumped together in the analyses that follow.

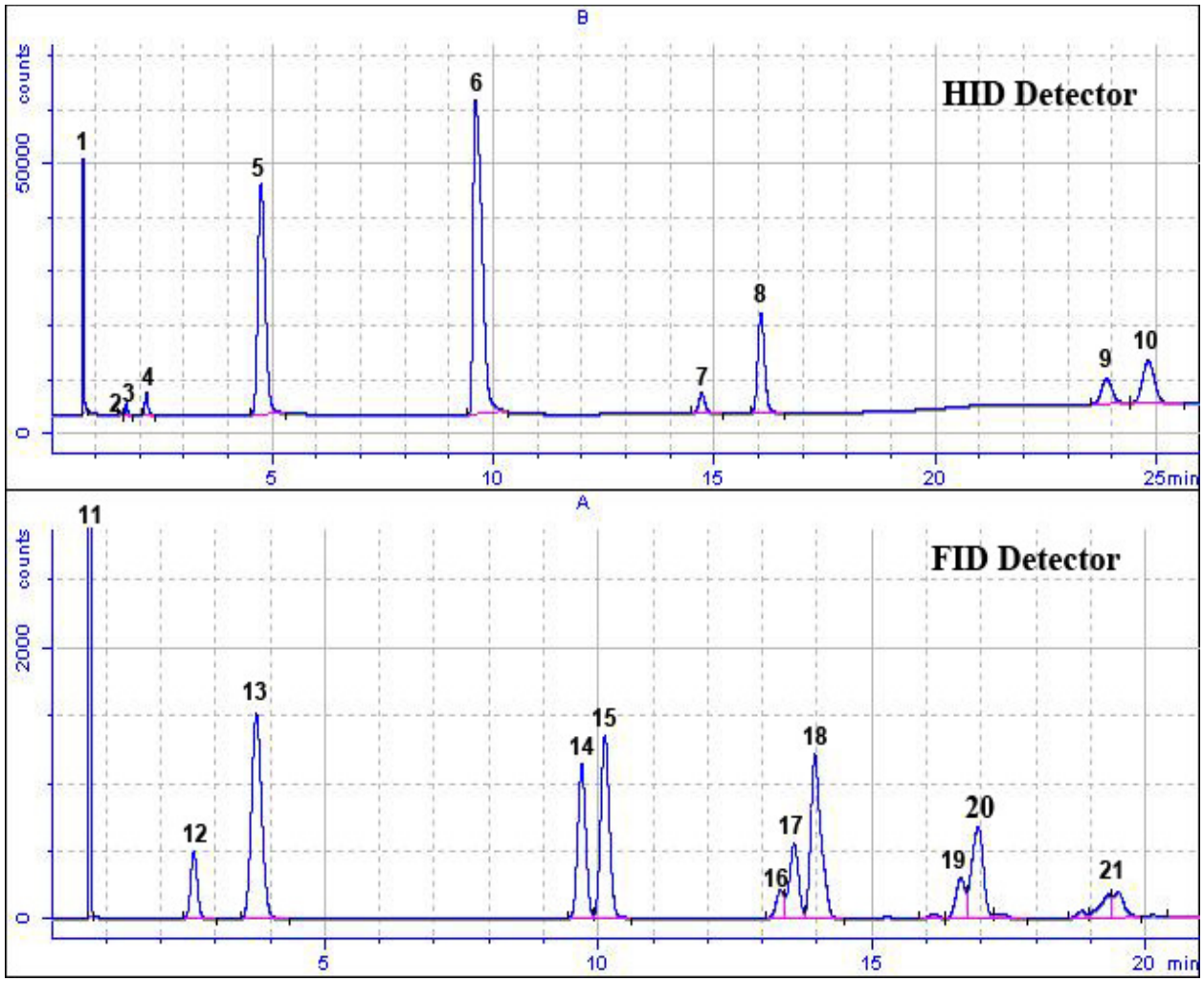

Figure 36. Gas chromatogram of volatiles from a bagasse hydrothermal base run at 500 °C. Top: as recorded by the HID detector. Bottom: as recorded by the FID detector. (1) hydrogen (2) oxygen (3) nitrogen (4) carbon monoxide (5) methane (6) carbon dioxide (7) ethylene (8) ethane (9) propylene (10) propane (11) methane (12) ethylene (13) ethane (14) propylene (15) propane (16) isobutane (17) 1-butene and 1,3-butadiene (unresolved) (18) *n*-butane (19) 1-pentane (20) *n*-pentane (21) *n*-hexane.

One index for system repeatability and ruggedness is to compare the composition of volatile products generated under identical conditions. A total of 4 hydrothermal runs were conducted at the standard, baseline experimental conditions to determine representative standard deviations. Table 18 contains the mean molar composition and associated standard deviation for every gas component as determined from these runs.

Table 18. Mean volatile species distribution and standard deviation for 4 baseline runs.

Volatile Species	Mean Composition [mol %]	Abs. Standard Deviation [mol %]
H_2	24.82	± 1.09
CO	1.52	± 0.23
CO_2	40.68	± 1.05
CH_4	20.17	± 1.39
C_2	4.59	± 0.19
C_3	3.38	± 0.07
C_4	2.49	± 0.03
C_5	1.48	± 0.04
C_6+	0.88	± 0.15

The standard deviation of each component is below 5.0 %, except for CH_4 (6.91%), CO (15.10%) and the C_6+ fraction (17.37%). Methane formation appears to exhibit a linear dependence on pressure with yield, increasing as pressure rises, as depicted in Figure 37. This pressure dependence may account for the higher deviation of methane given in Table 18. The fraction including hexanes and higher hydrocarbons likely includes additional error because of the greater uncertainty associated with the integration of the areas under their much smaller peaks. The higher standard deviation displayed by CO cannot be readily explained; the variation in CO is apparently a function of some unidentified reaction parameter. The reader is hereby advised that experiments were not typically repeated at conditions deviating from those of the standard baseline parameters. Nonetheless, it is logical to assume that the remarkably tight standard deviations recorded for the gases evolved at 500 ºC will also extend to the gases generated at the other operating temperatures.

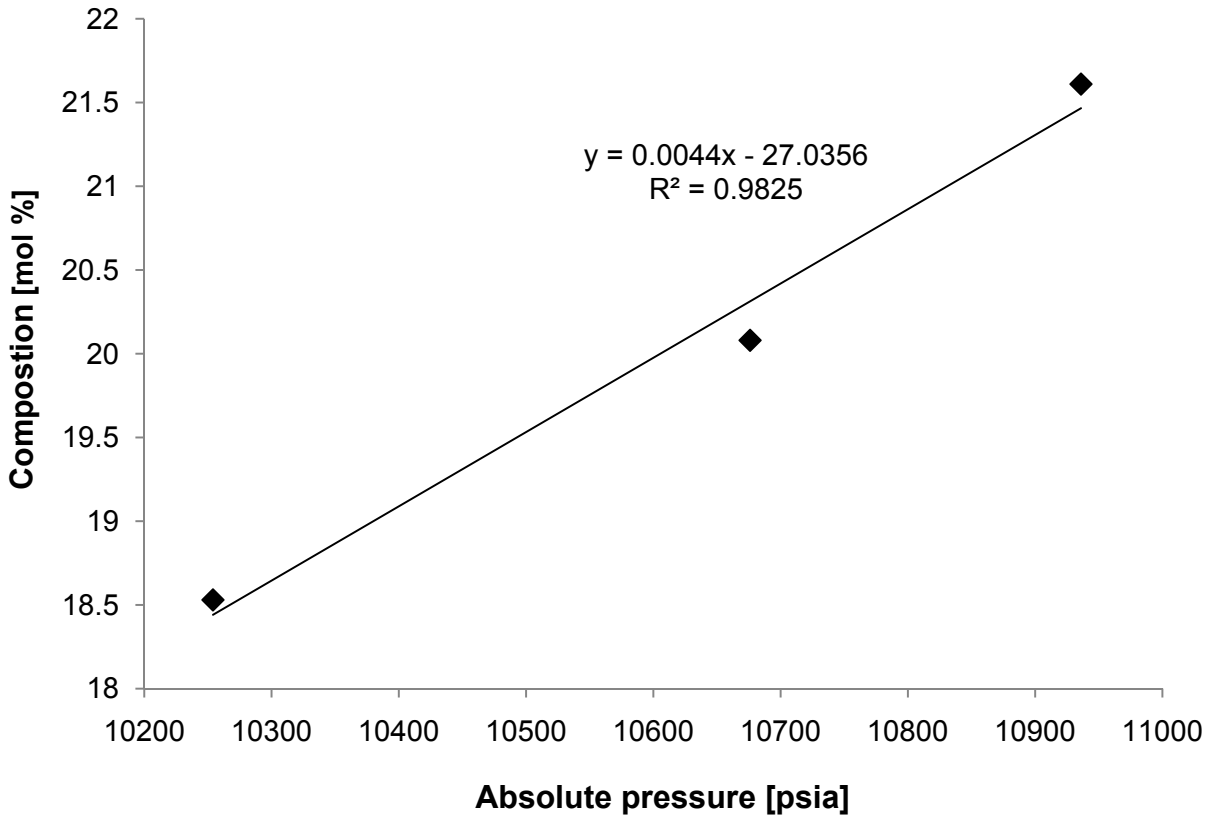

Figure 37. Pressure dependence of methane formation at 500 °C.

4.2 Temperature Influence

Figure 38 shows the total product weight distribution from bagasse as a function of temperature. Readers are advised that the line segments connecting the individual data points in the graphs are provided only as visual aids to identify general trends in the data and do not reflect actual experimental behavior in these intervals. At 300 °C the total yield of volatiles is only 5.77 wt %; increasing the temperature to 400 °C roughly doubles overall gas production to 11.97 wt %. Gas-forming reactions become of greater importance at elevated temperatures, as indicated by the progressively higher volatile yields at 500 and 600 °C (35.13 and 50.78 wt %, respectively). The yield of organic semi-volatiles reaches a maximum 57.3 wt % at a temperature of 400 °C, which is only marginally higher than the 56.3 wt % yield occurring at 300 °C. Raising the temperature beyond 400 °C curtails the production of semi-volatiles by 9.0

wt % at 500 °C and by 22.4 wt % at 600 °C. The solids yield decreases with increasing temperature going from 38.2 wt % at 300 °C to 14.3 wt % at 600 °C. However, the steepest decline in solids formation occurs between 400 and 500 °C, where the solids yield is cut by more than 47%. It is relevant to note the similarity between the decreasing solids yield curve and that of the increasing volatiles yield curve. Until 500 °C, much of the additional volatiles yield comes primarily at the expense of solids production. Decreases in semi-volatile formation help sustain the further increase in gas yield above 500 °C.

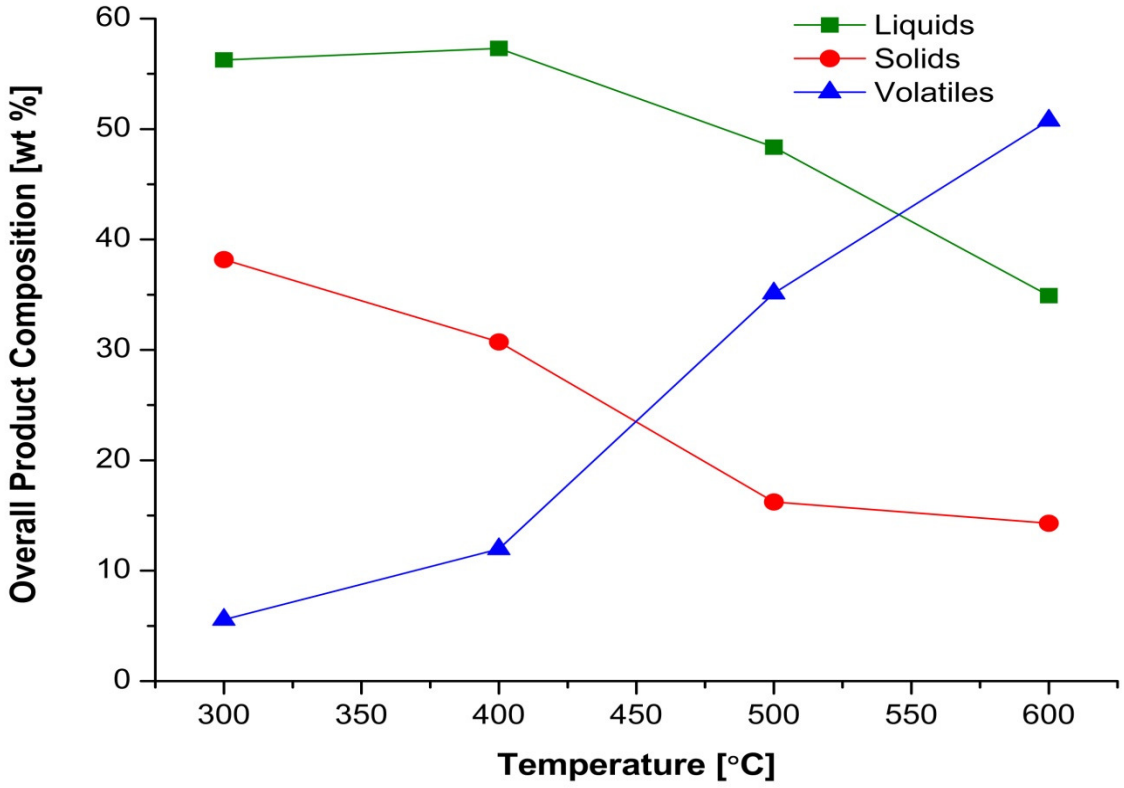

Figure 38. Total product distribution from sugarcane bagasse as a function of temperature.

The influence of temperature on the hydrothermal dissolution of bagasse can be evaluated alternatively by inspecting the overall change in substrate mass, as given by the solids conversion column in Table 19. The final solids quantity represents the sum of unconverted bagasse, asphaltenes, char, and inorganic content. The ash content of the solids can be estimated

using an average ash content of 4.0 wt % for bagasse, if it is assumed that the mass of mineral matter remains constant throughout the hydrothermal reaction. Ash comprises a larger share of the solids fraction with increasing temperature, rising from 10.5 wt % at 300 °C to 28 wt % at 600 °C. The solid product from the standard, baseline reaction at 500 °C contains an average ash content of 23 wt %. Unless otherwise specified, all solid product values and conversion levels are provided on a dry, uncorrected ash basis.

The largest increases in bagasse hydrothermal conversion occur between 300 to 400 °C (7.5 wt %) and 400 to 500 °C (12.2 wt %). Raising the temperature from 500 to 600 °C, however, induces only a modest 4.2 wt % increase in bagasse destruction. The results presented here suggest that bagasse dissolution in heated, aqueous media follows an approximately logarithmic temperature dependency. An elevation in process temperature from 300 to 500 °C provides the necessary thermal momentum to surmount the activation energy barrier for strongly endothermic gasification and C-C cleavage reactions resulting in substantial biomass consumption. The waning growth in bagasse conversion at 600 °C signals that most of the readily hydrolyzable bagasse has already been expended. Any remaining unconverted bagasse presumably contains a sizeable portion of recalcitrant lignin, which can only be processed under more austere supercritical water conditions. Approximately 72 wt % of the solids produced from bagasse treatment in supercritical water at 600 °C are of organic origin, which is 5 wt % less than those produced at 500 °C.

It is hypothesized that the sharply lower increase in bagasse conversion at 600 °C is a consequence of higher coke and char formation that occurs at elevated temperatures. Although some of the coke is undoubtedly gasified as evidenced by the higher volatiles yield at 600 °C than at 500 °C, much higher temperatures would be required to gasify coke in sufficient

quantities as to match the increases in biomass substrate conversion experienced at 400 and 500 °C. A quick check of the CO and H_2 molar yields at 600 °C in Figure 39 confirms that hydrogasification of the char and coke is not a major reaction. Hydrogasification of char produces an equimolar mixture of CO and H_2 (syngas), yet the H_2 molar yield from bagasse hydrothermolysis at 600 °C is almost 15 times higher than that of the CO molar yield.

Table 19. Overall mass balances and higher heating values from the hydrothermal conversion of bagasse performed using various process temperatures.

T [°C]	P_{max} [bar]	ρ [g·cm^{-3}]	RT [min]	Liquids [wt %]	Solids [wt %]	Volatiles [wt %]	Conversion [wt %]	Gas HHV [MJ·kg^{-1}]
300	94	0.714	5	95.52	1.48	0.22	61.8	12.40
400	619	0.618	5	96.76	1.18	0.46	69.3	41.52
500	707	0.410	5	97.18	0.71	1.36	81.5	54.38
600	813	0.463	5	94.94	0.55	1.96	85.7	54.73

The molar yields for the individual volatile fractions as a function of temperature are displayed in Figure 39. Aside from CO, it can be seen that permanent gas formation is enhanced as the reaction temperature is increased. For instance, the yield of H_2 at 500 °C and 5 min residence time (3.097 mmol·g^{-1}) is 3.6 times higher than at 400 °C, whereas the yield of H_2 at 600 °C and 5 min residence time (4.441 mmol·g^{-1}) is 5.2 times higher than at 400 °C. The traversal of the CH_4 and H_2 yield curves as the temperature is raised from 500 to 600 °C suggests that methanation reactions become of increasing importance at higher temperatures. The increasing yields observed with rising temperature for each of the individual gas phase species, apart from CO and the C_4+ group, signifies that temperature acts primarily to accelerate the reaction rates of gas evolution pathways depicted previously in Figure 9, *viz*. primary intermediates to gases (path 3), tar and oil to gases (path 5), and char to gases (path 8).

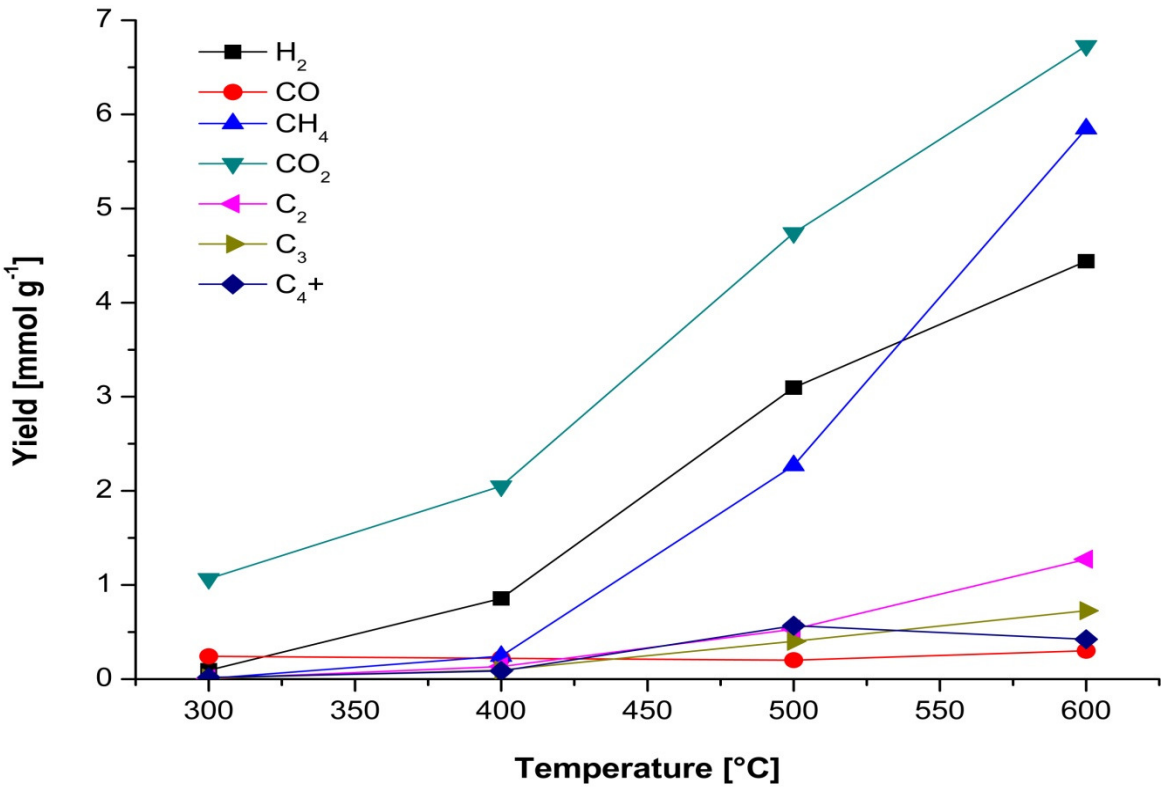

Figure 39. Molar yields of individual gas species as a function of temperature.

The molar composition of the volatiles produced in the experimental HT tests as a function of temperature is shown in Figure 40. The general trend observed in Figure 40a is that increasing process temperature leads to higher mole fractions of H_2 and CH_4 and lower fractions of CO and CO_2. The H_2 mole fraction rises abruptly from 6.5 mol % at 300 °C to 23 mol % at 400 °C. Between 400 and 600 °C, the composition of hydrogen in the volatile product reaches a plateau with a crest at 500 °C of 26 mol %. The mole fraction of CH_4 increases from 0.5 mol % at 300 °C to 30 mol % at 600 °C, with a dramatic 190% increase occurring between 400 °C (i.e., 6.7 mol % CH_4) and 500 °C (i.e., 19.2 mol % CH_4). The level of CO drops sharply from 17 mol % at 300 °C to 1.7 mol % at 500 °C. The mole fraction of CO drops only slightly to 1.5 mol % as the temperature advances to 600 °C. CO_2 exhibits an exponential loss in mole fraction with increasing temperature, decreasing from 74 mol % at 300 °C to 34 mol % at 600 °C. At 300 °C, the predominant gases, CO and CO_2, are formed via the Boudouard reaction (Eqn. 10) and the

steam-reforming reactions (Eqns. 8 and 9). At higher temperatures the CO is immediately consumed in the water-gas shift (WGS) reaction (Eqn. 7) to form H_2 and H_2O; this hypothesis accounts for the negligible levels of CO at higher temperatures. CH_4 is presumably formed via both pyrolysis methanation (Eqns. 1–3) and gasification methanation (Eqns. 13 and 14). The H_2 consumed in these reactions likely counterbalances the amount of H_2 produced from the WGS reaction. The pyrolysis methanation reaction driven by CO_2 (Eqn. 3) would also explain the rapid reduction in CO_2 seen at elevated temperatures.

The effect of temperature on the C_2–C_6+ hydrocarbon molar composition is displayed in Figure 40b. The C_2 and C_3 molar fractions both exhibit rising levels with increasing process temperature, whereas the higher hydrocarbons (C_4+) reach a maximum mole fraction at 500 °C, before dropping significantly at 600 °C. The molar distribution of volatile hydrocarbons provided by Figure 40b offers some insight into the mechanisms surrounding the hydrothermal evolution of hydrocarbons from bagasse. There is a distinct change in the molar distribution of volatile hydrocarbons as conditions in the bomb are toggled between subcritical (300 ºC) and near-critical (400 ºC). At 300 ºC, the distribution favors C4 and C3 formation, whereas at 400 C and above the production of C_2 predominates. Subcritical environments may be more conducive to oxidative coupling of methane, thereby clarifying the low yield of CH_4 observed at 300 ºC.

Closer scrutiny of the changes in the molar composition occurring between 500 and 600 °C, as shown in Table 20, provides a clearer understanding of volatile hydrocarbon production in SCW at higher temperatures. The production of C_2 and C_3 gases increases nearly 42% and 10%, respectively, while the production of C_4, C_5, and C_6+ gases decreases 35%, 72%, and 76%, respectively. These results suggest that at temperatures exceeding 500 °C the higher alkanes in hydrothermal systems undergo traditional pyrolytic decomposition, or thermal “cracking”.

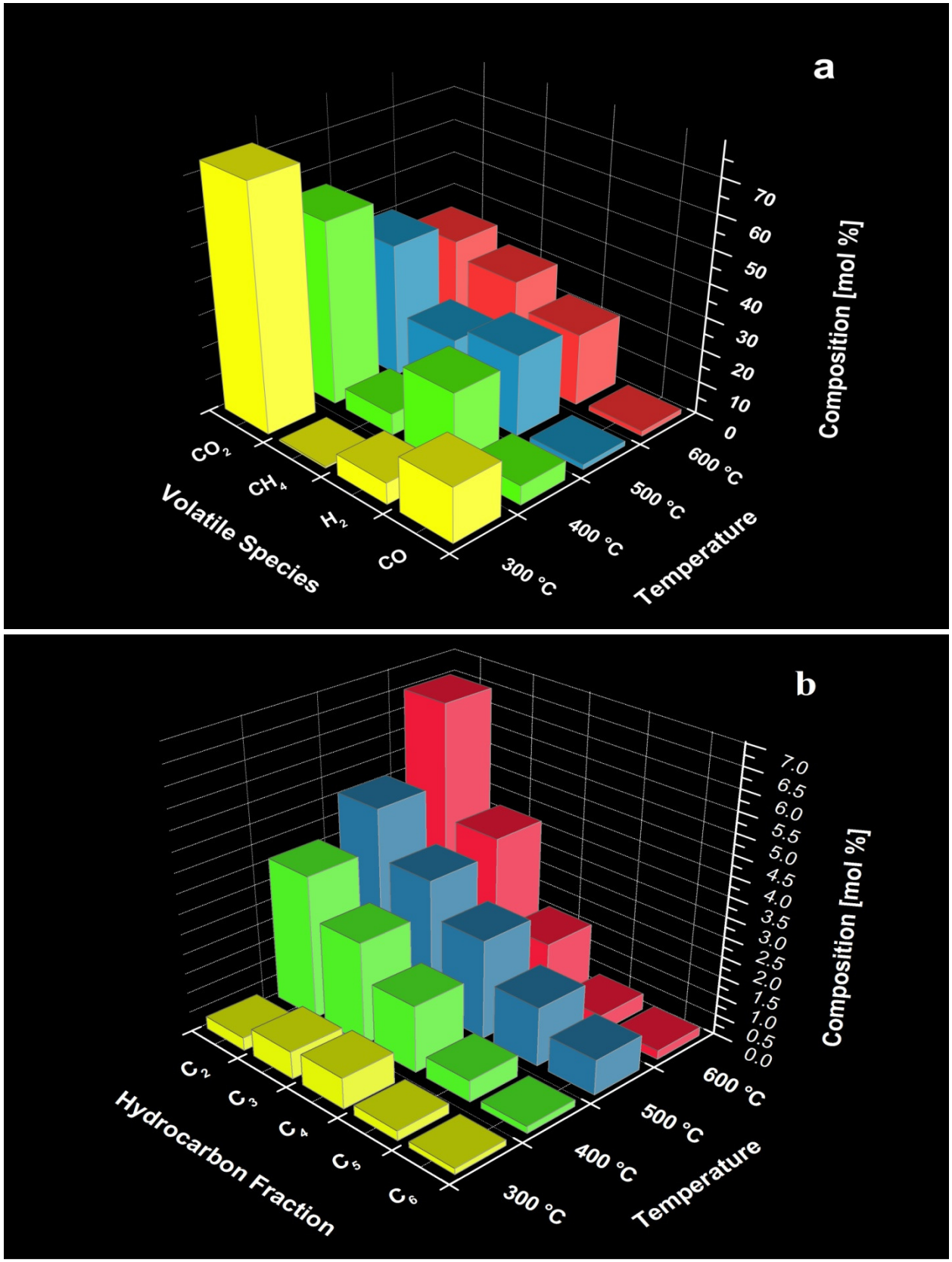

Figure 40. Effect of temperature on volatiles product distribution a). Fixed gases; b). C_2–C_6+ hydrocarbon fraction.

Table 20. Change in hydrocarbon composition between 500 and 600 °C.

Hydrocarbon Fraction	Concentration at 500 °C [mol %]	Concentration at 600 °C [mol %]	% Change
C_1	19.23	29.62	54.0 %
C_2	4.59	6.51	41.8 %
C_3	3.38	3.73	10.4 %
C_4	2.49	1.62	-34.9 %
C_5	1.48	0.42	-71.6 %
C_6+	0.89	0.22	-75.2 %

Several criteria were used to assess the gasification performance of the hydrothermal tests. The carbon gasification ratio, or carbon gasification efficiency (CE), is defined as the extent of carbon conversion from a biomass substrate to volatile hydrocarbons, as shown below:

$$CE = \frac{\sum_i m_{C,i}}{m_{C,\,biomass}} \times 100 \tag{41}$$

where $m_{C,i}$ and $m_{C,biomass}$ refer to the mass of carbon in the individual product gases and in the biomass used in the hydrothermal test, respectively. The biomass used in the hydrothermal residue was computed as the difference in mass between the initial, dry bagasse and the dried solid residue. The mass of the solid residue was not adjusted for the ash content in bagasse. The overall gasification efficiency (GE) was determined using Eqn. 42:

$$GE = \frac{\sum_i m_i}{m_{biomass}} \times 100 \tag{42}$$

where m_i and $m_{biomass}$ designate the mass of the individual product gases and the biomass used in the hydrothermal run, respectively.

The variation in CE and GE with process temperature is depicted in Figure 41. Clearly, the conversion of sugarcane bagasse to gas products is significantly enhanced at elevated temperatures.

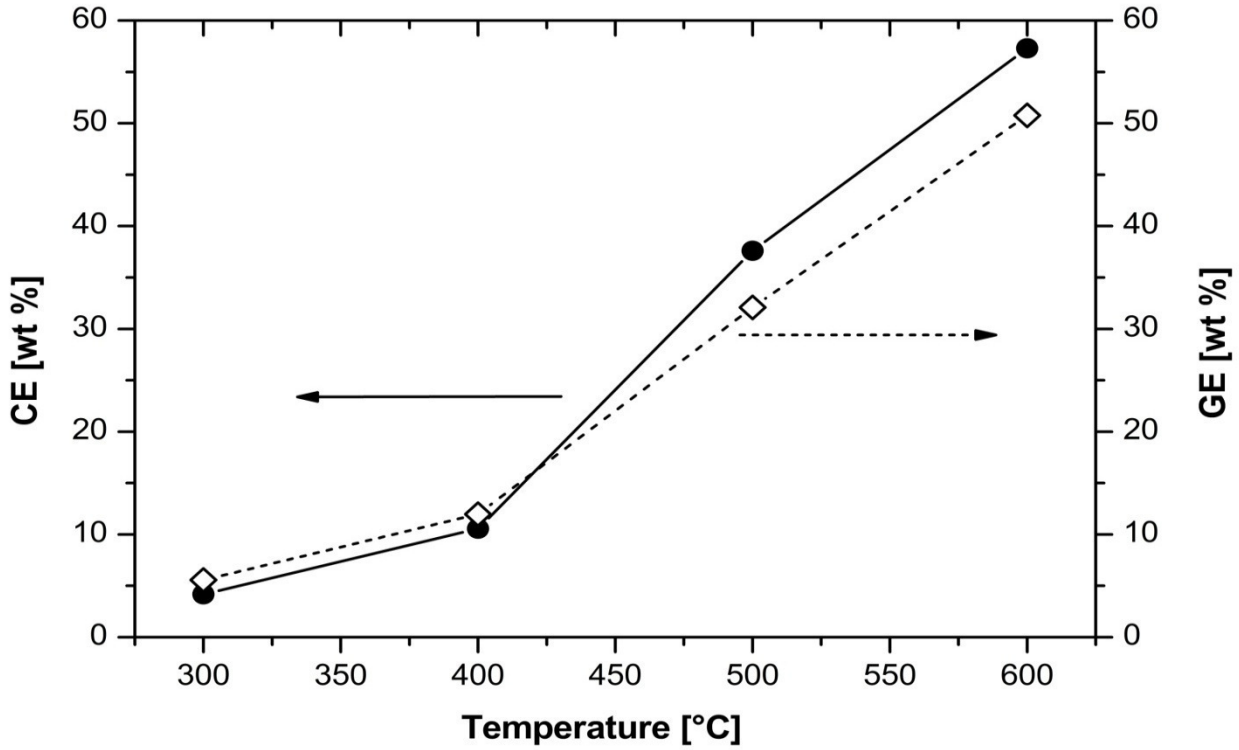

Figure 41. Variation in carbon conversion efficiency (CE) and total gasification efficiency (GE) with respect to process temperature.

The heat of combustion for the gas products provides another effective tool for comparing the effect of temperature on the volatile product exergy. The higher heating value (HHV) of the volatile products as a function of temperature is recorded in Table 19. An increase in the process temperature is accompanied by a corollary rise in HHV of the product gas until 500 °C, when the HHV of the volatiles stabilizes. The HHV of the product gas more than triples between 300 and 400 °C. This underscores that a fundamental change in gasification chemistry occurs between subcritical and near-critical conditions. A more subtle shift in volatile-phase chemistry occurs between 400 and 500 °C, when the HHV of the product gas increases by 31%. The overwhelming presence of CO_2 in the product gas at 300 °C (74.8 mol %) is abated at 400 °C (56.5 mol %) and fades away even further by 500 °C (40.1 mol %). Hence, it can be concluded that traditional pyrolytic reactions predominate at 300 °C. Under near-critical conditions at 400 °C, pyrolysis reactions appear to be counterbalanced by gasification and

depolymerization reactions. This accounts for the drop in CO_2 molar yield and the increase in both H2 and hydrocarbon content at 400 °C. Pyrolysis loses its sway under supercritical conditions at 500 and 600 °C, where WGS, methanation, and depolymerization can be considered as the primary drivers of volatile formation.

4.3 Residence Time Influence

The effect of residence time on the hydrothermal gasification of a 4 wt % loading of sugarcane bagasse was monitored for a specified duration of time at 500 °C. The reaction times used ranged from 1 min to 60 min. A polished cylindrical sample of new Hastelloy C-22 having dimensions of ¼ in. diameter and ⅜ in. length was placed inside the bomb in both the 30 and 60 min time trials for future corrosion studies. The overall mass balances from the individual residence time experiments are provided in Table 21. On cursory inspection, the higher semi-volatile mass losses occurring at longer residence times would appear to be related to a possible pressure leak in the bomb, as evidenced by the lower maximum pressure values. However, closer examination reveals that the intermediate length run at 5 min, which has relatively low mass loss, has a maximum pressure of 707 bar, just 3 bar higher than that of the 30 min run. Furthermore, the previous supposition is not borne out in simple time plots of the pressure data shown in Appendix D, which reveal a stable, uniform wavelike pressure curve at 500 °C for the entire 30 min run and the final 25 min of the 60 min run. The wavy appearance of the pressure curve at the higher residence times is simply a function of the temperature hysteresis induced by the feedback controller at the maximum set-point temperature. The shorter residence time trials (1 and 5 min) do not exhibit this behavior because it takes approximately 450 s at temperature to complete a single hysteresis cycle and these tests were at temperature for roughly 300 s.

The differences in the maximum operating pressure are presumably related to the manner in which the bomb itself was positioned in the furnace. Hydrothermal runs were usually performed by lowering the bomb to a level that was either flush with or slightly below the bottom rim of the cap. It was noted that slight changes (e.g., ± ½ in.) in the submersion depth of the bomb were accompanied by variations in the internal pressure of up to 10%. Deeper submersion of the bomb resulted in higher internal pressures and vice-versa. Thus, the lower maximum operating pressures recorded during some of the time trials are a result of altered heat transfer characteristics caused by changes in the bomb submersion depth.

Any impact on the internal pressure due to the presence of the small cylindrical samples in the 30 and 60 min runs is believed to be negligible as each cylinder represents less than 1% of the total internal bomb surface area and occupies merely 0.027% of the entire bomb volume. At the end of these runs, the small Hastelloy C-22 cylinders were decanted into a beaker along with a small quantity of semi-volatiles with a concerted effort made to avoid marring the cylinder surface. Unfortunately, the decanted portion of the semi-volatiles was lost during this procedure, which helps explain the larger mass losses in the longer residence time trials.

Table 21. Overall mass balances and volatile higher heating values from the hydrothermal conversion of bagasse performed using various residence times.

RT [min]	T [°C]	P_{max} [bar]	ρ [g·cm^{-3}]	Liquids [wt %]	Solids [wt %]	Volatiles [wt %]	Conversion [wt %]	Gas HHV [MJ·kg^{-1}]
1	500	742	0.429	96.45	0.81	1.23	79.1	55.34
5	500	707	0.429	97.18	0.71	1.36	81.5	54.38
10	500	763	0.440	96.28	0.65	1.40	83.0	55.27
30	500	704	0.408	83.78	0.51	1.56	86.8	53.18
60	500	651	0.375	76.90	0.34	1.82	91.2	49.86

The overall product yield from bagasse as a function of residence time is depicted in Figure 42. As mentioned earlier, the quantity of organic semi-volatiles from bagasse was

computed by difference and, therefore, the aforementioned overall semi-volatiles recovery losses did not thwart an evaluation of the product distribution obtained from the hydrothermolysis of bagasse. From Figure 42 it can be seen that organic liquids production is largely unaffected by residence time. The 5.4 % dip in liquid yield between 30 and 60 min is the only significant decline recorded. Figure 42 also reveals that residence time does have a noticeable effect on the yields of solids and volatiles. The production of solids decreases monotonically over time, while the generation of volatiles increases monotonically over time. Both the rate of volatiles formation and the rate of solids production shift dramatically after 5 min. The volatiles formation rate between 1 and 5 min is 3.7 times higher than for the time period after 5 min. Likewise, the rate of solids loss is 3.4 times higher between 1 and 5 min than it is for the time period after 5 min.

The overall conversion of bagasse increases logarithmically with time as shown below:

$$y = a - b \cdot \ln(x + c) \tag{43}$$

where a, b, and c are constants obtained during nonlinear regression curve fitting. A fit of the preceding logarithmic function to the bagasse conversion data returned a correlation coefficient value of 0.9947. The bagasse conversion values provided in Table 21 rise by 4.0 wt % if they are corrected for ash content on the basis that starting bagasse samples had an average 4.0 wt % inorganic matter. Thus, the remaining carbon content in the solid residues from the 30 and 60 min hydrothermal runs is below 5 and 10 wt %, respectively. It is speculated that solid carbon content from a 90 min hydrothermal run would be less than 1 wt %. A lower yield of carbonaceous solids is advantageous because it eliminates the need to invest in traditional high-temperature, post-treatment gasification units or to dispose of the solids altogether through conventional landfilling. A logical question to ponder concerns what level of solid carbon

conversion is necessary for a hydrothermal process to become economically competitive and beyond which level such conversion becomes profligate.

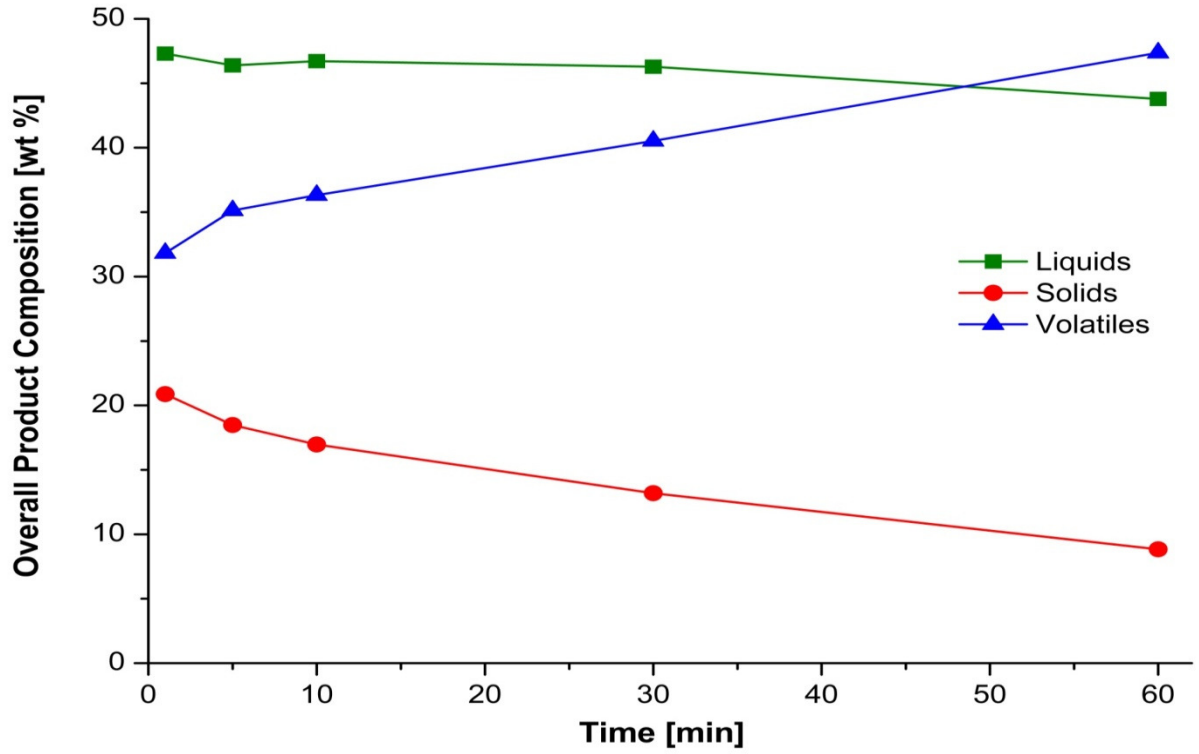

Figure 42. Overall product distribution from sugarcane bagasse as a function of residence time.

The temporal variation of the molar yields of volatiles from bagasse hydrothermolysis is shown in Figure 43. After only 1 min, 2.0 mmol·g^{-1} of CH_4, 2.9 mmol·g^{-1} of H_2, and 4.2 mmol·g^{-1} of CO_2 are produced. The molar yield of CO is cut nearly in half from 0.32 to 0.17 mmol·g^{-1} as the reaction proceeds from 1 to 10 min. The yield of H_2 continues to rise until reaching a plateau between 10 and 30 min at 3.2 mmol·g^{-1}. The CO_2 yield also rises before stabilizing between 5 and 10 min at 4.7 mmol·g^{-1}. The sustained rise in both H_2 and CO_2 molar yields through 5 min coupled with the plunge in CO levels during the early minutes of the hydrothermal reaction point to the water-gas shift reaction (Eqn. 11). CH_4 yield more than doubles from 2.0 mmol·g^{-1} at 1 min to 4.3 mmol·g^{-1} at 30 min. The moderate 12.9% increase in CH_4 between 1 and 5 min could

be a result of pyrolytic methanation (Eqn. 1), which would also help explain the rapid decline in CO during this period. Hydrogasification of solid residues (Eqn. 12) may account for both the 87.2% increase in CH_4 yield between 5 and 30 min and the simultaneous 4.5 wt % decrease in solids production over the same interval. The higher hydrocarbon fractions exhibit a temporal variation in molar yield that is identical to CH_4, albeit at substantially reduced levels.

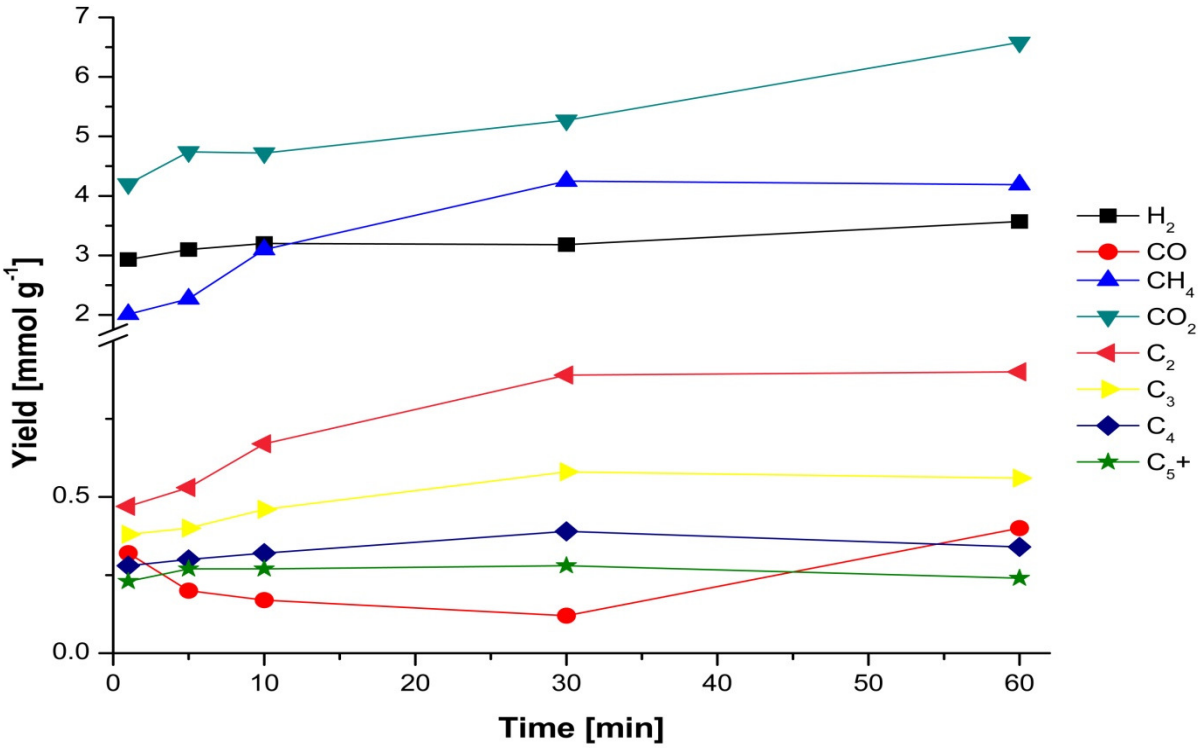

Figure 43. Temporal variation in the molar yields of volatile species.

Figure 44 reveals the influence of time on the molar composition of the gas products obtained from hydrothermally treated bagasse. It can be seen in Figure 44a that the mole fraction of CH_4 reaches a peak value of 28.4 mol % at 30 min residence time. Meanwhile, the mole fractions of H_2 and CO decline to minimums of 20.8 and 0.8 mol %, respectively, at 30 min residence time. The juxtaposition of the individual molar composition curves for H_2 and CH_4 is particularly interesting. The curves appear almost as mirror reflections and intersect each other in close proximity to 10 min residence time with an equal concentration of 23.5 mol % per gas.

The parallel nature of the H_2 and CH_4 curves raises the possibility that the formation and consumption of these two gases is strongly interrelated during the hydrothermal conversion process. During the initial 5 min temperature ramp preceding the soak period there is significant formation of CO_2 as evidenced by its 42 mol % yield at 1 min residence time. CO_2 in this interval is likely generated from both hydropyrolysis and steam reforming processes (Eqns. 5 and 8). At the 1 min residence time, there is also a substantial amount of H_2 (25.8 mol %) and CH_4 (17.5 mol %) present. The low level of CO (2.7 mol %) detected at 1 min residence time taken together with the relatively high levels of H_2, CH_4, and CO_2 suggests that a large quantity of CO was rapidly formed and subsequently consumed during the 5 min preliminary heating period.

From Figure 44b it can be seen that the levels of C_4–C_6+ volatiles are nearly unchanged between 1 and 10 min residence time. The amounts of C_5 and C_6+ decline by 43% and 33%, respectively, between 10 and 60 min. The C_4 fraction increases approximately 4% between 5 and 10 min to 2.65 mol %, before decreasing to 2.01 mol % by 60 min. The C_3 fraction rises from 3.39 mol % at 5 min to 3.97 mol % at 30 min and then falls to 3.32 mol % at 60 min. The C_2 component increases from 4.14 mol % at 1 min to a maximum of 6.04 mol % at 30 min before dropping to 5.30 mol % at 60 min. Any analysis of the effect of time on an individual hydrocarbon fraction cannot be made independently of the other volatile components. It is assumed that the early increases in the C_2 components up to 5 min residence time are due to pyrolytic reactions involving the hydrothermal reaction intermediates. The steep increase in the quantity of C_2 between 5 and 30 min residence time, however, is accompanied by a large decrease in the H_2 fraction and smaller decreases in the C_5 and C_6+ fractions. The observed increases in both the CH_4 and C_2+ fractions are in agreement with those seen in other studies of biomass and coal [234, 318-320].

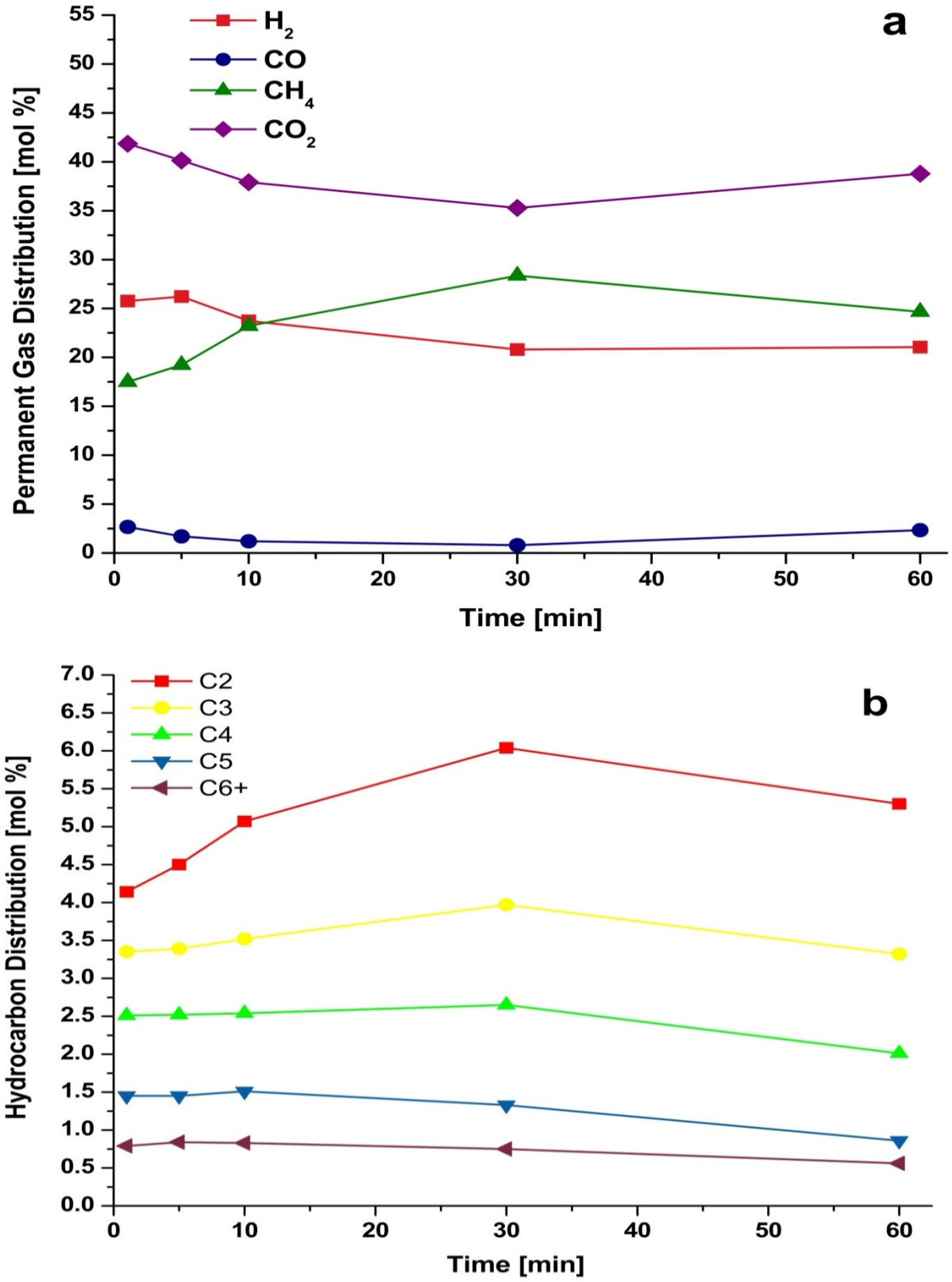

Figure 44. Volatiles product distribution as a function of residence time a) Fixed gases; b) C_2 – C_6+ hydrocarbon fraction.

The dependence of the CE and GE on reaction residence time is depicted in Figure 45. It is suspected that carbon hydrogasification and WGS reactions are both prominent during the first 5 min of the reaction, given the initial steep rise in the CE and GE curves. The increasing separation between the CE and GE curves between 5 and 30 min suggests that methanation and depolymerization reactions are prevalent in this time interval. Hydrogasification and WGS reactions likely resume their precedence after 30 min. The slower rise in the CE curve after 30 min may indicate that the hydrogasification reactions are consuming carbon from semi-volatile organics as the available supply of solid carbon begins to dwindle. The decline in the quantity of liquid organics after 30 min, as shown in Figure 42, validates the preceding hypothesis.

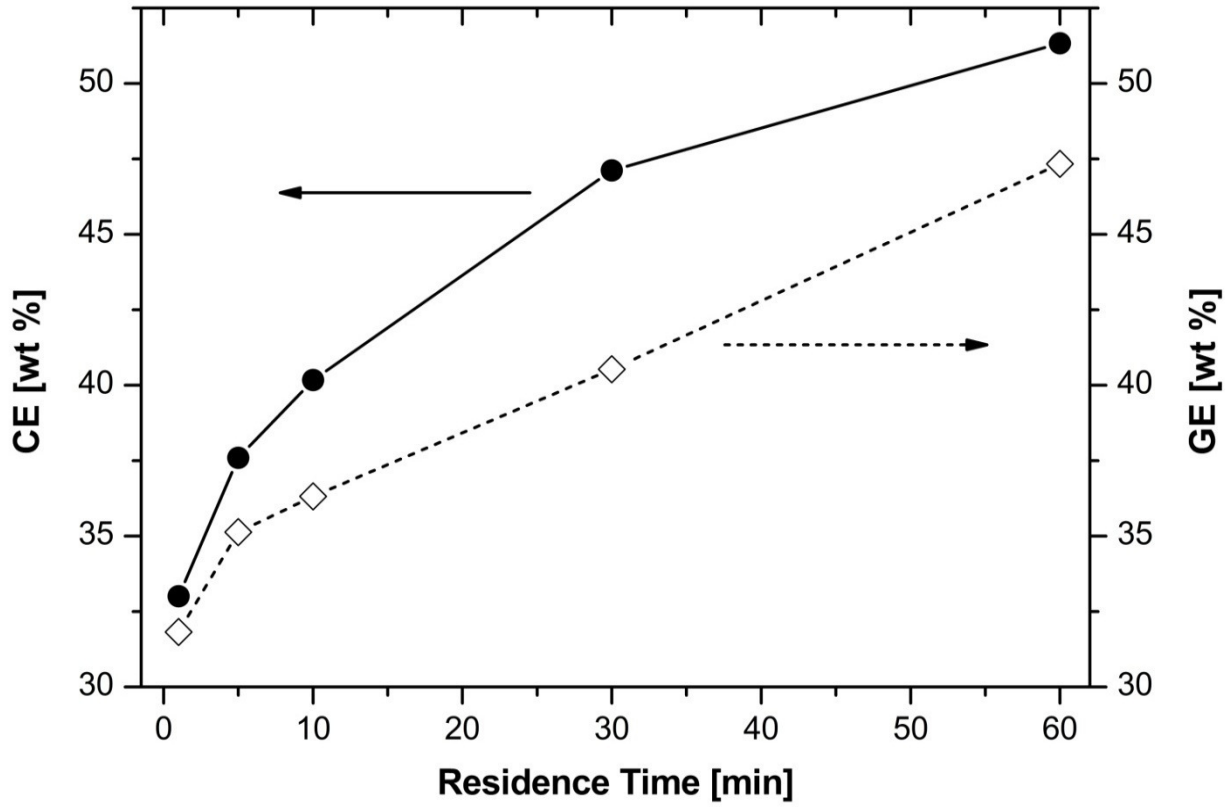

Figure 45. Temporal variation in carbon conversion efficiency (CE) and total gasification efficiency (GE)

The HHV of the gas product is relatively constant during the first 10 min of hydrothermal treatment, as shown in Table 21. The gross calorific values of the volatile products formed at 30

min (53.18 $MJ \cdot kg^{-1}$) and 60 min (49.86 $MJ \cdot kg^{-1}$) are 3.8 and 9.8% lower, respectively, than that at 10 min. An examination of the variation in volatile molar composition and yield with time, as represented by Figures 43 and 44, helps explain the observed decrease in the GCV of the volatiles with time. The molar composition of H_2 decreases, while that of CH_4 increases between 5 and 10 min. During this same time span, the actual molar yield of H_2 increases slightly by 0.1 mol % and that of CH_4 increases by 0.73 mol %. The molar fractions of CO and CO_2, which both act as energetic deadweights, decline between 5 and 10 min, whereas the molar composition of the C_2 hydrocarbon fraction increases. Ultimately, the volatile product obtained at 10 min has a HHV of 55.27 $MJ \cdot kg^{-1}$, which is statistically identical to the HHV of the volatile product obtained at 1 min. A combination of rising CO_2, CH_4, and C_2 molar yields and a static H_2 molar yield contribute to the decline in gas product HHV at longer residence times. A nearly threefold increase in the CO molar yield between 30 and 60 min also causes a further drop in the HHV of the volatile product.

4.4 Weight Loading Influence

To determine the influence of biomass concentration on the distribution and yield of products, hydrothermal experiments were performed at 500 °C and 5 min residence time with three different biomass/water weight loadings, *viz*. 1:12.5 (8.0 wt %) , 1:25.0 (4.0 wt %), and 1:37.5 (2.7 wt %). The total percentage mass balance for the various weight loading runs is presented in Table 22. It can be seen that amount of total liquid product decreases slightly with increased bagasse weight loading. The degree of bagasse conversion is nearly similar at the 2.7 and 4.0 wt % biomass loadings. However, the conversion of bagasse drops by nearly 6 wt % when the bagasse concentration is doubled from 4.0 to 8.0 wt %. The decrease in bagasse conversion at the highest weight loading level may be a sign that there is insufficient contact

between the supercritical fluid and the bagasse particles when higher concentrations of biomass substrate are present.

Table 22. Overall mass balances and volatile higher heating values from the hydrothermal conversion of bagasse performed using various biomass to water weight loadings.

Weight Loading	T [°C]	P_{max} [bar]	ρ [g cm^{-3}]	RT [min]	Liquids [wt %]	Solids [wt %]	Volatiles [wt %]	Conversion [wt %]	Gas HHV [MJ kg^{-1}]
1:37.5	500	687	0.398	5	97.12	0.47	1.00	81.8	54.09
1:25.0	500	707	0.410	5	97.18	0.71	1.36	81.5	54.38
1:12.5	500	782	0.449	5	94.87	1.81	1.90	75.6	50.65

The effect of weight loading on the product distribution resulting from bagasse hydrothermolysis is shown in Figure 46. Volatiles production decreases linearly with increasing biomass weight loading, falling 12.8 wt % over the entire span of weight loadings. Initially, the solids yield rises negligibly (i.e., 1.7% gain) between the 2.7 and 4.0 wt % loadings followed by a 31.4% gain between the 4.0 and 8.0 wt % loadings. Although the yield of semi-volatiles rises monotonically with increasing biomass concentration, it does appear that semi-volatile generation is more heavily impacted at lower weight loadings. For instance, the semi-volatiles yield rises 6.8% when the bagasse concentration is increased by 50% from 2.7 to 4.0 wt %; semi-volatile production rises only 7.8% when bagasse concentration is doubled from 4.0 to 8.0 wt %.

The molar yields of the individual volatile components in the product gas are plotted as a function of the dry bagasse concentration in Figure 47. Increasing the bagasse concentration from 2.7 to 8.0 wt % causes the H_2 and CO_2 yields to drop linearly by 42.7 and 31.8%, respectively. Similarly, the CO yield declines 43.5% over the same bagasse weight loading range. The CH_4 yield decreases 17.5% when bagasse concentration is increased by 50% from 2.7 to 4.0 wt %. Doubling the bagasse concentration to 8.0 wt %, however, only slices the CH_4 yield by 7.8%, suggesting that the mass yield of CH_4 is not affected to the same degree by higher

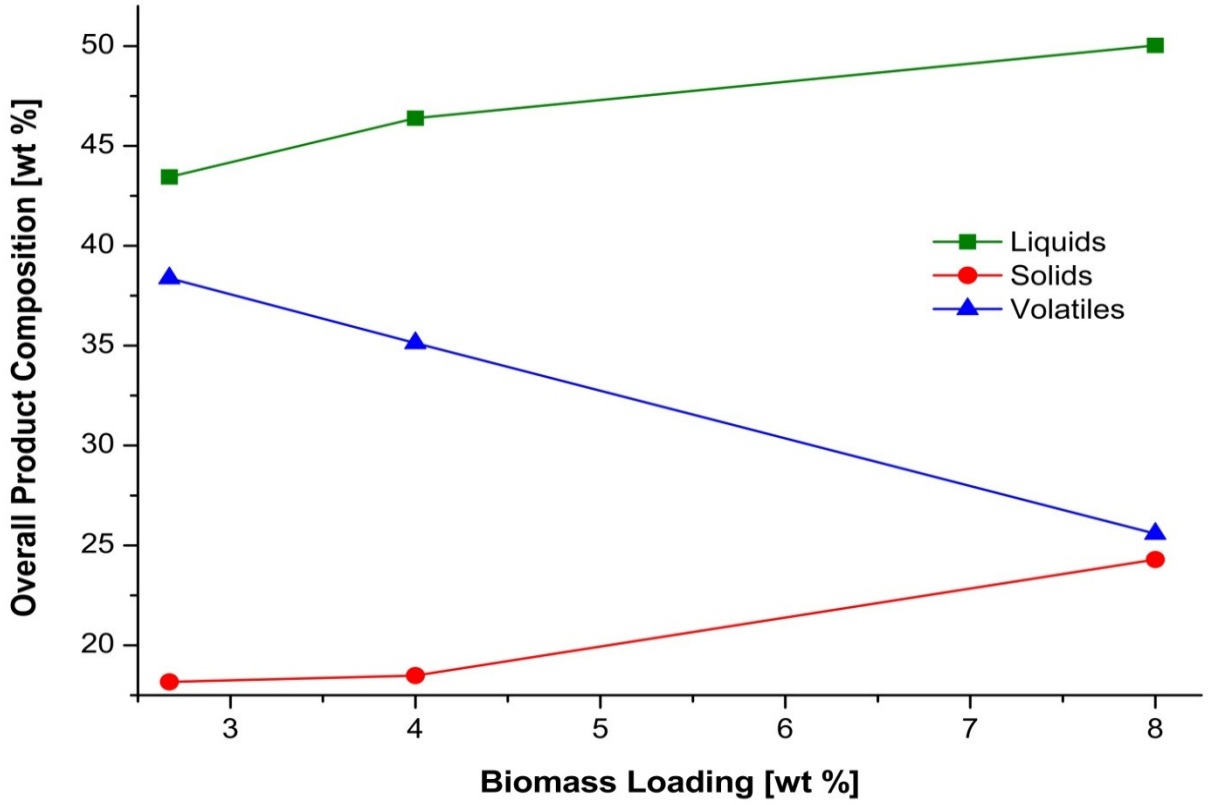

Figure 46. Distribution of products resulting from the hydrothermal treatment of sugarcane bagasse as a function of biomass weight loading.

biomass loadings as are those of H_2 and CO_2. The molar yields of the higher hydrocarbon fractions (C_2–C_5+) experience behavior akin to that of CH_4, wherein significantly steeper declines in yield are observed upon increasing the bagasse weight loading from 2.7 to 4.0 wt % than from 4.0 to 8.0 wt %.

The molar distribution of fixed gases as a function of bagasse weight loading is provided in Figure 48a. Upon increasing the biomass weight loading from 2.7 to 4.0 wt %, the mole fractions of H_2 and CO rise 21.1 and 13.3%, respectively, the mole fraction of CH_4 falls 17.7%, and the mole fraction of CO_2 experiences no significant change. Further increasing the weight loading from 4.0 to 8.0 wt % results in the following mole fraction changes: CH_4 increases 6.6%, H_2 decreases 3.9%, CO_2 decreases 2.9%, and CO remains unchanged. Similar to findings

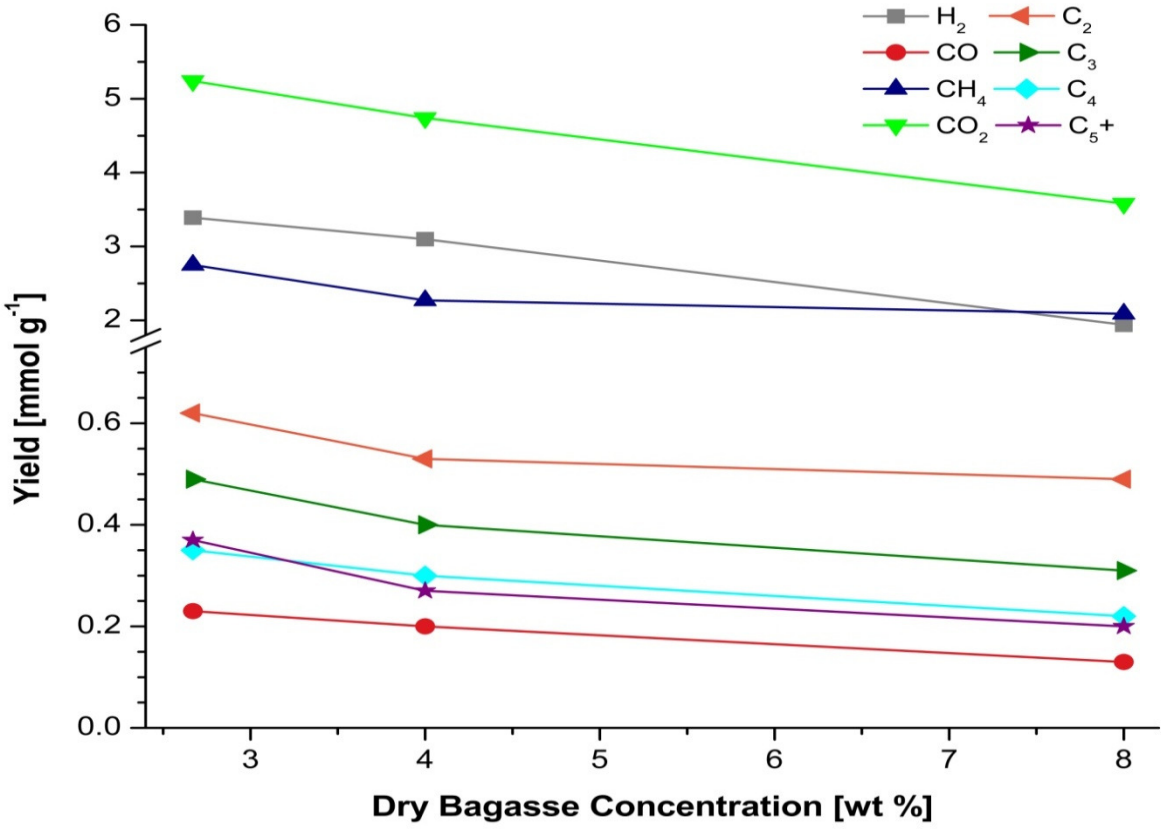

Figure 47. Molar yields of individual gas species as a function of biomass weight loading.

by Savage and coworkers [321] for the gasification of lignin (details previously described) the relative stability of the molar fraction of CO_2 suggests that CO_2 is the only gas that is not influenced by the biomass loading. The composition of the C_2–C_6+ hydrocarbon product gas is given Figure 48b. Not surprisingly, the relative differences in the corresponding individual molar fractions of the C_3–C_5 components recorded from the 2.7 and 4.0 wt % loading trials are extremely low (≤ 1.5% per component). The relative difference between the C_6+ molar fractions for the previous two weight loadings is a bit higher at 12% mainly because of the greater uncertainty associated with the measurement of this hydrocarbon fraction using the GC-FID. The differences in the corresponding individual C_2–C_4 molar fractions from the 4.0 and 8.0 wt % loadings are between 3.1 and 6.8%. Continuing, there are 10.3 and 36.9% differences in the respective C_5 and C_6+ molar fractions collected from the corresponding 4.0 and 8.0 wt % loading

experiments. The C_2 molar fraction obtained from the lowest weight loading run is about 20% higher than the C_2 molar fractions obtained from the two higher weight loading runs.

The reduced concentration of bagasse particles in the lower weight loading run may grant enhanced access to the particles by the water and intermediates. Mass transfer limitations between the particle surface and both volatile and aqueous phase reactants will be reduced if the particle is more completely enveloped by the surrounding fluid. Therefore, it is theorized that bagasse particles and resultant solid residues from the lowest weight loading run will experience a greater degree of cracking than in the higher weight loading runs, which would provide a possible explanation for the unexpected increase in the C_2 fraction from the 2.7 wt % loading case. The corollary reduction in the H_2 molar fraction in the 2.7 wt % loading run offers further proof that the solid components in this run underwent more extensive hydrocracking than those from the higher weight loading runs.

The effect of biomass concentration on the CE and GE is illustrated in Figure 49. In broad terms, it can be seen that the use of higher biomass weight loadings significantly reduces biomass gasification, as shown in Figure 46. The overall decline in biomass gasification causes both the CE and GE to fall. It is believed that mass transfer resistance becomes a key factor as the biomass concentration of the slurry is increased. Interestingly, the initial increase in biomass loading from 2.7 to 4.0 wt % elicits a 50% greater decline in the CE than in the GE. From this result, it can be concluded that heterogeneous reactions involved in the volatilization of carbonaceous material (e.g., carbon-water gasification, gasification methanation, etc.) are more strongly affected by the initial shock in weight loading than homogeneous reactions (e.g., pyrolysis methanation, WGS, etc.), which simply transfer carbon atoms between different gaseous species.

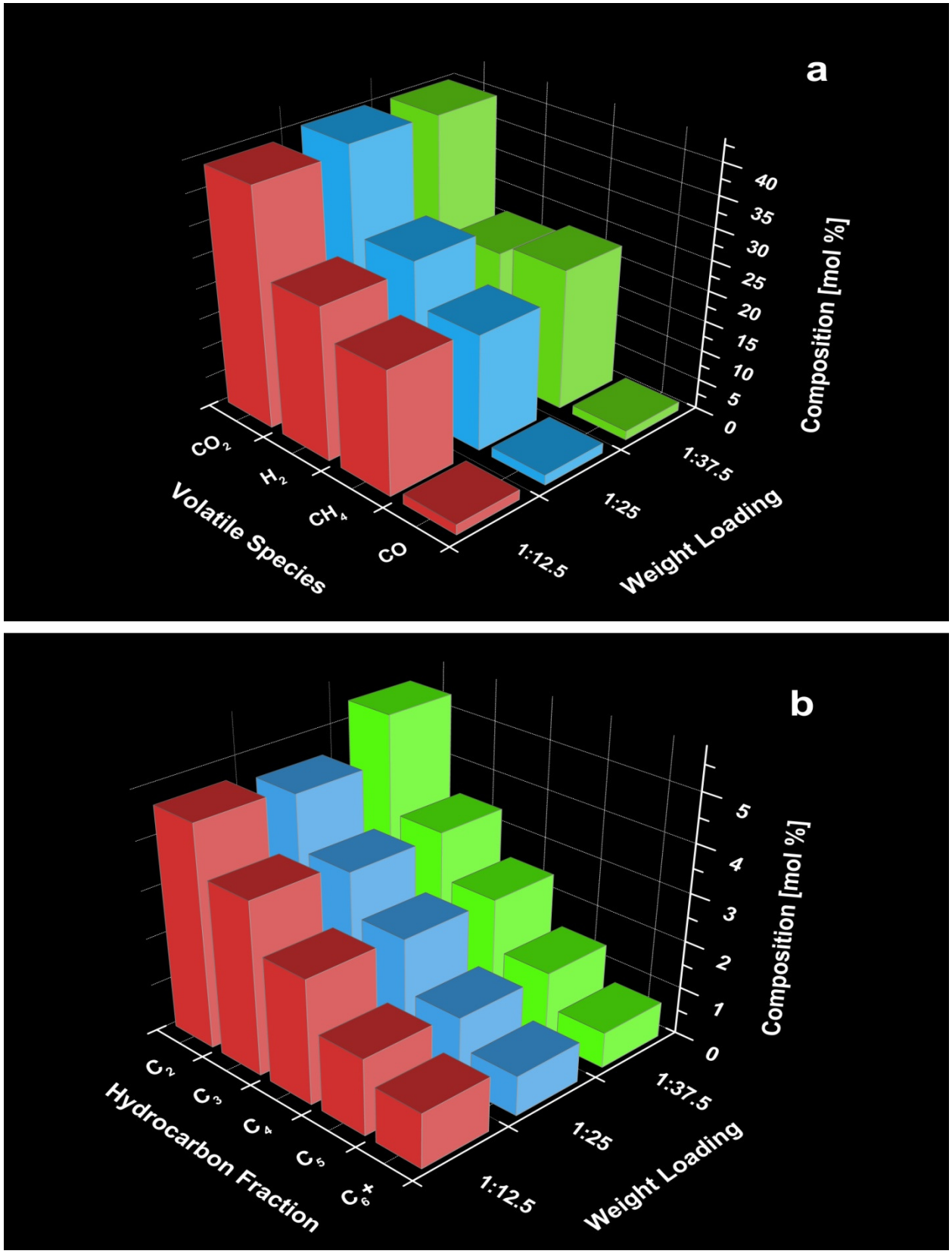

Figure 48. Influence of biomass weight loading on volatiles distribution a) Fixed Gases; b) C_2–C_6+ hydrocarbon fraction.

The HHV of the volatile products is unaffected when the biomass loading is increased from 2.7 to 4.0 wt %. However, the HHV of the gases decreases by 6.9% when the biomass loading is increased from 4.0 to 8.0 wt %. The 37.4% drop in the molar yield of H_2 between these same weight loadings is responsible for the decline in HHV.

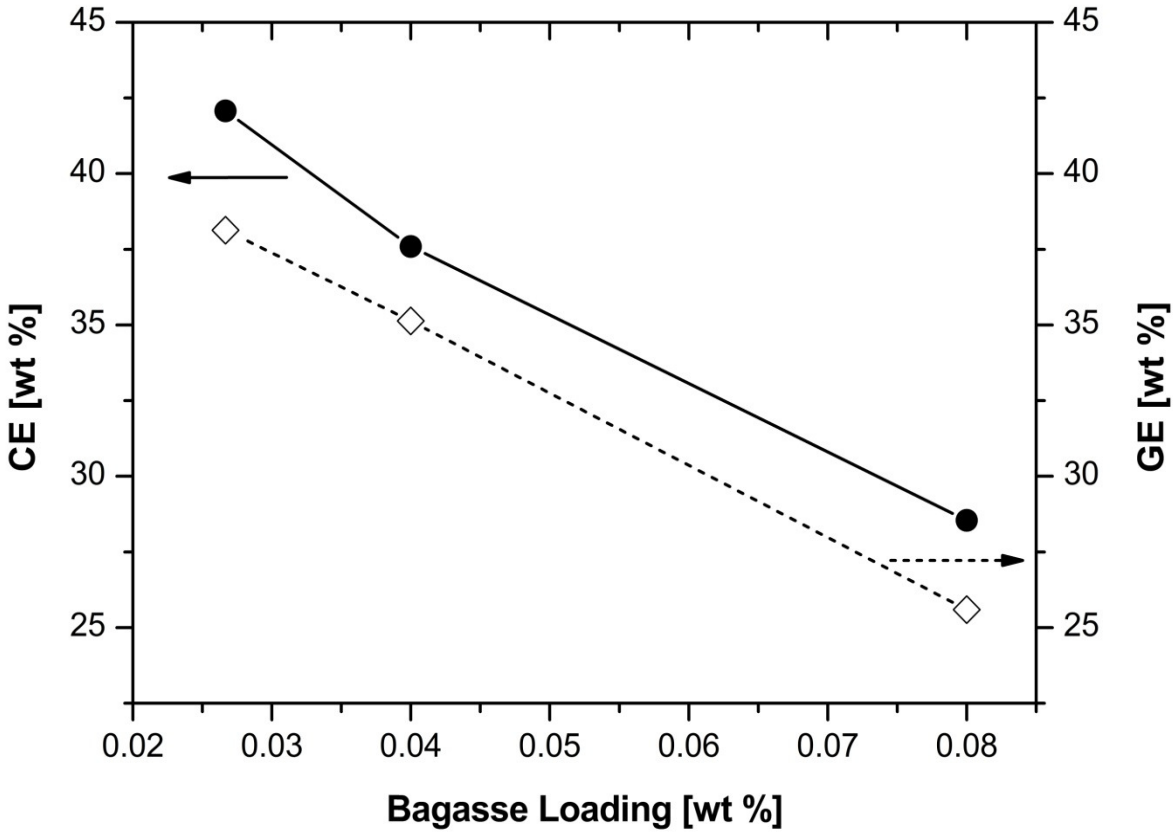

Figure 49. Carbon conversion efficiency (CE) and total gasification efficiency (GE) dependence on biomass loading.

4.5 Particle Size Effects

The effect of particle size on product distribution and yields was studied by using three different particle size mesh fractions, *viz*. 18/25 (850–1000 μm), 45/60 (250–355 μm), and 140/230 (63–106 μm), along with unsieved bagasse that was ground to less than 2 mm. All of the runs were conducted using the base conditions of 500 °C, 5 min residence time, and 4 wt % biomass loading. Table 23 provides the total hydrothermal reaction mass balance and operating

parameters for hydrothermal runs performed using various particle sizes. The large and intermediate particle size fractions of bagasse were converted to nearly the same extent, as seen in Table 23. The hydrothermal conversion of bagasse experienced by the smallest particle size fraction of bagasse was a minimum of 9.0 wt % lower than that of the larger particle size fractions. This result is particularly intriguing because it runs contrary to conventional chemical engineering pedagogy. Normally, it is assumed that the larger surface area intrinsic to smaller particles enhances the probability that successful reactions will occur. Additionally, smaller particles usually feature improved heat and mass transfer characteristics over larger particles. Here, the increased surface area of the 63–106 μm particle size fraction appears to have inexplicably hindered the conversion of the substrate.

A study on the role of particle size on the nonisothermal pyrolysis of hazelnut shells does offer some confirmation for the previous result [322]. Hazelnut shells with size fractions ranging from less than 0.150 mm to greater than 1.400 mm were pyrolyzed from ambient room temperature to 900 ºC at 20 ºC·min^{-1}. It was found that that the decomposition rate increased with increasing particle size, such that the + 1.400 mm fraction had the highest decomposition rate (7.3 mg·min^{-1}) and the - 0.150 mm fraction had the lowest decomposition rate (4.7 mg·min^{-1}). The interested reader is directed to the discussion section in Chapter 5 for a further treatment of this topic.

The standard, baseline hydrothermal run with unsieved bagasse had a conversion level that was approximately 3 wt % lower than those of the larger mesh size fractions and 6 wt % above that of the smallest mesh size fraction. This result is consistent with the fact that 84 wt % of the unsieved bagasse has a particle diameter greater than 125 μm. The HHV of the product gases does not appear to depend on particle size as can be seen from the data in Table 23.

Table 23. Overall mass balances from the hydrothermal conversion of bagasse performed using various particle sizes.

Mesh Size Fraction	T [°C]	P_{max} [bar]	ρ [g·cm^{-3}]	RT [min]	Liquids [wt %]	Solids [wt %]	Gases [wt %]	Conversion [wt %]	Gas HHV [MJ·kg^{-1}]
18/25	500	734	0.425	5	97.62	0.60	1.35	84.2	52.76
45/60	500	727	0.421	5	97.40	0.59	1.35	84.5	56.07
140/230	500	700	0.406	5	96.70	0.94	1.20	75.2	54.52
Unsieved	500	707	0.410	5	97.18	0.71	1.36	81.5	54.38

The variation in the overall product distribution from bagasse hydrothermal conversion as a function of particle size is plotted in Figure 50. There is no significant change in the yield of any product phase when decreasing from the 18/25 to the 45/60 mesh size fraction. Semi-volatiles production is reduced by 11.3% when particle size is lowered from the 45/60 to the 140/230 mesh size fraction. Similarly, the formation of volatiles shifts downward by 10.5% as the mesh size fraction is decreased from the intermediate to the smallest particle size fraction. Separately, there is a 60% increase in solids production when going from the 45/60 to 140/230 particle mesh size fraction. The yield of volatiles from the unsieved bagasse run (i.e., all of the particles are below 9.5 mm) and those of the 18/25 and 45/60 mesh size runs are nearly equivalent. Generation of semi-volatiles from the unsieved bagasse is 5.9% lower than the average yield from the 18/25 and 45/60 mesh size fractions. The solids production for the unsieved bagasse run is 18.5 wt %, or a 17.2% increase over the average of the 18/25 and 45/60 mesh size fractions.

The molar yields of the individual volatile components from the hydrothermal product gas are represented as a function of particle size in Figure 51. The majority of volatiles exhibit an insignificant loss in molar yield when the particle mesh size is decreased from 18/25 to 45/60. The exceptions to this trend are H_2 and CO, which increase by 11.4 and 25%, respectively, when particle size is reduced from the 18/25 to the 45/60 mesh size fraction. Interestingly, all molar

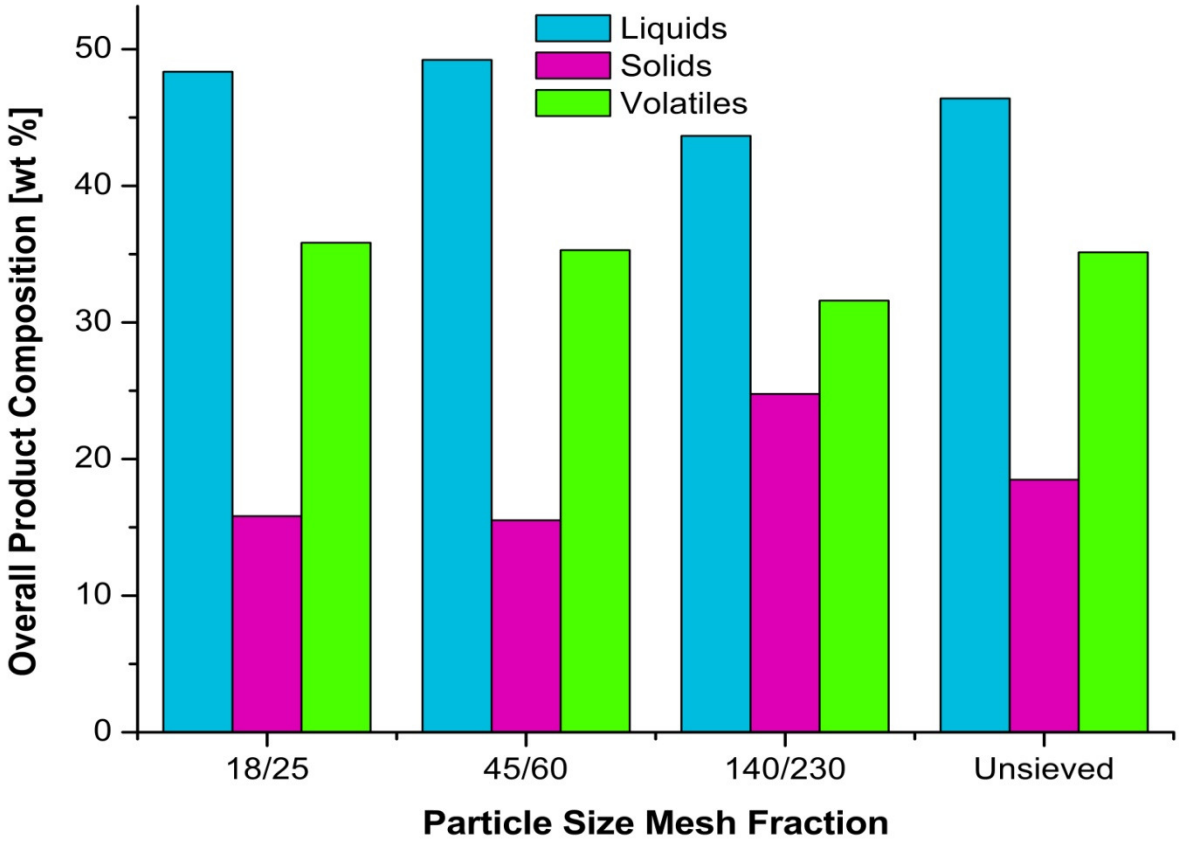

Figure 50. Variation in hydrothermal product distribution as a function of bagasse particle size.

gas yields decreased by an average of 29.1% (σ = 1.00%, SE = 0.35%) when particle size was lowered from the 45/60 to the 140/230 mesh size fraction. The molar yields of CO_2 and the hydrocarbons obtained from the unsieved bagasse run correspond closely with those of the 45/60 mesh size fraction. The molar yields of H_2 and CO from the unsieved bagasse run, however, match those of the 18/25 mesh size fraction. If the small fraction of particulates below 140 mesh size is discounted, then 56.4 wt % of the unsieved bagasse corresponds to a larger particle size fraction (above 45 mesh size) while the remaining 43.6 wt % falls in an intermediate particle size range (45/140 mesh size), on a normalized basis. Given the near parity in the two fractions, it would appear that larger particles have a greater influence on the formation of H_2 and CO, whereas CO_2 and hydrocarbon production are controlled more by intermediate size particles.

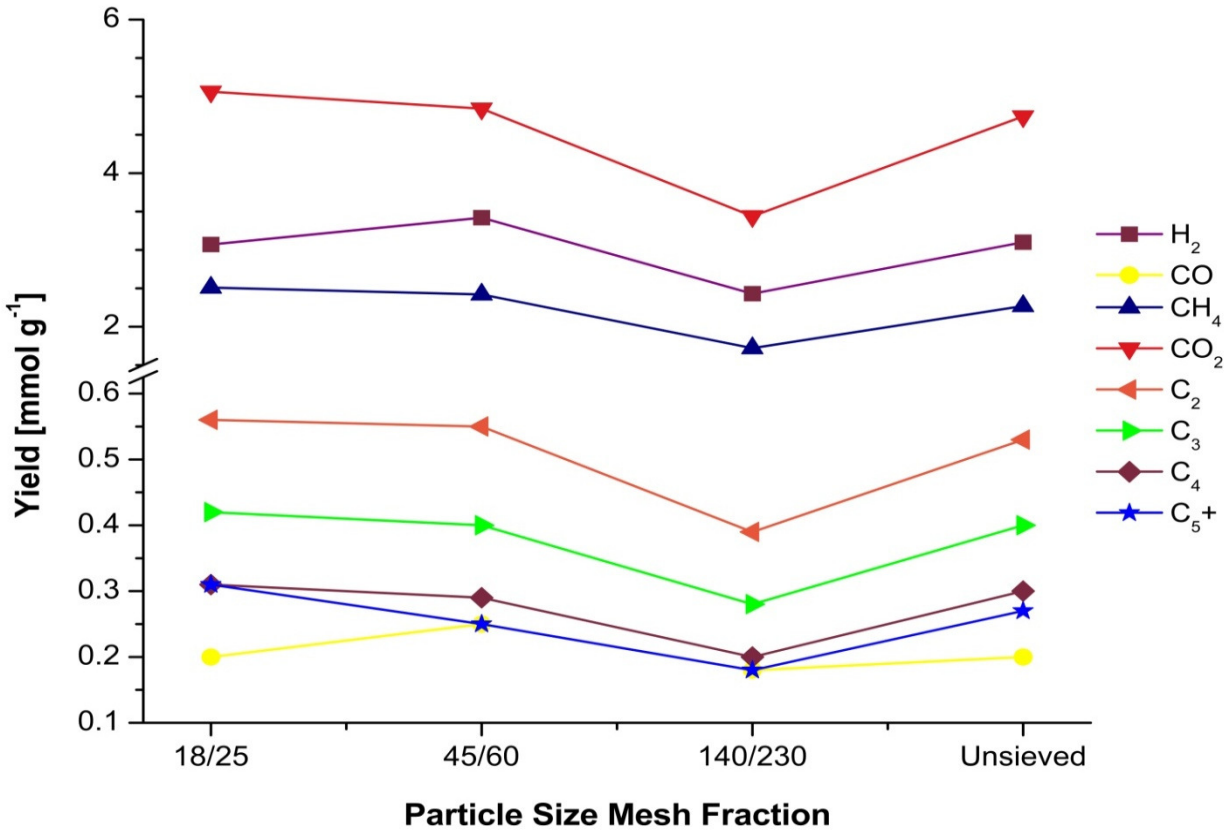

Figure 51. Molar yields of individual gas species as a function of particle size.

It is germane to the present overview of results to note the pH measurements obtained for the aqueous phase products from the various particle size fractions. The 18/25 and 45/60 mesh size fractions were nearly identical with a pH of 4.03 and 4.01, respectively. The ground, unsieved bagasse had a mean pH of 4.15 and the 140/230 mesh size fraction had a pH of 4.30. The reduced acidity in the semi-volatile product from the finest particle size is an indication that the chemical composition for this fraction is not in line with those of the larger particle sizes.

Figure 52a portrays the distribution of fixed gases obtained from bagasse hydrothermal conversion as a function of residence time. The unsieved bagasse and 140/230 mesh size experiments have nearly the same distribution of light volatile species. The largest particle size fraction has a higher mole fraction of CH_4 and CO_2 (4.9 and 1.9%, respectively) and a lower mole fraction of H_2 and CO (5.9 and 7.6%, respectively) than the equivalent components

obtained for the unsieved bagasse run. The 45/60 mesh size fraction has a higher mole fraction of CO, H_2, and CH_4 (18.2, 10.9, and 1.4%, respectively) and a lower mole fraction of CO_2 (2.8%) than for the same constituents from the unsieved bagasse experiment. The volatiles distribution obtained from the unsieved bagasse can be calculated as the sum of the contributions of the individual corresponding particle size fractions by applying the superposition principle:

$$Y_X = \left(\frac{\sum_i W_i}{W_\mathrm{T}} \right) n_X + \left(\frac{\sum_j W_j}{W_\mathrm{T}} \right) n_X + \left(\frac{\sum_k W_k}{W_\mathrm{T}} \right) n_X \tag{44}$$

where Y_X is the calculated value for species X, W_i, W_j, and W_k, are the weights for particle size fractions i, j, and k, respectively, W_T represents the total weight of the particle size distribution, and n_X is the measured mole fraction of species X in the evolved volatile products. It is assumed that particle sizes corresponding to mesh size 35/45 and above (i.e., ≥ 355 μm) will behave similarly. Likewise, particles sizes between 45/60 and 120/140 mesh size (i.e., 106–355 μm) were treated as a second group, and finally, particles sizes at or below 120/140 mesh size (i.e. < 106 μm) were lumped together as a third group. The mass fractions for the mesh size ranges listed above in order of appearance are as listed: 53.6, 41.5, and 4.9 wt %. H_2 was used to test the applicability of the above theory. The mole fraction of H_2 from the unsieved bagasse run was 26.22 mol %, while the mole fraction of H_2 obtained using the superposition hypothesis is 25.94 mol %, representing a mere 1.0% decrease in the observed experimental value. This calculation reveals that the distribution of gases in a bagasse sample can well be approximated by the individual contributions from the respective particle size fractions.

From Figure 52b it can be seen that the C_2–C_6+ fractions from the both the largest and smallest and smallest mesh size fractions closely resemble those of the unsieved bagasse sample, with the exception of the C_4 fraction from the 140/230 fraction which is 8.7% lower than that of

the unsieved bagasse and the C_6+ fractions from both the 18/25 and 140/230 mesh size fractions which are 14.3 and 8.3% lower than that of the corresponding fraction from the unsieved bagasse. Curiously, the intermediate size fraction has a decreased mole fraction of every hydrocarbon component in comparison to that of the unsieved bagasse. Furthermore, the mole fraction difference between the 45/60 mesh size fraction and the unsieved fraction increases linearly with increasing hydrocarbon number.

A conceivable explanation for the consistently lower C_2–C_6+ hydrocarbon yields expressed by the intermediate particle size fraction involves the possibility that the ratio of pith to fiber in this bagasse fraction is markedly different than those of the other fractions. As mentioned in Chapter 2, the morphological and chemical constitutions of pith and fiber are not alike and, thus, they will likely behave differently under hydrothermal environments. A compositional analysis of the fiber bundle and pith fractions from Mexican sugarcane bagasse indicated that the pith fraction contains 2.9 wt % more pentosans and 12.6 wt % more soluble extractives, both hydrophilic and hydrophobic, than the fiber bundle fraction [323]. Therefore, it is anticipated that the pith fraction with its higher level of low molecular-weight carbohydrates should yield a higher proportion of C_2-C_6 hydrocarbons than the fiber fraction after HT treatment. The Mexican sugarcane bagasse study also examined the dimensional characteristics of both bagasse fractions using 50 cells of each type and determined that the mean length of a fiber is 1.13 mm (± 0.56 mm) and that of a parenchyma cell is 0.29 mm (± 0.01 mm). Interestingly, the average length of the parenchyma cells in pith falls in the middle of the intermediate particle size range (0.250 to 0.355 mm) used in this study. It is suspected that a future compositional analysis of the bagasse used in the current study would reveal that the 45/60 mesh size range contains a greater preponderance of pith particles than the other size fractions.

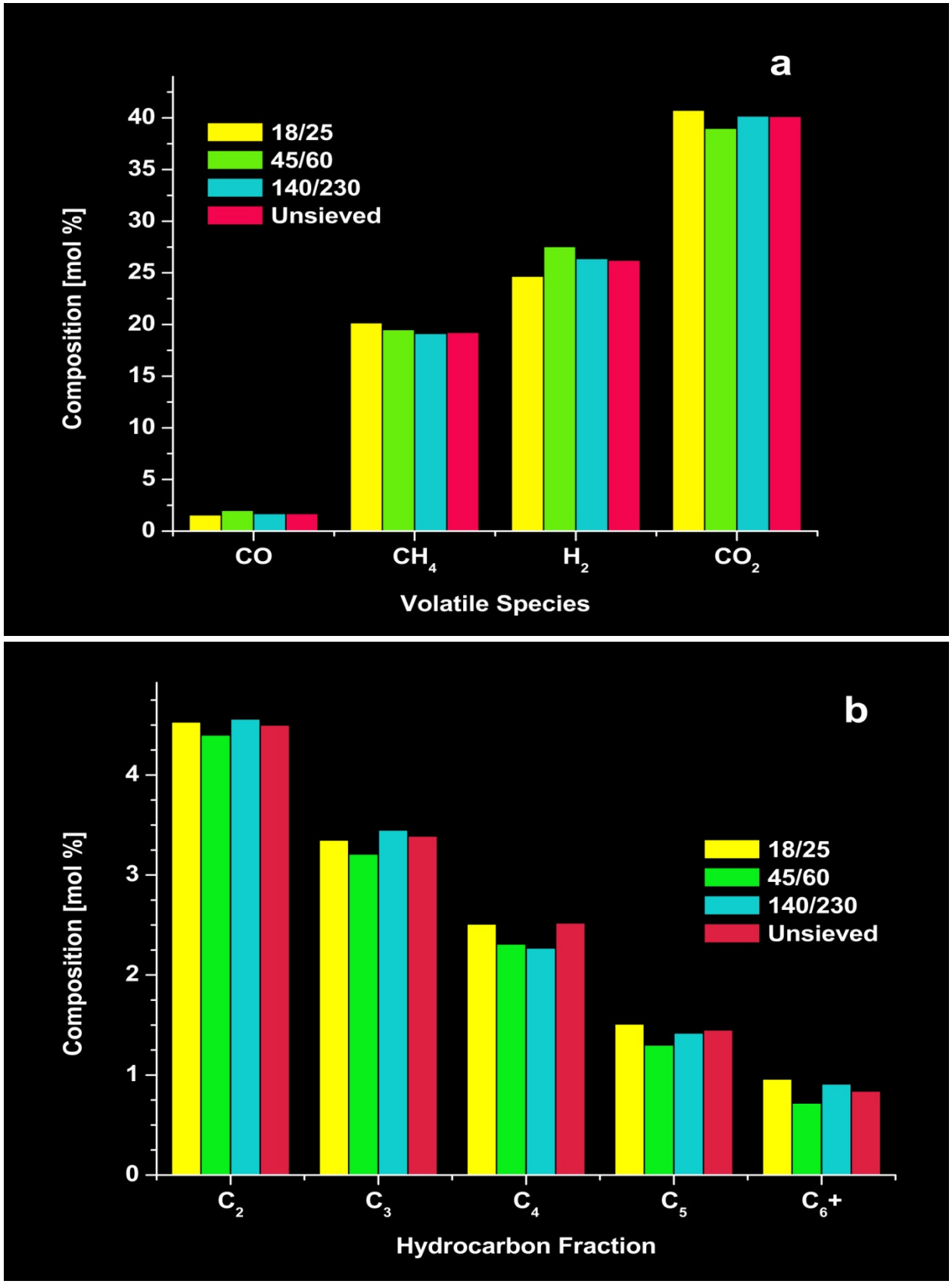

Figure 52. Particle size effect on volatiles distribution a) Fixed gases; b) $C_2 - C_6+$ fraction.

The effect of particle size on the CE and GE is shown in Figure 53. The particles between 0.850–1.000 mm had the highest CE (39.33 wt %) and GE (35.83 wt %). A decrease in the particle size fraction to 0.250–0.355 mm was accompanied by a negligible decrease in both the CE and GE. However, the CE and GE dropped 4.41 and 3.70 wt %, respectively, when the particle size fraction was further decreased to 0.063–0.106 mm. The observation that the CE and GE are lowest for the smallest particle size was unexpected, given that smaller particles have more surface area available from which to support heterogeneous reactions that can evolve gas-phase products. Furthermore, heat and mass transfer limitations in the particle bulk should be significantly reduced in smaller particles, allowing them to react more completely. Nevertheless, these results concur with the earlier finding that the conversion of bagasse is lowest for the smallest particle size fraction.

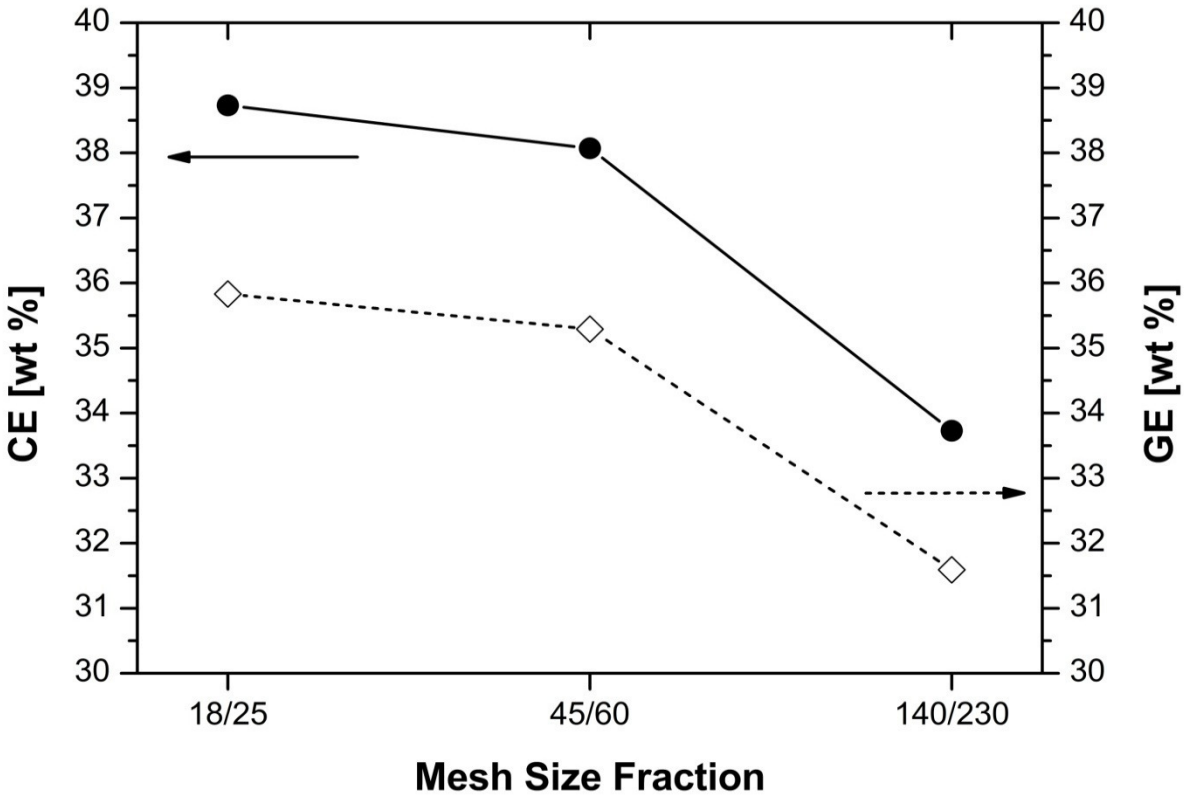

Figure 53. Variation in carbon conversion efficiency (CE) and total gasification efficiency (GE) with respect to particle size.

4.6 Model Bagasse Components

After the tests in the preliminary experimental design had been completed, several questions arose regarding the results. Foremost among these was whether the distribution and yield of volatiles obtained using sugarcane bagasse were unique to this substrate. In order to ascertain the "uniqueness" of the volatiles production from the hydrothermolysis of bagasse, experiments were conducted using model compounds that closely approximate the major lignocellulosic components found in sugarcane bagasse.

Long, fibrous cellulose was chosen to represent the cellulosic component from sugarcane bagasse. Xylan comprises over 99% of the total hemicellulose fraction in the sugarcane bagasse used in these experiments. Consequently, xylan (from oat spelts) was selected as a reasonable model candidate for the hemicellulose fraction in sugarcane bagasse. The type of extraction method used to isolate lignin from biomass is known to cause important structural changes that can affect the gasification behavior of the biomass [324, 325]. It was decided that alkali lignin best approximated the native lignin in bagasse. The model lignocellulosic hydrothermal experiments were conducted using the standard experimental conditions (i.e., 4 wt % biomass loading, 500 °C, 5 min residence time, and unsieved bagasse having a particle size less than 2mm). The overall mass balances from the hydrothermolysis of the model lignocellulosic compounds are presented in Table 24. Cellulose had the highest overall conversion of the lignocellulosic components at 93.4 wt %, followed closely by xylan at 89.0 wt %. The hydrothermal conversion of lignin trailed far behind at 76.8 wt %. The recalcitrant nature of lignin is thought to have inhibited its hydrothermal conversion. The conversion for the standard, baseline run of bagasse was 81.1 wt %, which when corrected for ash content increases to 85.1 wt %.

Table 24. Overall mass balances and volatile higher heating values from the hydrothermal conversion of representative bagasse constituents.

Component	T [°C]	P_{max} [bar]	ρ [g·cm^{-3}]	RT [min]	Liquids [wt %]	Solids [wt %]	Gases [wt %]	Conversion [wt %]	Gas HHV [MJ·kg^{-1}]
Cellulose	500	723	0.419	5	97.86	0.26	1.51	93.4	52.95
Xylan	500	729	0.422	5	97.75	0.43	1.33	89.0	54.06
Lignin	500	703	0.408	5	97.79	0.88	1.12	76.8	61.27
Bagasse	500	707	0.410	5	97.18	0.71	1.36	81.5	54.38

The overall product distribution on a mass basis for the lignocellulosic components and a standard bagasse run is provided in Figure 54. It can be seen that cellulose has the lowest level of solids formation and the highest level of volatiles production. There is a 63% reduction in solids and an 11% increase in gas products when the hydrotreatment of cellulose is compared to that of bagasse.

Figure 54 reveals near parity in the level of semi-volatiles generation from the lignin and bagasse hydrothermal experiments. The semi-volatile levels from the cellulose and xylan runs are also practically identical, but they are approximately 8 wt % lower than those of the lignin and bagasse runs. Cellulose has the highest total volatile yield at 38.9 wt %; volatile yields decline progressively for xylan (34.4 wt %) and lignin (29.7 wt %). The volatile yield of bagasse is 2.2% higher than that of xylan. The higher semi-volatile levels for the lignin and bagasse HT tests may indicate that lignocellulosic compounds have a higher propensity to form semi-volatiles than volatiles. It is speculated that hydrothermally treated lignin degrades primarily via condensation [14] and bond cleavage [14, 326] reaction routes giving rise to carbonaceous residues and high molecular-weight liquid organics (e.g., asphaltenes, tars, phenols, aldehydes, furans, etc.), whereas hydrothermal decomposition of cellulose and hemicelluloses occurs largely via hydrolysis reactions that evolve volatile organic compounds (VOCs).

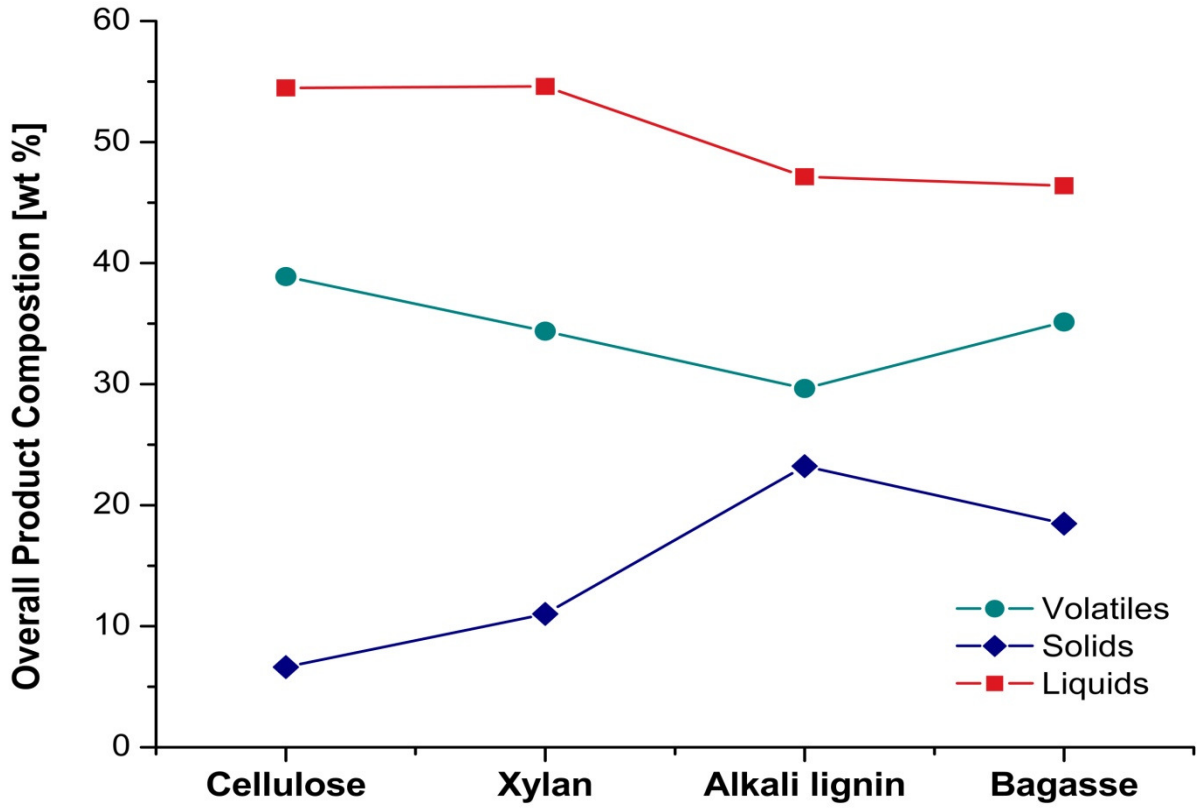

Figure 54. Overall product distribution from hydrothermal treatment of various lignocellulosic compounds.

Figure 55 shows the molar yields of the individual gases from the HT treatment of bagasse and the representative lignocellulosic constituents of bagasse at 500 °C. Xylan produces 18.4% more CH_4 than does cellulose and lignin produces 47.2% more CH_4 than does xylan. A similar result was obtained by Resende *et al.* [318, 321], who compared the supercritical water gasification of cellulose and lignin at 600 °C. The noticeably lower production of C_2-C_4 hydrocarbons afforded by alkali lignin in comparison to the other model compounds and bagasse is an important observation that becomes even more salient when it is discovered that the level of C_5+ production from alkali lignin is roughly equivalent to that of xylan and bagasse. These results suggest that lignin may be less susceptible to cracking than other types of lignocellulose. They also indicate that bagasse degradation in SCW behaves more like that of xylan than lignin.

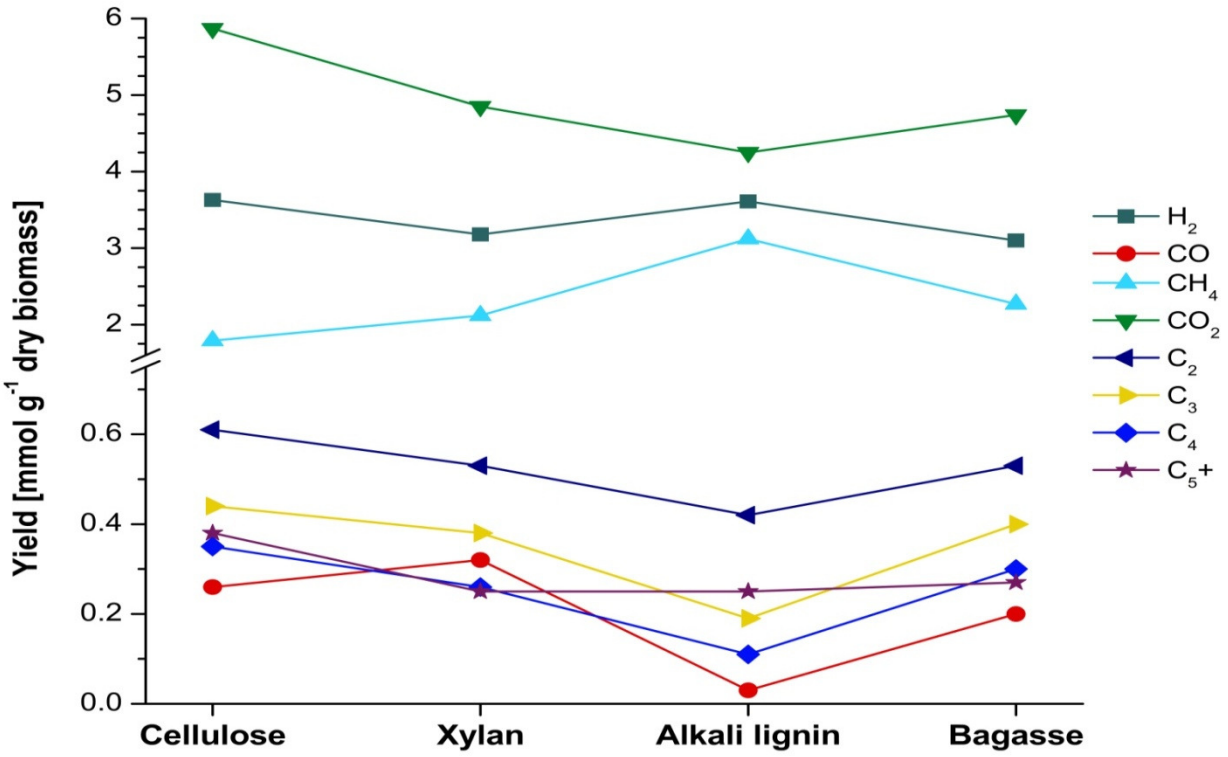

Figure 55. Volatile molar yields from hydrothermally treated lignocellulosic components.

Although it is known that there are some interactions that occur between the cellulose, hemicellulose, and lignin components during biomass thermal degradation [269, 327-329], it was assumed that these would not significantly interfere with the distribution and yields of the volatile components. Given the above assumption, the gasification behavior of an actual biomass sample can be represented as a weighted average of the yields obtained from the gasification of the respective individual components, as shown in Eqn. 45:

$$Y_{\mathrm{av},i} = Y_{\mathrm{c},i} X_{\mathrm{c}} + Y_{\mathrm{x},i} X_{\mathrm{x}} + Y_{\mathrm{l},i} X_{\mathrm{l}} \tag{45}$$

where $Y_{av,i}$ is the weighted average for a given gaseous species, i; $Y_{c,i}$, $Y_{x,i}$, $Y_{l,i}$ are the yields for species i obtained from the independent gasification of cellulose, xylan, and lignin, respectively; X_c, X_x, and X_l denote the actual biomass weight fractions of cellulose, xylan, and lignin, respectively. If the weighted averages from the hydrothermal conversion of the model lignocellulosic components agree with the experimental results obtained from the hydrothermal

conversion of bagasse, then it can be concluded that the gasification behavior exhibited by various biomass types is to a large extent governed by the actual composition of the particular biomass type. However, if there is a discrepancy between the results obtained from the compositional paradigm for bagasse and that of the actual bagasse, then it can be reasoned that the gasification behavior exhibited by bagasse is either a function of some other constituent inherent to sugarcane (e.g., extractives, lignans, terpenes, waxes, inorganic matter, etc.), a function of the reactor, or some intermediate combination thereof.

In Table 25, the molar compositions of the volatiles from model lignocellulosic compounds, bagasse, and the bagasse model paradigm are compared. The predicted compositional values of the fixed gases from the bagasse paradigm deviate by no more than 8% from the actual compositional values of the fixed gases recorded from bagasse hydrothermolysis. The predicted values of the C_2 and C_5 hydrocarbon fraction compositions were within 5% of the actual compositional values obtained using bagasse. The compositional paradigm performed less accurately for the C_3, C_4, and C_6+ hydrocarbon fractions, where a 15.5–21.5% variance exists between the individual molar composition values obtained from the weighted average model and those from actual bagasse. The compositional paradigm slightly overestimates the permanent gas fractions and underestimates the hydrocarbon fractions, except that of the C_6+ fraction. The compositional values of the C_3 and C_4 fractions from the bagasse are equivalent to those obtained from cellulose, which explains the predictive failure in the compositional paradigm for these two fractions. The compositional profile of the gases obtained from bagasse paints an informative picture regarding the hydrothermal evolution of volatiles derived from actual biomass. The fixed gases are formed in amounts that are proportional to the compositional fractions of the representative lignocellulosic constituents. The compositional values of the C_2–C_5 hydrocarbon

fractions obtained from bagasse do not conform to the pattern above for fixed gases but instead closely approximate the C_2–C_5 compositional yields obtained from cellulose. Hence, it is assumed that the formation of hydrocarbons during bagasse hydrothermal treatment follows a mechanistic pathway that is similar to that found during the hydrothermal treatment of cellulose.

Table 25. Volatiles composition obtained from lignocellulosic compounds, bagasse, and a compositional paradigm for bagasse (mol %).

Species	Cellulose	Xylan	Lignin	Bagasse	Paradigm	Deviation
H_2	27.23	26.75	30.13	26.22	27.82	6.10
CO	1.97	2.73	0.26	1.70	1.76	3.53
CH_4	13.41	17.82	26.01	19.23	17.72	-7.85
CO_2	44.00	40.82	35.46	40.14	41.03	2.22
C_2	4.57	4.49	3.49	4.50	4.28	-4.89
C_3	3.32	3.16	1.63	3.39	2.86	-15.63
C_4	2.64	2.16	0.94	2.52	2.09	-17.06
C_5	1.69	1.39	0.92	1.45	1.42	-2.11
C_6+	1.14	0.68	1.16	0.84	1.02	21.43

The volatiles molar composition data contained in Table 25 is also presented in graphical format in Figure 56. It is evident from Figure 56a that there is distinct dissimilarity in the fixed gas composition from lignin and those from the other model compounds and bagasse. The considerably lower yields of oxygenated volatiles (i.e., CO and CO_2) from lignin HT are almost certainly a reflection of the lower oxygen content in lignin. Alkali lignin has roughly 29 wt % O, whereas xylan and cellulose have 48 and 49 wt % O, respectively. The bagasse samples had 47 wt % O, so theoretically the molar yields of CO and CO_2 from bagasse would be predicted to be equivalent to those from xylan. Indeed, the experimentally determined volatile O content from bagasse is about the same as that from xylan. An analysis of the semi-volatiles would establish whether the decreased O content in the volatiles from bagasse and xylan is compensated for by an increase in the level of oxygenated semi-volatiles.

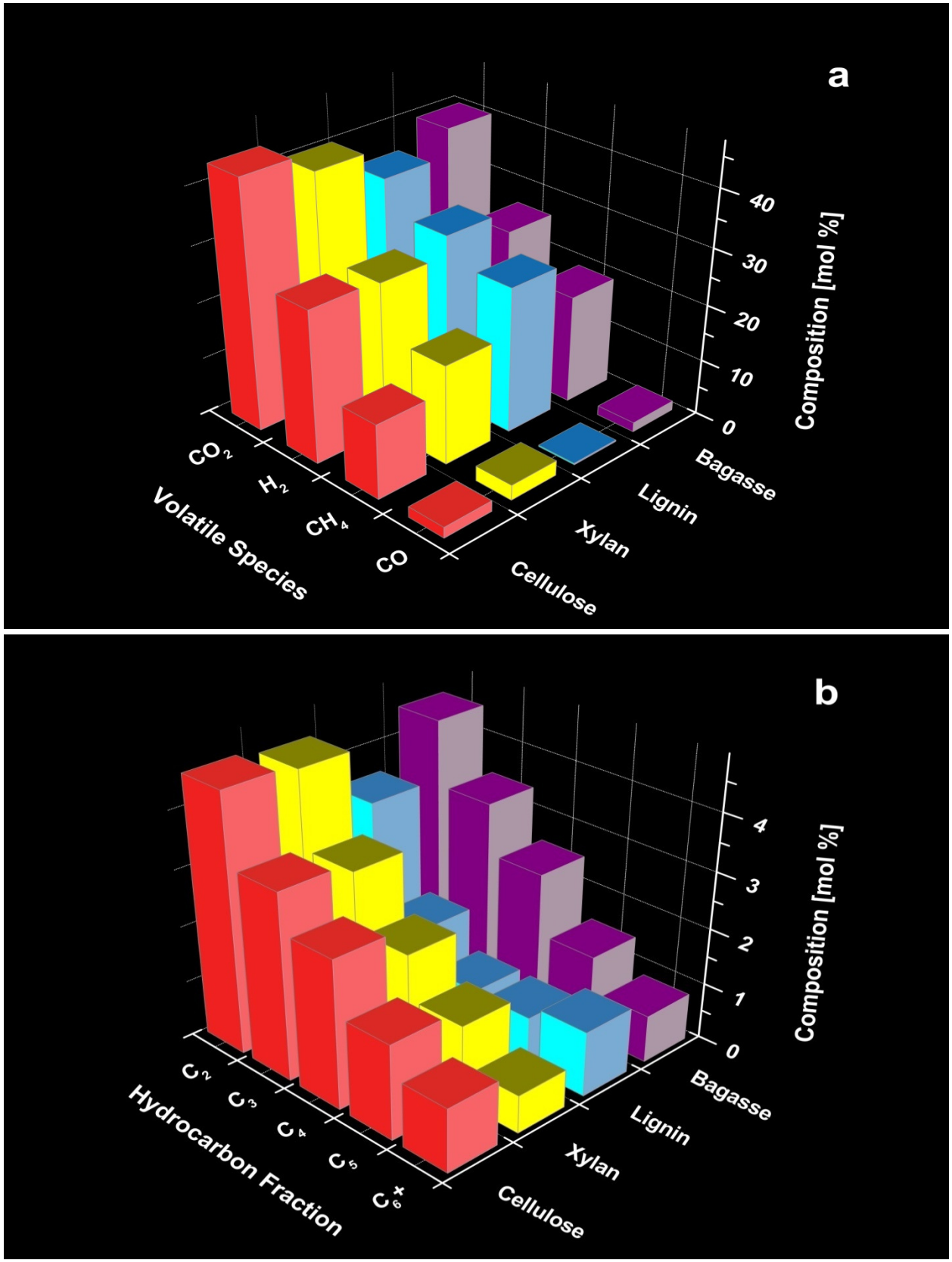

Figure 56. Volatiles composition for various model compounds and bagasse a) Fixed gases; b) C_2–C_6+ fraction.

4.7 Catalysts

4.7.1 Li/MgO

Lithium doped magnesite (Li/MgO) has been established as a successful catalyst for both oxidative coupling of methane and oxidative dehydrogenation [330-333]. Furthermore, Li/MgO also actively catalyzes the WGS reaction. Keiski *et al*. [334] studied the catalysis of water/CO mixtures using various catalysts, including Li/MgO. They demonstrated that increasing the amount of water relative to the amount of CO increased the conversion yields of CO. For Li/MgO, at a reaction temperature of 480 °C, the highest water to CO molar ratio used was 10:1, corresponding to a CO conversion of 99.87%. Based on these studies, Li/MgO was chosen as a suitable catalyst for converting methane, ethane, and propane in the hydrothermal product gas to ethylene and propylene.

A Li/MgO catalyst containing 3 wt % Li was prepared according to the procedure given in Chapter 2. A total of 0.299 g of Li/MgO was added to 1.42 g of dry bagasse for a catalyst loading of 21 wt %. In Table 26, the overall mass balances and reaction conditions are provided for bagasse hydrothermal conversion runs performed with assorted catalysts and reductants. A very high level of biomass conversion (91.9 wt %) is obtained when Li/MgO is added to the system. The hydrothermal conversion of bagasse using Li/MgO exceeds the conversion of bagasse in the uncatalyzed baseline run by more than 10 wt %. The Li/MgO catalyzed run reaches a substrate conversion level of 95.9 wt % when adjusting for the ash content present in the bagasse. The gasification efficiency of a catalyst can also be gauged in terms of the volatile yield per gram catalyst used. A total of 1.75 g of volatiles was produced for every 1 g of Li/MgO used. There was a 4.1% reduction in the HHV of the volatiles derived from the Li/MgO catalyzed run versus that of the uncatalyzed baseline run.

Table 26. Overall mass balances and volatile higher heating values from the hydrothermal conversion of bagasse performed using various catalysts and reductants.

Catalyst/ Reductant	Catalyst Amount [g]	T [°C]	P_{max} [bar]	ρ [g·cm^{-3}]	RT [min]	Liquids [wt %]	Solids [wt %]	Gases [wt %]	Conversion [wt %]	Gas HHV [MJ·kg^{-1}]
Li/MgO	0.299	500	729	0.422	5	98.58	0.31	1.42	91.9	52.16
MnO_2 (1)[28]	0.398	500	703	0.408	5	97.63	0.31	1.06	89.4	53.38
MnO_2 (2)[29]	0.398	500	730	0.423	5	97.45	0.41	1.07	91.9	51.31
CO	0.174	500	713	0.413	5	94.28	0.61	1.24	84.3	42.30
$NaBH_4$	0.100	500	788	0.452	5	96.56	0.19	1.65	95.0	64.02
None	None	500	707	0.410	5	97.18	0.71	1.36	81.5	54.38

Catalyst influence on the total product composition from bagasse hydrothermolysis is depicted in Figure 57. The addition of Li/MgO to the system increases the production of semi-volatiles by 18.9% over that from uncatalyzed bagasse. Li/MgO has little effect on gas production, with an increase of 4.6 wt % over the uncatalyzed baseline run. The formation of solid residue was curtailed by 56.3% when Li/MgO is used. The substantial decrease in char production indicates that the Li/MgO catalyst promotes cracking and reforming of the larger organic molecules. It is possible that hydrogen abstraction from these larger molecules may produce radicals that could react to form some of the olefins seen in the C_3 and C_4 fractions. Conceivably, the catalyst could bind with surface sites on the biomass particle and, thereby, act to lower the resistance to mass transfer within the particle bulk. The larger uptick seen in semi-volatiles generation than in volatiles production may imply that the additional volatiles formation occurs via secondary cracking reactions among the intermediate semi-volatile compounds rather than directly from biomass gasification reactions or C-C bond cleavage of the solid residues.

[28] Repetition 1
[29] Repetition 2

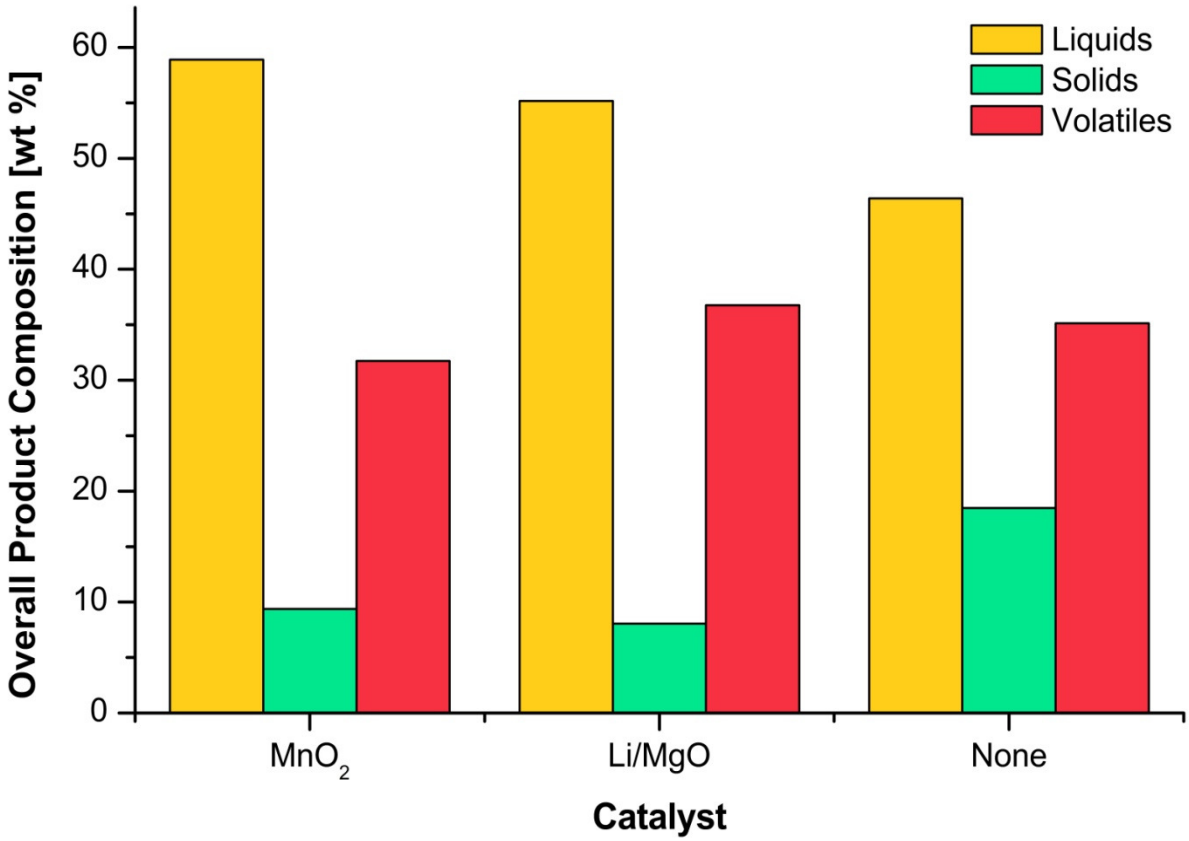

Figure 57. Catalyst influence on overall product distribution from bagasse hydrothermolysis.

The weight yields of the non-hydrocarbon (i.e., H_2, CO, and CO_2) and hydrocarbon volatile fractions for the run containing Li/MgO are supplied in Figures 58a and 58b, respectively. There is a minimal decrease in H_2 yield (2.6%), a relatively steep decline in CO production (40.8%), and an increase in CO_2 formation (9.6%) when the Li/MgO run is contrasted with the uncatalyzed run. A comparison of the hydrocarbon production from the Li/MgO run versus the uncatalyzed run reveals that the fractional yields from the Li/MgO run are between 12.6% (C_2) to 35.8% (C_6+) higher than for the respective fractions in the uncatalyzed run. The dashed curve provided in Figure 58b plainly illustrates that Li/MgO has a greater selectivity toward C_3 hydrocarbons than C_2 hydrocarbons. The unselective nature of the uncatalyzed bagasse run is manifest in the nearly straight run between the C_2 to C_4 fractions.

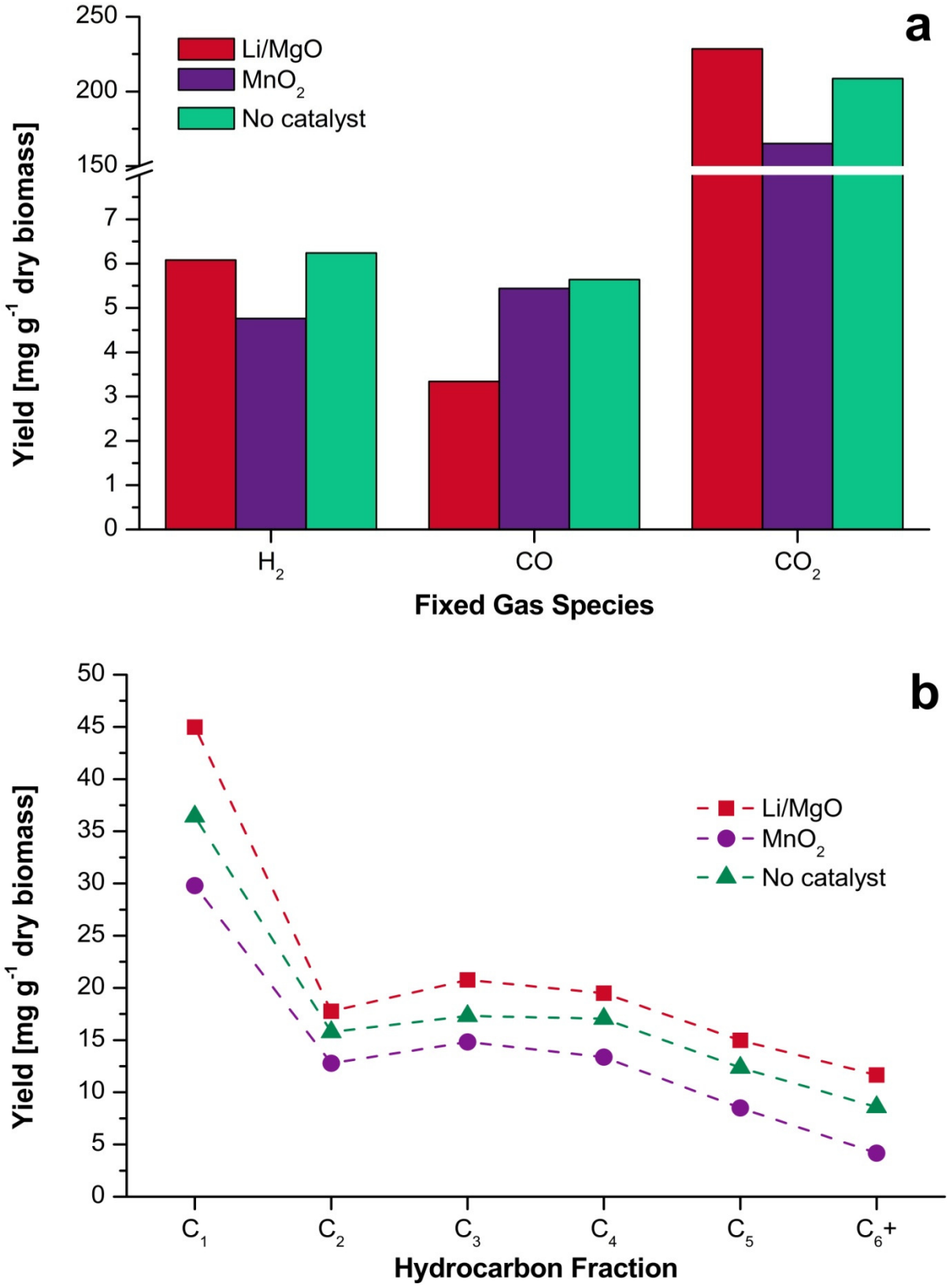

Figure 58. Volatile mass yields as a function of catalyst a) Non-hydrocarbon species; b) C_1–C_6+ fraction.

The distribution of the gaseous products obtained from the experimental run using Li/MgO can be observed in Figure 59. In Figure 59a, the level of CO_2 production is nearly identical to that of the uncatalyzed run, however, the yield of H_2 is 2.83 mol % lower than that of the uncatalyzed run, while the yield of CH_4 is 2.51 mol % higher than in the uncatalyzed run. The mole fraction of CO (0.93 mol %) using the Li/MgO catalyst is 45% lower than in the run with no catalyst. The extremely low mole fraction of CO is attributed to the catalytic role that Li/MgO plays in the WGS reaction. This ignores the fact that the H_2 yield is significantly lower than that of the uncatalyzed run. The additional hydrogen generated by the catalytic promotion of the WGS reaction may have been consumed in one of the pyrolysis methanation reactions (Eqns. 1 and 2), thereby accounting for its drop in relation to that of the uncatalyzed run. The decreased mole fraction of H_2 obtained using the Li/MgO catalyst may actually be attributable to the use of the Li dopant. It is possible that lithium reacted with hydrogen in the form of hydroxyl radicals to yield lithium hydroxide (LiOH). Thus, more atomic hydrogen would be sequestered in the semi-volatile phase. A check of the pH values in Table 27 for the aqueous semi-volatile product from the run containing Li/MgO reveals that a slightly basic bio-oil was indeed formed. Further testing is required to determine whether the increased basicity of the aqueous phase is a result of the presence of LiOH or if it is because of the presence of magnesium hydroxide ($Mg(OH)_2$). The existence of the latter in large quantities is unlikely given that the level of H_2 from the Li/MgO did not drop sharply.

The C_2–C_6+ fraction distribution for the Li/MgO catalyst run is displayed in Figure 59b. Every hydrocarbon fraction is consistently higher than the counterpart fraction generated in the absence of Li/MgO catalyst. The mole fraction of the C_3, C_4, and C_5 hydrocarbons from the Li/MgO run exceeded those from the non-catalyzed run by 10, 11, and 25%, respectively.

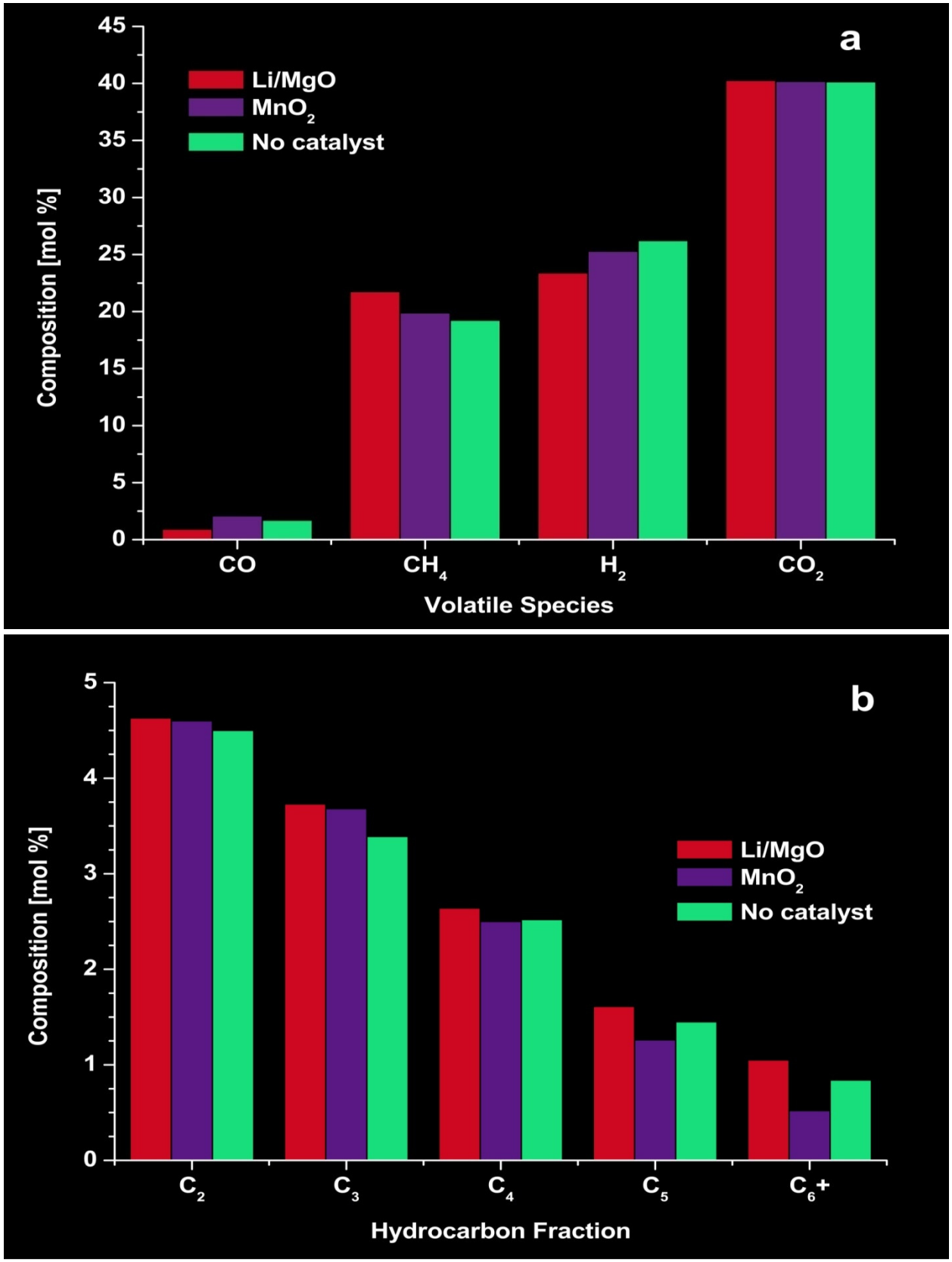

Figure 59. Catalyst influence on volatiles distribution a) Fixed gas species; b) C_2–C_6+ hydrocarbon fraction.

Table 27. pH of aqueous bio-oil fraction from bagasse hydrothermal runs[30].

Temperature [°C]	pH	Time [min]	pH	Additive	pH
300	3.22 (σ = ± 0.04)	1	4.03	$NaBH_4$	7.67 (σ = ± 0.35)
400	3.65 (σ = ± 0.00)	5	4.15 (σ = ± 0.01)	CO	4.12
500	4.15 (σ = ± 0.01)	10	4.25	MnO_2	6.96 (σ = ± 0.11)
600	5.06			Li/MgO	7.60
				Ti bomb	3.85

Analysis of the ratios of alkanes to olefins in the individual hydrocarbon fractions sheds further light on the catalytic nature of Li/MgO. Table 28 details the weight partition between paraffins and olefins for the C_2–C_4 fractions for Li/MgO, MnO_2, and a standard run performed with no catalyst. The ethane/ethylene ratio is constant irrespective of the usage of Li/MgO. Therefore, Li/MgO is not selective to the formation of ethylene. Table 28 shows that the share of propylene in the C_3 fraction rises by 6 wt % when Li/MgO is added to the run. This finding indicates that Li/MgO in supercritical water is able to activate propane to form propyl radicals via an oxidative dehydrogenation step.

Table 28. Comparison of olefin versus paraffin yields for catalyst runs as percent of C_x.

Catalyst	C_2H_4	C_2H_6	C_3H_6	C_3H_8	C_4 olefins	C_4 paraffins
LiMgO	16	84	48	52	28	72
MnO_2	18	82	49	51	28	72
No Catalyst	16	84	42	58	25	75

The effect of various additives on the CE and GE of bagasse hydrothermal conversion is illustrated in Figure 60. The use of Li/MgO as a catalyst improves the GE for bagasse HT by 4.7%. A 3.1% increase in CE occurs when Li/MgO is added to the bagasse slurry.

[30] All runs were performed using the standard, baseline conditions other than the free variable listed

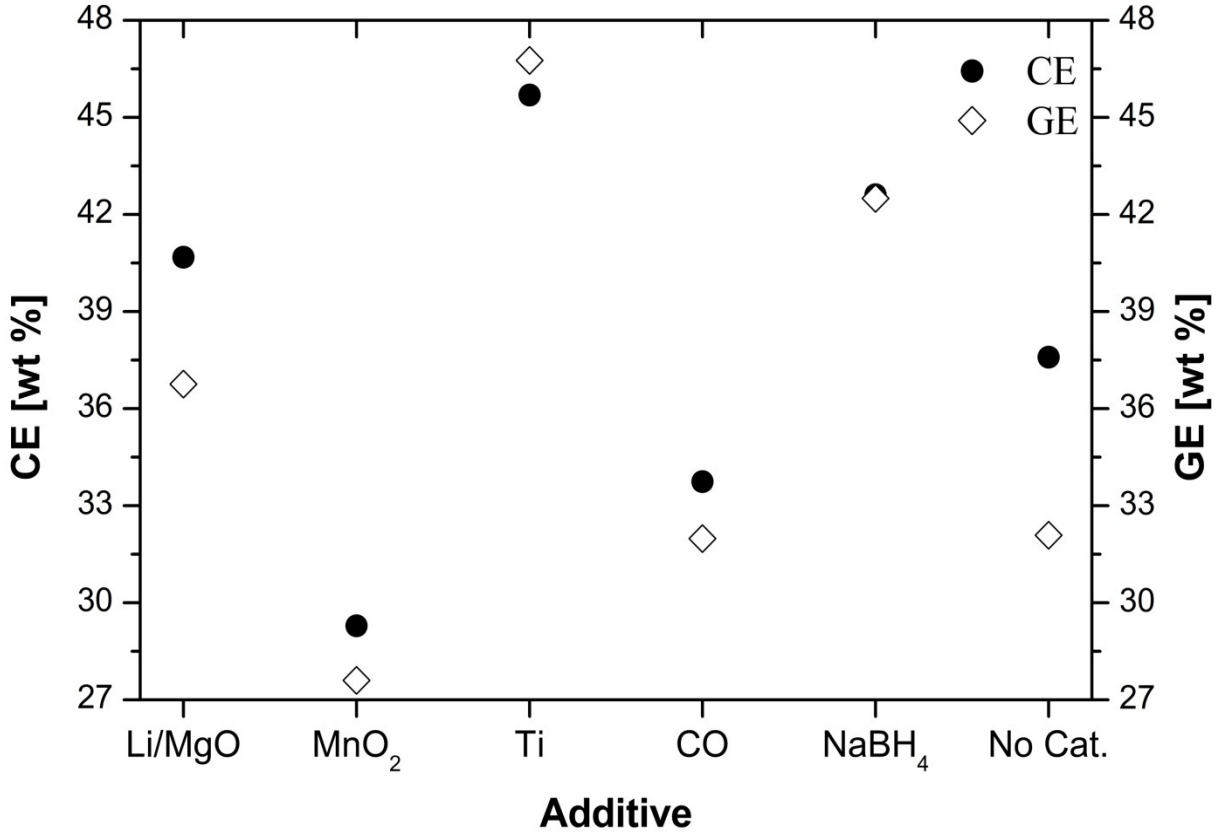

Figure 60. Change in CE and GE with respect to additives or reactor wall metal.

4.7.2 MnO_2

The influence of MnO_2 on the hydrothermolysis of bagasse was explored using two independent runs that were both conducted with identical catalyst weight loadings as listed in Table 26. The agreement in the overall mass balances obtained from the individual runs is another indicator of the experimental repeatability of the current hydrothermal system configuration. The mean conversion of bagasse is 90.7 wt % when MnO_2 is added to the bagasse slurry. This conversion level is more than 9 wt % higher than that of uncatalyzed bagasse and statistically equivalent to the conversion level acquired through the use of the Li/MgO catalyst. Adjustment for the ash content in bagasse increases the average conversion level for the MnO_2-catalyzed runs to 94.7 wt %.

The influence of MnO_2 on the overall product composition derived from the SCW treatment of bagasse is given in Figure 57. The total production of solids using MnO_2 is on average 49% lower than for that of an uncatalyzed run, while the level of gas production dips 9.6% in comparison to that of the run with no catalyst. Formation of semi-volatiles climbs 27% when MnO_2 is added to the baseline run.

The molar distribution of fixed gases from the first replicate run containing MnO_2 is depicted in Figure 59a. Apart from the 22.4 % increase in the mole fraction of CO observed in the MnO_2 run with respect to that in the uncatalyzed run, the compositional variation in the light gas fractions obtained from the MnO_2 and uncatalyzed base runs is insignificant. In comparison with the uncatalyzed run, the mole fraction of CH_4 increases 3.4%, the mole fraction of H_2 decreases 3.6%, and there is no difference in the CO_2 mole fraction for the MnO_2 run. Despite the lackluster change in the molar fraction of the permanent gases (except CO) when using MnO_2, this evidence was encouraging because it implied that more of the methane was oxidatively dehydrogenated to C_2 and C_3 fractions rather than being converted to H_2 and CO_2. Confirmation of this assumption is offered in Figure 59b, where it can be seen that the molar fraction of C_2's and C_3's from the MnO_2 run are 2.2 and 8.6% higher, respectively, than those from the uncatalyzed run. C_4 molar fractions obtained using MnO_2 and without using MnO_2 are almost identical. The C_5 and C_6+ fractions from the MnO_2 run are 13.1 and 38.1% lower, respectively, than those obtained using no catalyst. Paraffin to olefin proportions based on weight yields for the $C_2 - C_4$ fractions from the first MnO_2 run are provided in Table 28. A comparison with the uncatalyzed baseline run reveals that MnO_2 does have some selectivity for C_2H_4 at 500 °C. However, MnO_2 has the highest selectivity toward the formation of C_3H_6 as can be seen in Table 28, where there is nearly an equal weight fraction of both C_3H_6 and C_3H_8 and

nearly 7 wt % more C_3H_6 is formed than in the case of the uncatalyzed run. Finally, the use of MnO_2 leads to an additional 3 wt % of unsaturated C_4 hydrocarbons when contrasted with the base run containing no catalyst, as shown in Table 28.

4.8 Reductants

4.8.1 CO

To determine the influence of CO on the hydrothermal conversion of bagasse an experiment was conducted similar to the standard baseline run at 500 °C, except that the He used in the standard testing procedure was replaced with CO. After sealing the bomb, it was flushed with CO five times and finally pressurized to 7.221 bar abs., corresponding to an initial charge of 173.7 mg CO. The mass yields of the individual volatile species from the CO hydrothermal experiment are shown in Figure 61. The mass yields of H_2, CH_4, and CO_2 from the CO reductant run are 40, 47, and 43 % lower, respectively, than for the yields of the same components from the baseline hydrothermal run. The fixed gas product also contained 141 mg CO, which is 16.6 times higher than when CO is added as a reductant. The HHV of the volatiles evolved during the CO run is 42.30 $MJ \cdot kg^{-1}$ (see Table 26). This value is 22.2% lower than the HHV of volatiles obtained from an uncatalyzed, baseline hydrothermal experiment. The mass yields of the C_2–C_5 gas fractions from the CO run are an average of 34.7% ($\sigma = \pm$ 0.81%) lower than the respective fractions from the uncatalyzed run. The mass yield of the C_6+ fraction from the CO run is 27.7% less than that from the uncatalyzed run.

The use of CO as a reductant increases the mass yield of organic semi-volatiles from bagasse by 5.9 wt %. Likewise, the mass yields of volatiles and solids decrease by 3.1 and 2.8 wt %, respectively, when CO is used in the bagasse hydrothermal system.

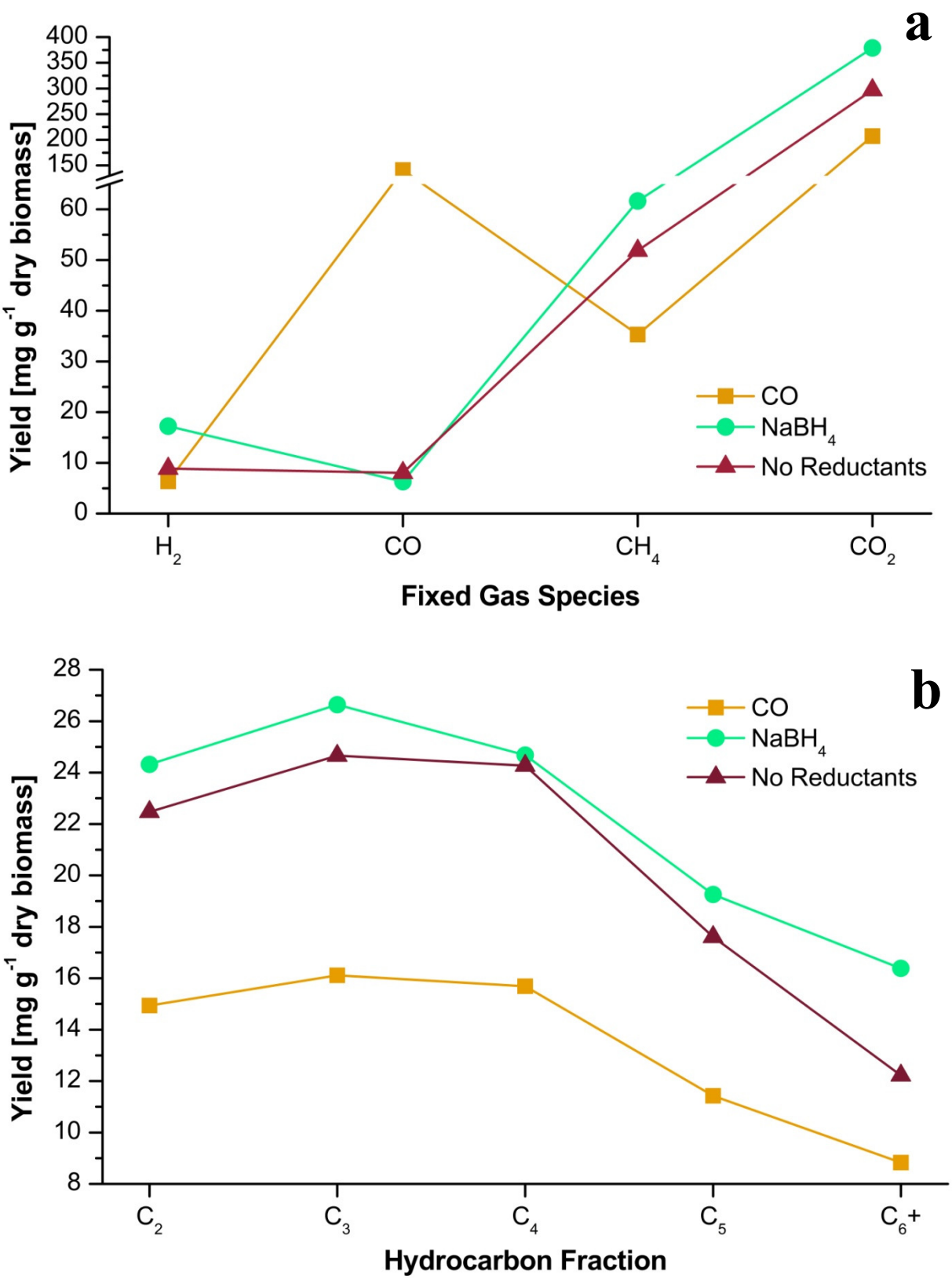

Figure 61. Volatile mass yields as a function of reductant a) Fixed gas species; b) C_2–C_6+ fraction.

In Figure 64, the distribution of volatile products obtained from CO is shown in relation to the distribution of gases obtained from a typical bagasse run at 500 °C under a He blanket. The most striking feature in Figure 64a is the difference in the CO levels; the hydrothermal run conducted under an inert environment generated only 1.7 mol % CO, whereas the run performed in a reducing atmosphere generated 30.5 mol % CO (i.e., on a corrected basis for initial CO charge). It is equally important to note the decreases in CH_4 (19.2 to 13.3 mol %), H_2 (26.2 to 19.1 mol %), and CO_2 (40.1 to 28.5 mol %) mole fraction when switching from an inert to a reductive atmosphere. Figure 64b compares the distributions of the hydrocarbon fractions obtained from bagasse that was reacted both in the presence and absence of CO. Interestingly, the C_2–C_5 fractions obtained from the inert run with He are all produced with exactly 50% greater abundance than those acquired from the reductive run with CO. The mole fraction of the C_6 fraction obtained from the inert run, however, is only 36% higher than that obtained from the reductive run.

4.8.2 $NaBH_4$

Originally a 1.0 g quantity of $NaBH_4$ was sealed inside a glass ampoule placed inside the bomb along with the typical 1:25 weight loading of bagasse to water. The bomb was then purged with He and pressurized to 5.001 bar before being reacted for 5 min at 500 °C. The final pressure in the bomb at SATP was 32.0161 bar. Unfortunately, an accurate quantitation of the H_2 gas generated from this experiment was rendered impossible because the amount of H_2 evolved exceeded the linear operating range for the GC-HID. The H_2 clearly overloaded the micro-packed column as can be seen by the split peak in Figure 62a, which is a typical feature

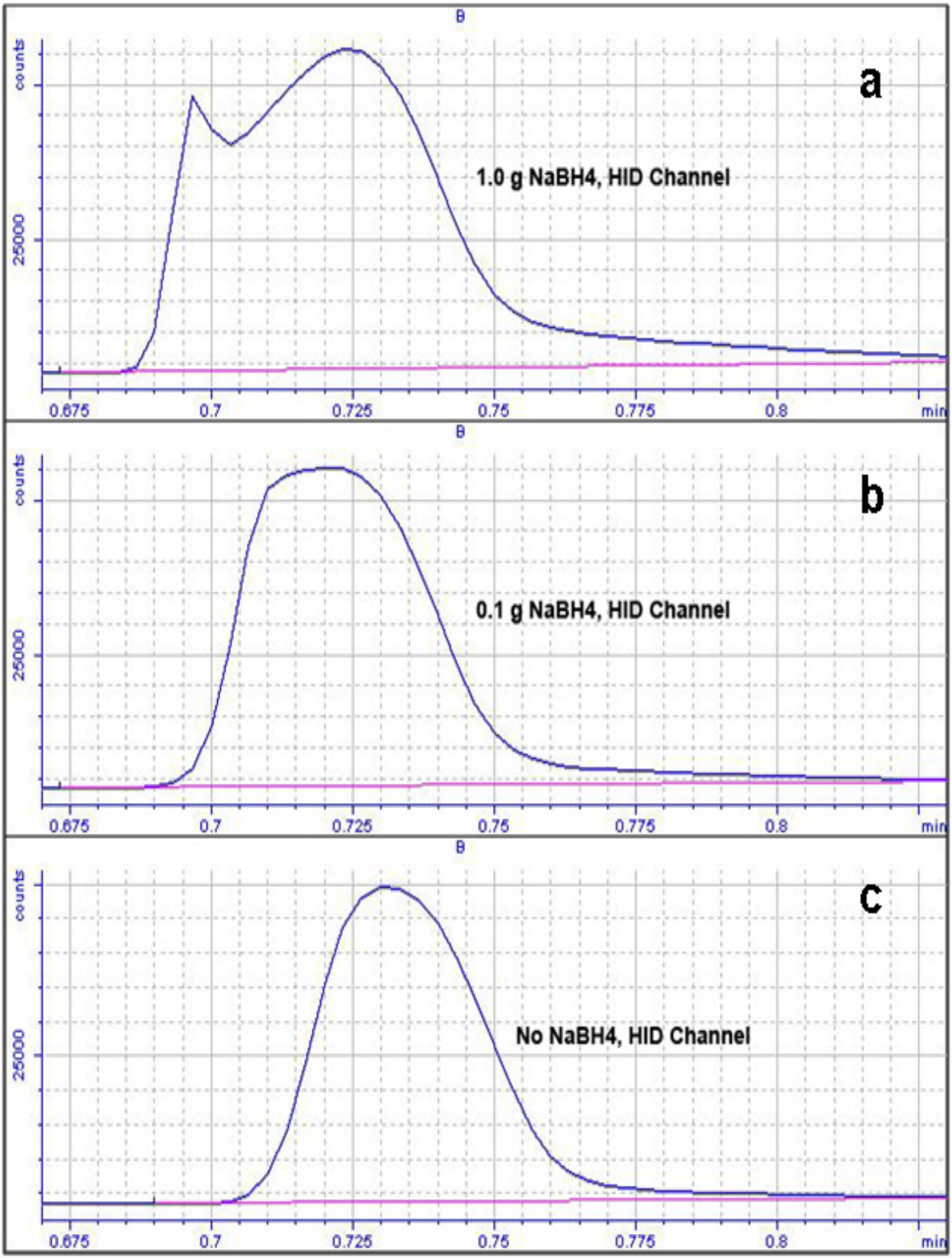

Figure 62. Hydrogen peak in the volatile products detected by GC-FID for hydrothermal runs containing a) 1.0 g $NaBH_4$; b) 0.1 g $NaBH_4$; c) No $NaBH_4$.

To avoid further chromatographic detection complications it was decided to sharply lower the amount of $NaBH_4$ to 0.1 g. This run was performed identically to the first $NaBH_4$ run, with an initial He charge pressure of 5.903 bar and 1.43 g of bagasse to give a 7 wt % loading of $NaBH_4$. It is relevant to note that the melting point of $NaBH_4$ occurs at 505 °C. Based on the average 2.15% maximum upper hysteresis of the furnace setpoint temperature, it is conceivable that the $NaBH_4$ also existed in the liquid state during the experiment. Shortly after the bomb was lowered into the furnace, the glass ampoule burst releasing the $NaBH_4$ into the bagasse slurry as evidenced by the much steeper rise in the pressure slope compared to that of a standard run conducted at 500 °C with no $NaBH_4$, as recorded on the pressure plot shown in Figure 63.

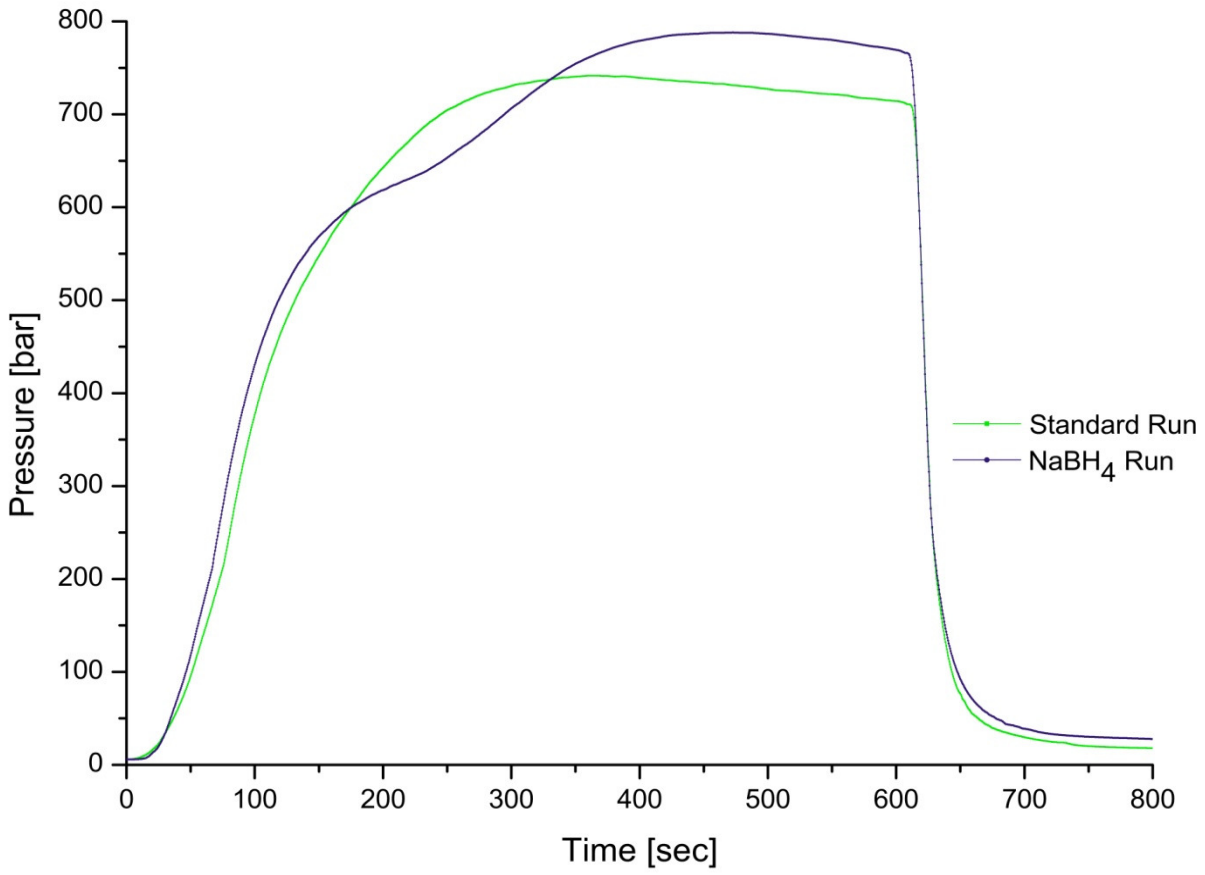

Figure 63. Rise in system pressure associated with the release of hydrogen from $NaBH_4$ compared with a standard run containing no $NaBH_4$.

Approximately 180 s into the run the rise of the slope declines indicating that all of the hydrogen from the $NaBH_4$ has been released into the system by this point. The final bomb pressure in this second run at SATP was 22.573 bar, which was 50% higher than the average final bomb pressure of 15.168 bar recorded for hydrothermal bagasse experiments conducted with no additives. The hydrogen peak obtained on the GC-HID from the volatile product from this second run with $NaBH_4$ is shown in Figure 62b. The flat plateau at the top of the hydrogen peak is indicative of detector saturation. The area under the curve can be used as a rough first approximation of the H_2 mole fraction, although by looking at the length of the plateau with respect to the peak shape it can be inferred that a substantial portion of the H_2 component was not recorded. The hydrogen peak shape obtained from a typical hydrothermal bagasse conversion run performed at 500 °C for 5 min residence time is shown in Figure 62c for comparison. Thus, the values of H_2 reported herein for the $NaBH_4$ run are extremely conservative and likely much lower than the true production levels of H_2.

The addition of sodium borohydride had an impressive impact on the distribution of solid, liquid, and volatile organic product yields. The production of organic semi-volatiles decreased by 14.4 wt % when reducing hydride was added to the HT run. Volatiles formation increased by nearly 74%, while the solids residue level fell by 73% when sodium borohydride was used as a reductant. These results indicate that the reducing hydrogen species likely acted upon both the liquid and solid intermediate compounds, besides the original carbohydrates contained in the bagasse substrate.

The distribution of gaseous species from the second $NaBH_4$ run is provided in Figure 64. In Figure 64a, it can be seen that there is an almost equimolar relationship between H_2 and CO_2, with mole fractions of 35.5 and 35.7 mol %, respectively. The mole fraction of CH_4 is 15.9 mol

%, or about half that of H_2 and CO_2. Finally, the mole fraction of CO is relatively low at 0.93 mol %. In contrast, the run conducted with no $NaBH_4$ has 20.7% more CH_4, 12.5% more CO_2, 82.8% more CO, and 26.0% less H_2. If the 2.64 mmol of hydrogen from the addition of 1.0 g of $NaBH_4$ are accounted for, then the revised product distribution for the $NaBH_4$ becomes: 27.5 mol % H_2, 1.0 mol % CO, 17.9 mol % CH_4, and 40.1 mol % of CO_2. Using these modified figures, the CO_2 levels between the two runs are identical and there is just 5% more hydrogen production in the $NaBH_4$ run than in the typical run without $NaBH_4$. The level of CH_4 production rises only 7.3 mol % in the $NaBH_4$-free run over that in the $NaBH_4$ run. In actuality, the H_2 production in the $NaBH_4$ run is undoubtedly much higher than that from the $NaBH_4$-free run because of the aforementioned usage of "low values" recorded by the GC-FID.

The molar distribution of the C_2–C_6+ fractions using $NaBH_4$, as shown in Figure 64b, is reminiscent of that for the CO reductant run. The run conducted without $NaBH_4$ has 32% more of the C_2, C_3, and C5 fractions, 41% more of the C_4 fraction, and just 7% more of the C_6+ fraction than the run containing $NaBH_4$. Similar to the CO run, the decrease in the C_6+ fraction obtained with the $NaBH_4$ run in relation to that from the run without $NaBH_4$ is substantially less than the differences for the other fractions. This finding again leads to the conclusion that the lighter volatiles are being consumed in reactions with the reductants or intermediary species generated via reactions with reductants. The higher fractions of C_6+ components in both the CO and $NaBH_4$ runs suggests that the reductants exhibit a diminished selectivity toward C_1-C_5 hydrocarbons and a higher selectivity toward volatile aromatics.

Unlike the CO reductant run, the run conducted with $NaBH_4$ produced a slightly basic aqueous semi-volatile product. The pH of the bio-oil fraction from $NaBH_4$ was determined to be 7.67, as shown in Table 27. It is speculated that the aqueous phase contains sodium hydroxide.

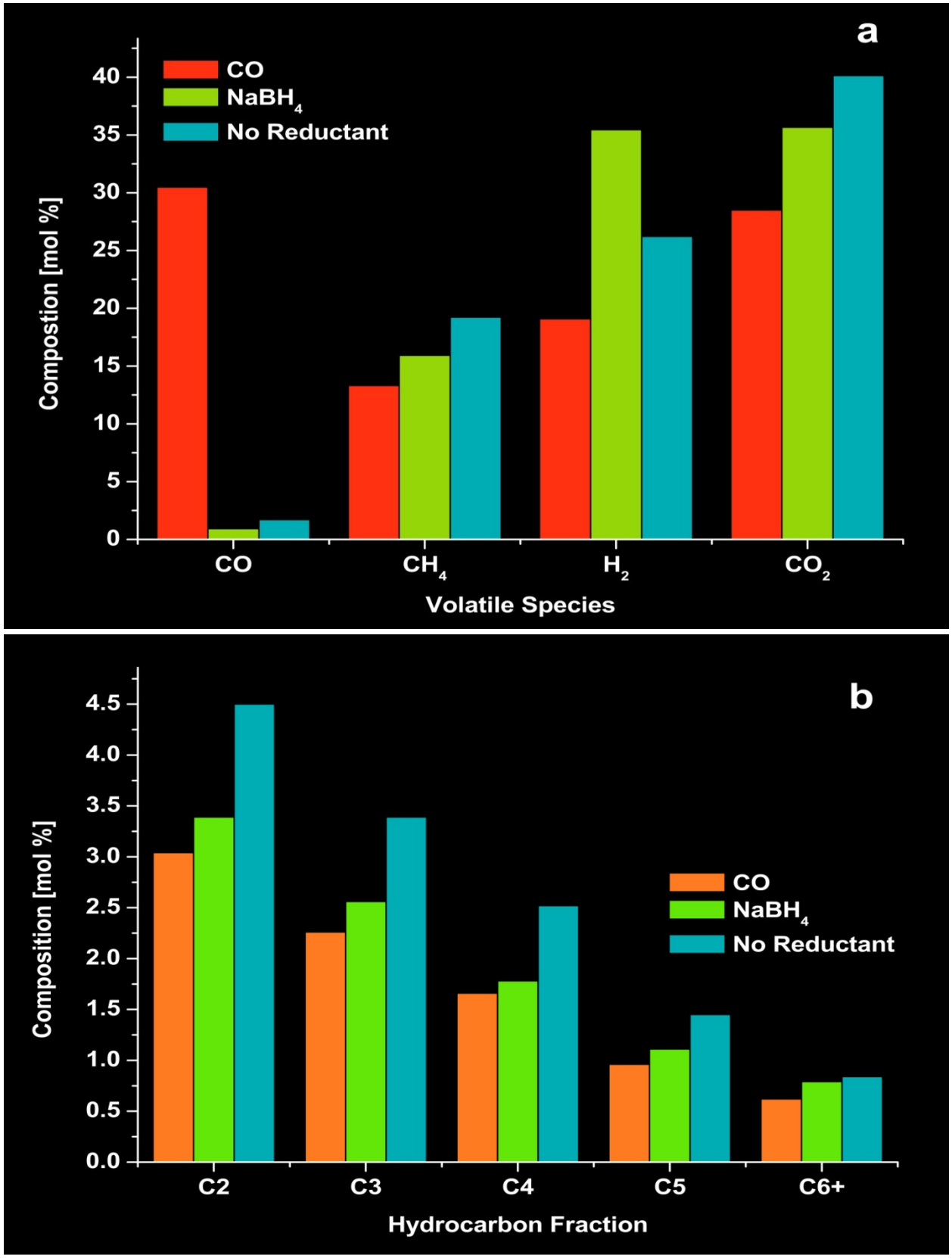

Figure 64. Reductant effect on volatiles distribution a) Fixed gas species; b) C_2–C_6+ hydrocarbon fraction.

4.9 Apparent Rate Kinetics

All kinetic rate experiments were carried out using the standard experimental conditions (i.e., 500 °C and 4 wt % bagasse loading) with reaction times ranging from 1 min to 60 min. As mentioned earlier, the reaction time is considered to be the duration that the bomb was at reaction temperature; it does not include the time required to reach reaction temperature, unless otherwise specified. No preliminary supposition was made regarding the overall reaction order for the bagasse degradation so as to avoid prejudicing the subsequent kinetic analysis. According to Essen's method [335], kinetic data can be analyzed by plotting either time versus $\ln([B]_0/[B]_t)$ for first-order reactions or time versus $\{([B]_0/[B]_t)^{n-1} - 1\}$ for n^{th}-order reactions and then determining which plot is the most linear. Initially, the concentration and time data were linearly regressed to integrated forms of the rate laws, shown in Table 29, using Essen's method. All possible rate orders from zero-order to fourth-order incremented by fractional half-orders were examined.

Table 29. Integrated rate laws for several reaction orders.

Reaction Order	Differential Equation	Integrated Equation
0	$-d[B]/dt = k$	$k = (1/t)([B]_0 - [B]_t)$
1	$-d[B]/dt = k[B]$	$k = (1/t)\ln([B]_0/[B]_t)$
2	$-d[B]/dt = k[B]^2$	$k = (1/t[B]_0)([B]_0/[B]_t - 1)$
3	$-d[B]/dt = k[B]^3$	$k = (1/2t([B]_0)^2)(([B]_0/[B]_t)^2 - 1)$
4	$-d[B]/dt = k[B]^3$	$k = (1/2t([B]_0)^3)(([B]_0/[B]_t)^3 - 1)$
n	$-d[B]/dt = k[B]^n$	$k = (1/t(n-1)([B]_0)^{n-1})(([B]_0/[B]_t)^{n-1} - 1)$

It was impossible to accurately ascertain the apparent overall reaction order from the Essen plots themselves because the fitted kinetic data appear reasonably linear in every rate model. Evaluation of the regression correlation coefficients was of limited utility in narrowing the field of potential apparent total rate order candidates. The first- and second-order rate models

had a decidedly higher goodness of fit than the other rate models, yet the similitude in the linearity of the first- and second-order Essen plots, as shown in Figure 65, combined with their nearly identical correlation coefficients (i.e., 0.9915 and 0.9932, respectively) prevented decisive discrimination between the first- and second-order rate possibilities.

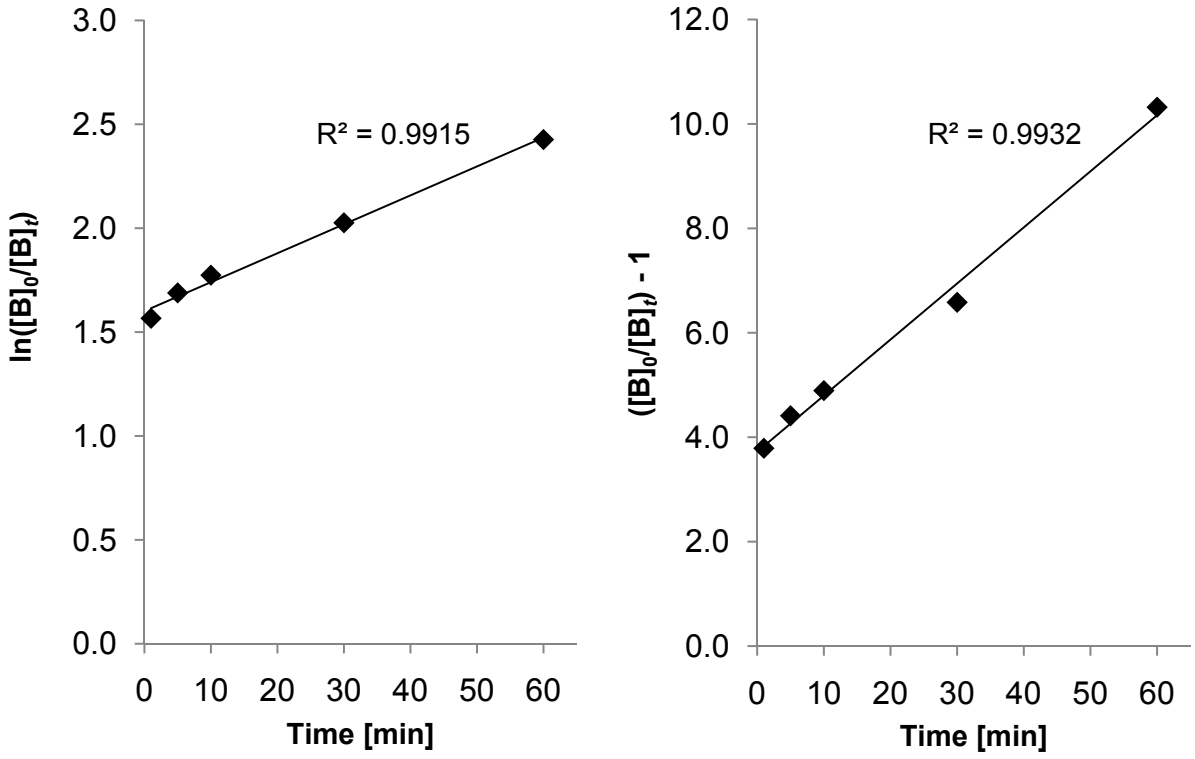

Figure 65. Essen plots for bagasse hydrothermal decomposition at 500 °C and a 4 wt % bagasse loading a) 1st order reaction kinetics; b) 2nd order reaction kinetics.

As an aside, it should be noted that minor differences in correlation coefficients calculated for different rate models are "rarely meaningful" because "each correlation coefficient is calculated using a different model" [335]. Nevertheless, this point is often overlooked in literature where assertions are routinely made that mistakenly claim "a rate equation fits better because the regression coefficient is closer to 1.0." Claiming that the bagasse hydrothermal reaction process follows an apparent overall second-order rate dependence would have been a reckless declaration, especially considering that an analysis of variance of the error in the slopes of the first- and second-order rate curves indicated that the first-order rate model has a variance

of 0.000249, while the second-order rate model has a variance of 0.001713. A subsequent F-test on the statistical significance of the difference in variances of slope error revealed that we can be between 90 and 95% confident that the first-order model fits the experimental data better than the second-order model. This confidence level resides outside the conventionally acceptable 5% rejection region and, therefore, this finding cannot be used to buttress the argument that the hydrothermal process unequivocally follows pseudo first-order kinetics.

The Levenberg-Marquardt (LM) algorithm is an iterative technique that is commonly used to solve nonlinear least-squares minimization problems. When the results are far from the minimum, the LM algorithm uses the method of steepest descent to adjust step sizes. As the solution approaches the minimum, the LM algorithm utilizes the Hessian matrix method to establish step sizes. The first- and second-order nonlinear curves resulting from the application of the LM algorithm to the bagasse hydrothermal kinetic data are compared in Figure 66.

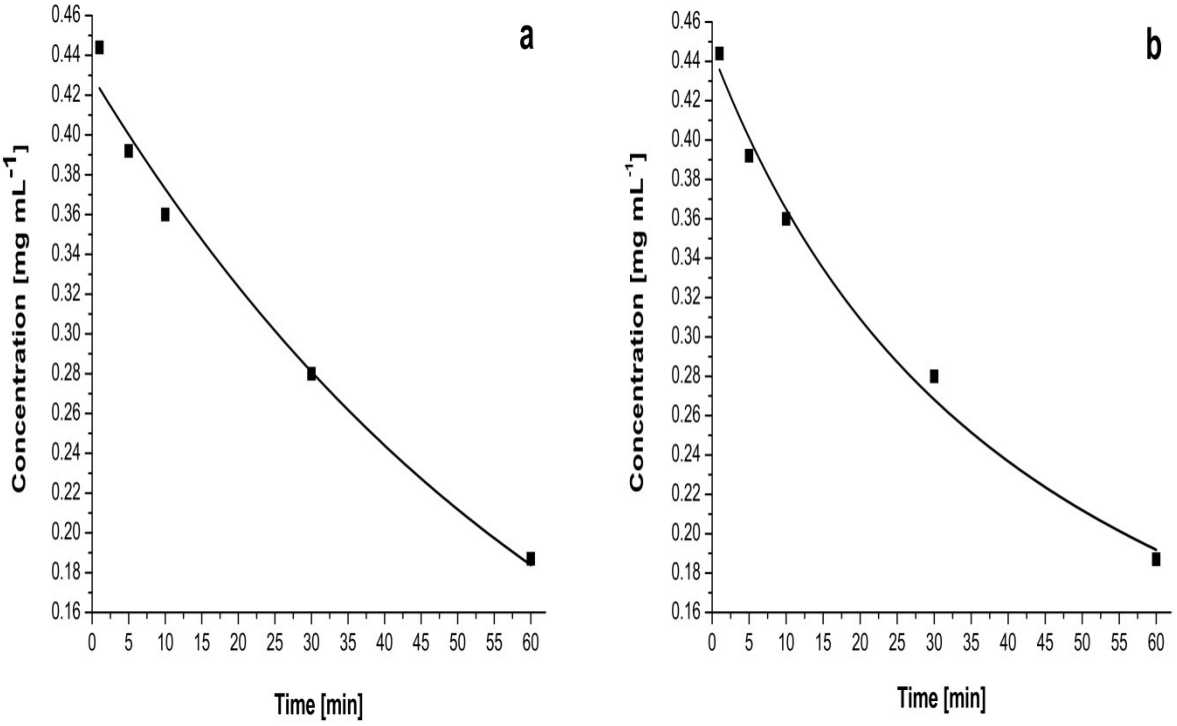

Figure 66. Levenberg-Marquardt nonlinear least-squares curve fit to bagasse hydrothermal kinetic data assuming a) 1st order reaction kinetics; b) 2nd order reaction kinetics.

From Figure 66, it can be seen that the second-order nonlinear curve more closely approximates the actual behavior of the early kinetic measurements than does the first-order nonlinear curve. The R^2 value for the second-order nonlinear model is 0.9928, which is marginally higher than the R^2 value of 0.9889 for the first-order nonlinear model. It was hypothesized that omission of the concentration datum at 1 min could shed more light on the apparent reaction kinetics. When the LM algorithm was reapplied to the remaining four experimental data points, the coefficient of determination for the first-order nonlinear model (i.e., 0.9990) slightly outperforms that of the second-order nonlinear model (i.e., 0.9926). This observation clearly demonstrated that the overall kinetic reaction rate for the hydrothermal dissolution of bagasse cannot be described in terms of a single, simple apparent rate order.

Steinfeld *et al*. [336] noted that "there are no known examples of fourth-, fifth-, or higher order reactions in the chemical literature. The highest order which has been empirically encountered for chemical reactions is third order." Hence, it may seem preposterous to suggest that the apparent reaction kinetics for bagasse hydrothermolysis are described by a 5^{th} order or higher rate process during the first 30 minutes. Nevertheless, rate orders of this magnitude are not without precedence in biomass studies. Recently, it was observed that Cr fixation in aspen wood treated with chromated copper arsenate (CCA) at 30 °C follows reaction kinetics that are higher than 4^{th} order during the first hour [337].

The kinetic modeling of complex processes, such as biomass hydrothermolysis reactions, requires the identification of all possible reaction steps, without which the modeling exercise essentially becomes phenomenological. It is generally accepted that kinetic parameters derived for complex systems are devoid of any mechanistic relevance and are beholden to the scope of experimental conditions employed for a particular process [338]. Consequently, the scientific

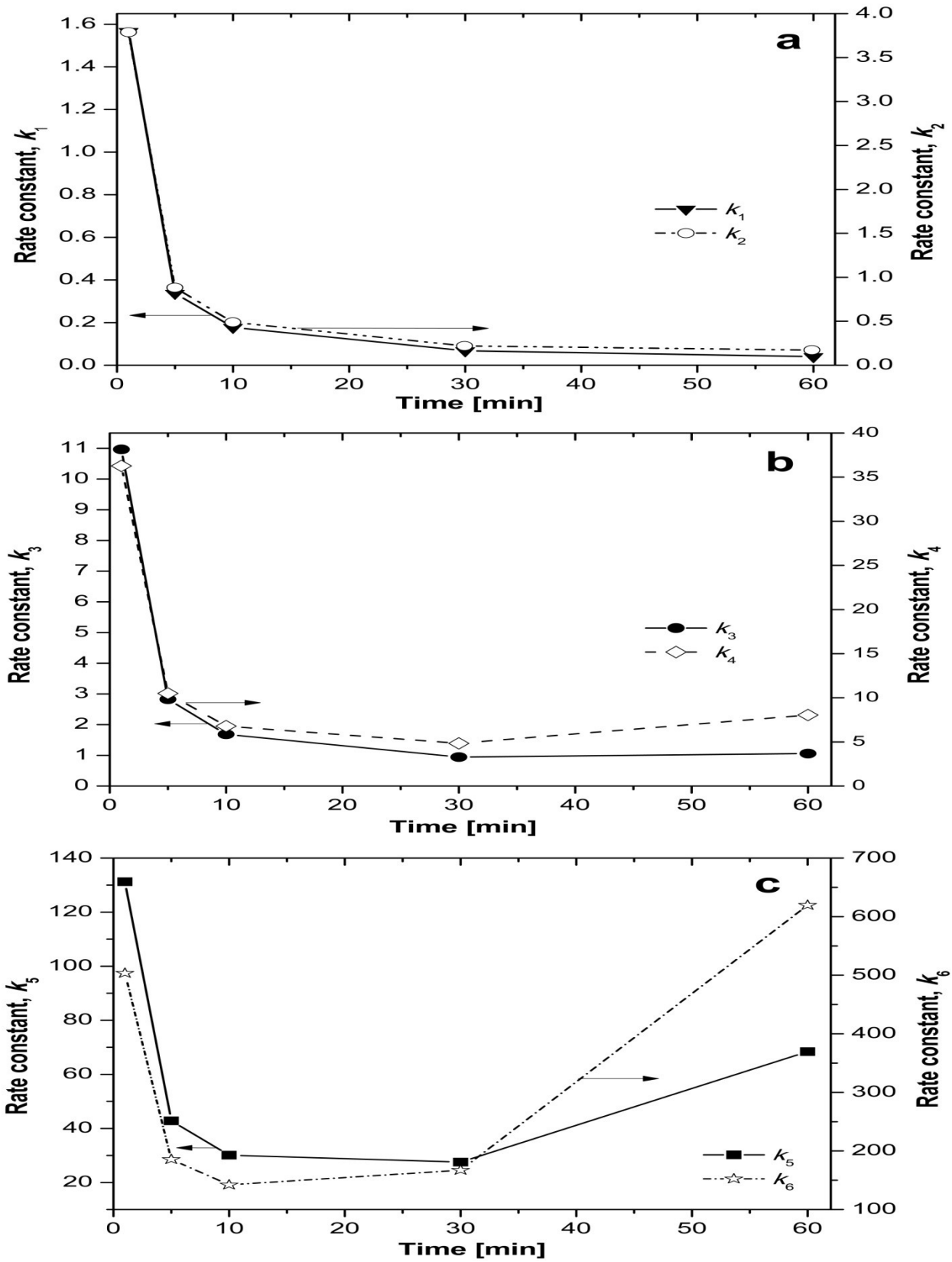

Figure 67. Van't Hoff plots for bagasse hydrothermolysis at 500 °C and 4 wt % bagasse loading a) k_1 vs. k_2; b) k_3 vs. k_4; c) k_5 vs. k_6.

community has long sought to develop a single parameter that can be used to represent the effects of different operational variables and, thereby, enable comparison of different complex reaction systems. In 1930, Geniesse and Reuter [339] proposed a simple function correlating the effects of temperature and time on the yields of volatiles and gasoline from the cracking of oil. The time-temperature cracking index (*CI*) they used can be expressed as:

$$CI = 2^{\left(\frac{T_c - 480}{17}\right)t} \tag{46}$$

in which T_c is the cracking temperature (°C) and t is the time (min). The previous relationship mathematically represents a reaction rate that increases by a factor of 1.503 for every 17 °C rise in temperature. Since the development of the *CI* index, many researchers have endeavored to devise similar empirical functions that correlate the effectiveness of biomass pretreatment methods with the treatment severity [50, 340-342]. Almost all of the severity functions incorporate the effects of temperature and time into a single factor. The severity factor enjoying the widest appeal among biomass researchers was put forth by Overend and Chornet in 1987 [50] and is known as the "reaction ordinate," R_o:

$$R_o = \tau \exp\left[\frac{\left(T_r - T_b\right)}{\varphi}\right] \tag{47}$$

where T_r is the absolute reaction temperature, T_b is a base temperature, usually set to 373.15 K, τ represents the entire time interval in minutes for which T_r exceeds T_b, and φ is a severity parameter having units of K. According to Chum and coworkers [343], the severity parameter φ should be "determined experimentally," yet frequently in biomass pretreatment studies φ is arbitrarily set to 14.75, even though this may not be the optimum value. Specifying a value of 14.75 for φ implies that reactions adhering to Eqn. 46 will have a reaction rate that increases by a factor of 1.970 for every 10 °C rise in temperature; this is nearly equivalent to the oft-repeated

rule of thumb embodied by the Arrhenius law, wherein the reaction rate approximately doubles for every 10 °C increase in temperature [344]. Overend and Chornet [50] clarified that the reaction ordinate expression in Eqn. 47 "[implicitly assumes] that the overall kinetics follow a first-law concentration dependence and that the rate constant has an Arrhenius-type dependence on temperature, although the apparent activation energy may itself be a function of temperature." It was later demonstrated by Chum *et al*. [343] that R_o is indeed related to the activation energy via the severity parameter, φ:

$$\varphi = \frac{RT_f^2}{E_a} \tag{48}$$

where T_f is a "floor" temperature (K) representing the "middle of the range of experimental conditions." Incorporation of the floor temperature in Eqn. 48 helps to mitigate the error observed in the "reaction ordinate approximation" to the actual Arrhenius first-order rate expression over larger experimental temperature ranges. The linearized first-order rate law given subsequently in Eqn. 74 can be expressed in terms of the severity parameter as shown here:

$$\ln\left[-\ln\left(1-\alpha\right)\right] = \ln A - \frac{E_a}{RT_r} + \ln\left(R_o\right) - \left[\frac{\left(T_r - T_f\right)}{\varphi}\right] \tag{49}$$

where ln *t* provided subsequently in Eqn. 77 is equal to the latter two terms in Eqn. 49. It is advisable to utilize a correction to the reaction ordinate when very large temperature ranges are employed:

(50)

Transforming Eqn. 49 into the linear form, $Y = mX + B$, allows the kinetic data to be fitted using linear least squares, where $Y = \ln[-\ln(1-\alpha)]$ and $X = \ln(R_o) = \ln t + (T_r - T_f)/\varphi$. The derived slope is denoted by m and the intercept value, B, is given by the term $\{\ln A - (E_a/RT_r) - [(T_r - T_f)/\varphi]\}$. The term X is designated by the quantity $\ln(R_o)_{corr}$ when the corrected reaction ordinate function is used. The simplex optimization routine built into Microsoft EXCEL Solver [345] was used to identify the best value of the severity parameter, φ, based upon the computed value of E_a that maximized the coefficient of determination.

The Arrhenius parameters and reaction rate constants obtained using the procedure outlined above are given in Table 30. It can be seen that the nature of the water can dramatically alter the rate of reaction. For instance, the difference in the reaction rate constant upon going from a subcritical to a near-critical environment is about 4 orders of magnitude. The reaction rate constant increases by an additional 2 orders of magnitude when going from near-critical conditions at 400 ºC to supercritical conditions at 500 ºC. The slight decrease in the activation energy at 400 ºC may simply be an artifact or it may represent an actual decline in the amount of energy that is necessary to initiate chemical reactions near the critical point of water. The experimental activation energies show good agreement with those obtained for cellobiose decomposition in in SCW by Sasaki *et al*. [49] (104.5 kJ·mol^{-1}) and Kabyemela *et al.* [48].

Table 30. Arrhenius parameters and reaction rate constants obtained for bagasse hydrothermal treatment at various temperatures on the basis of treatment severity.

Conditions	Temperature [°C]	φ [K]	Severity [ln $(R_o)_{corr}$]	Severity [log $(R_o)_{corr}$]	A [min^{-1}]	E_a [kJ·mol^{-1}]	k [min^{-1}]
Subcritical	300	18.34	12.12	5.68	4.43×10^{10}	101.50	9.42×10^{-8}
Near-critical	400	24.27	13.29	6.37	9.72×10^{8}	93.76	5.55×10^{-4}
Supercritical	500	26.93	15.24	7.45	1.28×10^{9}	101.44	3.24×10^{-2}
Supercritical	600	31.25	16.01	7.95	4.83×10^{8}	103.32	0.489

The effects of time and temperature on the hydrothermal conversion of sugarcane bagasse are compared in the reaction severity plot shown in Figure 68. The time treatment study was conducted using a 4.0 wt % bagasse loading at 500 °C. The residence times used in the development of the severity plot were adjusted to include the 5 min heating ramp period, giving a span of reaction times from 6 to 65 min. The temperature treatment study was performed using the standard 4.0 wt % loading and an adjusted residence time of 10 min (i.e., denotes the typical 5 min run used throughout this paper). The temperatures used ranged from 300 to 600 °C in 100 °C increments.

The large gap in the natural log of the corrected reaction ordinate parameter ($\ln [R_o]_{corr}$) between 400 and 500 °C indicates that there is a substantial increase in treatment severity in hydrothermal systems upon proceeding from near-critical to supercritical conditions. This is a salient observation because it is often erroneously conjectured that the severity of every biomass treatment in supercritical water is identical, irrespective of the actual supercritical water conditions used. The sharp increase in treatment severity in the current case corresponds well with the steep drops in water density and the dielectric constant of 34% and 53%, respectively, when raising the temperature from 400 °C (619 bar) and 500 °C (707 bar). A comparison of the linear fits to the time and temperature curves can be used to correlate the impact each parameter has on the overall biomass conversion. Increasing the temperature from 500 to 600 °C for a fixed 10 min reaction converts the same amount of bagasse as does extending the total reaction time from 10 to 28 min at a fixed reaction temperature of 500 °C. Hence, it can be empirically claimed that a 10 °C rise in temperature for a given hydrothermal conversion reaction is equivalent to a 1.8 min extension of reaction time. Optimization of the ensuing temperature versus time opportunity cost tradeoff will ultimately necessitate an economic assessment.

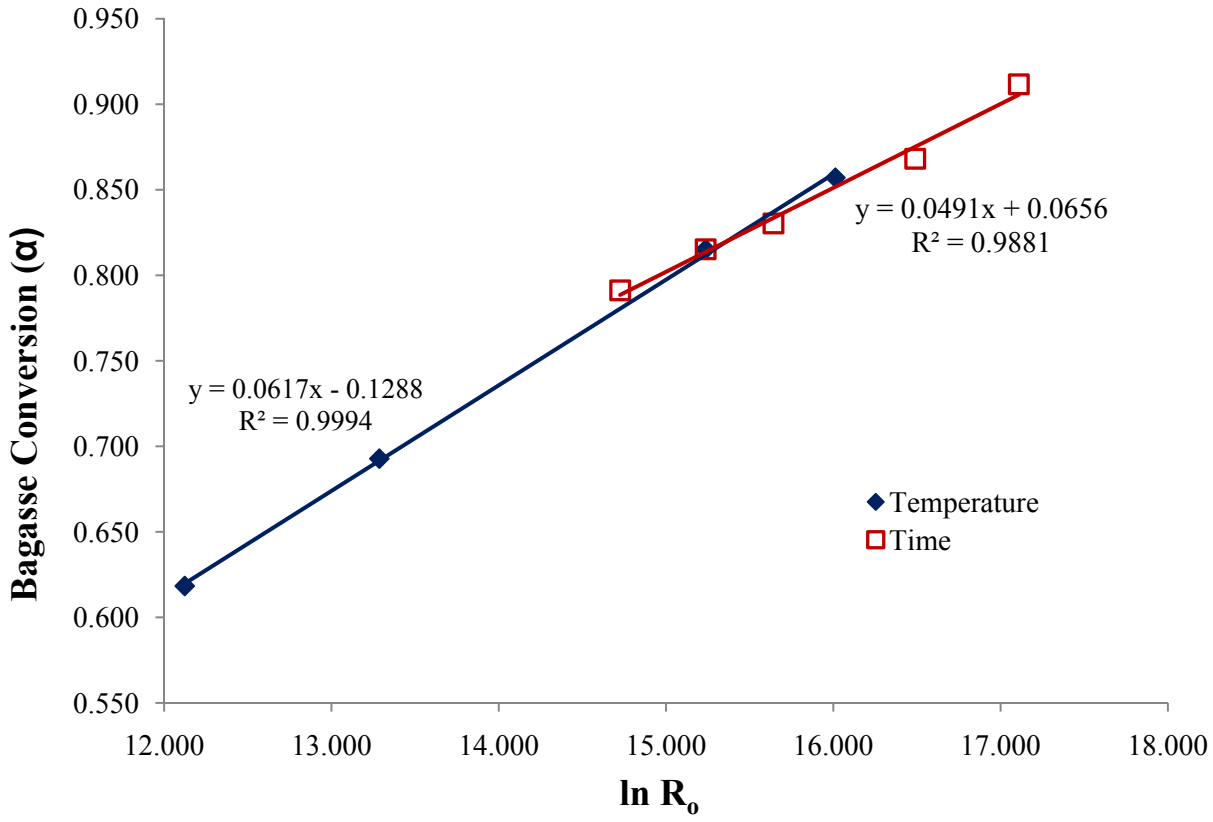

Figure 68. Comparison of bagasse conversion for separate time and temperature treatments as a function of reaction severity.

4.10 Isotopic Determination of Molecular Hydrogen Evolution

It is often routinely assumed that the molecular hydrogen formed during biomass hydrothermolysis originates from the biomass itself [346]. Under this scenario, water serves strictly as a reactive medium rather than a reactant [12]. When water acts as a solvent, hydrogen is evolved from the biomass via a pyrolytic mechanism. Hydrogen gas can also be formed from the water during the steam reforming process or the water gas shift reaction. In steam reforming, water is an active participant in the reaction, preferentially oxidizing the organic carbon in the biomass to carbon dioxide. The hydrogen atoms in both the biomass and water are thus liberated and combine to form molecular hydrogen. Indeed, 57.5% of the atomic hydrogen in H_2 gas formed during sugarcane bagasse hydrolysis, as shown afterward in Eqn. 53, is theoretically derived from water alone. Ergo, it is logical to postulate that the H_2 gas generated from biomass

hydrothermal treatment is derived from both water and biomass. Furthermore, there is a reasonable probability that some portion of the hydrogen content in the hydrocarbons evolved during supercritical water processing of biomass originates from the water itself.

An isotopic labeling technique was employed to demonstrate that hydrogen evolved during the hydrothermal decomposition of sugarcane bagasse is derived not only from the biomass substrate but also the water itself. Hydrogen isotope labeling has been used extensively to examine the mechanisms involved in various chemical reactions, including carbon-hydrogen bond activation processes, heterogeneous and homogeneous metal catalysis, and hydrogen-deuterium (H-D) exchange in organic compounds (e.g., aldehydes, aromatics, carboxylic acids, phenols, and hydrocarbons) subjected to supercritical water treatment [347, 348]. The standard bagasse hydrothermal reaction was performed with bone-dry bagasse using high purity deuterium oxide (D_2O) instead of H_2O. The volatile products were subsequently analyzed using GC-FID-HID. It was expected that the analysis of the product gas would help discriminate the dominant source of the H_2 gas. The presence of D_2, HD, or any perdeuterated hydrocarbon volatiles would be construed as definitive proof that water was behaving as a reactant in the hydrothermal decomposition of bagasse. However, it was anticipated that the chromatographic analysis of the product gas would be rather complex given the difficulty in resolving H_2 and D_2 [349].

Unfortunately, the GC-FID-HID was unable to accurately differentiate between H_2 and D_2 at the standard hydrogen peak location. Despite this setback, an analysis of the GC-FID-HID data identified anomalous behavior in the CH_4 peak shape. The CH_4 peak data from a standard, nondeuterated bagasse hydrothermal run is compared with that of a deuterated hydrothermal bagasse run in Figure 69. At first glance, the widths of the two CH_4 peaks appear almost

identical. The CH_4 curve from the nondeuterated run extends from about 0.67 to 0.73 s, while the CH_4 curve from the deuterated run extends from roughly 0.66 to 0.7275 s. The area shaded in crimson in Figure 69a is used to emphasize to the peak broadening that has occurred in the deuterated run. This ostensibly subtle difference must be viewed in context of the extreme sensitivity of flame ionization detectors to hydrocarbons. Moreover, the CH_4 peak width in the standard, nondeuterated runs using GC-FID was consistently at or slightly below 0.6 s. Thus, a compelling argument can be made to support the claim that the peak broadening observed in the deuterated run using GC-FID is a result of perdeuteration of the methane molecule.

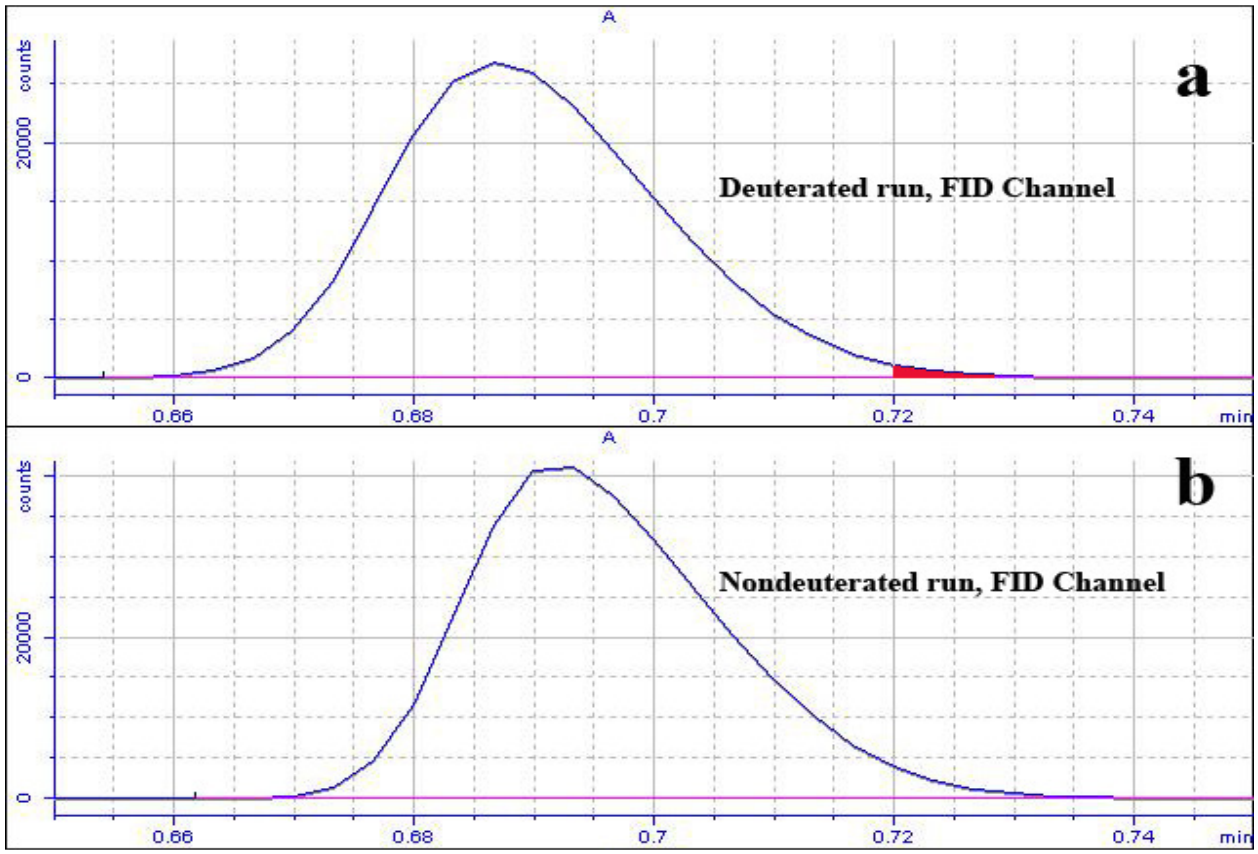

Figure 69. CH_4 peak shape from GC-FID for a) Deuterated bagasse HT run b) Nondeuterated bagasse HT run.

The difference between the CH_4 peak shapes obtained from GC-HID for a standard, nondeuterated bagasse hydrothermal run and a deuterated bagasse hydrothermal run is illustrated in Figure 70. The CH_4 curve in the nondeuterated run extends from 4.64 to 5.10 s, while the CH_4

curve in the deuterated run stretches from 4.35 to 4.95 s. The substantial broadening of the CH_4 peak width by 0.15 s in the deuterated run provides convincing evidence that the methane molecule has undergone H-D exchange. In addition, the turgid lump centered near 4.75 s in the deuterated run affords overwhelming affirmation that CH_4 has been perdeuterated. The extent of CH_4 deuteration cannot be determined from the GC-FID-HID data. Hence, it can only be surmised that the methane obtained in the deuterated bagasse hydrothermal run exists as CH_3D, CH_2D_2, CHD_3, or CD_4. The formation of deuterated methane requires the presence of either deuterium (D_2) or HD.

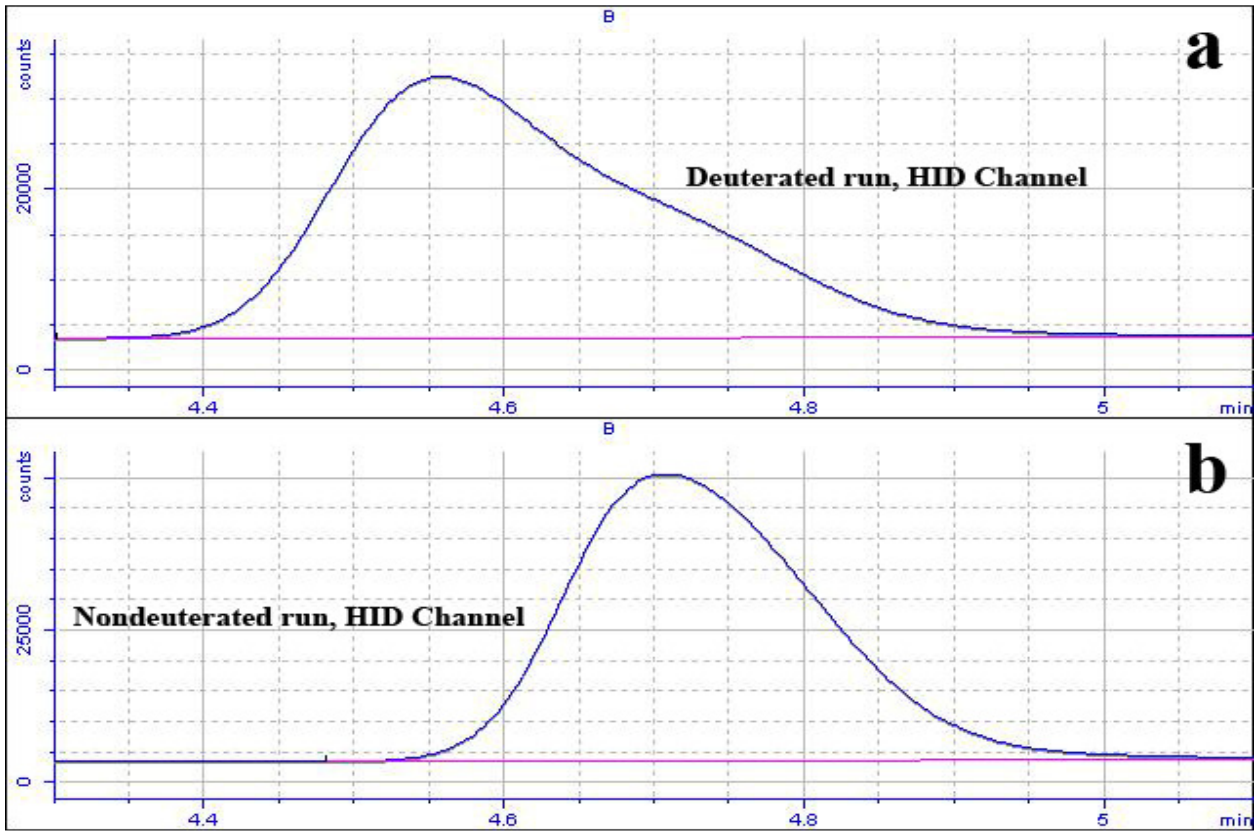

Figure 70. CH_4 peak shape from GC-HID for a) Deuterated bagasse HT run b) Nondeuterated bagasse HT run.

4.11 Reactor Wall Effects

It is known that metal reactor walls often participate as catalysts in the reactive systems they contain. Keller and Bhasin [350] commented that the walls also may have an ability to store

oxygen as denoted by the catalytic formation of carbon oxides inside their stainless steel vessels. To explore the possibility that the Hastelloy X wall was participating in the reactions, a bagasse hydrothermal test was performed in a titanium bomb under the standard reaction conditions. The titanium bomb was an identical replica of the Hastelloy X bomb. It was hypothesized that there should be no statistically significant difference in the total product yield or the volatiles distribution if the metal walls truly made no impact on the hydrothermolytic reaction.

The overall mass balances and the HHV of the volatiles from bagasse runs conducted in the titanium bomb are contrasted against those conducted in the Hastelloy X reactor at baseline conditions in Table 31. The hydrothermal conversion of bagasse is only slightly lower (1.3 wt %) in the titanium bomb than in the Hastelloy X bomb. The HHV of the volatiles formed in the titanium bomb is nearly 31% lower than in the Hastelloy X bomb.

Table 31. Comparison of the overall mass balances and volatile higher heating values from the hydrothermal conversion of bagasse performed in a titanium bomb and a Hastelloy X bomb.

Bomb	T [°C]	P_{max} [bar]	ρ [g·cm^{-3}]	RT [min]	Liquids [wt %]	Solids [wt %]	Volatiles [wt %]	Conversion [wt %]	Gas HHV [MJ·kg^{-1}]
Titanium	500	630	0.361	5	95.64	0.76	0.97	80.2	37.67
Hastelloy X	500	707	0.410	5	97.18	0.71	1.36	81.5	54.38

In Figure 71, the total product composition from the supercritical water treatment of bagasse in a titanium bomb is contrasted with that of the standard baseline experiment conducted in the Hastelloy X bomb. The quantity of liquids obtained from bagasse increases by 10 wt % when the Hastelloy X bomb is replaced with the titanium bomb. Volatiles generation from bagasse in the titanium bomb is 8.7 wt % lower than in the Hastelloy X bomb. The production of solids increases slightly by 1.3 wt % when the titanium bomb is used in place of the Hastelloy X bomb. The differences in the yields of liquids and gases obtained from the Hastelloy X and

titanium bombs hinted that the type of metal alloy in the reactor walls may indeed have an influence on the outcome of biomass hydrothermal reactions.

It was apparent that there was a distinct dissimilarity in the gases evolved from the two different metal bombs even before the compositional analysis on the volatiles from the titanium headspace was completed. Immediately upon opening the cap of the titanium bomb, a pungent odor that was redolent of H_2S permeated the laboratory. Measurement of the headspace above the saved semi-volatile fraction after 12 weeks indicated the presence of at least 60 ppm of H_2S remaining. Volatiles from the standard, baseline runs conducted at 500 °C in the Hastelloy X bomb had a strong gasoline smell.

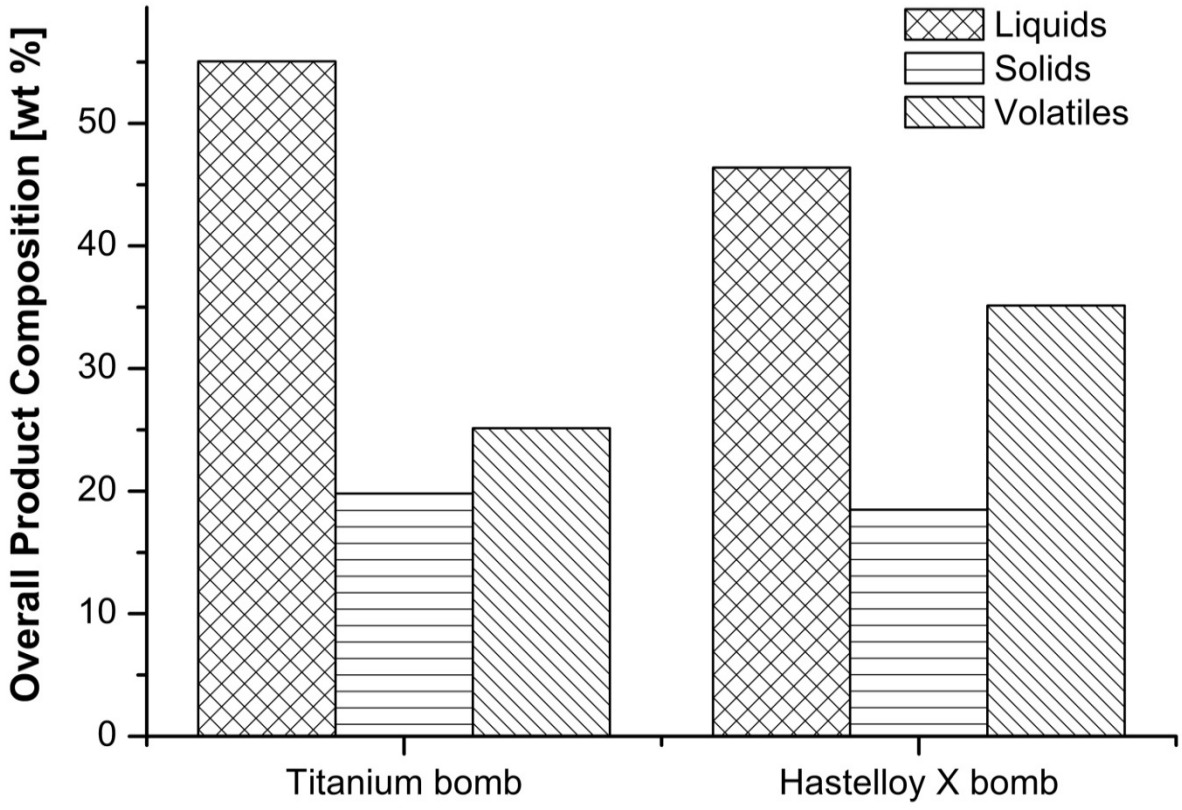

Figure 71. Comparison of overall product distributions from bagasse treated in different metal bombs.

The mass yields of the volatiles obtained from hydrothermal treatment of bagasse in the different metal bombs are presented in Figure 72. The yields of all the individual fixed gas

species from the titanium bomb exhibit a significant deviation from those of the Hastelloy X bomb. For instance, the total mass yields of CO_2 and CH_4 from bagasse treated in the titanium bomb increased by 14 and 16%, respectively, over the yields of the same gases obtained using the Hastelloy X bomb. The yield of H_2 decreased 27% when the titanium bomb was used instead of the Hastelloy X bomb. Most notably, the yield of CO from the titanium bomb was 13 times greater than from the Hastelloy X bomb. The astonishing increase in CO yield in the titanium bomb is a clear indicator that the difference in the metal content of the reactor walls is causing a shift in the gas product yields. The large CO increase can be rationalized if it is assumed that the Boudouard reaction (Eqn. 9) occurs freely in the titanium bomb. Interestingly, the Boudouard reaction was never able to account for a significant portion of the volatile yields from bagasse gasification in the Hastelloy X bomb. Additional CO formation could occur through the reverse WGS reaction. These two reactions would consume both H_2 and CO_2. However, CO_2 yields increased when bagasse was reacted in the titanium bomb. The increase in CO_2 and CH_4 yields can both be accounted for using the gasification methanation reaction (Eqn. 12), which has a low activation energy barrier. A review of the pH values in Table 27 may uncover the reason behind the lower yield of H_2 from the titanium bomb. The pH values of the aqueous phases recovered from the titanium bomb and the Hastelloy X bomb were 3.85 and 4.15, respectively. These results imply that hydrogen is more likely to remain in solution and favor acid formation in the titanium bomb.

The mass yields of the C_2-C_5 hydrocarbons obtained from the hydrothermal conversion of bagasse are consistently higher in the case of the Hastelloy X bomb run than that of the titanium bomb trial, as shown in Figure 72b. The reduced presence of higher hydrocarbons from the Ti bomb suggests that Ti may catalyze the cleavage of higher molecular-weight intermediates.

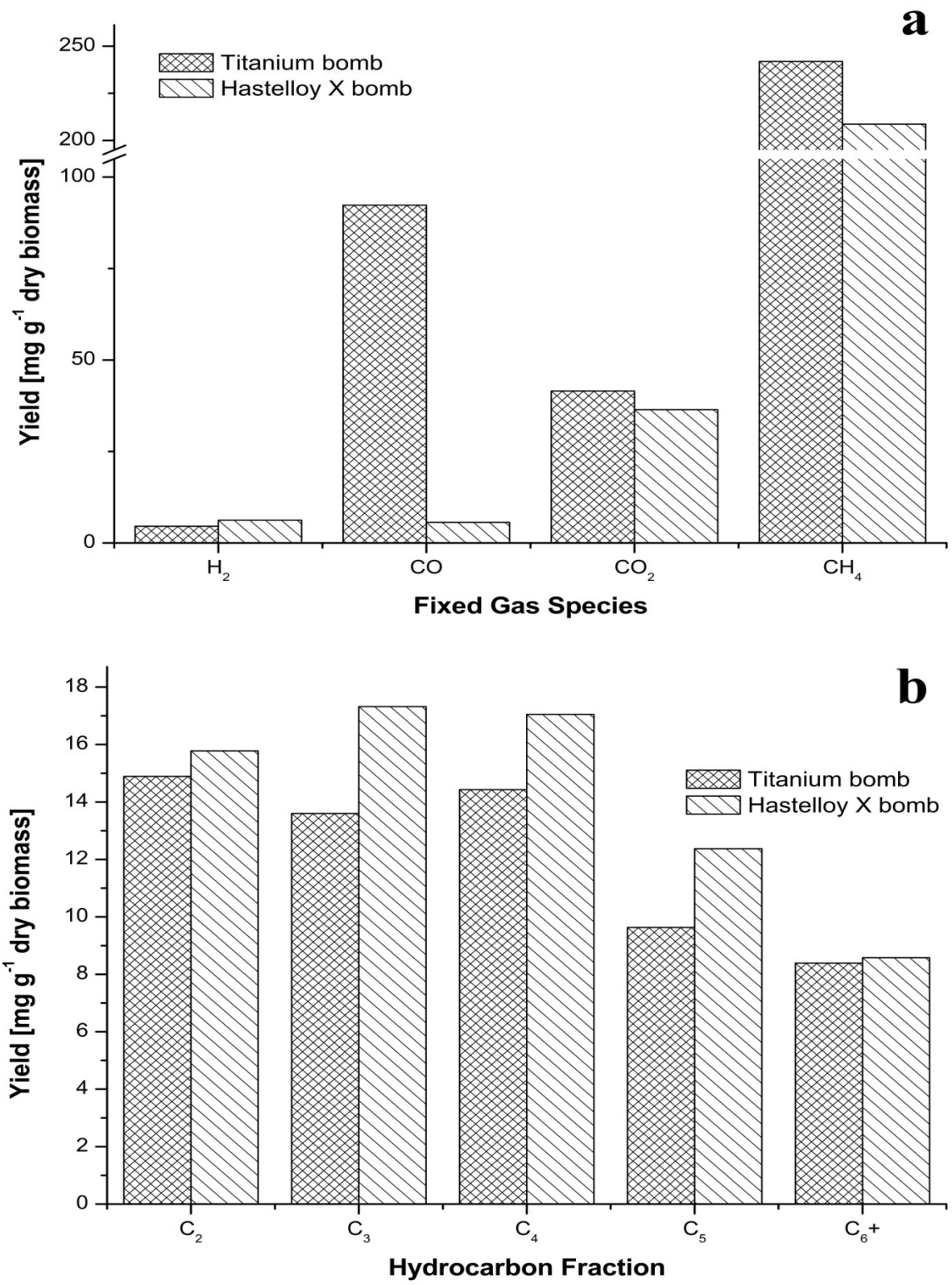

Figure 72. Mass yields of volatiles from different metal bombs for a) Fixed Gases Species b) Hydrocarbon Fraction

Figure 73 depicts the gas composition for bagasse hydrothermolysis performed in a titanium bomb and a Hastelloy X bomb. The molar fractions of C_2–C_6+ hydrocarbons from the titanium bomb range from 23 to 38% below those from the Hastelloy X bomb. Again, the decrease in the hydrocarbon component fraction in the titanium bomb may be an indicator that Ti is more catalytically active than the Fe, Ni, and Cr constituents of the Hastelloy X bomb. It is possible that the Ti promotes more cracking of the hydrocarbons than the Hastelloy X transition metals. The lighter fragments from cracking in the Ti bomb must either enter the liquid phase or they must be consumed to produce more CO. These suppositions are reflected in the CE and GE data presented earlier in Figure 60. The CE is slightly less than the GE for the Ti bomb, which indicates that the lighter carbon-bearing fragments must wind up in the liquid phase. The 15 wt % increase in GE for the Ti bomb over the Hastelloy X bomb also cements the notion that Ti is acting as a gasification catalyst.

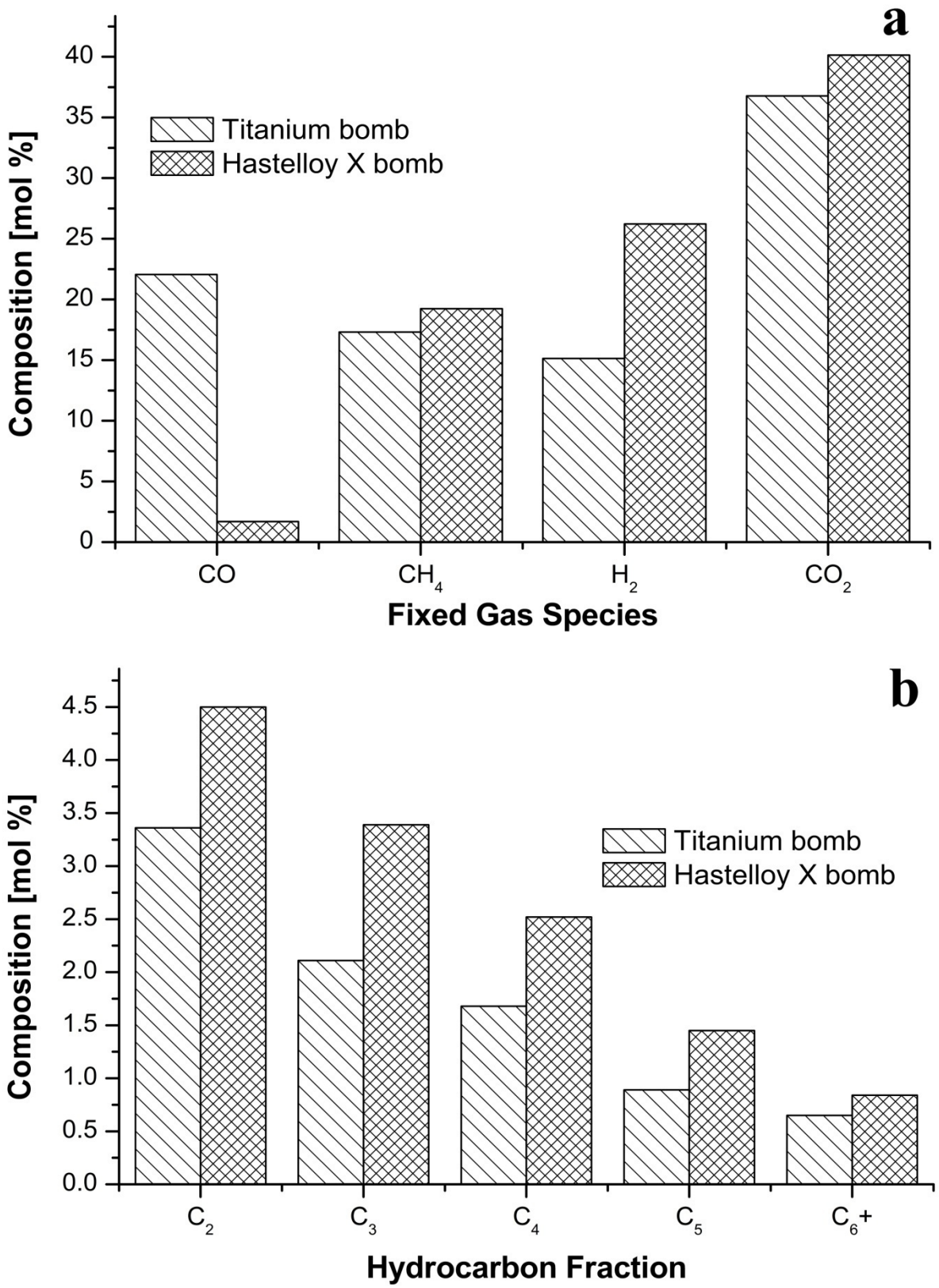

Figure 73. Molar distribution of volatiles from different metal bombs a) Fixed gas species b) C_2–C_6+ fraction.

Chapter 5. DISCUSSION

The steep rise in the C_1 and C_2 fractions observed at elevated temperatures can be further rationalized by considering the extremely favorable exothermic heats of reaction for both methane and ethane formation, as shown in the following equations:

$$C + 2H_2 \rightarrow CH_4 \qquad \Delta H_{427°C} = -85.3 \text{ kJ/g·mol} \qquad (51)$$

$$2C + 3H_2 \rightarrow C_2H_6 \qquad \Delta H_{427°C} = -100.4 \text{ kJ/g·mol} \qquad (52)$$

An interesting theory postulated by Espinal *et al*. [269] further supports the formation of methane and ethane at high temperatures. They used density functional theory to study hydrogen reactions with carbonaceous surfaces in an effort to understand the chemical mechanisms involved in carbon hydrogasification. They discovered that hydrogen is dissociatively chemisorbed on various active sites in the carbon material to form $-CH_3$ and $-CH_2-CH_3$ groups. The single C-C bonds connecting these groups to the surface are the weakest links in the carbon structure and at the high temperatures associated with hydrothermal treatment they are cleaved to form methyl and ethyl radicals. The volatilized methyl and ethyl radicals can then form methane and ethane via hydrogen abstraction from H_2 molecules or via radical recombination with other alkyl radicals or hydrogen atoms.

The increase in the CE to GE ratio as the temperature was raised above 400 °C indicates that the bagasse degradation chemistry is likely moving from pyrolytic mechanisms, such as hydrolysis, decarbonylation, and decarboxylation, to a gasification route wherein thermal cleavage of carbon-carbon bonds plays a significant role. Such a transformation would yield a higher concentration of alkenes and alkanes at the expense of lighter oxygenated VOCs (e.g., carbonyls and alcohols) and fixed gases, thereby providing a higher CE ratio with respect to the overall gasification yield.

The 9.8% decrease in the energy value of the volatiles produced at 60 min residence time versus those produced at 10 min residence time, as shown previously in Table 21, provides useful information regarding the impact of reaction time on hydrothermal chemistry. The drop in the HHV between 10 and 60 min occurs mainly because the production of CO_2, which has no heating value whatsoever, continues to increase, while the production of H_2, which has the highest heating value, remains relatively stable throughout this period. A 73% increase in the mass yield of CO between 30 and 60 min (4.88 to 18.35 mg) also exerted a downward influence on the HHV because of the negligible energy value in CO. The slight decline in the yield of organic semi-volatiles after 10 min is another important finding. Taken together, these results indicate that at longer reaction times the intermediate products decay via thermal cracking. Consequently, it would be expected that the yield of the fixed gases should increase. The yield of H_2 remains static because it is consumed in a reverse WGS reaction to produce CO at long residence times. The rising level of CO_2 at extended reaction times is noteworthy because it too is a reactant in the reverse WGS reactant. This suggests that O radical species may be involved in the oxygenolysis of the organic semi-volatile compounds and solid residues at later stages of the hydrothermal conversion process.

Qu *et al*. [291] observed diminishing oil yields beyond a reaction time of 10 min during the liquefaction of *Cunninghamia lanceolata* in subcritical water. They speculated that condensation and re-polymerization of liquid intermediates leading to char formation was responsible for the lower oil yields at extended reaction times. Given the absence of any increase in solid residue between 30 and 60 min in the current investigation, it seems likely that the small loss in semi-volatiles during this interval resulted instead from cracking of heavy molecular weight liquid products to lighter molecular weight gases.

The mirror symmetry existing between the solids and volatiles curves in Figure 42 suggests that biomass is rapidly gasified during the first 5 min of reaction, whereas the gasification of intermediate organic solid compounds and char occurs at a much slower rate thereafter. The improved gasification efficiency observed even at prolonged residence times diverges from other recently published results [234, 265]. Continuous flow studies involving the gasification of glucose [234] and corn silage [265] in supercritical water indicated that extending the reaction beyond 3.6 and 1.7 min, respectively, did not enhance gasification efficiency. It is unclear whether the difference in gasification efficiency at longer reaction times stems mainly from differences in the reactor system selection (i.e., continuous flow vs. batch), feedstock choice, or operating parameters.

In gasification processes, carbon dioxide can be generated via steam-reforming, water-gas shift, combustion, or aqueous pyrolysis reactions [318]. Combustion reactions in the current process are highly unlikely because they were conducted under an inert blanket of helium. It is possible for hydropyrolysis of bagasse to occur for a brief period during the heating ramp before the water becomes supercritical. Aqueous pyrolysis reactions at high temperatures are generally associated with high char and CO_2 production yields [351]. Another glance at Figure 42 reveals that the yield of solid residues is at its highest level during the first minute of the reaction. Thus, there is a strong likelihood that hydropyrolysis is involved to some degree in the formation of the permanent gases seen during the first minute of reaction. However, steam reforming of bagasse and organic intermediates (Eqn. 9) is assumed to be responsible for the majority of the CO_2 generated once the water in the system becomes supercritical.

Hydropyrolysis (Eqn. 6) and steam reforming processes (Eqns. 8 and 9) are both viable routes for the initial production of CO and H_2. The CO must be largely consumed in the

exothermic WGS reaction to form additional H_2 and CO_2 (Eqn. 12). Support for the WGS theory is provided by results from Lee *et al*. [273], who studied the gasification of glucose in supercritical water at residence times under 1 min. A plot of their gas yield data at 600 °C revealed that the CO level abruptly drops after 24 s, while the level of H_2 continues to rise but at a reduced rate. The lower rate of H_2 production suggests that the initial steam reforming reactions are of very short duration, probably less than 30 s. Some CH_4 and CO_2 can also be formed during the heating ramp period via the slightly endothermic hydrogasification reaction (Eqn. 13). Methane production occurring between 1 and 30 min residence time is attributable to three highly exothermic pyrolysis methanation reactions (Eqns. 1–3). Such a scheme would account for the simultaneous loss of H_2 over the same residence interval. More H_2 may be expended via an exothermic methanation reaction (Eqn. 14), which would also consume additional solid carbon. A gasification study of 5 wt % corn silage in supercritical water in a continuous flow reactor at 700 °C and 250 bar also demonstrated a rising level of CH_4 from less than 1 min residence time until the run ended at 4 min [265]. Between 30 and 60 min residence time the level of CH_4 decreases by 13%, while the level of CO and CO_2 rise by 66% and 10%, respectively. The H_2 fraction remains nearly flat over the same time frame, increasing just 1%. The decrease in CH_4 is associated with the methane dissociation reaction (Eqn. 15) which results in the generation of CO and H_2. Based on the flat curve for H_2 over the 30 to 60 min residence time period, the H_2 formed from methane dissociation must participate in further reactions, perhaps including the energetically favorable methanol formation reaction (Eqn. 4).

The mole fractions of CH_4 and H_2 observed in these experiments at 10 min residence time are approximately 150% higher than yields of the same gases obtained at the identical residence time by Resende *et al*. [318] for a gasification run conducted at 500 °C with a 9.0 wt %

loading of microcrystalline cellulose. The mole fraction of CO_2 observed by these authors at the 10 min residence time was roughly 5 mol % higher than that obtained via the current bagasse hydrothermal experiment, whereas their mole fraction of CO was over one order of magnitude greater than that obtained here. It was speculated that the large difference in gas mole fractions between the current bagasse experiments and those obtained by Resende *et al*. [318] using cellulose must be associated with the substrate. Much of the hydrogen missing (i.e., in the form of CH_4 and H_2) from the cellulose product gases but present in those of the bagasse were deemed to originate from the lignin component of bagasse. A more recent study by Resende *et al*. [321] on the noncatalytic gasification of lignin has resolved some of the uncertainty. Organosolv lignin was gasified in supercritical water at 600 °C using a 9.0 wt % loading of lignin. At 10 min residence time approximately 8 mol % H_2 and 32.5 mol % CH_4 were obtained. If a hypothetical gas yield basis of 1 mol is used, the collective quantity of hydrogen contained in the H_2 and CH_4 from the organosolv lignin is 1.47 g, which is almost identical to the 1.43 g of hydrogen calculated via the same summative calculation for the case of bagasse hydrothermal conversion. Clearly, lignin is a supporting actor in the formation of hydrogen via biomass hydrothermal conversion but a stubborn question lingers regarding the magnitude of this role.

By way of explanation, lignin generally comprises less than 30 wt % of the total dry mass of bagasse as shown earlier in Table 14. The organosolv lignin used by Resende *et al*. [321], however, contained 92.4 wt % lignin. The bagasse used in the current experiments contained approximately 21.4 wt % lignin. The disparity in actual lignin loading between the organosolv lignin and bagasse tests becomes almost tenfold (8.316 and 0.854 wt %, respectively) after adjusting for the difference in the experimental weight loadings (9.0 and 4.0 wt %, respectively). It is pertinent to interject in this discussion that isolated lignin compounds (i.e., kraft, organosolv,

etc.) behave differently in pyrolytic reactions than that of lignin found in actual biomass because of structural changes occurring during the extraction of these model lignin compounds [352]. A French laboratory [352] examined the irradiative flash pyrolysis of model lignins using an image furnace with a 5 kW xenon arc lamp with a flash time of 1 s. The average H_2 production was 13 mol % lower in organosolv lignin (37 mol %) than in kraft lignin (50 mol %).

Notwithstanding the differences between isolated and native lignins, the fact that a loading of lignin in sugarcane bagasse one order of magnitude lower than that of a relatively pure model lignin produces an equimolar fraction of hydrogen in relation to the organosolv lignin casts substantial doubt on the theory that lignin is the primary operator in hydrogen production in hydrothermal biomass systems. Naturally, the hemicelluloses present in bagasse are another suspect source of the hydrogen evolved during hydrothermal conversion. However, hydrogen typically constitutes about 6.0 wt % of hemicellulose, 6.4 wt % of cellulose, and 5.7 wt % of lignin [353]. The only outstanding possibility not yet considered as a source of the hydrogen obtained from hydrothermolysis involves the water itself. The balanced chemical reaction leading to the theoretical maximum yield of hydrogen from the bagasse used in the current hydrothermal experimentation can be written as:

$$CH_{1.7}O_{0.85} + 1.15H_2O \rightarrow 2H_2 + CO_2 \quad (53)$$

Assuming a 1 mol basis of dry bagasse, Eqn. 53 reveals that a theoretical maximum of 4.032 g of atomic hydrogen can be formed. Of this amount, 1.714 g is derived from the bagasse; the other 2.318 g results from the hydrolysis of water. Accordingly, 57.5 wt % of the atomic hydrogen generated via hydrothermolysis comes from the water. It is statistically improbable that the gaseous product obtained from the actual bagasse hydrothermal conversion contains no hydrogen originating from the hydrolysis of water. Therefore, it can be safely concluded that the water

must be the font for a significant portion of the hydrogen yield from the thermolytic conversion of bagasse.

The results obtained from the various bagasse concentration tests demonstrate that there is a tradeoff in product distribution with respect to biomass weight loading. From a process engineering perspective, it would be desirable to enhance gas and liquids generation and curtail solids formation. From the curves shown in Figure 46, it is hypothesized that raising the bagasse loading much beyond 10 wt % (1:10) will result in diminishing volatiles and semi-volatiles returns at the expense of substantial char production. Moreover, the use of bagasse loadings higher than 20 wt % (1:5) is likely to pose serious operational challenges in process flow reactors based on difficulties encountered already at the bench scale during the use of such high biomass weight loadings. An analysis of Figure 46 performed in tandem with Table 22 provides a further piece of singularly useful information regarding the production of semi-volatile organics with respect to the overall liquid yield. The fact that the yield of semi-volatiles increases monotonically in Figure 46 implies that the overall liquid loss shown in Table 22 at the 8.0 wt % bagasse loading with respect to the lower weight loadings is caused by a reduction in the amount of water present rather than aqueous-phase organics. This is an important discovery because it signifies that the chemistry of hydrothermal reactions may be altered at higher biomass loadings. Such changes may involve greater self-ionization of water and an increased prevalence of free radical chemical reactions involving hydroxyl ($OH\cdot$) and hydroperoxyl ($HO_2\cdot$) radicals.

The large drop in H_2 and CO_2 molar yields combined with the strong semblance of their curves in Figure 47 lends itself to the interpretation that a higher weight loading of bagasse encourages the reverse WGS, in which equimolar amounts of H_2 and CO_2 are consumed. Pyrolysis methanation (Eqns. 1 and 3) may account for the reduced level of CH_4 loss at higher

loadings. Eqn. 3 also requires a molar input of H_2 that is 4 times greater than that of CO_2, which would explain the higher molar loss of H_2. Eqn. 1 is included because it provides a feasible route for the consumption of CO that is evolved from the reverse WGS reaction above. Additionally, the substantially lower molar yields of the fixed gases at increased bagasse weight loading are bolstered by recent data in the literature. Savage's laboratory [321] gasified lignin in supercritical water in the absence of catalysts at 500 °C for 10 min using 5.0, 9.0 and 33.0 wt % lignin loadings. Upon increasing the lignin loading from 5.0 to 9.0 wt %, it was observed that the molar yield of CO decreased by nearly 50%, while the molar yield of H_2, CH_4, and CO_2 each decreased by approximately 65%. The Savage group [318] also gasified cellulose in supercritical water under identical conditions. The CH_4 molar yield declined from 5.3 $mmol \cdot g^{-1}$ to less than 1.0 $mmol \cdot g^{-1}$ between 5.0 and 9.0 wt % cellulose loadings. The yields of H_2 and CO_2 registered insignificant increases over the same cellulose concentration interval. Interestingly, the presence of CO was only detected at the 9.0 wt % loading, having a yield of about 3 $mmol \cdot g^{-1}$.

The results obtained from the particle size study imply that the smallest particles in the unsieved bagasse samples are contributing to increased solid residue formation and reduced semi-volatile production. This finding disagrees with most of those found in the literature for biomass pyrolysis. A particle size study involving the slow pyrolysis of hazelnut shells at 900 °C indicated that the largest particle size fraction (i.e., > 1.4 mm) had the highest char yield (27.2 wt %), whereas the smallest particle size fraction (i.e., < 0.15 mm) had the lowest char yield (21.2 wt %) [322]. A Spanish group [354] studied the pyrolysis of grape and olive bagasse at 500 °C using 4 different particle size fractions ranging from 0.4 to 2.00 mm. It was observed that there was no demonstrable influence of particle size on the solid, liquid, and solid phase

yields resulting from the pyrolysis of either grape or olive bagasse. An investigation of particle size influence on product yields from sugarcane bagasse pyrolysis was conducted by Rodriguez *et al*. [355]. The authors speculated that the absence of a demonstrable particle size effect on the pyrolyzed bagasse products might be due to the fibrous constitution of bagasse. It was determined that the main variation in sieved bagasse particles was due to differences arising from the aspect ratios of the fibers as most of the fibers had similar diameters but varying lengths. If the length of a particle is considerably larger than its diameter, then the principal route for pyrolysis will be along the radial axis and, hence, the decomposition behavior of particles with very small diameters should be identical in pyrolysis reactions. Nonetheless, neither of the two studies presented above observed increased solids production with smaller biomass particle sizes. This may suggest that either hydrothermal conversion processes act differently on different particle size fractions or that bagasse particles behave differently than those from other types of biomass.

The results from the current particle size study are borne out by the findings of Turkish group [356] that studied the influence of particle size on the pyrolysis of rapeseed. The rapeseed was divided into several fractions that ranged from 0.224 to 2.0 mm. Each particle size fraction was then pyrolyzed at 500 ºC for 30 min. The pyrolyzed intermediate size fraction (0.85-1.8 mm) produced the maximum yield of bio-oil (46.1 wt %) and the lowest yield of char (20.4 wt %). The smallest particle size fraction (0.224-0.425 mm) produced the lowest oil yield (42.9 wt %) and the highest yield of char (22.8 wt %).

The existence of a substantial chemical composition variation between the smallest particle size fraction and those of the larger particle size fractions may explain the presence of more solid residues from the smallest particle size fraction. Bridgeman *et al*. [357] evaluated the

influence of particle size on the compositional properties of two different energy crops, reed canary grass and switchgrass. Both crops were processed using ball milling and then partitioned into two size fractions (< 90 μm and 90-600 μm). An ultimate analysis revealed that the smaller particles from reed canary grass and switchgrass contained 66% and 121% more inorganic content, respectively, than the larger particles. The lignocellulosic content was also found to be substantially higher (by 32-36 wt %) in the larger particle size fraction for both energy crops. In particular, the cellulose content of the larger particles was approximately 50% higher than those of smaller particles. Therefore, it can be seen that the process of size reduction does not result in a uniform distribution of the various constituents in biomass for the different particle size fractions. Hence, the higher level of solid residue observed from the lowest particle fraction size in the present study can be explained by assuming that more inorganic mineral content was present in the 140/230 mesh size fraction. An ash test of the char collected from the various particle size fractions would provide confirmation of this hypothesis.

An alternative hypothesis for the higher solid residue yields obtained from the smallest particle size fraction also exists. It is possible that the finest particles have a tendency to sinter under supercritical conditions. The sintered particles would then agglomerate to form larger particles. It is posited that the sintering occurs when the surface atoms of fine particles diffuse through the microstructural lattices of adjacent fine particles. This mechanism would impart mechanical integrity and strength to the agglomerated particles rendering them more impervious to degradative attack from the supercritical environment.

The large decrease in solids formed from cellulose is consistent with results from literature, which have indicated that cellulose is completely converted in near critical water at 350 °C and 250 bar after just 45 s [225]. The level of solids formation in the xylan trial was 66%

higher than in the cellulose trial, but 53% lower than in the lignin trial. It is commonly observed that xylan and other hemicelluloses are more readily susceptible to hydrolysis than cellulose because the hemicellulose polymer lacks the highly crystalline, ordered structure that imparts cellulose with greater thermal resiliency [52, 358, 359]. Nevertheless, the current study demonstrated that cellulose was more readily solubilized than xylan in supercritical water at 500 °C for 5 min. The high level of solids produced in the lignin trial is unquestionably a function of lignin's inherently recalcitrant characteristics. The quantity of solids produced from the bagasse run was about 20% lower than from lignin.

The findings from Figure 55 can be justified if we assume that the HT process facilitates C-O bond cleavage in the methoxyl groups of lignin to produce methyl radicals directly. The methyl radicals then promptly react with any available hydrogen to form CH_4. The absence of methyl moieties in cellulose means any methane formation occurs through indirect mechanisms. The small fraction of methoxyl groups present in hemicelluloses [360, 361] will presumably lead to direct CH_4 formation, as in the case of lignin, explaining the slightly higher CH_4 content observed in the xylan HT trial versus that of the cellulose HT trial.

Hydrogen production was identical in both the cellulose and lignin runs, which was unusual considering that several papers indicate lignin yields substantially less hydrogen than cellulose in supercritical water gasification processes [269, 321, 362]. The H_2 levels from the bagasse and xylan HT experiments were also nearly equivalent, although they were about 0.5 mmol lower than those from cellulose and lignin. The volatiles composition profile for lignin stands in stark contrast to those of cellulose, xylan, and even bagasse because of a virtual dearth of CO (0.03 $mmol \cdot g^{-1}$) and a CO_2 yield that is greatly reduced (4.25 $mmol \cdot g^{-1}$). This is reasonable given the substantially lower oxygen content in lignin than in cellulose, xylan, or

bagasse. The yields of the C_2–C_4 fractions are also lowest for the lignin HT run, though the yield of the C_5+ fraction from lignin is the same as those from the xylan and bagasse. The findings above help to further reinforce the postulation that supercritical water treatment of lignin is dominated by condensation and bond-cleavage reactions that result in either solid residues or high molecular weight semi-volatiles (e.g, tars, aromatics, phenols, etc.). Volatile products that form will be comprised chiefly of H_2, CH_4, and higher weight VOCs.

In light of the significant difference in the mass fractions of volatiles derived from the gasification of lignin and that of cellulose, the comparable decline in the molar yields of light gases obtained from the gasification of bagasse and that of lignin is noteworthy. Similarly, the solid and liquid phase mass fractions obtained from the SCW conversion of bagasse closely resemble those from lignin. The sugarcane bagasse used in the current study had roughly twice as much cellulose per gram of bagasse than lignin. In spite of its relatively low presence in bagasse, these results demonstrate that lignin plays a dominant role in the conversion of bagasse during hydrothermolysis.

The catalytic oxidative coupling of methane (OCM) using reducible metal oxides to form ethane and ethylene (and higher olefins in lesser yields) has attracted considerable attention in the petrochemical industry because of the economic potential associated with converting a relatively inexpensive component comprising 90 mol % of natural gas into hydrocarbons having a higher commodity value [332]. The immense appeal of OCM to both scientists and oil refiners alike was not lost upon Hutchings *et al*. [363], who observed that in one year alone (1988) over 60 scientific papers on OCM were presented at three major conferences. In the OCM process, methane molecules on the surface of the catalyst are first dehydrogenated to form methyl radicals ($CH_3^{\bullet}$) on the catalytic oxide surface. The methyl radicals then emanate into the gas phase where

they undergo coupling to form ethane. Some debate exists over the actual mechanism involved and several kinetic schemes have been theorized, *viz*: a Langmuir-Hinshelwood mechanism, an Eley-Rideal mechanism, or a Rideal redox type of mechanism [364-366]. The overall scheme can be elucidated as follows [367]:

$$2CH_3^{\bullet} \rightarrow C_2H_6 \quad (54)$$

$$C_2H_6 + O^- \rightarrow C_2H_5^{\bullet} + OH^- \quad (55)$$

$$C_2H_5 + O^{2-} \rightarrow O\text{-}C_2H_5^- + e^- \quad (56)$$

$$O\text{-}C_2H_5^- \rightarrow C_2H_4 + OH^- \quad (57)$$

CO and CO_2 are formed via competitive routes:

$$CH_3^{\bullet} + O^{2-} \rightarrow O\text{-}CH_3^- \rightarrow CO, CO_2 \quad (58)$$

$$CH_3^{\bullet} + O_2 \rightarrow CH_3O_2^{\bullet} \rightarrow CO, CO_2 \quad (59)$$

Catalysts have also been developed to promote the oxidative dehydrogenation (ODH) of ethane and propane to ethylene and propylene, respectively. The mechanism employed in the ODH of ethane and propane is similar to that of OCM, except that the ethyl and propyl radicals can also undergo unimolecular decomposition or oxidative dehydrogenation to form ethylene and propylene, respectively.

The use of oxidative dehydrogenation catalysts requires an oxidant source, which is normally assumed to be molecular oxygen. In the current experimental design, however, all thermolytic runs were conducted in an inert environment to avoid the introduction of additional variables that could influence the hydrothermal reaction and alter the distribution and yield of products. Some studies have been executed that indicate CO_2 can be used successfully as an oxygen source in catalytic methane reforming [368-372]. Irrespective of the oxygen source, it

has been shown that the reaction rate for oxidation in supercritical water is largely independent of the oxygen concentration [20].

Although the central discourse in this section is focused on the effects caused by external catalyst addition to the bagasse slurry, it is worthwhile to ponder, if only briefly, the importance of the preceding observation. It has been proposed that the inorganic content in biomass may act as an intrinsic catalytic agent during thermochemical reactions. In the current study, however, there was no observable evidence that the native mineral matter caused any change in hydrocarbon distribution or yields. This is an intriguing discovery because it is reported that sugarcane bagasse ash contains magnesite at levels ranging from 1.65 to 3.04 wt % of the entire ash mass [373, 374]. Using a basis of 1.0 g bagasse and assuming that bagasse has an average mineral content of 4.0 wt %, it can be determined that MgO comprises approximately 0.07 to 0.12 wt % of bagasse. The Li/MgO experiment utilized 299 mg of catalyst to give a 21.0 wt % catalyst loading, which represents a difference of 2 orders of magnitude compared to the levels of MgO naturally present in bagasse. Hence, it can be reasoned that the background levels of MgO found in bagasse are simply insufficient for catalytic dehydrogenation to occur. Alternatively, it could be argued that the addition of the Li^+ ion was the decisive factor that resulted in catalytic dehydrogenation of paraffins during the Li/MgO run. Such an argument, however, ignores the fact that MgO, itself, exhibits catalytic behavior as evinced by the reported 36.1% selectivity of MgO toward C_2H_4 formation (i.e., relative to CO, CO_2, and CH_4) during ethane dehydrogenation at 500 °C [375].

Studies by Hutchings *et al*. [363, 376] revealed that MgO as a catalyst on its own yields significant amounts of H_2 but that upon addition of Li^+ the selectivity to H_2 with respect to C_2 hydrocarbons diminishes. It is rationalized that the higher concentration of surface O^- species

resulting from the Li^+ doping facilitates the oxidation of some of the hydrogen evolved during the routine hydrothermal reactions to form water. This may also account for the slightly higher level of liquid product observed in Table 26 for the Li/MgO run with respect to that of the uncatalyzed run.

The fact that Li/MgO did not exhibit selectivity toward ethylene formation was surprising considering that this catalyst is widely regarded in the literature as "an effective catalyst for the conversion of ethane to ethylene" [366]. Although some data in the literature suggests that Li/MgO does not begin to activate ethane until a temperature of 600 °C [331, 366], other data indicates that the conversion of ethane using Li/MgO begins as low as 450 °C [333]. Even more puzzling than the dismal ethylene selectivity for Li/MgO is its apparent inability to catalyze the OCM, as evidenced by the higher yields of CH_4 using Li/MgO than without.

Bielański and Haber [367] declared unequivocally that oxygen activation in catalytic oxidation is a "crucial problem." It is known that $[Li^+O^-]$ centers in the Li/MgO atomic structure serve as the active sites in the generation of $CH_3^\bullet$ radicals [377], as shown below:

$$Li^+O^- + CH_4 \rightarrow Li^+OH^- + CH_3^\bullet \quad (60)$$

A possible reason that Li/MgO did not stimulate ethylene production lies in the finding by Hutchings *et al*. [363] that lattice oxygen in MgO is not activated in methane oxidation when gaseous oxygen is lacking. Consequently, methane oxidation in anoxic environments must proceed via formed CO_2 or adsorbed oxygen species. The levels of CO_2 and of the adsorbed oxygen in the bagasse slurry and reactor walls may have been insufficient for the reaction to proceed.

Reaction selectivity can also be influenced by the type of adsorbed oxygen species [378]. Adsorbed oxygen is subdivided into two categories: electrophilic and nucleophilic.

Electrophilic species, such as O^- (oxide), O_2^- (superoxide), and O_2^{-2} (peroxide), are thought to be involved in the deep oxidation of hydrocarbons, whereas nucleophilic species, such as the oxide ion, O^{-2}, are believed to be responsible for partial oxidation of electron deficient regions of hydrocarbon molecules. Unfortunately, there have been few direct measurements of the type of surface oxygen species adsorbed from various metal oxide catalysts.

It remains unclear why Li/MgO exhibits a higher selectivity for propylene than ethylene, yet this discovery is opposite those in the literature, where the predominant conversion products are C_2H_4, C_2H_6, CO, CO_2, H_2, and H_2O [363]. The Li/MgO run also produced a higher percentage yield of unsaturated C_4 hydrocarbons than the non-catalyzed standard run, as shown in Table 28.

The efficacy of manganese dioxide (MnO_2) as an OCM catalyst was initially exposed by Keller and Bhasin [350], who screened the catalytic viability of numerous metal oxides derived from 26 different metallic elements. Manganese was determined to be the most active element for C_2 formation from OCM. Work performed at the former ARCO Chemical Co. by Sofranko *et al*. [300] revealed that a 13 to 20 wt % loading of MnO_2 was the optimal amount required to obtain maximal methane conversion. A 30.1% conversion of methane and a 36.9% ethylene selectivity were recorded for a stream of methane reacted at 800 °C for 1 min using a 15 wt % loading of MnO_2 supported on silica. A comparative study of catalysts for OCM by Burch and Tsang [379] indicated that manganese oxide catalyst have the highest selectivity for both ethane and ethylene formation.

A mechanism is being proposed to explain the paradoxical selectivity of the Li/MgO and MnO_2 catalysts toward the C_3 olefins rather than the C_2 olefins, as ordinarily observed in

petrochemical refining. The thermal decomposition of propane can proceed via C-C bond dissociation to yield both ethyl and methyl radicals [380]:

$$C_3H_8 \rightarrow C_2H_5 + CH_3 \qquad E_a = +\ 356\ \text{kJ mol}^{-1} \qquad (61)$$

This reaction generally occurs in rich mixtures at temperatures in excess of 900 °C. The activation energy (E_a) required for the thermal destruction of propane to proceed is quite high, making this reaction energetically unfavorable for the current hydrothermal system which operates at a baseline temperature of 500 °C. Typically the ethyl radical will readily react with other ethyl radicals to form both C_2H_4 and C_2H_6. Ethyl radicals can also react with hydrogen radicals to yield C_2H_4 and H_2. Neither the yield of C_2H_4 or H_2 increases when catalysts are used in the hydrothermal conversion of bagasse. Thus, it is concluded that the propane evolved during the hydrothermal process degrades by another route. In lean mixtures, it is common for propane to react primarily with hydroxyl radicals:

$$C_3H_8 + OH \rightarrow n\text{-}C_3H_7 + HO_2 \qquad E_a = +\ 1.6\ \text{kJ·mol}^{-1} \qquad (62)$$

$$C_3H_8 + OH \rightarrow i\text{-}C_3H_7 + HO_2 \qquad E_a = -\ 6.7\ \text{kJ·mol}^{-1} \qquad (63)$$

The isopropyl radical readily degrades with little necessary energy to yield propylene and hydrogen radicals:

$$i\text{-}C_3H_7 \rightarrow C_3H_6 + H \qquad E_a = +\ 4.0\ \text{kJ·mol}^{-1} \qquad (64)$$

Thus, it is speculated that the propylene selectivity manifest by both MnO_2 and Li/MgO is a result of the favorable thermodynamic pathways presented above. The isopropyl radicals can also be formed from hydroperoxyl radicals but those routes require a higher heat of formation.

Carbon monoxide has been used as a reducing agent in the direct thermochemical liquefaction of coal since 1924 [176]. Further work [176, 178, 190, 191, 381] conducted with biomass (e.g., agricultural residues, urban wastes, and wood) revealed that an overpressure of

CO or H_2 was required to remove oxygen from the lignocellulosic substrate and produce liquid oils. In fact, it was calculated that reducing gases (i.e., CO and H_2) must be introduced at a minimum overpressure of 100 bar to boost oil yields from 35 to 58% [176]. Eager et al. [178] noted that a hybrid aspen poplar wood treated in a pressurized atmosphere of CO formed both alcohols and ketones but that in the absence of a CO environment the aqueous phase consisted primarily of ketones with a greatly reduced alcohol fraction. It was speculated that the higher levels of alcoholic compounds observed in the runs containing CO were a result of the reduction of the ketonic compounds. Moreover, it was noted oils produced in the absence of CO were more viscous than oils produced in its presence [381]. The exact reducing mechanism has not been elucidated and it is believed to involve a combination of dehydration and deoxgyenation reactions that are initiated by the reductant or by intermediate reducing species, such as formates. The "lost" oxygen then reappears among the products of the highly oxygenated aqueous phase and in the gas phase components as CO_2.

The dramatically higher levels of CO observed from the run pressurized with CO conflict with experimental findings in the literature [178, 381]. These earlier studies observed that the generation of CO_2 is roughly equimolar to the consumption of CO. Traditionally it has been thought that the CO serves as a reductive agent by transferring bound oxygen from the biomass substrate to the gas phase in the form of CO_2, possibly via decarboxylation and decarbonylation pathways [191]. Carbon monoxide is also known to participate in the WGS reaction generating further quantities of CO_2. In the current study, however, the mole fraction of CO was actually 2.0 mol % higher than that of CO_2, which eliminated consideration of the WGS reaction. The only viable explanation for the significant yield of CO involved Le Chatelier's principle. The initial charge of CO presumably drove the exothermic forward WGS reaction to eliminate the

excess CO mole fraction. Simultaneously, traditional steam-reforming (Eqn. 9) and methanation reactions (Eqn. 13) were also contributing to the formation of additional CO_2.

During the experimental run, the CO_2 reached excess levels and Le Chatelier's principle was again invoked. Several reaction routes were likely utilized in an attempt to lower the mole fraction of CO_2 in the system including the reverse WGS reaction in which both H_2 and CO_2 are consumed to liberate CO and water vapor. Additional CO_2 could have been removed via the Boudouard reaction, which liberates 2 moles of CO per mol of CO_2 consumed, and the reverse pyrolysis methanation reaction (Eqn. 2). The latter reaction, in conjunction with the methane dissociation reaction can be credited with the decrease in CH_4 levels, while the reverse WGS reaction accounts for the loss of H_2. The uniform one-third decrease in the mole fractions of the $C_2 - C_5$ fractions obtained from the CO run in relation to those from an inert run suggests that the formation of these fractions is inhibited to the same degree or that the these fractions are participating with intermediates and being consumed at the same rate. The slightly lower decrease seen in the C_6+ fraction lends some credence to the latter possibility, especially if the some of the C_6+ components are cyclic compounds, which may exhibit lower reactivity with the intermediary compounds produced under the reductive environment.

Sodium borohydride is widely recognized for its hydrogen storage capacity (i.e, 10.66 atomic wt % hydrogen) and its usefulness as an energy carrier because its electrooxidation can generate up to 8 electrons [382]. Hydrolysis can theoretically produce 4 moles of H_2 from $NaBH_4$, as shown in Eqn. 65, while hydrothermolysis can liberate up to three atoms of hydrogen, as shown in Eqn. 66 [383].

$$NaBH_4 + (2 + x)H_2O \rightarrow NaBO_2 \cdot xH_2O + 4H_2 \quad (65)$$

(66)

The ability of $NaBH_4$ to reduce water soluble carbohydrate derivatives in aqueous media is also well-documented in literature [384-387]. Schlesinger *et al*. [387] highlighted the selectivity of $NaBH_4$ to reduce carbonyl groups in organic compounds, when they determined that acetone could be effectively reduced to isopropanol upon reaction with $NaBH_4$, Based upon these findings it was determined that $NaBH_4$ could serve as an efficient reducing agent during the hydrothermal conversion of bagasse.

The volatile mass yields obtained from the sodium borohydride run were somewhat surprising when taken in context with those of the standard, baseline run. The level of H_2 increased by 9.23 mol %, while the level of CO_2 decreased by 4.47 mol % when sodium borohydride was added. The mass yields of all C_1-C_6+ hydrocarbons also increased when sodium borohydride was added to the bagasse as shown in Figure 61b. It was expected that the addition of reducing equivalents of hydride ion would enhance the production of both hydrogen and other reduced products, such as hydrocarbons. According to Catallo *et al*. [348], who studied the hydrothermal decomposition of glucose in Hastelloy bombs at 400 °C both with and without the addition of hydride species, increased levels reducing H species can inhibit hydrolytic reactions that "steal substrate carbon atoms and generate oxidized products, notably CO_2. The present results suggest that the addition of hydride species does promote production of reduced products but the reduced hydrogen equivalents do not appear to hinder biomass oxidation contributing to CO_2 formation. There are three possibilities that may account for this observation, *viz*.

- An insufficient amount of sodium borohydride was added to the reactor allowing biomass oxidation reactions, including CO_2 production, to occur unimpeded

- Carbon dioxide formation occurs via an independent reaction route that is unaffected by the presence of hydride species
- The level of CO_2 did decline at some point during the hydrothermal run but these declines were offset by increased production from the WGS reaction, which was galvanized as a result of Le Chatelier's principle

The kinetics of heterogeneous solid-state decomposition reactions are commonly described using the fundamental rate equation below:

$$\frac{d\alpha}{dt} = kf(\alpha) \tag{67}$$

where α denotes the extent of conversion, t is the duration of the reaction, k is a temperature-dependent rate constant, and $f(\alpha)$ is the reaction model chosen to represent the decomposition process. The degree of conversion, α, is defined as:

$$\alpha = \frac{(m_0 - m_t)}{(m_0 - m_\infty)} \tag{68}$$

in which m_0 is the initial mass of the biomass sample, m_t is the mass of the remaining sample at time t, and m_∞ is the final mass of the sample. The majority of reactions exhibit Arrhenius temperature dependence, thereby allowing the rate constant, k, to be expressed in terms of temperature via the Arrhenius rate expression:

$$k = A\exp\left[-\frac{E_a}{RT_r}\right] \tag{69}$$

where A is the frequency factor, E_a is the apparent activation energy, R is the universal gas constant (8.314472 J·(mol·K)$^{-1}$), and T_r is the absolute reaction temperature (K). The terms A and E_a are commonly known as the Arrhenius parameters. Insertion of the Arrhenius equation

into the rate expression in Eqn. 67 yields the standard solid-state decomposition kinetic relationship:

$$\frac{d\alpha}{dt} = A\exp\left[-\frac{E_a}{RT_r}\right]f(\alpha) \tag{70}$$

Determination of the Arrhenius parameters in isothermal systems requires rate constants be obtained at several temperatures (e.g., three or more) [388, 389]. Otherwise there is the possibility of incurring substantial error in the derived Arrhenius parameters. Time constraints prevented execution of the 15 additional experiments that would have been necessary to generate rate constants from the ancillary reaction temperatures (i.e., 300, 400, and 600 °C). Accordingly, evaluation of the Arrhenius parameters using a traditional kinetic approach was not possible.

Elucidation of comprehensive chemical kinetic models encompassing a variety of elementary reaction pathways is a difficult proposition for hydrothermal biomass systems, where unrecognized operational factors and unknown intermediates, products, and reaction routes abound. Hence, a global kinetic analysis was applied to obtain the overall rate of reaction for the hydrothermal decomposition of bagasse. The dissolution of bagasse in supercritical water was assumed to proceed via the following reaction:

$$\mathrm{B} + \mathrm{W} \rightarrow \mathrm{P} \tag{71}$$

where B represents bagasse, W stands for supercritical water, and P denotes the products. Normally, the kinetics for such a reaction would be assumed to follow a second-order rate law that is proportional to the product of the bagasse and supercritical water concentrations, as shown below:

(72)

where [B] and [W] represent the concentration of bagasse and supercritical water, respectively. If it is assumed that water serves strictly in the capacity of an extractive solvent medium, then the reaction kinetics in Eqn. 71 would depend exclusively on the bagasse concentration and the reaction could be described using the traditional first order rate law:

$$-\frac{d[\mathrm{B}]}{dt} = \frac{d[\mathrm{P}]}{dt} = k[\mathrm{B}] \tag{73}$$

where [P] corresponds to the product concentration. Separating variables and integrating between the boundary limits of $[\mathrm{B}]_0$ at $t = 0$ and $[\mathrm{B}]_t$ at time t provides the following expression:

$$[\mathrm{B}]_t = [\mathrm{B}]_0 \exp(-kt) \tag{74}$$

The rate law can also be expressed in terms of the extent of conversion, α, as shown below:

$$k = \frac{1}{t}\ln\left(\frac{1}{1-\alpha}\right) \tag{75}$$

Eqn. 73 is often written in terms of the linearized form below:

$$\ln[\mathrm{B}]_t = \ln[\mathrm{B}]_0 - kt \tag{76}$$

Substituting the Arrhenius equation into Eqn. 75 and linearizing the expression yields:

$$\ln\left[-\ln(1-\alpha)\right] = \ln A + \ln t - \frac{E_\mathrm{a}}{RT_\mathrm{r}} \tag{77}$$

An alternative format for Eqn. 73 is also commonly encountered:

$$kt = \ln\left(\frac{[\mathrm{B}]_0}{[\mathrm{B}]_t}\right) \tag{78}$$

The rapid decomposition of short-lived intermediates and transient species sometimes follows a rate that is second-order or higher with respect to a single component. The following equation provides the differential rate expression for a reaction that follows second-order kinetics with respect to a single reactant (e.g., bagasse in this case):

$$-\frac{d[\mathrm{B}]}{dt} = k[\mathrm{B}]^2 \tag{79}$$

Integration between the same limits used in the integration of the first-order rate law above yields a linearized expression similar to the one in Eqn. 76:

$$\frac{1}{[\mathrm{B}]_t} = \frac{1}{[\mathrm{B}]_0} + kt \tag{80}$$

Rearrangement of Eqn. 80 yields the following expression for $[\mathrm{B}]_t$:

$$[\mathrm{B}]_t = \frac{[\mathrm{B}]_0}{1 + [\mathrm{B}]_0 kt} \tag{81}$$

Frequently, researchers attempting to determine the rate law order for a particular species in a given reaction containing more than one reagent will run the reaction using an excess of every reagent except the desired species, effectively "drowning out" the potential impact of these other species on the kinetic order of the reaction [390, 391]. Consequently, the concentration of these other reagents will remain roughly constant over the duration of the reaction, while only the concentration of the desired species will vary significantly with time. If the dependence on the concentration of the desired species is first-order, the reaction is assumed to follow "pseudo first-order" kinetics. The current experiments could be considered flooded because they were run using a minimum 20-fold stoichiometric molar excess of water. Therefore, the customary first-order rate law given by Eqn. 73 for the bagasse hydrothermal conversion reaction in Eqn. 71 can be modified as shown here:

(82)

where k here signifies the overall rate constant for the second-order reaction and k_{app} denotes the pseudo, or apparent, first-order rate constant with respect to bagasse. The relationship between k and k_{app} for a specified concentration of supercritical water is given by:

$$k_{app} = k[W] \quad (83)$$

Although it is likely that supercritical water participates as a reactive agent in the hydrothermal decomposition of bagasse, it was impossible to assess the impact of supercritical water on the overall reaction rate because of the high concentration of water used.

The inability to discriminate between various rate orders using the Essen plots illustrates an inherent weakness in Essen's method; reactions with complex reaction rate dependencies often appear to follow simple first- or second-order kinetics in Essen plots [335]. It was deemed unacceptable to capitulate to the indeterminate results obtained from the linear least-squares model fitting and associated Essen plots and acquiesce that the reaction order, with respect to bagasse, must be pseudo first-order simply because of the flooded reaction conditions. Instead, the Levenberg-Marquardt (LM) algorithm [392-395] for nonlinear weighted least-squares regression was used to fit the concentration and time data to the nonlinearized first- and second-order rate laws given previously in Eqns. 34 and 39, respectively. Nonlinear least-squares ostensibly provides a better statistical fit of experimental data and a more accurate value of k than linear least-squares [390]. The least-squares method determines the optimum parameters of a model function when the sum of the squares of the residuals (SSR) is minimized. The partial derivatives of the SSR in the nonlinear case contain the rate constant parameter, k, whereas the derivatives in the linear least-squares method are functions of neither the slope nor the intercept. For this reason, nonlinear least-squares techniques are more effective than linear least-squares methods when fitting data to kinetic rate models.

Unsatisfied to merely describe the kinetics of the bagasse hydrothermal reaction as following a complex rate law, another attempt at uncovering the bona fide rate orders for the thermolytic decay of bagasse was undertaken using Van't Hoff's method. In Van't Hoff's

method, the rate constant, k, is computed from the integrated rate equations provided in Table 29. A plot of k_n versus t is constructed for assorted values of the reaction order, n. The rate constant, k_n, for a given value of n should be constant in a Van't Hoff plot. If there is a progressive increase in k_n over time, then the actual reaction order is lower. Conversely, if there is a systematic decrease in k_n over time, then the actual reaction order is higher. Van't Hoff plots were created from the bagasse hydrothermolysis kinetic data up to a rate order, n, of 6, as shown in Figure 67. Construction of a single, comprehensive Van't Hoff plot was abandoned because the broad span of rate constant values (i.e., over 4 orders of magnitude) would have necessitated an equally expansive ordinate scale that threatened to obscure small variations in the rate constant behavior at lower rate orders. Instead, Van't Hoff plots were prepared for reaction order pairs having roughly comparable rate constant values. It can be seen that the hydrothermal degradation of bagasse follows apparent kinetics that are higher than 6th order during the first 10 minutes of the reaction. Between 10 and 30 minutes, bagasse destruction can be closely approximated using 5^{th} order kinetics. The bagasse hydrothermal process is governed by 2^{nd} or 3^{rd} order kinetics between 30 and 60 minutes.

On the basis of the preceding kinetic study it can be argued that the apparent reaction order for the hydrothermal conversion of bagasse follows either pseudo 1^{st} order kinetics or mixed order kinetics. The pseudo 1^{st} order claim can be supported by the fact that the hydrothermal conversion of bagasse was performed using a large excess of water, whose resulting high concentration varied negligibly over the course of the reaction. The reaction behavior can then be described as pseudo 0^{th} order with respect to the concentration of the water [396]. The degradation of the sugarcane bagasse, which was present at a much lower concentration and said to be "isolated", could then be adequately expressed as a pseudo 1^{st} order

reaction according to the Essen plots and the adjusted Levenberg-Marquardt nonlinear least-squares curve fit (i.e., excludes the datum point at 1 min residence time) presented previously.

The Essen plots suggest that a 2nd order reaction can be also used to represent the decomposition of bagasse, while the Van't Hoff plots indicate that the hydrothermolysis of bagasse occurs as a complex mixed order reaction. The contention for 2nd order reaction kinetics is supported by the fact that the apparent rate constant in Eqn. 83 does in fact contain a concentration and is technically pressure-dependent [397]. The pressure dependence of the rate constant for condensed-phase reactions is generally sufficiently weak at the pressures commonly encountered in industrial applications that it is simply neglected. However, the pressures in the supercritical regime of the current study are relatively high compared to those typically seen in industry so that pressure may indeed influence the rate constant in the hydrothermal conversion of bagasse. It is also probable that the system follows gas-phase kinetics, which are pressure dependent, because in the supercritical regime water is no longer considered a liquid but instead a fluid.

The optimal severity parameters in Table 30 deviate considerably from $\varphi = 14.75$, which is the value customarily used to evaluate biomass pretreatment processes. This finding is in accordance with those of other researchers, including van Walsum's laboratory [51] which attempted to describe the pseudo reaction kinetics for degradation products from dilute-acid hydrolysis of corn stover using the traditional severity parameter value. Van Walsum and coworkers concluded that the "severity function as it is commonly described functioned poorly as a means of discriminating between different reaction conditions making use of variable temperature combinations of temperature and reaction time" but that "manipulation of the temperature contribution [i.e., the severity parameter] to the severity function could in most cases

improve the correlation of product accumulation to reaction severity, and that this required manipulation was different for different compounds." Further corroborating this claim are results from Chum *et al*. [343] showing that a value of $\varphi = 11.0 \pm 1$ provided a better fit to experimental data on the dilute-acid hydrolyzed removal of xylan and glucan from aspen wood. Lignin removal from aspen wood using organosolv pretreatment was suitably modeled using a value of $\varphi = 10.0 \pm 1$.

The most probable hydrogen production routes in sugarcane bagasse hydrothermolysis based on the data presented in previous sections involve steam reforming or WGS reactions. Steam reforming of bagasse with D_2O can result in the generation of H_2, HD, or D_2. WGS of bagasse using D_2O, however, can only result in the evolution of D_2 as shown:

$$CO + D_2O \rightarrow CO_2 + D_2 \tag{84}$$

Any methane formed from the deuterated WGS reaction above must be entirely deuterated as follows:

$$CO + 2D_2 \rightarrow CD_4 + \tfrac{1}{2}O_2 \tag{85}$$

$$CO + 3D_2 \rightarrow CD_4 + D_2O \tag{86}$$

$$CO_2 + 4D_2 \rightarrow CD_4 + D_2O \tag{87}$$

Much of the sulfur that is present in sugarcane bagasse is bound to alkali metals in the form of sulfate (SO_4^{-2}). The half-cell reactions below provide the standard electrode potential for the reduction of sulfate ion to sulfur dioxide (SO_2) in aqueous solution, sulfur dioxide to solid sulfur, and, finally, sulfur to hydrogen sulfide gas (H_2S).

$$SO_4^{-2}(aq) + 4H^+(aq) + 2e^- \rightarrow SO_2(aq) + 2H_2O(l) \qquad E^0_{cell} = +0.17\ V \tag{88}$$

$$SO_2(aq) + 4H^+(aq) + 4e^- \rightarrow S(s) + 2H_2O(l) \qquad E^0_{cell} = +0.50\ V \tag{89}$$

$$S(s) + 2H^+(aq) + 2e^- \rightarrow H_2S(g) \qquad E^0_{cell} = +0.14\ V \tag{90}$$

The net reaction for the reduction of SO_4^{-2} to H_2S can be determined by adding the previous reactions together and cancelling out components found in equimolar amounts on both sides of the reaction, as shown below:

$$SO_4^{-2}(aq) + 10H^+(aq) + 8e^- \rightarrow H_2S(g) + 4H_2O(l) \qquad E^0_{cell} = +0.33\ V \qquad (91)$$

The overall Gibbs free energy change for the net reaction was obtained by summing the change in Gibbs free energy for each reaction and then dividing by the total number of electrons lost or gained. Electrodes with higher standard reduction potentials are more readily reduced than those electrodes with lower standard reduction potentials. Species that are reduced are known as oxidizing agents and, conversely, species that are oxidized are known as reducing agents. The half-cell redox reactions for the three metals appearing in the greatest concentration in Hastelloy X are shown below in order of decreasing abundance:

$$Fe^{+2} + 2e^- \rightarrow Fe(s) \qquad E^0_{cell} = -0.44\ V \qquad (92)$$

$$Cr^{+3} + 3e^- \rightarrow Cr(s) \qquad E^0_{cell} = -0.77\ V \qquad (93)$$

$$Ni^{+2} + 2e^- \rightarrow Ni(s) \qquad E^0_{cell} = -0.25\ V \qquad (94)$$

$$Ni(s) + H_2O(l) \rightarrow NiO(s) + 2H^+(aq) + 2e^- \qquad E^0_{cell} = +0.13\ V \qquad (95)$$

The half-cell reactions for titanium are as given below:

$$Ti^{+2} + 2e^- \rightarrow Ti(s) \qquad E^0_{cell} = -1.63\ V \qquad (96)$$

$$TiO(s) + 2H^+(aq) + 2e^- \rightarrow Ti(s) + 2H_2O \qquad E^0_{cell} = -1.33\ V \qquad (97)$$

At standard conditions the electrochemical cell potential can be determined using the following equation:

$$E^0_{cell} = E^0_{cathode} - E^0_{anode} \qquad (98)$$

If E^0_{cell} is positive for a redox reaction couple, the reaction occurs spontaneously. The highest standard electrochemical cell potential among the Hastelloy X anode metals and the

sulfate ion cathodes is + 1.10 V for chromium (III). This is considerably lower than the standard cell potential for either Ti^{+2} (+ 1.99 V) or titanium oxide (+ 1.66 V). Therefore, production of H_2S would be anticipated when bagasse is hydrothermally converted in titanium reactors. Hydrogen sulfide generation in the Hastelloy X bomb is not a certainty because of the complex electrochemical interplay between the various metal species. In fact, Ni (IV) oxide can behave as a stronger oxidant than sulfur dioxide.

Almost all of the prior work on the hydrothermal conversion of sugarcane bagasse [398-403] has been focused on the fractionation of bagasse into its representative constituents under subcritical conditions, as shown in Table 32. Sasaki *et al*. [398] treated bagasse in a semi-batch, tubular percolation reactor [236, 404] that was placed in a metal salt bath heated to 200 °C. DI water preheated to 200 °C was fed to the reactor using two HPLC pumps at a flow rate of 10 $mL \cdot min^{-1}$ via a valved injection port and then both the bath and process water were heated simultaneously at a rate of 0.51 $°C \cdot min^{-1}$ to 330 °C. An aqueous extract fraction was collected continuously and sampled every 20 min. Nearly 60% of the initial bagasse weight loading was solubilized between 200–230 °C. The aqueous organic compounds at these low temperatures consisted chiefly of hemicellulose hydrolysates and aromatic compounds derived from lignin. An additional 30 wt % of the starting bagasse was extracted mainly as glucose and cellobiose between 230–280 °C, along with a few aromatic compounds. Therefore, almost 90 wt % of their original bagasse loading was converted to an aqueous organic fraction.

The remaining bagasse hydrothermal fractionation studies in subcritical water were conducted at temperatures not exceeding 230 °C [399-403]. Three of these studies were conducted using semi-batch tubular percolation reactors [400, 402, 403]. Allen *et al*. [400] determined that the quantity of bagasse solubilized was unchanged when the system was

switched from batch mode to continuous operation. Oddly, this result disagrees with the finding in the present study which shows that at 300 °C only 56 wt % of the initial bagasse charge is converted to organic semi-volatiles. The bulk of the remaining bagasse is converted to solid residue (38 wt %), while a small amount appears in the volatiles (6 wt %). Adjusting for the minor amount of ash content (4.0 wt %) in the starting bagasse brings about an inconsequential change in the product distribution levels. The difference in the results is most likely a result of the introduction of a water stream to the system. It is reasoned that the semi-continuous flow of water led to better mixing with the bagasse inside the reactor, thereby resulting in more efficient diffusional mass transfer between the bagasse substrate particles and the surrounding solvent medium. At 400 °C under near-critical conditions (i.e., P = 619 bar), the most noticeable changes in the overall product distribution are to the solids and volatiles levels. The volatiles content doubles to 12 wt %, while the solids fraction decreases to 31 wt %.

Table 32. Comparison of sugarcane bagasse hydrothermal conversion studies.

Feedstock	Particle Size	Process Type	T [°C]	P [bar]	Time [min]	Severity [log R_o]	Biomass Conversion	Ref.
Bagasse	NA	Percolation	195	100	110	4.8	50	[403]
Sugarcane	1 mm	Percolation	230	345	2	4.1	41	[402]
Energy cane	1 mm	Percolation	230	345	2	4.1	46	[402]
Bagasse	NA	Steam Explosion	210	NA	2	3.5	28	[401]
Bagasse/ leaves[31]	Unground	Percolation	230	50	2	4.0	50	[400]
Bagasse	> 37 μm	Percolation	280	NA	157[32]	7.5	90	[398]
Bagasse	< 2 mm	Batch SCW	500	707	10[33]	6.6	82	This study

[31] Conversion not sensitive to form of sugarcane used or its moisture content (8 or 50 wt %)
[32] Calculated based on 0.51 °C min^{-1} heating rate provided
[33] Includes 5 min heating period

Considering the magnetic appeal of hydrothermal biomass conversion processes during the last two decades, it is unusual that there has been comparatively little research carried out on the reaction dynamics driving these systems. Most of the work on hydrothermal reaction kinetics has been conducted using model biomass compounds as noted in Chapter 2. Some of this perceived reluctance to perform detailed kinetic studies on biomass hydrothermolysis stems from the complex nature of the hydrothermal reactions themselves. The presence of numerous intermediates, many of which remain unidentified, is a serious complicating factor in any detailed kinetic analysis. The fact that almost every compound can be formed using parallel reaction routes poses a further setback for the interpretation of individual component kinetics. Moreover, the existence of reversible reactions, including the reversible isomerization of glyceraldehyde to dihydroxyacetone and enediol isomerization via the LBAE transformation, adds yet another impediment in the development of a comprehensive reaction kinetic model. The scientific community may also be hesitant to engage in hydrothermolytic kinetic work because a "complete" kinetic model must incorporate all the factors that influence the hydrothermal process, such as temperature, heating rate, residence time, weight loading, particle size, water density, biomass type, etc. Construction of an exhaustive kinetic model is not only a laborious effort, but it is also a potentially risky endeavor because:

1) the failure to identify and properly record the concentration of every intermediate and compound formed casts doubt on the validity of such a "complete" kinetic model
2) there is a possibility that the model has overlooked various confounding variables, such as reactive impurities, that could also give rise to the observed kinetic behavior

3) it must be assumed that a detailed hydrothermal kinetic model is only applicable to the specific system being described and therefore any changes to the operational parameters of the system automatically invalidate the kinetic model
4) any such comprehensive kinetic model is only as good as the data used in its formulation; thus, a high degree of uncertainty in kinetic data measurements will be reflected in the corresponding kinetic model.

The preceding difficulties associated with comprehensive chemical kinetic analyses of hydrothermal systems should not be construed as an implicit discouragement regarding the development of tractable kinetic models but rather as obstacles that must be overcome. Indeed, the formulation of accurate kinetic models describing the rate of reaction for hydrothermal biomass conversion processes is requisite to acquire a better understanding of the reaction mechanisms involved. The kinetic approach applied in the analysis of the bagasse hydrothermal reaction dynamics herein provides a useful framework from which the overall apparent reaction kinetics can begin to be qualitatively evaluated. Nonetheless, the global kinetic rate model that was developed for the current bagasse hydrothermal conversion system illustrates the formidable challenges entailed. For instance, the use of traditional linear least squares regression techniques was unable to differentiate between first and second order kinetics, with both the first and second order models giving a coefficient of determination higher than 0.991.

The volatile product was also evaluated on the basis of the ratio of hydrogen atoms to carbon atoms (H/C) and the ratio of oxygen atoms to carbon atoms (O/C) to better characterize the energetic quality of the gas. Van Krevelen diagrams [405] are commonly used to visualize changes occurring in the H/C and O/C ratios during biomass processing. The Van Krevelen diagram provides a convenient graphical method for representing simple reaction processes.

Methanation reactions involve a diagonal shift from high O/C ratios to high H/C ratios. Dehydration occurs with a shift toward lower O/C and H/C ratios. Decarboxylation reactions require a shift from higher to lower O/C ratios. A Van Krevelen diagram for the bagasse hydrothermal conversion results is provided in Figure 74. The reaction time (denoted by blue triangles) proceeds from left to right in the following order: 30 min, 10 min, 5 min, 1 min, 60 min. Thus, it can be seen that increasing reaction time generally causes methanation of the volatile gas product until a residence time of 30 min has been reached. This trend abruptly ends at 60 min, which is attributed to the increasing oxygenolysis of organic intermediates and solid residues at extended reaction times. Hydrolysis may also occur in the period between 30 and 60 min, as evidenced by the higher content of H and O atoms. The effect of raising the temperature is the antithesis of increasing the residence time on the Van Krevelen plot. It can be seen that increasing temperature (right to left, inverted green triangles) results in a dramatic methanation of the volatile gas product. Other compounds are provided as a matter of reference for the O/C and H/C ratios obtained from the supercritical water treatment of bagasse.

The Van Krevelen plot may also provide assistance in assessing the opportunity cost between higher operation temperatures and longer process times. It can be seen that a residence time of 30 min at 500 ºC results in a volatile product that is nearest in nature to those of the petroleum compounds that are situated along the ordinate of the Van Krevelen diagram. Bagasse processed at 600 ºC for 5 min has the identical O/C ratio (0.71) as that of bagasse processed at 500 ºC for 10 min. The additional 100 ºC does raise the H/C ratio from 2.41 to 2.55, yet a further increase in reaction time at 500 ºC to 30 min provides an H/C ratio of 2.48. Ultimately, the economic trade-off decision will also depend on the type of product that is desired (e.g., natural gas, hydrocarbon, specialty chemical, etc.)

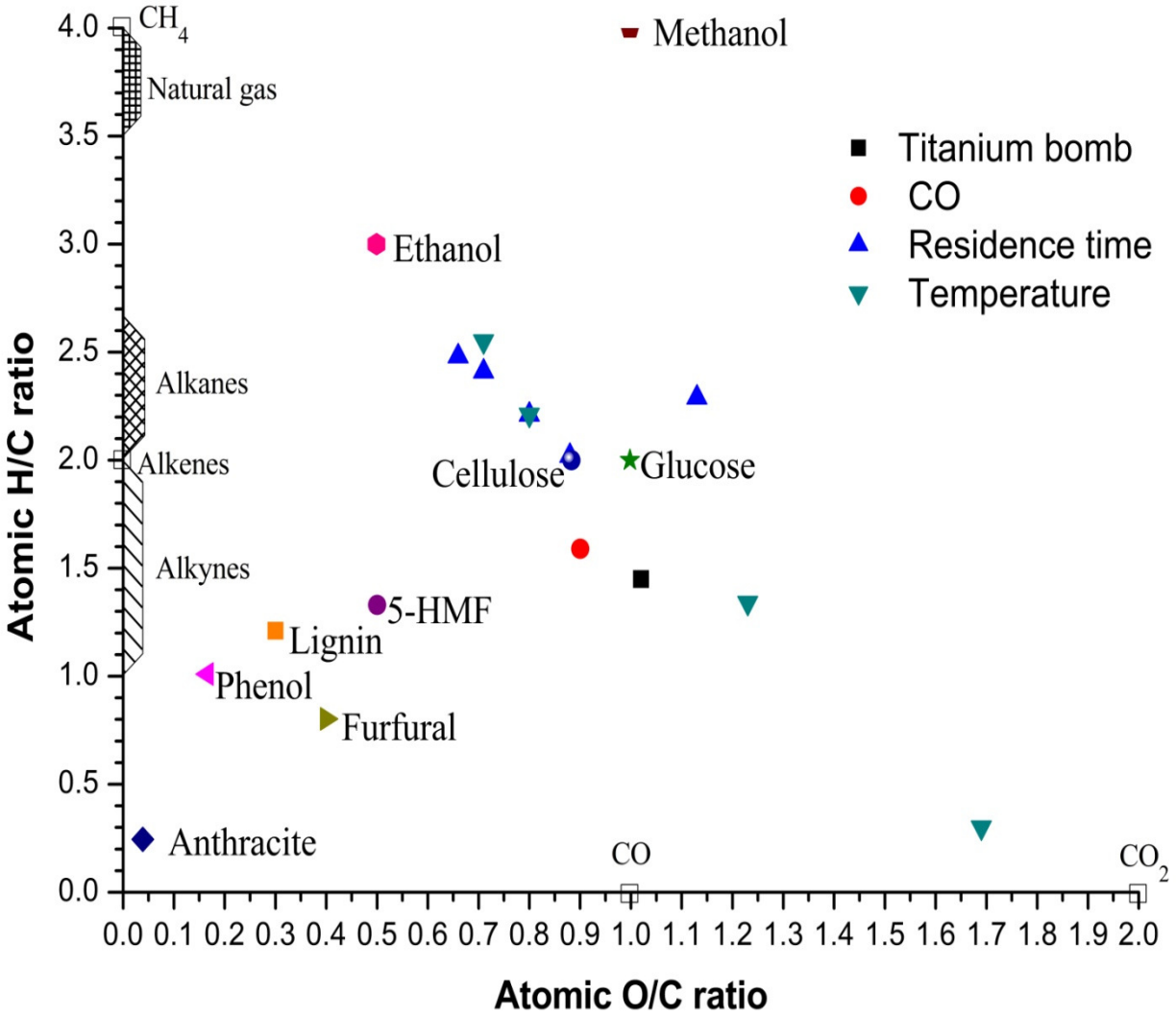

Figure 74. Van Krevelen Diagram for Bagasse Hydrothermal Conversion Compared with Various Chemicals and Biomass Types

Chapter 6. STATEMENT OF MAJOR CLAIMS

The volatile product yields and distributions obtained from sugarcane bagasse hydrothermal treatment were comprehensively investigated. The effects of primary process variables, such as temperature, residence time, biomass concentration, and particle size, and secondary external parameters, such as catalysts, reductants, and metallic reactor walls, on volatiles formation were examined.

Temperature had the greatest influence on gas production and distribution. The largest increase in gas yield occurred between 400 and 500 °C, with production rising from 11.97 to 35.13 wt %. At 600ºC, the volatile phase represented just over 50 wt % of the total phase yield of products from bagasse. The H_2 mass yield increased almost exponentially with rising temperature as evinced by a 1000% increase in H_2 formation between 300 and 600 ºC. The dramatic shifts in gas composition and yield with temperature can broadly be explained by a change in the degradation chemistry of bagasse. At subcritical and near-critical temperatures bagasse decomposition is largely regulated by pyrolytic mechanisms, whereas at supercritical temperatures the degradation of bagasse occurs primarily via gasification reactions.

Bagasse conversion increased 12.1 wt % when reaction times were extended from 1 to 60 min. Over this same time interval, there was a 49% increase in the mass yield of volatile products from bagasse, which points to mounting importance of thermal cracking reactions with time. A decreasing volatile heating value after 10 min, however, suggests that thermal cracking of intermediate compounds is accompanied by oxygenolysis of semi-volatiles and solid residues. Increased biomass weight loading resulted in decreased volatiles formation and higher solids production. Generation of solid residue jumped more than 31% between the 4.0 and 8.0 wt % biomass loadings. Biomass conversion declined by approximately 6% at the highest biomass

concentration. The use of very fine particles (63–106 μm) resulted in roughly 10% lower bagasse conversion than in the cases where larger bagasse particles were employed. This result does not conform to chemical engineering fundamentals wherein small particles would be expected to have more available surface area with which to react, thereby providing higher biomass conversion yields than larger particles. It is posited that the smallest bagasse particles either have a higher inorganic content or that they can sinter under hydrothermal conditions to form agglomerates with greater structural integrity. Intermediate size particles (250–355 μm) exhibited an interesting decrease in molar volatile yields relative to unsieved bagasse. It is possible that this size fraction has a higher content of pith rather than fiber. The superposition principle was able to adequately approximate the gaseous distribution of an actual bagasse sample using weighted averages from the individual size fractions.

The use of catalysts improved bagasse conversion by about 10%. An unexpected selectivity of the catalysts to C_3 olefins was observed for both catalysts. A possible mechanism for the increased proportion of propylene relative to that of propane was postulated. The reductants used in the hydrothermal bagasse treatment studies did not behave similarly. Charging the bomb with CO resulted in a significantly larger final CO content, whereas the yields of the other volatile compounds all declined in comparison to a standard, baseline run at 500 °C. The addition of a reducing hydride ($NaBH_4$) to the hydrothermal system resulted in the conversion of roughly 99 wt% of the starting bagasse (on a dafb basis).

An isotopic exchange study performed with deuterium oxide revealed that H and D are exchanged in the methane product formed during hydrothermal conversion of bagasse. Thus, it was established that at least some portion of the hydrogen present in the hydrocarbons evolved during SCW biomass treatment are derived from the water, instead of entirely from the biomass.

Further tests with GC-C-IRMS or cryogenic GC would be required to validate these findings conclusively.

Traditional apparent rate kinetic techniques were used to evaluate the hydrothermal bagasse system. The limitations of such methods to a complex degradation process involving multiple reaction steps were made apparent. Essen's method was incapable of discriminating between 1st and 2nd order rate laws, whereas Van't Hoff's method was able to expose the peculiar kinetic profile for bagasse decomposition in supercritical water. Incorporation of a severity function allowed the influence of disparate parameters, such as temperature and residence time, on product composition and yield to be evaluated on a uniform basis. It is believed that this paper represents the first time the severity parameter has been applied to supercritical water gasification of biomass. At 500 °C, an equivalent amount of bagasse could be converted by either increasing the temperature 10 °C or by extending the residence time by 1.8 min. The optimal severity parameter at 500 °C was found to be 26.92, which is considerably higher than the typical value of 14.75 used for subcritical processes. The large departure in these values offers proof that conditions in supercritical environments are much harsher than those in subcritical environments. Arrhenius parameters for bagasse hydrothermal conversion were calculated on the basis of treatment severity. The activation energy and frequency factor for bagasse conversion performed at 500 °C under baseline conditions were determined to be 101.4 $kJ \cdot mol^{-1}$ and 1.28×10^{9} min^{-1}, respectively.

The visible differences between the gas composition and yields, most notably for CO, for bagasse hydrothermolysis runs conducted in the titanium bomb and those conducted in the Hastelloy X bomb help support the theory that the metal walls of the reactor are likely acting as catalysts in the hydrothermal conversion reactions.

REFERENCES

[1] Garcìa-Pèrez, M.; Chaala, A.; Yang, J.; Roy, C., Co-Pyrolysis of Sugarcane Bagasse with Petroleum Residue. Part I: Thermogravimetric Analysis. *Fuel* **2001,** *80*, 1245-1258.

[2] Dayton, D. C.; Chum, H. L., Symposium on Biomass Fuels: An Introduction. *Energy & Fuels* **1996,** *10* (2), 267-268.

[3] Greer, D., Creating Cellulosic Ethanol: Spinning Straw into Fuel. *BioCycle* **2005,** *46* (4), 61-67.

[4] USDA/Agricultural Research Service, Controlling Kudzu With Naturally Occurring Fungus; *ScienceDaily*, p. 1; [published online July 20, 2009]. (accessed January 18, 2010).

[5] Cogon Grass Becoming Scourge of the South. *New York Times* Oct 20, 2003.

[6] Berl, E., Production of Oil from Plant Material. *Science* **1944,** *99*, 309-312.

[7] Heinemann, H., Petroleum-Type Hydrocarbons from Sugar Cane. *Petroleum Refiner* **1950,** *29* (2), 111-114.

[8] ASCL American Sugar Cane League The Louisiana Sugar Industry. 2005 http://www.amscl.org/SugarIndustry.pdf (accessed May 30, 2006).

[9] Meier, D.; Faix, O., State of the Art of Applied Fast Pyrolysis of Lignocellulosic Materials - a Review. *Bioresource Technology* **1999,** *68* (1), 71-77.

[10] De Filippis, P.; Borgianni, C.; Paolucci, M.; Pochetti, F., Gasification Process of Cuban Bagasse in a Two-Stage Reactor. *Biomass & Bioenergy* **2004,** *27* (3), 247-252.

[11] Kruse, A.; Henningsen, T.; Sinağ, A.; Pfeiffer, J., Biomass Gasification in Supercritical Water: Influence of the Dry Matter Content and the Formation of Phenols. *Industrial & Engineering Chemistry Research* **2003,** *42* (16), 3711-3717.

[12] Kruse, A.; Dinjus, E., Hot Compressed Water as Reaction Medium and Reactant 2. Degradation Reactions. *Journal of Supercritical Fluids* **2007,** *41*, 361-379.

[13] Watanabe, M.; Sato, T.; Inomata, H.; Smith, J., Richard L.; Arai, K.; Kruse, A.; Dinjus, E., Chemical Reactions of C_1 Compounds in Near-Critical and Supercritical Water. *Chemical Reviews* **2004,** *104* (12), 5803-5821.

[14] Siskin, M.; Katritzky, A. R., Reactivity of Organic Compounds in Hot Water: Geochemical and Technological Implications. *Science* **1991,** *254* (5029), 231-237.

[15] Savage, P. E., Organic Chemical Reactions in Supercritical Water. *Chemical Reviews* **1999,** *99* (2), 603-622.

[16] Matsumura, Y.; Minowa, T.; Potic, B.; Kersten, S. R. A.; Prins, W.; van Swaaij, W. P. M.; van de Beld, B.; Elliott, D. C.; Neuenschwander, G. G.; Kruse, A.; Antal, M. J., Biomass Gasification in Near- and Super-Critical Water: Status and Prospects. *Biomass & Bioenergy* **2005,** *29* (4), 269-292.

[17] Schmieder, H.; Abeln, J.; Boukis, N.; Dinjus, E.; Kruse, A.; Kluth, M.; Petrich, G.; Sadri, E.; Schacht, M., Hydrothermal Gasification of Biomass and Organic Wastes. *Journal of Supercritical Fluids* **2000,** *17*, 145-153.

[18] Kruse, A., Hydrothermal Biomass Gasification. *Journal of Supercritical Fluids* **2009,** *47*, 391-399.

[19] Bröll, D.; Kaul, C.; Krämer, A.; Krammer, P.; Richter, T.; Jung, M.; Vogel, H.; Zehner, P., Chemistry in Supercritical Water. *Angewandte Chemie International Edition* **1999,** *38*, 2998-3014.

[20] Shaw, R. W.; Brill, T. B.; Clifford, A. A.; Eckert, C. A.; Franck, E. U., Supercritical Water: A Medium for Chemistry. *C&EN* December 23, 1991, pp 26-39.

[21] Junk, T.; Catallo, W. J., Preparative Supercritical Deuterium Exchange in Arenes and Heterocycles. *Tetrahedron Letters* **1996,** *37*, 3445-3448.

[22] Yao, J.; Evilia, R. F., Deuteration of Extremely Weak Organic Acids by Enhanced Acid-Base Reactivity in Supercritical Deuteroxide Solution. *Journal of the American Chemical Society* **1994,** *116*, 11229-11233.

[23] Peterson, A. A.; Vogel, F.; Lachance, R. P.; Fröling, M.; Antal Jr., M. J.; Tester, J. W., Thermochemical Biofuel Production in Hydrothermal Media: A Review of Sub- and Supercritical Water Technologies. *Energy & Environmental Science* **2008,** *1*, 32-65.

[24] Rabenau, A., The Role of Hydrothermal Synthesis in Preparative Chemistry. *Angewandte Chemie International Edition* **1985,** *24*, 1026-1040.

[25] de Sénarmont, H., *Annales des Chimie et des Physique* **1851,** *32*, 129.

[26] Simoneit, B. R. T.; Lonsdale, P. F., Hydrothermal Petroleum in Mineralized Mounds at the Seabed of Guaymas Basin. *Nature* **1982,** *295*, 198-202.

[27] Simoneit, B. R. T., Hydrothermal Effects on Organic Matter - High Versus Low Temperature Components. *Organic Geochemistry* **1984,** *6*, 857-864.

[28] Bazylinski, D. A.; Farrington, J. W.; Jannasch, H. W., Hydrocarbons in Surface Sediments from a Guaymas Basin Hydrothermal Vent Site. *Organic Geochemistry* **1988,** *12* (6), 547-558.

[29] Didyk, B. M.; Simoneit, B. R. T., Hydrothermal Oil of the Guaymas Basin and Implications for Petroleum Formation Mechanisms. *Nature* **1989,** *342*, 65-69.

[30] de Ronde, C. E. J., Personal Communication, 2009.

[31] Kruse, A.; Gawlik, A., Biomass Conversion in Water at 330-410 °C and 30-50 MPa. Identification of Key Compounds for Indicating Different Chemical Reaction Pathways. *Industrial & Engineering Chemistry Research* **2003,** *42* (2), 267-279.

[32] Sinağ, A.; Kruse, A.; Schwarzkopf, V., Formation and Degradation Pathways of Intermediate Products Formed During the Hydropyrolysis of Glucose as a Model Substance for Wet Biomass in a Tubular Reactor. *Engineering Life Science* **2003,** *3* (12), 469-473.

[33] Ogihara, Y.; Smith, J., R. L.; Inomata, H.; Arai, K., Direct Observation of Cellulose Dissolution in Subcritical and Supercritical Water Over a Wide Range of Water Densities (500-1000 kg/m^3). *Cellulose* **2005,** *12*, 595-606.

[34] Hashaikeh, R.; Fang, Z.; Butler, I. S.; Kozinski, J. A., Sequential Hydrothermal Gasification of Biomass to Hydrogen. *Proceedings of the Combustion Institute* **2005,** *30*, 2231-2237.

[35] Osada, M.; Sato, T.; Watanabe, M.; Shirai, M.; Arai, K., Catalytic Gasification of Wood Biomass in Subcritical and Supercritical Water. *Combustion Science and Technology* **2006,** *178* (1-3), 537-552.

[36] Kishida, H.; Jin, F.; Yan, X.; Moriya, T.; Enomoto, H., Formation of Lactic Acid from Glycoaldehyde by Alkaline Hydrothermal Reaction. *Carbohydrate Research* **2006,** *341*, 2619-2623.

[37] Fang, Z.; Minowa, T.; Fang, C.; Smith, J., Richard L.; Inomata, H.; Kozinski, J. A., Catalytic Hydrothermal Gasification of Cellulose and Glucose. *International Journal of Hydrogen Energy* **2008,** *33*, 981-990.

[38] Sinağ, A.; Gülbay, S.; Uskan, B.; Güllü, M., Comparative Studies of Intermediates Produced from Hydrothermal Treatments of Sawdust and Cellulose. *The Journal of Supercritical Fluids* **2009,** *50*, 121-127.

[39] Demirbaş, A., Hydrogen-Rich Gas from Fruit Shells via Supercritical Water Extraction. *International Journal of Hydrogen Energy* **2004,** *29* (12), 1237-1243.

[40] Kabyemela, B. M.; Adschiri, T.; Malaluan, R. M.; Arai, K., Kinetics of Glucose Epimerization and Decomposition in Subcritical and Supercritical Water. *Industrial & Engineering Chemistry Research* **1997,** *36* (5), 1552-1558.

[41] Matsumura, Y.; Yanachi, S.; Yoshida, T., Glucose Decomposition Kinetics in Water at 25 MPa in the Temperature Range of 448-673 K. *Industrial & Engineering Chemistry Research* **2006,** *45* (6), 1875-1879.

[42] Yoshida, T.; Yanachi, S.; Matsumura, Y., Glucose Decomposition in Water under Supercritical Pressure at 448-498 K. *Journal of the Japan Institute of Energy* **2007,** *86* (9), 700-706.

[43] Kabyemela, B. M.; Adschiri, T.; Malaluan, R. M.; Arai, K., Glucose and Fructose Decomposition in Subcritical and Supercritical Water: Detailed Reaction Pathway, Mechanisms, and Kinetics. *Industrial & Engineering Chemistry Research* **1999,** *38* (8), 2888-2895.

[44] Khajavi, S. H.; Kimura, Y.; Oomori, T.; Matsuno, R.; Adachi, S., Kinetics on Sucrose Decomposition in Subcritical Water. *LWT* **2005,** *38*, 297-302.

[45] Khajavi, S. H.; Kimura, Y.; Oomori, T.; Matsuno, R.; Adachi, S., Decomposition Kinetics of Maltose in Subcritical Water. *Bioscience, Biotechnology, and Biochemistry* **2004,** *68* (1), 91-95.

[46] Sasaki, M.; Adschiri, T.; Arai, K., Kinetics of Cellulose Conversion at 25 MPa in Sub- and Supercritical Water. *AIChE Journal* **2004,** *50* (1), 192-202.

[47] Kamio, E.; Sato, H.; Takahashi, S.; Noda, H.; Fukuhara, C.; Okamura, T., Liquefaction Kinetics of Cellulose Treated by Hot Compressed Water Under Variable Temperature Conditions. *Journal of Material Science* **2007,** *43* (7), 2179-2188.

[48] Kabyemela, B. M.; Adschiri, T.; Malaluan, R. M.; Arai, K., Mechanism and Kinetics of Cellobiose Decomposition in Sub- and Supercritical Water. *Industrial & Engineering Chemistry Research* **1998,** *37* (2), 357-361.

[49] Sasaki, M.; Furukawa, M.; Minami, K.; Adschiri, T.; Arai, K., Kinetics and Mechanism of Cellobiose Hydrolysis and Retro-Aldol Condensation in Subcritical and Supercritical Water. *Industrial & Engineering Chemistry Research* **2002,** *41* (26), 6642-6649.

[50] Overend, R. P.; Chornet, E., Fractionation of Lignocellulosics by Steam-Aqueous Pretreatments. *Philosophical Transactions of the Royal Society of London Series A-Mathematical Physical and Engineering Sciences* **1987,** *321* (1561), 523-536.

[51] Chen, S.-F.; Mowery, R. A.; Chambliss, C. K.; van Walsum, G. P., Pseudo Reaction Kinetics of Organic Degradation Products in Dilute-Acid-Catalyzed Corn Stover Pretreatment Hydrolysates. *Biotechnology and Bioengineering* **2007,** *98* (6), 1135-1145.

[52] Garrote, G.; Kabel, M.; Schols, H. A.; Falqué, E.; Domínguez, H.; Parajó, J. C., Effects of *Eucalyptus globulus* Wood Autohydrolysis Conditions on the Reaction Products. *Journal of Agricultural and Food Chemistry* **2007,** *55* (22), 9006-9013.

[53] Rogalinski, T.; Ingram, T.; Brunner, G., Hydrolysis of Lignocellulosic Biomass in Water Under Elevated Temperatures and Pressures. *Journal of Supercritical Fluids* **2008,** *47*, 54-63.

[54] Klass, D. L., *Biomass for Renewable Energy, Fuels, and Chemicals*. Academic Press: San Diego, Calif., 1998; 651 p.

[55] Brown, R. C., *Biorenewable Resources: Engineering New Products from Agriculture*. Iowa State Press: Ames, Iowa, 2003; 286 p.

[56] Blažej, A.; Košik, M., *Phytomass: A Raw Material for Chemistry and Biotechnology*. Ellis Horwood Ltd.: Chichester, England, 1993; 450 p.

[57] Whittaker, R. H.; Likens, G. E.; Lieth, H., Scope and Purpose of This Volume. In *Primary Productivity of the Biosphere*, Lieth, H.; Whittaker, R. H., Eds. Springer-Verlag: New York, N.Y., 1975; pp 3-5.

[58] Whittaker, R. H.; Likens, G. E., The Biosphere and Man. In *Primary Productivity of the Biosphere*, Lieth, H.; Whittaker, R. H., Eds. Springer Verlag: New York, N.Y., 1975; pp 305-328.

[59] Kamm, B.; Kamm, M.; Schmidt, M.; Hirth, T.; Schulze, M., Lignocellulose-Based Chemical Products and Product Family Trees. In *Biorefineries-Industrial Processes and Products, Status Quo and Future Directions*, Kamm, B.; Gruber, P. R.; Kamm, M., Eds. Wiley-VCH Verlag GmbH: Weinheim, Germany, 2006; Vol. 2, pp 97-149.

[60] Fengel, D.; Wegener, G., *Wood: Chemistry, Ultrastructure, Reactions*. Walter de Gruyter & Co.: Berlin, Germany, 1983; 613 p.

[61] Gruber, E., *Papier* **1976,** *30*, 533-537.

[62] Bailey, J. E.; Ollis, D. F., *Biochemical Engineering Fundamentals*. 2nd ed.; McGraw-Hill: New York, N.Y., 1986; 984 p.

[63] Murwanashyaka, J. N.; Pakdel, H.; Roy, C., Step-Wise and One-Step Vacuum Pyrolysis of Birch-Derived Biomass to Monitor the Evolution of Phenols. *Journal of Analytical and Applied Pyrolysis* **2001,** *60* (2), 219-231.

[64] Arseneau, D. F., Competitive Reactions in the Thermal Decomposition of Cellulose. *Canadian Journal of Chemistry* **1971,** *49*, 632-638.

[65] Thompson, N. S., Hemicellulose as a Biomass Resource. In *Wood and Agricultural Residues: Research on Use for Feed, Fuels, and Chemicals*, Soltes, E. J., Ed. Academic Press: New York, NY, 1983; pp 101-119.

[66] McKinney, J. W., *Paper Trade Journal* **1946,** *122* (4), 58.

[67] Abatzoglou, N.; Koeberle, P. G.; Chornet, E.; Overend, R. P.; Koukios, E. G., Dilute Acid Hydrolysis of Lignocellulosics: An Application to Medium Consistency Suspensions of Hardwoods Using a Plug Flow Reactor. *Canadian Journal of Chemical Engineering* **1990,** *68*, 627-638.

[68] Alén, R.; Kuoppala, E.; Oesch, P., Formation of the Main Degradation Compound Groups from Wood and its Components During Pyrolysis. *Journal of Analytical and Applied Pyrolysis* **1996,** *36* (2), 137-148.

[69] Payen, A., *Comptes Rendus* **1838,** *7*, 1052.

[70] Chum, H. L.; Baizer, M. M., *The Electrochemistry of Biomass and Derived Materials*. American Chemical Society: Washington, DC, 1985; 314 p.

[71] Sederoff, R. R.; MacKay, J. J.; Ralph, J.; Hatfield, R. D., Unexpected Variation in Lignin. *Current Opinion in Plant Biology* **1999,** *2*, 145-152.

[72] Pearl, I. A., *The Chemistry of Lignin*. Marcel Dekker: New York, NY, 1967; 339 p.

[73] Freudenberg, K.; Neish, A. C., *Constitution and Biosynthesis of Lignin*. Springer-Verlag: New York, N.Y., 1968; 129 p.

[74] Nimz, H., Beech Lignin-Proposal of a Constitutional Scheme. *Angewandte Chemie International Edition* **1974,** *13* (5), 313-321.

[75] Adler, E., Lignin Chemistry — Past, Present and Future. *Wood Science and Technology* **1977,** *11* (3), 169-218.

[76] Glasser, W. G.; Glasser, H. R., Simulation of Reactions with Lignin by Computer (Simrel). II. A Model for Softwood Lignin. *Holzforschung* **1974,** *28* (1), 5-11.

[77] Sakakibara, A., A Structural Model of Softwood Lignin. *Wood Science and Technology* **1981,** *14* (2), 89-100.

[78] Forss, K. G.; Fremer, K. E., Vol. 4, in Proceedings of the The Ekman-Days 1981 International Symposium on Wood and Pulping Chemistry, Stockholm, Sweden; June 9-12, 1981; pp 29-38.

[79] Brunow, G., *Oxidative Coupling of Phenols and the Biosynthesis of Lignin*. American Chemical Society: Washington, DC, 1998; 131-147 p.

[80] Himmel, M. E.; Baker, J. O.; Overend, R. P., *Enzymatic Conversion of Biomass for Fuel Production*. American Chemical Society: Washingon, DC, 1994.

[81] Bagby, M. O.; Nelson, G. H.; Helman, E. G.; Clark, E. F., Determination of Lignin in Non-Wood Plant Fiber Sources. *Tappi* **1971,** *54*, 1876-1878.

[82] Shafizadeh, F., Introduction to Pyrolysis of Biomass. *Journal of Analytical and Applied Pyrolysis* **1982,** *3* (4), 283-305.

[83] Scurfield, G., Reaction Wood: Its Structure and Function. *Science* **1973,** *179* (4074), 647-655.

[84] Brunow, G., Lignin Chemistry and Its Role in Biomass Conversion. In *Biorefineries-Industrial Processes and Products, Status Quo and Future Directions*, Kamm, B.; Gruber, P. R.; Kamm, M., Eds. Wiley-VCH Verlag: Weinheim, Germany, 2006; Vol. 1, pp 151-163.

[85] Várhegyi, G.; Antal Jr., M. J.; Jakab, E.; Szabó, P., Kinetic Modeling of Biomass Pyrolysis. *Journal of Analytical and Applied Pyrolysis* **1997,** *42*, 73-87.

[86] FAO Food and Agriculture Organization of the United Nations FAOSTAT. 2009 http://faostat.fao.org/site/567/DesktopDefault.aspx?PageID=567#ancor (accessed February 27, 2009).

[87] Azucarera del Guadalfeo S.A. . 2009 http://www.az-guadalfeo.com/en/sugar.html (accessed February 28, 2009).

[88] Blume, H., *Geography of Sugar Cane*. Verlag Dr. Albert Bartens: Berlin, Germany, 1985; 371 p.

[89] Burr, G. O.; Hartt, C. E.; Brodie, H. W.; Tanimoto, T.; Kortschak, H. P.; Takahashi, D.; Ashton, F. M.; Coleman, R. E., The Sugarcane Plant. *Annual Reviews of Plant Physiology* **1957,** *8* (1), 275-308.

[90] Hunsigi, G., *Production of Sugarcane: Theory and Practice*. Springer-Verlag: Berlin, Germany, 1993; 245 p.

[91] Renewable Biological Systems for Alternative Sustainable Energy Production. In *FAO Agricultural Services Bulletin*, Miyamoto, K., Ed. FAO: Rome, Italy, 1997; p 108.

[92] Chae, S. R.; Hwang, E. J.; Shin, H. S., Single Cell Protein Production of *Euglena gracilis* and Carbon Dioxide Fixation in an Innovative Photo-Bioreactor. *Bioresource Technology* **2006,** *97* (2), 322-329.

[93] Chisti, Y., Biodiesel from Microalgae Beats Bioethanol. *Trends in Biotechnology* **2008,** *26* (3), 126-131.

[94] Dismukes, G. C.; Carrieri, D.; Bennette, N.; Ananyev, G. M.; Posewitz, M. C., Aquatic Phototrophs: Efficient Alternatives to Land-Based Crops for Biofuels. *Current Opinion in Biotechnology* **2008,** *19* (3), 235-240.

[95] Gross, M., Algal Biofuel Hopes. *Current Biology* **2008,** *18* (2), R46-R47.

[96] Li, Y.; Horsman, M.; Wu, N.; Lan, C. Q.; Dubois-Calero, N., Biofuels from Microalgae. *Biotechnology Progress* **2008,** *24* (4), 815-820.

[97] Thompson, G. D., Production of Biomass by Sugarcane. *Proceedings of Australian Society of Sugar Cane Technologists* **1978,** *52*, 180-187.

[98] Thompson, G. D., Comparisons of the Growth of Plant and First Ratoon Crops at Pongola. *Proceedings of Australian Society of Sugar Cane Technologists* **1988,** *62*, 180-184.

[99] Klass, D. L., Biomass for Renewable Energy and Fuels. In *Encyclopedia of Energy*, Cleveland, C., Ed. Elsevier Amsterdam, The Netherlands, 2004; Vol. 1, pp 193-212.

[100] Polack, J. A.; West, M., Bioconversions of Sugar Cane Products. In *Secondary Bioconversions of Sugar Cane Products*, U.S. - Republic of China Symposium, Philadelphia, Pa.: 1978;

[101] Reijnders, L., Microalgal and Terrestrial Transport Biofuels to Displace Fossil Fuels. *Energies* **2009,** *2*, 48-56.

[102] Ledón, A. C.; González, F. A. Z., Industrializacion de la Fotosintesis Mediante la Caña de Azucar. *Asociación de Técnicos Azucareros de Cuba* **1950,** *24*, 581-590.

[103] Alexander, A. G., *The Energy Cane Alternative*. Elsevier Science Publishers: Amsterdam, The Netherlands, 1985.

[104] Huber, G. W.; Iborra, S.; Corma, A., Synthesis of Transportation Fuels from Biomass: Chemistry, Catalysts, and Engineering. *Chemical Reviews* **2006,** *106* (9), 4044-4098.

[105] Chisti, Y., Response to Reijnders: Do Biofuels from Microalgae Beat Biofuels from Terrestrial Plants? *Trends in Biotechnology* **2008,** *26* (7), 351-352.

[106] Biswas, B. C., Agroclimatology of the Sugarcane Crop. In *Technical Note No. 193*, World Meterological Organization: Geneva, Switzerland, 1988.

[107] James, G., *Sugarcane*. 2nd ed.; Blackwell Science: Oxford, UK, 2004; 216 p.

[108] Babu, C. N., *Sugarcane*. 2nd ed.; Allied Publishers: New Delhi, India, 1990; 252 p.

[109] Dixon, T. F., Spontaneous Combustion in Bagasse Stockpiles. *Proceedings of Australian Society of Sugar Cane Technologists* **1988,** *10*, 53-61.

[110] Paturau, J. M., By-Products of the Cane Sugar Industry Elsevier Science Publishers: Amsterdam, The Netherlands, 1989; p 435.

[111] van der Poel, P. W.; Schiweck, H.; Schwartz, T. K., *Sugar Technology: Beet and Cane Sugar Manufacture*. Dr. Albert Bartens KG Verlag: Berlin, Germany, 1998.

[112] Ouensanga, A.; Picard, C., Thermal Degradation of Sugar Cane Bagasse. *Thermochimica Acta* **1988,** *125*, 89-97.

[113] Rao, P. J. M., *Industrial Utilization of Sugar Cane and Its Co-products*. ISPCK Publishers: New Delhi, India, 1997; 558 p.

[114] Lipinsky, E. S., Hydrolysis of Cellulose: Mechanisms of Enzymatic and Acid Catalysis. In *Advances in Chemistry 181*, Brown, R. D., Jr.; Jarasek, L., Eds. American Chemical Society: Washington, DC, 1979; pp 1-23.

[115] Várhegyi, G.; Antal Jr., M. J.; Szekely, T.; Szabo, P., Kinetics of the Thermal Decomposition of Cellulose, Hemicellulose, and Sugar Cane Bagasse. *Energy & Fuels* **1989,** *3*, 329-335.

[116] Oak Ridge National Laboratory Bioenergy Conversion Factors. http://bioenergy.ornl.gov/papers/misc/energy_conv.html (accessed January 10, 2010).

[117] Hugot, E., *Handbook of Cane Sugar Engineering*. 3rd ed.; Elsevier Science Publishers: Amsterdam, The Netherlands, 1986; 915 p.

[118] Behne, E. R., Vol. 5, in Proceedings of the Proceedings of the 5th Conference of the Queensland Society of Sugar Cane Technologists, 1934; p 175.

[119] Nicolai, A. L., Combustion Calculations by Graphical Methods - Wood and Bagasse. *Combustion* **1942,** *14* (2), 40-44.

[120] Playne, M. J., Increased Digestibility of Bagasses by Pretreatment with Alkalis and Steam Explosion. *Biotechnology and Bioengineering* **1984,** *26* (5), 426-433.

[121] Sun, J.-X.; Xu, F.; Sun, X.-F.; Sun, R.-C.; Wu, S.-B., Comparative Study of Lignins from Ultrasonic Irradiated Sugar-Cane Bagasse. *Polymer International* **2004,** *53*, 1711-1721.

[122] El-Ashmawy, A. E.; El-Kalyoubi, S.; Fahmy, Y., Hemicelluloses of Bagasse and Rice Straw. *Egyptian Journal of Chemistry* **1975,** *18* (1), 149-156.

[123] Miranda, R.; Blanco, C. S.; Tristan, F.; Ramirez, E., *Pyrolysis of Sugarcane Bagasse: Kinetics Studies*, in Proceedings of the 2005.

[124] Trickett, R. C.; Neytzell-de Wilde, F. G., Dilute Acid Hydrolysis of Bagasse Hemicellulose. *ChemSA* **1982,** *8* (3), 11-15.

[125] Kadam, K. L., Environmental Benefits on a Life Cycle Basis of Using Bagasse-Derived Ethanol as a Gasoline Oxygenate in India. *Energy Policy* **2002,** *30*, 371-384.

[126] Irvine, J. E.; Benda, G. T. A., *Genetic Potential and Restraints in Saccharum as Energy Source*, in Proceedings of the Symposium on Alternative Uses of Sugarcane for Development in Puerto Rico, Caribe Hilton Hotel, San Juan, Puerto Rico; March 26-27, 1979.

[127] Han, Y. W.; Catalano, E. A.; Ciegler, A., Chemical and Physical Properties of Sugarcane Bagasse Irradiated with γ Rays. *Journal of Agricultural and Food Chemistry* **1983,** *31*, 34-38.

[128] Saska, M.; Ozer, E., Aqueous Extraction of Sugarcane Bagasse Hemicellulose and Production of Xylose Syrup. *Biotechnology and Bioengineering* **1995,** *45* (6), 517-523.

[129] Hessey, R. W. G., Bagasse - A Chemurgic Raw Material. *South African Sugar Journal* **1942,** *26* (7), 329-337.

[130] Rumble, J., Jr. *Reference Materials 8491, 8492, 8493, and 8494* NIST: Gaithersburg, Md., November 06, 2001; p 6, (accessed November 06).

[131] Nathan, R. A., Fuels from Sugar Crops. Systems Study for Sugarcane, Sweet Sorghum, and Sugar Beets. Publication No. TID-22781, US DOE Technical Information Center: Oak Ridge, Tenn., 1978; 137 pp.

[132] Morris, M.; Waldheim, L.; Linero, F. A. B.; Lamônica, H. M., Increased Power Generation from Sugar Cane Biomass - The Results of a Technical and Economic Evaluation of the Benefits of Using Advanced Gasification Technology in a Typical Brazilian Sugar Mill. *International Sugar Journal* **2002,** *104* (1242), 243-244,247-248,267.

[133] Garcia-Perez, M.; Chaala, A.; Yang, J.; Roy, C., Co-Pyrolysis of Sugarcane Bagasse with Petroleum Residue. Part I: Thermogravimetric Analysis. *Fuel* **2001,** *80* (9), 1245-1258.

[134] Drummond, A. R. F.; Drummond, I. W., Pyrolysis of Sugar Cane Bagasse in a Wire-Mesh Reactor. *Industrial & Engineering Chemistry Research* **1996,** *35* (4), 1263-1268.

[135] Edwards, B., Energy Use in Cane and Beet Factories. *Proceedings of Australian Society of Sugar Cane Technologists* **1991**, 227-229.

[136] Atchison, J. E., *Bagasse Becoming a Major Raw Material for Manufacture of Pulp and Paper*, in Proceedings of the Proceedings of the ISSCT, Elsevier Publishing Co.: New York, N.Y., 1962; pp 1185-1205.

[137] Atchison, J. E., Making the Right Choices for Successful Bagasse Newsprint Production: Part 2. *Tappi* **1993,** *76* (1), 187-193.

[138] Rangamannar, G.; Ramasamy, D., Biotechnological Aspects of Various Bagasse Storage Systems. *IPPTA* **1986,** *23*, 32-38.

[139] Rangamannar, G.; Michelsen, J.; Rangan, S. G., Improved Wet Bulk Storage of Bagasse for Newsprint Pulp Production - Part I. In *Secondary Improved Wet Bulk Storage of Bagasse for Newsprint Pulp Production - Part I*, TAPPI Pulping Conference, Atlanta, Ga., TAPPI Press: Norcross, Ga.; 1993; pp 91-95

[140] Sharma, R. K.; Yadav, K. R.; Maheshwari, V. L.; Kothari, R. M., Bagasse Preservation: A Need for a Biotechnological Approach. *Critical Reviews in Biotechnology* **2000,** *20* (4), 237-263.

[141] Covey, G.; Rainey, T.; Shore, D., The Potential for Bagasse Pulping in Australia. *Appita Journal* **2006,** *59* (1), 17-22.

[142] Dawson, M. W.; Cox, L. M.; Dixon, T. F., Storage of Bagasse: Loose Covered Piles or Bales? *Proceedings of Australian Society of Sugar Cane Technologists* **1994,** *16*, 220-228.

[143] Doble, M.; Kruthiventi, A. K., *Green Chemistry and Engineering*. Academic Press: Amsterdam, The Netherlands, 2007; 326 p.

[144] Fang, Z.; Minowa, T.; Smith, J., R. L.; Ogi, T.; Kozinski, J. A., Liquefaction and Gasification of Cellulose with Na_2CO_3 in Subcritical Water at 350 °C. *Industrial and Engineering Chemistry Research* **2004,** *43*, 2454-2463.

[145] Potic, B.; Kersten, S. R. A.; Prins, W.; van Swaaij, W. P. M., A High-Throughput Screening Technique for Conversion in Hot Compressed Water. *Industrial & Engineering Chemistry Research* **2004,** *43* (16), 4580-4584.

[146] Abdelmoez, W.; Yoshida, H., Simulation of Fast Reactions in Batch Reactors Under Sub-Critical Water Condition. *AIChE Journal* **2006,** *52* (10), 3600-3611.

[147] Hashaikeh, R.; Fang, Z.; Hawari, J.; Butler, I. S.; Kozinski, J. A., Hydrothermal Dissolution of Willow in Hot Compressed Water. *Fuel* **2007,** *86* (10-11), 1614-1622.

[148] Harvey, A. H.; Peskin, A. P.; Klein, S. A., NIST/ASME Steam Formulation for General and Scientific Use. NIST Standard Reference Database 10, Version 2.21; NIST, U.S. Department of Commerce: 1996.

[149] Atkins, P. W., *Physical Chemistry*. 5th ed.; W. H. Freeman and Co.: New York, NY, 1994; 1031 p.

[150] Josephson, J., Supercritical Fluids. *Environmental Science and Technology* **1982,** *16* (10), 548A-551A.

[151] Connoly, J. F., Solubility of Hydrocarbons in Water Near the Critical Solution Temperatures. *Journal of Chemical and Engineering Data* **1966,** *11* (1), 13-16.

[152] Martynova, O. I., Solubility of Inorganic Compounds in Subcritical and Supercritical Water. In *High Temperature, High Pressure Electrochemistry in Aqueous Solutions*, Jones, D. d. G.; Stachle, R. W., Eds. National Association of Corrosion Engineers: Houston, Texas, 1976.

[153] Pitzer, K. S.; Pabalan, R. T., Thermodynamics of NaCl in Steam. *Geochimica Cosmochimica Acta* **1986,** *50* (7), 1445-1454.

[154] Armellini, F. J.; Tester, J. W., Solubility of Sodium Chloride and Sulfate in Sub- and Supercritical Water Vapor from 450-500 °C and 100-250 bar. *Fluid Phase Equilibria* **1993,** *84*, 123-142.

[155] Lu, J.; Brown, J. S.; Liotta, C. L.; Eckert, C. A., Polarity and Hydrogen-Bonding of Ambient to Near-Critical Water: Kamlet-Taft Solvent Parameters. *Chemical Communications* **2001,** (665-666).

[156] Hoffman, M.; Conradi, M. S., Are There Hydrogen Bonds in Supercritical Water? *Journal of the American Chemical Society* **1997,** *119* (16), 3811-3817.

[157] Eigen, M.; de Maeyer, L., Untersuchungen uber die Kinetik der Neutralisation. I. *Zeitschrift für Elektrochemie* **1955,** *59*, 986.

[158] Xu, X.; De Almeida, C.; Antal Jr., M. J., Mechanism and Kinetics of the Acid-Catalyzed Dehydration of Ethanol in Supercritical Water. *Journal of Supercritical Fluids* **1990,** *3* (4), 228-232.

[159] Klein, M. T.; Torry, L. A.; Wu, B. C.; Townsend, S. H.; Paspek, S. C., Hydrolysis in Supercritical Water: Solvent Effects as a Probe of the Reaction Mechanism. *The Journal of Supercritical Fluids* **1990,** *3* (4), 222-227.

[160] Kruse, A., Supercritical Water Gasification. *Biofuels Bioproducts & Biorefining* **2008,** *2* (5), 415-437.

[161] Clifford, T., *Fundamentals of Supercritical Fluids*. Oxford University Press: Oxford, U.K., 1999; 210 p.

[162] Chen, G.; Andries, J.; Spliethoff, H.; Leung, D. Y. C., Experimental Investigation of Biomass Waste (Rice Straw, Cotton Stalk, and Pine Sawdust) Pyrolysis Characteristics. *Energy Sources* **2003,** *25* (4), 331-337.

[163] Fisher, T.; Hajaligol, M.; Waymack, B.; Kellogg, D., Pyrolysis Behavior and Kinetics of Biomass Derived Materials. *Journal of Analytical and Applied Pyrolysis* **2002,** *62* (2), 331-349.

[164] Horne, P. A.; Williams, P. T., Influence of Temperature on the Products from the Flash Pyrolysis of Biomass. *Fuel* **1996,** *75* (9), 1051-1059.

[165] Rezaiyan, J.; Cheremisinoff, N. P., *Gasification Technologies: A Primer for Engineers and Scientists*. CRC Press, Taylor and Francis Group: Boca Raton, Fla., 2005; Vol. 105, 366 p.

[166] Demirbaş, A., Hydrogen Production from Biomass by the Gasification Process. *Energy Sources* **2002,** *24* (1), 59-68.

[167] DynaMotive, *Fast Pyrolysis of Bagasse to Produce BioOil Fuel for Power Generation*, in Proceedings of the 2nd World Sugar By-Products Conference Proceedings, Miami, Fla.; February 21-22, 2001; DynaMotive Energy Systems Corporation.

[168] Maschio, G.; Koufopanos, C.; Lucchesi, A., Pyrolysis, a Promising Route for Biomass Utilization. *Bioresource Technology* **1992,** *42* (3), 219-231.

[169] Graham, R. G.; Bergougnou, M. A.; Mok, L. K. S.; de Lasa, H. I., Fast Pyrolysis (Ultrapyrolysis) of Biomass Using Solid Heat Carriers. In *Fundamentals of Thermochemical Conversion*, Overend, R. P.; Milne, T. A.; Mudge, L. K., Eds. Elsevier Applied Science, Ltd.: London, U.K., 1985; pp 397-410.

[170] Bridgwater, A. V.; Meier, D.; Radlein, D., An Overview of Fast Pyrolysis of Biomass. *Organic Geochemistry* **1999,** *30* (12), 1479-1493.

[171] Xu, C.; Lad, N., Production of Heavy Oils with High Calorific Values by Direct Liquefaction of Woody Biomass in Sub/Near-Critical Water. *Energy & Fuels* **2008,** *22* (1), 635-642.

[172] Oasmaa, A.; Peacocke, C. *A Guide to Physical Property Characterization of Biomass-Derived Fast Pyrolysis Liquids* Technical Research Centre of Finland: Espoo, Finland, 2001; p 65.

[173] Grange, P.; Laurent, E.; Maggi, R.; Centeno, A.; Delmon, B., Hydrotreatment of Pyrolysis Oils from Biomass: Reactivity of the Various Categories of Oxygenated Compounds and Preliminary Techno-Economical Study. *Catalysis Today* **1996,** *29* (1-4), 297-301.

[174] Elliott, D. C.; Neuenschwander, G. G.; Hart, T. R.; Butner, R. S.; Zacher, A. H.; Engelhard, M. H.; Young, J. S.; McCready, D. E., Chemical Processing in High-Pressure Aqueous Environments. 7. Process Development for Catalytic Gasification of Wet Biomass Feedstocks. *Industrial & Engineering Chemistry Research* **2004,** *43* (9), 1999-2004.

[175] Nelson, D. A.; Molton, P. M.; Russel, J. A.; Hallen, R. T., Application of Direct Thermal Liquefaction for the Conversion of Cellulosic Biomass. *Industrial & Engineering Chemistry Product Research and Development* **1984,** *23* (3), 471-475.

[176] Molton, P. M., Liquid Fuel is Produced from Waste by Direct Thermochemical Reaction. *Chemistry International* **1980,** *4*, 20-24.

[177] Miller, R.; Molton, P. M.; Russel, J.; Donovan, J., *Fuels from Biomass and Wastes*. Ann Arbor Science Publishers: Ann Arbor, Mich., 1981; 451 p.

[178] Eager, R. L.; Mathews, J. F.; Pepper, J. M.; Zohdi, H., Studies on the Products Resulting from the Conversion of Aspen Poplar to an Oil. *Canadian Journal of Chemistry* **1981,** *59*, 2191-2198.

[179] Bergius, F. Nobel Prize Lecture. 2009 http://nobelprize.org/nobel_prizes/chemistry/laureates/1931/bergius-lecture.pdf.

[180] Bouvier, J. M.; Gelus, M.; Maugendre, S., Direct Liquefaction of Wood by Solvolysis. In *Pyrolysis Oils from Biomass Producing, Analyzing, and Upgrading*, Soltes, E. J.; Milne, T. A., Eds. American Chemical Society: Washington, D.C., 1988; pp 129-138.

[181] Elliott, D. C.; Sealock, L. J., Jr.; Butner, R. S., Product Analysis from Direct Liquefaction of Several High-Moisture Feedstocks. In *Pyrolysis Oils from Biomass Producing, Analyzing, and Upgrading*, Soltes, E. J.; Milne, T. A., Eds. American Chemical Society: Washington, D.C., 1988; pp 179-188.

[182] Soltes, E. J., Of Biomass, Pyrolysis, and Liquids Thereof. In *Pyrolysis Oils from Biomass Producing, Analyzing, and Upgrading*, Soltes, E. J.; Milne, T. A., Eds. American Chemical Society: Washington, D.C., 1988; pp 1-7.

[183] Klass, D. L., Fuels from Biomass and Wastes - An Introduction. In *Fuels from Biomass and Wastes*, Klass, D. L.; Emert, G. H., Eds. Ann Arbor Science Publishers: Ann Arbor, Mich., 1981; pp 1-41.

[184] Elliott, D. C.; Beckman, D.; Bridgwater, A. V.; Diebold, J. P.; Gevert, S. B.; Solantausta, Y., Direct Thermochemical Liquefaction of Biomass: 1983-1990. *Energy & Fuels* **1991,** *5*, 399-410.

[185] Elliott, D. C., Historical Developments in Hydroprocessing Bio-oils. *Energy & Fuels* **2007,** *21* (3), 1792-1815.

[186] Goudriaan, F.; Peferoen, D. G. R., Liquid Fuels from Biomass via a Hydrothermal Process. *Chemical Engineering Science* **1990,** *45* (8), 2279-2734.

[187] Goudriaan, F.; van de Beld, B.; Boerefijn, F. R.; Bos, G. M.; Naber, J. E.; van der Wal, S.; Zeevalkink, J. A., *Thermal Efficiency of the HTU Process for Biomass Liquefaction*, in Proceedings of the Progress in Thermochemical Biomass Conversion, Tyrol, Austria; September 18-21, 2000, 2000; Bridgwater, A. V., Ed. pp 1312-1325.

[188] Goudriaan, F. Bio-Energy Research Group, Aston University HTU Pilot Plant on Stream. Dec 2000, http://www.pyne.co.uk/Resources/user/PyNews%2010.pdf (accessed January 02, 2010).

[189] Naber, J. E.; Goudriaan, F., Successfully Using Biomass to Harness Renewable Energy in an Efficient and Cost-Effective Way. In *Secondary Successfully Using Biomass to Harness Renewable Energy in an Efficient and Cost-Effective Way*, EMINENT Workshop, Riga, Latvia, 2004. http://www.cpi.umist.ac.uk/eminent/Confidential/meeting/RigaMeeting/Riga%20Workshop/PresenatieHTUBiofuel.ppt.

[190] Appell, H. R.; Fu, Y. C.; Friedman, S.; Yavorsky, P. M. *Converting Organic Wastes to Oil: A Replenishable Energy Source* Report of Investigations No. 7560; United States Department of Interior, Bureau of Mines: Washington, D.C., 1971; p 20.

[191] Appell, H. R.; Fu, Y. C.; Illig, E. G.; Steffgen, F. W.; Miller, R. D. *Conversion of Cellulosic Wastes to Oil* Report of Investigations, No. 8013; United States Department of Interior, Bureau of Mines: Washington, D.C., 1975; p 28.

[192] Ogi, T.; Yokoyama, S.-y., Liquid Fuel Production from Woody Biomass by Direct Liquefaction. *Sekiyu Gakkaishi* **1993,** *36* (2), 73-84.

[193] Amin, S.; Reid, R. C.; Modell, M., Reforming and Decomposition of Glucose in an Aqueous Phase. In *Secondary Reforming and Decomposition of Glucose in an Aqueous Phase*, Intersociety Conference on Environmental Systems, San Francisco, Calif., July 21-24, 1975; 1975; p 8

[194] Modell, M. Gasification Process. U.S. Patent No. 4,338,199, September 12, 1978.

[195] Modell, M. Processing Methods for the Oxidation of Organics in Supercritical Water. U.S. Patent No. 4,338,199, 1982.

[196] Modell, M. Processing Methods for the Oxidation of Organics in Supercritical Water. U.S. Patent No. 4,453,190, 1985.

[197] Boocock, D. G. B.; Mackay, D.; McPherson, M.; Nadeau, S.; Thurier, R., Direct Hydrogenation of Hybrid Poplar Wood to Liquid and Gaseous Fuels. *Canadian Journal of Chemical Engineering* **1979,** *57*, 98-101.

[198] Elliott, D. C., Process Development for Direct Liquefaction of Biomass. In *Fuels from Biomass and Wastes*, Klass, D. L.; Emert, G. H., Eds. Ann Arbor Science Publishers: Ann Arbor, Mich., 1981; pp 435-450.

[199] Pober, K. W.; Bauer, H. F., The Nature of Pyrolytic Oil from Municipal Solid Waste. In *Fuels from Waste*, Anderson, L. L.; Tillman, D. A., Eds. Academic Press, Inc.: New York, N.Y., 1977; pp 73-86.

[200] Elliott, D. C. *Analysis and Upgrading of Biomass Liquefaction Products, IEA Co-operative Project D1 Biomass Liquefaction Test Facility Project Final Report* Vol. 4; National Energy Administration: Stockholm, Sweden, 1985.

[201] Turn, S. Q., Biomass Integrated Gasifier Combined Cycle Technology: Application in the Cane Sugar Industry. *International Sugar Journal* **1999,** *101* (1205), 267-272.

[202] Brown, K., Producing Renewable Hydrogen from Biomass. *BioCycle* **2004,** (January), 54-55.

[203] Asadullah, M.; Miyazawa, T.; Ito, S.; Kunimori, K.; Yamada, M.; Tomishige, K., Novel Biomass Gasification Method with High Efficiency: Catalytic Gasification at Low Temperature. *Green Chemistry* **2002,** *4* (4), 385-389.

[204] Zanzi, R.; Sjostrom, K.; Bjornbom, E., Rapid Pyrolysis of Agricultural Residues at High Temperature. *Biomass & Bioenergy* **2002,** *23* (5), 357-366.

[205] Rei, M.-H.; Yang, S. J.; Hong, C. H., Catalytic Gasification of Rice Hull and Other Biomass. The General Effect of Catalyst. *Agricultural Wastes* **1986,** *18* (4), 269-281.

[206] Antal Jr., M. J., Biomass Pyrolysis: A Review of the Literature. Part 1 - Carbohydrate Pyrolysis. *Advances in Solar Energy* **1982,** *1*, 61-111.

[207] Thurner, F.; Mann, U., Kinetic Investigation of Wood Pyrolysis. *Industrial & Engineering Chemistry Process Design and Development* **1981,** *20* (3), 482-488.

[208] Hajaligol, M. R.; Howard, J. B.; Longwell, J. P.; Peters, W. A., Product Compositions and Kinetics for Rapid Pyrolysis of Cellulose. *Industrial & Engineering Chemistry Process Design and Development* **1982,** *21* (3), 457-465.

[209] Jegers, H. E.; Klein, M. T., Primary and Secondary Lignin Pyrolysis Reaction Pathways. *Industrial & Engineering Chemistry Process Design and Development* **1985,** *24* (1), 173-183.

[210] Nunn, T. R.; Howard, J. B.; Longwell, J. P.; Peters, W. A., Product Compositions and Kinetics in the Rapid Pyrolysis of Sweet Gum Hardwood. *Industrial & Engineering Chemistry Process Design and Development* **1985,** *24* (3), 836-844.

[211] Nunn, T. R.; Howard, J. B.; Longwell, J. P.; Peters, W. A., Product Compositions and Kinetics in the Rapid Pyrolysis of Milled Wood Lignin. *Industrial & Engineering Chemistry Process Design and Development* **1985,** *24* (3), 844-52.

[212] Chan, R. W.-C.; Krieger, B. B., Kinetics of Dielectric-Loss Microwave Degradation of Polymers: Lignin. *Journal of Applied Polymer Science* **1981,** *26* (5), 1533-1553.

[213] DeGroot, W. F.; Pan, W.-P.; Rahman, M. D.; Richards, G. N., First Chemical Events in Pyrolysis of Wood. *Journal of Analytical and Applied Pyrolysis* **1988,** *13* (3), 221-231.

[214] Cetin, E.; Moghtaderi, B.; Gupta, R.; Wall, T. F., Influence of Pyrolysis Conditions on the Structure and Gasification Reactivity of Biomass Chars. *Fuel* **2004,** *83* (16), 2139-2150.

[215] Kwon, T. W.; Kim, J. R.; Kim, S. D.; Park, W. H., Catalytic Steam Gasification of Lignite Char. *Fuel* **1989,** *68*, 416-421.

[216] Asami, K.; Ohtsuka, Y., *Catalytic Behavior of Iron in the Gasification of Coal with Hydrogen*, in Proceedings of the Third International Conference on Spillover, Kyoto, Japan; August 17-20, 1993; Inui, T.; Fujimoto, K.; Uchijima, T.; Masai, M., Eds. Elsevier Science Publishers: Amsterdam, The Netherlands, 1993; pp 413-416.

[217] Lu, Y.; Guo, L.; Zhang, X.; Yan, Q., Thermodynamic Modeling and Analysis of Biomass Gasification for Hydrogen Production in Supercritical Water. *Chemical Engineering Journal* **2007,** *131* (1-3), 233-244.

[218] Minowa, T.; Inoue, S., Hydrogen Production from Biomass by Catalytic Gasification in Hot Compressed Water. *Renewable Energy* **1999,** *16* (1-4), 1114-1117.

[219] Laser, M.; Schulman, D.; Allen, S. G.; Lichwa, J.; Antal, M. J.; Lynd, L. R., A Comparison of Liquid Hot Water and Steam Pretreatments of Sugar Cane Bagasse for Bioconversion to Ethanol. *Bioresource Technology* **2002,** *81* (1), 33-44.

[220] Allen, S. G.; Schulman, D.; Lichwa, J.; Antal, M. J.; Laser, M.; Lynd, L. R., A Comparison Between Hot Liquid Water and Steam Fractionation of Corn Fiber. *Industrial & Engineering Chemistry Research* **2001,** *40* (13), 2934-2941.

[221] Goto, M.; Obuchi, R.; Hirose, T.; Sakaki, T.; Shibata, M., Hydrothermal Conversion of Municipal Organic Waste into Resources. *Bioresource Technology* **2004,** *93*, 279-284.

[222] Jin, F.; Zhou, Z.; Kishita, A.; Enomoto, H., Hydrothermal Conversion of Biomass into Acetic Acid. *Journal of Materials Science* **2006,** *41*, 1495-1500.

[223] Karayildirim, T.; Sinağ, A.; Kruse, A., Char and Coke as Unwanted Side Reaction of the Hydrothermal Biomass Gasification. *Chemical Engineering Technology* **2008,** *31* (11), 1561-1568.

[224] Vasilakos, N. P.; Austgen, D. M., Hydrogen-Donor Solvents in Biomass Liquefaction. *Industrial and Engineering Chemistry Process Design and Development* **1985,** *24*, 304-311.

[225] Sasaki, M.; Kabyemela, B. M.; Malaluan, R.; HIrose, S.; Takeda, N.; Adschiri, T.; Arai, K., Cellulose Hydrolysis in Subcritical and Supercritical Water. *Journal of Supercritical Fluids* **1998,** *13*, 261-268.

[226] Sasaki, M.; Fang, Z.; Fukushima, Y.; Adschiri, T.; Arai, K., Dissolution and Hydrolysis of Cellulose in Subcritical and Supercritical Water. *Ind. Eng. Chem. Res.* **2000,** *39* (8), 2883-2890.

[227] Williams, P. T.; Onwudili, J., Composition of Products from the Supercritical Water Gasification of Glucose: A Model Biomass Compound. *Industrial & Engineering Chemistry Research* **2005,** *44* (23), 8739-8749.

[228] Ji, P.; Feng, W.; Chen, B.; Yuan, Q., Finding Appropriate Operating Conditions for Hydrogen Purification and Recovery in Supercritical Water Gasification of Biomass. *Chemical Engineering Journal* **2006,** *124*, 7-13.

[229] Saka, S., Recent Progress in Supercritical Fluid Science for Biofuel Production from Woody Biomass. *Forestry Studies in China* **2006,** *8* (3), 9-15.

[230] Ehara, K.; Saka, S., A Comparative Study on Chemical Conversion of Cellulose Between the Batch-Type and Flow-Type Systems in Supercritical Water. *Cellulose* **2002,** *9*, 301-311.

[231] Minowa, T.; Kondo, T.; Sudirjo, S. T., Thermochemical Liquefaction of Indonesian Biomass Residues. *Biomass & Bioenergy* **1998,** *14* (5-6), 517-524.

[232] Yu, D.; Aihara, M.; Antal Jr., M. J., Hydrogen Production by Steam Reforming Glucose in Supercritical Water. *Energy & Fuels* **1993,** *7* (5), 574-577.

[233] Srokol, Z.; Bouche, A.-G.; van Estrik, A.; Strik, R. C. J.; Maschmeyer, T.; Peters, J. A., Hydrothermal Upgrading of Biomass to Biofuel; Studies on Some Monosaccharide Model Compounds. *Carbohydrate Research* **2004,** *339* (10), 1717-1726.

[234] Hao, X. H.; Guo, L. J.; Mao, X.; Zhang, X. M.; Chen, X. J., Hydrogen Production from Glucose Used as a Model Compound of Biomass Gasified in Supercritical Water. *International Journal of Hydrogen Energy* **2003,** *28* (1), 55-64.

[235] Holgate, H. R.; Meyer, J. C.; Tester, J. W., Glucose Hydrolysis and Oxidation in Supercritical Water. *AIChE Journal* **1995,** *41* (3), 637-648.

[236] Antal Jr., M. J.; Mok, W. S. L., Mechanism of Formation of 5-(Hydroxymethyl)-2-furaldehyde from D-Fructose and Sucrose. *Carbohydrate Research* **1990,** *199* (1), 91-109.

[237] Antal Jr., M. J.; Várhegyi, G., Cellulose Pyrolysis Kinetics: The Current State of Knowledge. *Industrial & Engineering Chemistry Research* **1995,** *34* (3), 703-717.

[238] Bonn, G.; Rinderer, M.; Bobleter, O., Hydrothermal Degradation and Kinetic Studies of 1,3-Dihydroxy-2-Propanone and 2,3-Dihydroxypropanal. *Journal of Carbohydrate Chemistry* **1985,** *4* (1), 67-77.

[239] Bobleter, O.; Bonn, G., The Hydrothermolysis of Cellobiose and Its Reaction-Product D-Glucose. *Carbohydrate Research* **1983,** *124*, 185-193.

[240] Krishna, R.; Kallury, M. R.; Ambidge, C.; Tidwell, T. T.; Boocock, D. G. B.; Agblevor, F. A.; Stewart, D. J., Rapid Hydrothermolysis of Cellulose and Related Carbohydrates. *Carbohydrate Research* **1986,** *158*, 253-261.

[241] Antal Jr., M. J.; Mok, W. S. L.; Richards, G. N., Four-Carbon Model Compounds for the Reactions of Sugars in Water at High Temperature *Carbohydrate Research* **1990,** *199* (1), 111-115.

[242] Luijkx, G. C. A.; van Rantwijk, F.; van Bekkum, H., Hydrothermal Formation of 1,2,4-Benzenetriol from 5-Hydroxymethyl-2-furaldehyde and D-Fructose. *Carbohydrate Research* **1993,** *242*, 131-139.

[243] Watanabe, M.; Aizawa, Y.; Iida, T.; Levy, C.; Aida, T. M.; Inomata, H., Glucose Reactions Within the Heating Period and the Effect of Heating Rate on the Reactions in Hot Compressed Water. *Carbohydrate Research* **2005,** *340* (12), 1931-1939.

[244] Matsumura, Y.; Sasaki, M.; Okuda, K.; Takami, S.; Ohara, S.; Umetsu, M.; Adschiri, T., Supercritical Water Treatment of Biomass for Energy and Material Recovery. *Combustion Science and Technology* **2006,** *178* (1-3), 509-536.

[245] Aida, T. M.; Tajima, K.; Watanabe, M.; Saito, Y.; Kuroda, K.; Nonaka, T.; Hattori, H.; Smith, J., Richard L.; Arai, K., Reactions of D-Fructose in Water at Temperatures Up to 400 °C and Pressures Up to 100 MPa. *Journal of Supercritical Fluids* **2007,** *42* (1), 110-119.

[246] Aida, T. M.; Sato, Y.; Watanabe, M.; Tajima, K.; Nonaka, T.; Hattori, H.; Arai, K., Dehydration of D-Glucose in High Temperature Water at Pressures up to 80 MPa. *Journal of Supercritical Fluids* **2007,** *40* (3), 381-388.

[247] Goto, K.; Tajima, K.; Sasaki, M.; Adschiri, T.; Arai, K., Reaction Mechanism of Sugar Derivatives in Subcritical and Supercritical Water. *Kobunshi Ronbonshu* **2001,** *58* (12), 685-691.

[248] Adschiri, T.; Hirose, T.; Malaluan, R.; Arai, K., Noncatalytic Conversion of Cellulose in Supercritical Water and Subcritical Water. *Journal of Chemical Engineering of Japan* **1993,** *26* (6), 676-680.

[249] Bobleter, O.; Pape, G., Der hydrothermale Abbau von Glucose. *Monatshefte für Chemie* **1968,** *99* (1560-1567).

[250] Saeman, J. F., Kinetics of Wood Saccharification - Hydrolysis of Cellulose and Decomposition of Sugars in Dilute Acid at High Temperature. *Industrial & Engineering Chemistry* **1945,** *37* (1), 43-52.

[251] Asghari, F. S.; Yoshida, H., Acid-Catalyzed Production of 5-Hydroxymethyl Furfural from D-Fructose in Subcritical Water. *Industrial & Engineering Chemistry Research* **2006,** *45* (7), 2163-2173.

[252] Kamio, E.; Takahashi, S.; Noda, H.; Fukuhara, C.; Okamura, T., Effect of Heating Rate on Liquefaction of Cellulose by Hot Compressed Water. *Chemical Engineering Journal* **2008,** *137*, 328-338.

[253] Kamio, E.; Takahashi, S.; Noda, H.; Fukuhara, C.; Okamura, T., Liquefaction of Cellulose in Hot Compressed Water under Variable Temperatures. *Industrial & Engineering Chemistry Research* **2006,** *45* (14), 4944-4953.

[254] Matsumura, Y.; Sasaki, M.; Okuda, K.; Takami, S.; Ohara, S.; Umetsu, M.; Adschiri, T., Supercritical Water Treatment of Biomass for Energy and Material Recovery. *Combustion Science and Technology* **2006,** *178*, 509-536.

[255] Lindsay, W. T., Hydrogen Bonding and Water Structure. In *The ASME Handbook on Water Technology for Thermal Power Systems*, Cohen, P., Ed. ASME: New York, NY, 1981; p 371.

[256] Sasaki, M.; Goto, K.; Tajima, K.; Adschiri, T.; Arai, K., Rapid and Selective Retro-Aldol Condensation of Glucose to Glycolaldehyde in Supercritical Water. *Green Chemistry* **2002,** *4* (3), 285-287.

[257] Sakaki, T.; Shibata, M.; Sumi, T.; Yasuda, S., Saccharification of Cellulose Using a Hot-Compressed Water-Flow Reactor. *Industrial & Engineering Chemistry Research* **2002,** *41* (4), 661-665.

[258] Ehara, K.; Saka, S., Decomposition Behavior of Cellulose in Supercritical Water, Subcritical Water, and Their Combined Treatments. *Journal of Wood Science* **2005,** *51* (2), 148-153.

[259] Malaluan, R. M. A Study on Cellulose Decomposition in Subcritical and Supercritical Water. Ph.D. Dissertation, Tohoku University, Sendai, Japan, 1995.

[260] Feughelman, M., Optical Birefringence and Crystallinity of Wool Fibres in Formic Acid. *Nature* **1966,** *212* (5061), 497-498.

[261] Deguchi, S.; Tsujii, K.; Horikoshi, K., Cooking Cellulose in Hot and Compressed Water. *Chemical Communications* **2006**, 3293-3295.

[262] Xiang, Q.; Lee, Y. Y.; Torget, R. W., Kinetics of Glucose Decomposition During Dilute-Acid Hydrolysis of Lignocellulosic Biomass. *Applied Biochemistry and Biotechnology* **2004,** *113-116*, 1127-1138.

[263] Yu, Y.; Lou, X.; Wu, H., Some Recent Advances in Hydrolysis of Biomass in Hot-Compressed Water and Its Comparisons with Other Hydrolysis Methods *Energy & Fuels* **2008,** *22* (1), 46-60.

[264] Shoji, D.; Sugimoto, K.; Uchida, H.; Itatani, K.; Fujie, M.; Koda, S., Visualized Kinetic Aspects of Decomposition of a Wood Block in Sub- and Supercritical Water. *Industrial & Engineering Chemistry Research* **2005,** *44* (9), 2975-2981.

[265] D'Jesus, P.; Boukis, N.; Kraushaar-Czarnetzki, B.; Dinjus, E., Influence of Process Variables on Gasification of Corn Silage in Supercritical Water. *Industrial & Engineering Chemistry Research* **2006,** *45* (5), 1622-1630.

[266] Yokoyama, S.-y.; Ogi, T.; Koguchi, K.; Nakamura, E., Direct Liquefaction of Wood by Catalyst and Water. *Liquid Fuels Technology* **1984,** *2* (2), 155-163.

[267] Minowa, T.; Ogi, T.; Dote, Y.; Yokoyama, S.-y., Methane Production from Cellulose by Catalytic Gasification. *Renewable Energy* **1994,** *5* (5-8), 813-815.

[268] Hong, C.; Hu, H.; Zhu, S.; Wang, G.; Chen, G., Nonisothermal Catalytic Liquefaction of Corn Stalk in Subcritical and Supercritical Water. *Energy & Fuels* **2004,** *18*, 90-96.

[269] Yoshida, T.; Oshima, Y.; Matsumura, Y., Gasification of Biomass Model Compounds and Real Biomass in Supercritical Water. *Biomass & Bioenergy* **2004,** *26* (1), 71-78.

[270] Yoshida, T.; Matsumura, Y., Gasification of Cellulose, Xylan, and Lignin Mixtures in Supercritical Water. *Industrial and Engineering Chemistry Research* **2001,** *40*, 5469-5474.

[271] D'Jesus, P.; Boukis, N.; Kraushaar-Czarnetzki, B.; Dinjus, E., Gasification of Corn and Clover Grass in Supercritical Water. *Fuel* **2006,** *85*, 1032-1038.

[272] Wahyudiono; Kanetake, T.; Sasaki, M.; Goto, M., Decomposition of a Lignin Model Compound under Hydrothermal Conditions. *Chemical Engineering Technology* **2007,** *30* (8), 1113-1122.

[273] Lee, I. G.; Kim, M. S.; Ihm, S. K., Gasification of Glucose in Supercritical Water. *Industrial & Engineering Chemistry Research* **2002,** *41* (5), 1182-1188.

[274] Zhang, B.; von Keitz, M.; Valentas, K., Thermal Effects on Hydrothermal Biomass Liquefaction. *Applied Biochemistry and Biotechnology* **2008,** *147*, 143-150.

[275] Kersten, S. R. A.; Potic, B.; Prins, W.; van Swaaij, W. P. M., Gasification of Model Compounds and Wood in Hot Compressed Water. *Industrial & Engineering Chemistry Research* **2006,** *45* (12), 4169-4177.

[276] Catallo, W. J., Personal Communication, 2008.

[277] Boukis, N.; Diem, V.; Habicht, W.; Dinjus, E., Methanol Reforming in Supercritical Water. *Industrial & Engineering Chemistry Research* **2003,** *42* (4), 728-735.

[278] Lira, C. T.; McCrackin, P. J., Conversion of Lactic Acid to Acrylic Acid in Near-Critical Water. *Industrial & Engineering Chemistry Research* **1993,** *32* (11), 2608-2613.

[279] Kruse, A. Neue Konzepte zur Wasserstoffproduktion aus Kohlenhydraten durch hydrothermale Umwandlung. Habilitation thesis, Darmstadt Technical University, Darmstadt, Germany, 2008.

[280] Aziz, N. H.; Moussa, L. A. A., Influence of Gamma-Radiation on Mycotoxin Producing Moulds and Mycotoxins in Fruits. *Food Control* **2002,** *13*, 281-288.

[281] Aziz, N. H.; El-Far, F. M.; Shahin, A. A. M.; Roushy, S. M., Control of *Fusarium* Moulds and Fumonisin B_1 in Seeds by Gamma-Irradiation. *Food Control* **2007,** *18*, 1337-1342.

[282] Mahrous, S. R.; Aziz, N. H.; Shahin, A. A., Influence of Gamma-Irradiation on the Occurrence of Pathogenic Microorganisms and Nutritive Value of Some Cereal Grains. *Isotope and Radiation Research* **2003,** *35*, 551-586.

[283] Refai, M. K.; Aziz, N. H.; El-Far, F. M.; Hasan, A. A., Detection of Ochratoxin Produced by *A. ochraceus* in Feedstuffs and Its Control by Gamma Irradiation. *Applied Radiation and Isotopes* **1996,** *7*, 617-621.

[284] Parrington, J. R.; Knox, H. D.; Breneman, S. L.; Baum, E. M.; Feiner, F., *Nuclides and Isotopes*. 15th ed.; General Electric Co. and Knolls Atomic Power Laboratory: San Jose, Calif., 1996.

[285] Grzechnik, E.; Pitsch, H. Retsch, The Basic Principles of Sieve Analysis; 8; [published online October 28, 2004]. (accessed September 19, 2009,

[286] Operating Instructions for Sieving Machine AS 200 control; Document No. 98.018.0000; Haan, Germany, May 24, 2005; 28 p. http://www.retsch.com/dltmp/www/2248-71b823de4b07/manual_as200_control_30.018.xxxx_en.pdf (accessed September 19, 2009).

[287] Hastelloy X alloy. Publication No. H-3009A, Haynes International: Kokomo, Ind., 1997; 16 p. http://www.haynesintl.com/pdf/h3009.pdf

[288] High Performance Alloys, Inc. Hastelloy alloy X (HX) (UNS N06002). 2007 http://hpalloy.com/alloys/descriptions/HASTELLOY_X.html (accessed November 19, 2009).

[289] Hand Tube Bender Manual; Document No. MS-13-43; Swagelok Company: Cleveland, Ohio, October, 2009; 31 p. http://www.swagelok.com/downloads/webcatalogs/EN/MS-13-43.PDF (accessed November 30, 2009).

[290] Minowa, T.; Fang, Z., Hydrogen Production from Cellulose in Hot Compressed Water Using Reduced Nickel Catalyst: Product Distribution at Different Reaction Temperatures. *Journal of Chemical Engineering of Japan* **1998,** *31* (3), 488-491.

[291] Qu, Y.; Wei, X.; Zhong, C., Experimental Study on the Direct Liquefaction of *Cunninghamia lanceolata* in Water. *Energy* **2003,** *28*, 597-606.

[292] Xu, C.; Etcheverry, T., Hydro-Liquefaction of Woody Biomass in Sub- and Super-Critical Ethanol with Iron-Based Catalysts. *Fuel* **2008,** *87*, 335-345.

[293] Onwudili, J. A.; Williams, P. T. Role of Sodium Hydroxide in the Production of Hydrogen Gas from the Hydrothermal Gasification of Biomass; *International Journal of Hydrogen Energy*, p. 12; [published online 2009]. 10.1016/j.ijhydene.2009.05.082

[294] Song, C.; Hu, H.; Zhu, S.; Wang, G.; Chen, G., Nonisothermal Catalytic Liquefaction of Corn Stalk in Subcritical and Supercritical Water. *Energy & Fuels* **2004,** *18* (1), 90-96.

[295] Saka, S.; Ueno, T., Chemical Conversion of Various Celluloses to Glucose and its Derivatives in Supercritical Water. *Cellulose* **1999,** *6*, 177-191.

[296] Garrote, G.; Domínguez, H.; Parajó, J. C., Study on the Deacetylation of Hemicelluloses During Hydrothermal Processing of *Eucalyptus* Wood. *Holz als Roh- und Werkstoff* **2001,** *59*, 53-59.

[297] Elliott, D. C., Catalytic Hydrothermal Gasification of Biomass. *Biofuels Bioproducts & Biorefining* **2008,** *2*, 254-265.

[298] Elliott, D. C.; Sealock, L. J., Jr.; Baker, E. G., Chemical Processing in High-Pressure Aqueous Environments. 2. Development of Catalysts for Gasification. *Industrial & Engineering Chemistry Research* **1993,** *32* (8), 1542-1548.

[299] Elliott, D. C.; Hart, T. R.; Neuenschwander, G. G., Chemical Processing in High-Pressure Aqueous Environments. 8. Improved Catalysts for Hydrothermal Gasification. *Industrial & Engineering Chemistry Research* **2006,** *45* (11), 3776-3781.

[300] Sofranko, J. A.; Leonard, J. J.; Jones, C. A., The Oxidative Conversion of Methane to Higher Hydrocarbons. *Journal of Catalysis* **1987,** *103*, 302-310.

[301] Corrosion Materials Alloy Data Sheets. 2006 http://www.corrosionmaterials.com/technicalInfo.jsp?sel=tigrade2 (accessed December 6, 2009).

[302] Sluiter, A. H., B.; Ruiz, R.; Scarlata, C.; Sluiter, J.; Templeton, D. *Determination of Total Solids in Biomass and Total Dissolved Solids in Liquid Process Samples* NREL/TP-510-42621; NREL: Golden, Col., 2008; p 9.

[303] Sluiter, A.; Hames, B.; Ruiz, R.; Scarlata, C.; Sluiter, J.; Templeton, D. *Determination of Ash in Biomass* NREL/TP-510-42622; NREL: Golden, Co., 2008; p 5.

[304] Day, D.; DeQueiroz, G. A.; Chung, C. H.; Kim, M., By-Products from Bagasse. *International Sugar Journal* **2008,** *110*, 7-11.

[305] Webb, P. A., Volume and Density Determinations for Particle Technologists. Publication No. Micromeritics Analytical Services: Norcross, Ga., February 16, 2001; 16 p. http://www.particletesting.com/docs/density_determinations.pdf

[306] Anderko, A., Equation-of-State Methods for the Modelling of Phase Equilibria. *Fluid Phase Equilibria* **1990,** *61* (1-2), 145-225.

[307] Prausnitz, J. M.; Lichtenthaler, R. N.; de Azevedo, E. G., *Molecular Thermodynamics of Fluid-Phase Equilibria*. 3rd ed.; Prentice Hall PTR: Upper Saddle River, N.J., 1999; 860 p.

[308] Soave, G., Equilibrium Constants from a Modified Redlich-Kwong Equation of State. *Chemical Engineering Science* **1972,** *27*, 1197-1203.

[309] Peng, D.-Y.; Robinson, D. B., A New Two-Constant Equation of State. *Industrial & Engineering Chemistry Fundamentals* **1976,** *15* (1), 59-64.

[310] Riazi, M. R., PVT Relations and Equations of State. In *Characterization and Properties of Petroleum Fractions*, ASTM International: West Conshohocken, Pa., 2007; pp 197-231.

[311] Gao, G.; Daridon, J.-L.; Saint-Guirons, H.; Xans, P.; Montel, F., A Simple Correlation to Evaluate Binary Interaction Parameters of the Peng-Robinson Equation of State: Binary Light Hydrocarbon Systems. *Fluid Phase Equilibria* **1992,** *74*, 85-93.

[312] Bruno, T. J.; Hume, G. L., Hydrogen Component Fugacities in Binary Mixtures with Carbon Dioxide. *International Journal of Thermophysics* **1985,** *7* (5), 1053-1063.

[313] Huyskens, P. L.; Haulait-Pirson, M. C.; Siegel, G. G.; Kapuku, F., Gibbs Energy of Some Binary Systems Containing Hydrogen Bonds. *Journal of Physical Chemistry* **1988,** *92* (23), 6841-6847.

[314] Panayiotou, C.; Sanchez, I. C., Hydrogen Bonding in Fluids: An Equation-of-State Approach. *Journal of Physical Chemistry* **1991,** *95* (24), 10090-10097.

[315] Fine, R. A.; Millero, F. J., Compressibility of Water as a Function of Temperature and Pressure. *The Journal of Chemical Physics* **1973,** *59* (10), 5529-5536.

[316] Myers, G. E., *Analytical Methods in Conduction Heat Transfer*. 2nd ed.; AMCHT Publications: Madison, Wisc., 1998; 409 p.

[317] Welty, J. R.; Wicks, C. E.; Wilson, R. E., *Fundamentals of Momentum, Heat, and Mass Transfer*. 3rd ed.; John Wiley and Sons: New York, N.Y., 1984; 803 p.

[318] Resende, F. L. P.; Neff, M. E.; Savage, P. E., Noncatalytic Gasification of Cellulose in Supercritical Water. *Energy & Fuels* **2007,** *21* (6), 3637-3643.

[319] Antal Jr., M. J.; Allen, S. G.; Schulman, D.; Xu, X.; Divilio, R. J., Biomass Gasification in Supercritical Water. *Ind. Eng. Chem. Res.* **2000,** *39* (11), 4040-4053.

[320] Karcz, A.; Porada, S., Formation of C_1-C_3 Hydrocarbons During Pressure Pyrolysis and Hydrogasification in Relation to Structural Changes in Coal. *Fuel* **1995,** *74* (6), 806-809.

[321] Resende, F. L. P.; Fraley, S. A.; Berger, M. J.; Savage, P. E., Noncatalytic Gasification of Lignin in Supercritical Water. *Energy & Fuels* **2008,** *22* (2), 1328-1334.

[322] Haykiri-Acma, H., The Role of Particle Size in the Non-Isothermal Pyrolysis of Hazelnut Shell. *Journal of Analytical and Applied Pyrolysis* **2006,** *75*, 211-216.

[323] Sanjuán, R.; Anzaldo, J.; Vargas, J.; Turrado, J.; Patt, R., Morphological and Chemical Composition of Pith and Fibers from Mexican Sugarcane Bagasse. *Holz als Roh- und Werkstoff* **2001,** *59* (6), 447-450.

[324] Barros, A. M.; Dhanabalan, A.; Constantino, C. J. L.; Balogh, D. T.; Oliveira Jr., O. N., Langmuir Monolayers of Lignins Obtained with Different Isolation Methods. *Thin Solid Films* **1999,** *354* (1-2), 215-221.

[325] Cotrim, A. R.; Ferraz, A.; Gonçalves, A. R.; Silva, F. T.; Bruns, R. E., Identifying the Origins of Lignins and Monitoring Their Structural Changes by Means of FTIR-PCA and -SIMCA. *Bioresource Technology* **1999,** *68*, 29-34.

[326] Demirbaş, A., Mechanisms of Liquefaction and Pyrolysis Reactions of Biomass. *Energy Conversion and Management* **2000,** *41* (6), 633-646.

[327] Garcìa-Pèrez, M.; Chaala, A.; Roy, C., Vacuum Pyrolysis of Sugarcane Bagasse. *Journal of Analytical and Applied Pyrolysis* **2002,** *65* (2), 111-136.

[328] Åsa, L.; Bergman, R.; Bodin, A.; Gatenholm, P., Mechanism of Assembly of Xylan onto Cellulose Surfaces. *Langmuir* **2003,** *19* (12), 5072-5077.

[329] Hosoya, T.; Kawamoto, H.; Saka, S., Cellulose-Hemicellulose and Cellulose-Lignin Interactions in Wood Pyrolysis at Gasification Temperature. *Journal of Analytical and Applied Pyrolysis* **2007,** *80*, 118-125.

[330] Swaan, H. M.; Toebes, A.; Seshan, K.; van Ommen, J. G.; Ross, J. R. H., The Kinetic and Mechanistic Aspects of the Oxidative Dehydrogenation of Ethane over Li/Na/MgO Catalysts. *Catalysis Today* **1992,** *13*, 201-208.

[331] Cavani, F.; Trifirò, F., The Oxidative Dehydrogenation of Ethane and Propane as an Alternative Way for the Production of Light Olefins. *Catalysis Today* **1995,** *24*, 307-313.

[332] Korf, S. J.; Roos, J. A.; de Bruijn, N. A.; van Ommen, J. G.; Ross, J. R. H., Oxidative Coupling of Methane over Lithium Doped Magnesium Oxide Catalysts. *Catalysis Today* **1988,** *2*, 535-545.

[333] Heinemann, H.; Somorjai, G. A. *Conversion of Ethane and of Propane to Higher Olefin Hydrocarbons* Lawrence Berkeley Laboratory: Berkeley, Calif., 1992; p 25.

[334] Keiski, R. L.; Desponds, O.; Chang, Y.-F.; Somorjai, G. A., Kinetics of the Water-Gas Shift Reaction Over Several Alkane Activation and Water-Gas Shift Catalysts. *Applied Catalysis A: General* **1993,** *101*, 317-338.

[335] Masel, R. I., *Chemical Kinetics and Catalysis*. Wiley-Interscience: New York, NY, 2001; 952 p.

[336] Steinfeld, J. I.; Francisco, J. S.; Hase, W. L., *Chemical Kinetics and Dynamics*. 2nd ed.; Prentice Hall: Upper Saddle River, NJ, 1999; 518 p.

[337] Radivojevic, S.; Cooper, P. A. Springer-Verlag, The Effects of Wood Species and Treatment Retention on Kinetics of CCA-C Fixation Reactions; *Wood Science and Technology*, p. 14; [published online August 7, 2009]. 10.1007/s00226-009-0277-y (accessed November 11, 2009).

[338] Abatzoglou, N.; Chornet, E.; Belkacemi, K.; Overend, R. P., Phenomenological Kinetics of Complex systems: The Development of a Generalized Severity Parameter and Its Application to Lignocellulosics Fractionation. *Chemical Engineering Science* **1992,** *47* (5), 1109-1122.

[339] Geniesse, J. C.; Reuter, R., Effect of Time and Temperature on the Cracking of Oils. *Industrial & Engineering Chemistry* **1930,** *22* (12), 1274-1279.

[340] Vroom, K. E., The H Factor: A Means of Expressing Cooking Times and Temperatures as a Single Variable. *Pulp & Paper Canada* **1957,** *58* (3), 228-231.

[341] Brasch, D. J.; Free, K. W., Prehydrolysis-Kraft Pulping of *Pinus radiata* Grown in New Zealand. *TAPPI* **1965,** *48* (4), 245-248.

[342] Sjöström, E., *Wood Chemistry: Fundamentals and Applications*. 2nd ed.; Academic Press: San Diego, Calif., 1993; 293 p.

[343] Chum, H. L.; Johnson, D. K.; Black, S. K.; Overend, R. P., Pretreatment-Catalyst Effects and the Combined Severity Parameter. *Applied Biochemistry and Biotechnology* **1990,** *24/25*, 1-14.

[344] Fogler, H. S., *Elements of Chemical Reaction Engineering*. 2nd ed.; PTR Prentice-Hall: Englewood Cliffs, NJ, 1992; 838 p.

[345] Fylstra, D.; Lasdon, L.; Watson, J.; Warren, A., Design and Use of the Microsoft Excel Solver. *Interfaces* **1998,** *28* (5), 29-55.

[346] Calzavara, Y.; Joussot-Dubien, C.; Boissonnet, G.; Sarrade, S., Evaluation of Biomass Gasification in Supercritical Water Process for Hydrogen Production. *Energy Conversion and Management* **2005,** *46*, 615-631.

[347] Junk, T.; Catallo, W. J., Hydrogen Isotope Exchange Reactions Involving C-H (D, T) Bonds. *Chemical Society Reviews* **1997,** *26*, 401-406.

[348] Catallo, W. J.; Shupe, T. F.; Comeaux, J. L.; Junk, T. Transformation of Glucose to Volatile and Semi-Volatile Products in Hydrothermal (HT) Systems; *Biomass and Bioenergy*, p. 1-13; [published online Nov 2, 2009]. 10.1016/j.biombioe.2009.07.017

[349] Ishida, Y.; Taki, H.; Oyama, H.; Kitagawa, K.; Matsumoto, K., Discriminative Determination of Hydrogen Gas Formed from Tandem CO_2 Reforming and Shift Reaction by Isotope Labeling Followed by Cryogenic Gas Chromatography. *Fuel* **2006,** *85*, 2041-2045.

[350] Keller, G. E.; Bhasin, M. M., Synthesis of Ethylene via Oxidative Coupling of Methane. I. Determination of Active Catalysts. *Journal of Catalysis* **1982,** *73*, 9-19.

[351] Barth, T., Similarities and Differences in Hydrous Pyrolysis of Biomass and Source Rocks. *Organic Geochemistry* **1999,** *30* (12), 1495-1507.

[352] Baumlin, S.; Broust, F.; Bazer-Bachi, F.; Bourdeaux, T.; Herbinet, O.; Ndiaye, F. T.; Ferrer, M.; Lédé, J., Production of Hydrogen by Lignins Fast Pyrolysis. *International Journal of Hydrogen Energy* **2006,** *31* (15), 2179-2192.

[353] Cagnon, B.; Py, X.; Guillot, A.; Stoeckli, F.; Chambat, G., Contributions of Hemicellulose, Cellulose and Lignin to the Mass and the Porous Properties of Chars and Steam Activated Carbons from Various Lignocellulosic Precursors. *Bioresource Technology* **2009,** *100* (1), 292-298.

[354] Encinar, J. M.; Beltrán, F. J.; Bernalte, A.; Ramiro, A.; González, J. F., Pyrolysis of Two Agricultural Residues: Olive and Grape Bagasse. Influence of Particle Size and Temperature. *Biomass and Bioenergy* **1996,** *11* (5), 397-409.

[355] Rodriguez, R.; Magne, P.; Deglise, X., Sugarcane Bagasse as a Feedstock for an Industrial Fast Pyrolysis Process under Development. *Journal of Analytical and Applied Pyrolysis* **1987,** *12* (3-4), 301-318.

[356] Sensöz, S.; Angin, D.; Yorgun, S., Influence of Particle size on the Pyrolysis of Rapeseed (*Brassica napus L.*): Fuel Properties of Bio-oil. *Biomass and Bioenergy* **2000,** *19* (4), 271-279.

[357] Bridgeman, T. G.; Darvell, L. I.; Jones, J. M.; Williams, P. T.; Fahmi, R.; Bridgwater, A. V.; Barraclough, T.; Shield, I.; Yates, N.; Thain, S. C.; Donnison, I. S., Influence of Particle Size on the Analytical and Chemical Properties of Two Energy Crops. *Fuel* **2007,** *86* (1-2), 60-72.

[358] Maloney, M. T.; Chapman, T. W.; Baker, A. J., An Engineering Analysis of the Production of Xylose by Dilute Acid Hydrolysis of Hardwood Hemicellulose. *Biotechnology Progress* **1986,** *2* (4), 192-202.

[359] Garrote, G.; Domínguez, H.; Parajó, J. C., Hydrothermal Processing of Lignocellulosic Materials. *Holz als Roh- und Werkstoff* **1999,** *57*, 191-202.

[360] Sands, L.; Gray, W. Y., The Hemicelluloses of Mesquite Wood. *Journal of Biological Chemistry* **1933,** *101*, 573-581.

[361] O'Dwyer, M. H., CCLXXIX. The Hemicelluloses of the Wood of the English Oak. II. The Composition and Properties of Hemicellulose A, Isolated from Samples of Wood Dried Under Various Conditions. *Biochemical Journal* **1934,** *28*, 2116-2124.

[362] Yoshida, T.; Matsumura, Y., Gasification of Cellulose, Xylan, and Lignin Mixtures in Supercritical Water. *Industrial & Engineering Chemistry Research* **2001,** *40* (23), 5469-5474.

[363] Hutchings, G. J.; Scurrell, M. S.; Woodhouse, J. R., Oxidative Coupling of Methane using Oxide Catalysts. *Chemical Society Reviews* **1989,** *18*, 251-283.

[364] Labinger, J. A.; Ott, K. C., Mechanistic Studies on the Oxidative Coupling of Methane. *Journal of Physical Chemistry* **1987,** *91* (11), 2682-2684.

[365] Golpasha, R. D.; Karami, D.; Ahmadi, R.; Bagherzadeh, E., Kinetics and Mechanism of Oxidative Coupling of Methane over Sodium-Manganese Oxide Catalyst. *Chemical Engineering Technology* **1993,** *16*, 62-67.

[366] Morales, E.; Lunsford, J. H., Oxidative Dehydrogenation of Ethane over a Lithium-Promoted Magnesium Oxide Catalyst. *Journal of Catalysis* **1989,** *118*, 255-265.

[367] Bielański, A.; Haber, J., *Oxygen in Catalysis*. Marcel Dekker, Inc.: New York, NY, 1991; 472 p.

[368] Solymosi, F.; Németh, R., The Oxidative Dehydrogenation of Ethane with CO_2 over Mo_2C/SiO_2 Catalyst. *Catalysis Letters* **1999,** *62*, 197-200.

[369] Vernon, P. D. F.; Green, M. L. H.; Cheetham, A. K.; Ashcroft, A. T., Partial Oxidation of Methane to Synthesis Gas, and Carbon Dioxide as an Oxidising Agent for Methane Conversion. *Catalysis Today* **1992,** *13* (2-3), 417-426.

[370] Rostrupnielsen, J. R.; Hansen, J. H. B., CO2-Reforming of Methane over Transition Metals. *Journal of Catalysis* **1993,** *144* (1), 38-49.

[371] Krylov, O. V.; Mamedov, A. K.; Mirzabekova, S. R., Interaction of Carbon Dioxide with Methane on Oxide Catalysts. *Catalysis Today* **1998,** *42*, 211-215.

[372] Krylov, O. V.; Mamedov, A. K.; Mirzabekova, S. R., The Regularities in the Interaction of Alkanes with CO_2 on Oxide Catalysts. *Catalysis Today* **1995,** *24*, 371-375.

[373] Cordeiro, G. C.; Filho, R. D. T.; Fairbairn, E. d. M. R., Uses of Ultra-Fine Sugar Cane Bagasse Ash as Mineral Admixture for Concrete. *ACI Materials Journal* **2008,** *105* (5), 487-493.

[374] Vieira, C. M. F.; Borlini, M. C.; Monteiro, S. N., Incorporation of Ash from Sugar Cane Bagasse into Clay Bricks. *Industrial Ceramics* **2006,** *26* (2), 107-113.

[375] Burch, R.; Tsang, S. C., Investigations of the Partial Oxidation of Hydrocarbons on Methane Coupling Catalysts. *Applied Catalysis* **1990,** *65*, 259-280.

[376] Hutchings, G. J.; Scurrell, M. S.; Woodhouse, J. R., The Role of Surface O^- in the Selective Oxidation of Methane. *Journal of the Chemical Society, Chemical Communications* **1987**, 1388-1389.

[377] Olson, D. N.; Orera, V. M.; Chen, Y.; Abraham, M. M., Thermally Generated $[Li]^0$ Centers in CaO. *Physical Review B (Condensed Matter)* **1980,** *21* (3), 1258-1263.

[378] Oyama, S. T., Factors Affecting Selectivity in Catalytic Partial Oxidation and Combustion Reactions. In *Heterogeneous Hydrocarbon Oxidation*, Warren, B. K.; Oyama, S. T., Eds. American Chemical Society: Washington, D.C., 1996; pp 2-19.

[379] Burch, R.; Squire, G. D.; Tsang, S. C., Comparative Study of Catalysts for the Oxidative Coupling of Methane. *Applied Catalysis* **1988,** *43*, 105-116.

[380] Dagaut, P.; Cathonnet, M.; Boettner, J. C.; Gaillard, F., Kinetic Modeling of Propane Oxidation. *Combustion Science and Technology* **1987,** *56*, 23-63.

[381] Eager, R. L.; Mathews, J. F.; Pepper, J. M., Liquefaction of Aspen Poplar Wood. *Canadian Journal of Chemical Engineering* **1982,** *60* (2), 289-294.

[382] Demirci, U. B.; Miele, P., Sodium Tetrahydroborate as Energy/Hydrogen Carrier, Its History. *Comptes Rendus Chimie* **2009,** *12* (9), 943-950.

[383] Züttel, A.; Borgschulte, A.; Orimo, S.-I., Tetrahydroborates as New Hydrogen Storage Materials. *Script Materiala* **2007,** *56* (10), 823-828.

[384] Chaikin, S. W.; Brown, W. G., Reduction of Aldehydes, Ketones, and Acid Chlorides in Sodium Borohydride. *Journal of the American Chemical Society* **1949,** *71*, 122-125.

[385] Finholt, A. E. Ph.D. Dissertation, The University of Chicago, Chicago, Ill., 1946.

[386] Wolfrom, M. L.; Wood, H. B., Sodium Borohydride as a Reducing Agent for Sugar Lactones. *Journal of the American Chemical Society* **1951,** *73*, 2933-2934.

[387] Schlesinger, H. I.; Brown, H. C.; Hoekstra, H. R.; Rapp, L. R., Reactions of Diborane with Alkali Metal Hydrides and Their Addition Compounds. New Syntheses of Borohydrides. Sodium and Potassium Borohydrides. *Journal of the American Chemical Society* **1953,** *75* (1), 199-204.

[388] Hill Jr., C. G.; Grieger-Block, R. A., Kinetic Data: Generation, Interpretation, and Use. *Food Technology* **1980,** *34* (2), 56-66.

[389] Howell, B. A., The Utility of Variable Temperature Techniques in the Determination of Kinetic Parameters. *Thermochimica Acta* **2002,** *388*, 275-281.

[390] Espenson, J. H., *Chemical Kinetics and Reaction Mechanisms*. 2nd ed.; McGraw-Hill: New York, NY, 1995; 281 p.

[391] French, D., Kinetic Analysis of Consecutive Irreversible Second Order Reactions. *Journal of the American Chemical Society* **1950,** *72*, 4806-4807.

[392] Levenberg, K., A Method for the Solution of Certain Non-Linear Problems in Least Squares. *The Quarterly of Applied Mathematics* **1944,** *2*, 164-168.

[393] Marquardt, D., An Algorithm for Least-Squares Estimation of Nonlinear Parameters. *SIAM Journal on Applied Mathematics* **1963,** *11*, 431-441.

[394] Madsen, K.; Nielsen, H. B.; Tingleff, O. Technical University of Denmark, Methods for Non-Linear Least Squares Problems; 58; [published online April, 2004]. (accessed November 4, 2009,

[395] Lourakis, M. L. A.; Argyros, A. A., Is Levenberg-Marquardt the Most Efficient Optimization Algorithm for Implementing Bundle Adjustment:. *Computer Visions* **2005,** *2*, 1526-1531.

[396] Field, R. J., Chemical Reaction Kinetics. *Scholarpedia* **2008,** *3* (10), 4051.

[397] Glassman, I.; Yetter, R. A., *Combustion*. 4th ed.; Academic Press, Inc.: Burlington, Mass., 2008; 773 p.

[398] Sasaki, M.; Adschiri, T.; Arai, K., Fractionation of Sugarcane Bagasse by Hydrothermal Treatment. *Bioresource Technology* **2003,** *86*, 301-304.

[399] Boussarsar, H.; Rogé, B.; Mathlouthi, M., Optimization of Sugarcane Bagasse Conversion by Hydrothermal Treatment for the Recovery of Xylose. *Bioresource Technology* **2009,** *100* (24), 6537-6542.

[400] Allen, S. G.; Kam, L. C.; Zemann, A. J.; Antal Jr., M. J., Fractionation of Sugar Cane with Hot, Compressed, Liquid Water. *Industrial & Engineering Chemistry Research* **1996,** *35* (8), 2709-2715.

[401] Jollez, P.; Chornet, E.; Overend, R. P., Steam-Aqueous Fractionation of Sugar Cane Bagasse. In *Advances in Thermochemical Biomass Conversion*, Bridgwater, A. V., Ed. Chapman & Hall Publishers: London, England, U.K., 1994; Vol. 2, pp 1659-1669.

[402] Mok, W. S.-L.; Antal Jr., M. J., Uncatalyzed Solvolysis of Whole Biomass Hemicellulose by Hot Compressed Liquid Water. *Industrial & Engineering Chemistry Research* **1992,** *31* (4), 1157-1161.

[403] Bobleter, O.; Vidotti, R.; Zemann, A. J.; Prutsch, W., *Hydrothermal Pretreatment of Bagasse and Wheat Straw*, Vol. 2. Conversion and Utilisation of Biomass, in Proceedings of the Proceedings of the 5th E.C. International Conference on Biomass for Energy and Industry, Lisbon, Portugal; October 9-13, 1989; Grassi, G.; Gosse, G.; dos Santos, G., Eds. Elsevier Applied Science: London, U.K., 1990; pp 2.31-2.37.

[404] Mok, W. S.-L.; Antal Jr., M. J.; Varhegyi, G., Productive and Parasitic Pathways in Dilute Acid-Catalyzed Hydrolysis of Cellulose. *Industrial & Engineering Chemistry Research* **1992,** *31* (1), 94-100.

[405] van Krevelen, D. W., *Coal: Typology-Chemistry-Physics-Constitution*. Elsevier Publishing: Amsterdam, The Netherlands, 1961; 514 p.

[406] Markowski, M. L., Methods of Analysis Using Helium-Ionization and Discharge-Ionization Detector/Gas Chromatography. In *Specialty Gas Analysis*, Hogan, J. D., Ed. Wiley-VCH: New York, NY, 1997; p 200.

APPENDIX A. HELIUM IONIZATION DETECTOR

Operational Overview of the Helium Ionization Detector

The helium ionization detector (HID) is a specialized dielectric barrier discharge (DBD) detector designed for permanent gas analysis and, in particular, hydrogen detection. DBD detectors utilize metastable ionization to selectively detect very low concentrations of permanent gases and volatile organics. Typically, the sensitivity of DBD detectors is in the vicinity of a few parts per billion. In DBD detectors a high voltage ac discharge is used to create a plasma supply. A plasma source generates a beam of metastable He^* atoms from a He gas stream that is used to ionize analyte molecules. Analytes exiting the GC column are bombarded by counter flowing He^* atoms. During the ensuing collisions, the metastable atoms impart their high energy to the eluent molecules. The absorption of this energy excites the molecules to an energetically unstable state, which can only be counteracted by the ejection of an electron from an outer molecular orbital (i.e., ionization). An electrostatic field generated by a negatively biased electrode and a positively charged collector electrode prods the cations to migrate toward the bias electrode. The movement of ions induces a small current between the electrodes that can then be converted to a voltage signal by an electrometer. The analog voltage output is subsequently transformed into a digital response, which is proportional to the concentration of the given analyte in the sample.

A schematic of a typical HID is provided in Figure A1. The HID consists of an upper discharge chamber and a lower polarization chamber that are connected via a small hole. A continuous flow of purified helium (i.e., the discharge gas) supplies the upper discharge chamber, where a plasma arc is maintained. Analyte species in the helium carrier stream enter the HID through the upper section of the polarization chamber. The analytes

proceed across the polarization electrodes and exit at the chamber bottom. Generally, the number of metastable He^* atoms decreases with increasing sample concentration.

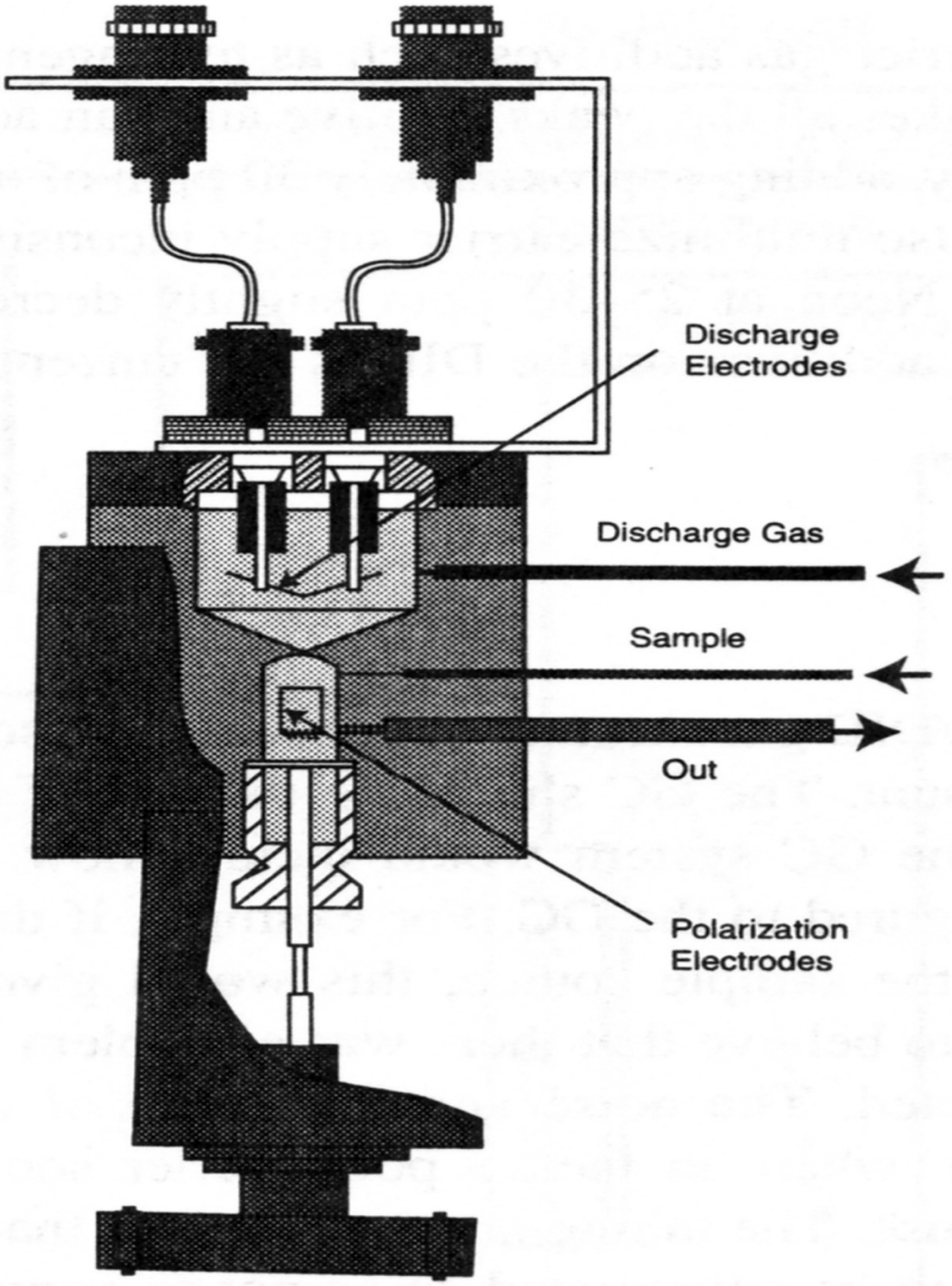

Figure A1. Helium ionization detector schematic (reprinted courtesy of Markowski [406]

APPENDIX B. MASS BALANCES

The following tables provide a complete mass balance for every hydrothermal run presented in this document. Each mass balance table includes the process conditions and the overall level of bagasse conversion for the given run. All of the hydrothermal runs were performed with a single free operational parameter, while all other process variables were held at the standard, baseline conditions previously described. Table B1 below lists every run by its free operational variable and the corresponding run identification code that is given near the top of each mass balance table.

Table B1. Experimental runs listed by their free operational variable and corresponding ID code

Free Variable	**ID**	**Free Variable**	**ID**	**Free Variable**	**ID**
Temperature		**Residence Time**		**Biomass Loading**	
300 °C	3TB2	1 min	5RT01	2.67 wt %	5WA1
400 °C	4TB3	5 min	5RT05	4.00 wt %	5WB1
500 °C Rep 1	5TB3	10 min	5RT10	8.00 wt %	5WC1
500 °C Rep 2	5TB4	30 min	5RT30	**Particle Size**	
500 °C Rep 3	5TB5	60 min	5RT60	18/25 mesh	5SBA1
500 °C Rep 4	5TB6			45/60 mesh	5SBB1
600 °C	6TB1			140/230 mesh	5SBC1
Model Compounds		**Catalysts**		**Reductants**	
Cellulose	5CB1	Li/MgO	Li/MgO	CO	CO (1)
Xylan	5XB1	MnO_2 Rep 1	MnO_2 (1)	$NaBH_4$	$NaBH_4$ (2)
Alkali lignin	5LB1	MnO_2 Rep 2	MnO_2 (2)		
Special Runs					
Titanium bomb	5TiB1				
Deuterium oxide	5DB1				

Hydrothermal Run Number: 3TB2 **Date:** 8/15/2009

Weight loading:	1 : 25	Initial pressure in bomb after He charge:	30.3 psia
Wet bagasse mass:	2.0139 g	Maximum pressure recorded in bomb:	1369.6 psia
Bagasse moisture:	5.20 %	Final bomb pressure before GC analysis:	63.5 psia
Dry bagasse mass:	1.9092 g	Bomb temperature before GC analysis:	25.6 °C
DI H_2O mass:	47.2 g	Density of liquid product:	1.0026 g cm^{-3}
DI H_2O pH:	5.65	Volume of liquid product:	46.8895 cm^3
Total H_2O mass:	47.3047 g	Volume of solid product:	0.0607 cm^3
Run temperature:	300 °C	Volume of gas product:	20.0988 cm^3
Nominal run duration:	5 min	Moles of gas product (less initial He):	0.0028 mol

Unfiltered liquids + beaker:	70.8968 g	Dried solids + beaker:	28.6669 g
Clean, dry beaker:	28.6638 g	Clean, dry beaker:	28.6638 g
Unfiltered liquids:	42.2330 g	Dried solids in beaker:	0.0031 g
(2) Wet Kimwipes (cap + threads):	1.5969 g	Unfiltered liquids from beaker:	42.2330 g
(2) Dry, unused Kimwipe(s)	0.9118 g	Dried solids from beaker:	0.0031 g
Semivolatiles inside cap:	0.6851 g	Semivolatiles in beaker:	42.2299 g
Sludge + 11.8 mL DI H_2O + boat:	18.8749 g	Dried solids + boat:	2.9785 g
Clean, dry Al weigh boat:	2.2731 g	Clean, dry Al weigh boat:	2.2731 g
Sludge + 11.8 mL DI H_2O:	16.6018 g	Dried solids in boat:	0.7054 g
– 11.8 mL DI H_2O:	11.8000 g		
Sludge (slurry + tars) in boat:	4.8018 g	Sludge (slurry + tars) in boat:	4.8018 g
		– Dried solids in boat:	0.7054 g
Dried solids + funnel + filter paper:	62.3487 g	Semivolatiles in boat:	4.0964 g
Size 0 funnel + 1.2 μm filter paper:	62.3285 g		
Dried, filtered solids in funnel:	0.0202 g	Total Semivolatiles Yield:	47.0114 g = 56.19%
		Total Solids Yield:	0.7287 g = 38.17%
		Total Volatiles Yield:	0.1077 g = 5.64%
		Total Losses:	1.3661 g
		% Losses:	2.78 %
		Conversion:	61.83 %

Observations: Unfiltered liquid has an orange-brown color similar to that of apple cider. Quantity of solids much higher at 300 °C. Solid residue is not viscous but has a very mushy texture, with a rusty sepia color. Filtrate has bright goldenrod color with a slightly sweet, burnt hickory aroma.

Hydrothermal Run Number: 4TB3 **Date:** 8/14/2009

Weight loading:	1 : 25	Initial pressure in bomb after He charge:	27.3 psia
Wet bagasse mass:	1.9946 g	Maximum pressure recorded in bomb:	8982.9 psia
Bagasse moisture:	5.20 %	Final bomb pressure before GC analysis:	144.0 psia
Dry bagasse mass:	1.8909 g	Bomb temperature before GC analysis:	25.6 °C
DI H_2O mass:	47.2 g	Density of liquid product:	1.001 g cm^{-3}
DI H_2O pH:	5.77	Volume of liquid product:	47.5509 cm^3
Total H_2O mass:	47.3037 g	Volume of solid product:	0.2605 cm^3
Run temperature:	400 °C	Volume of gas product:	19.2376 cm^3
Nominal run duration:	5 min	Moles of gas product (less initial He):	0.0070 mol

Unfiltered liquids + beaker:	76.5148 g	Dried solids + beaker:	29.4088 g
Clean, dry beaker:	29.2950 g	Clean, dry beaker:	29.2950 g
Unfiltered liquids:	47.2198 g	Dried solids in beaker:	0.1138 g
(2) Wet Kimwipes (cap + threads):	1.3107 g	Unfiltered liquids from beaker:	47.2198 g
(2) Dry, unused Kimwipe(s)	0.9004 g	Dried solids from beaker:	0.1138 g
Semivolatiles inside cap:	0.4103 g	Semivolatiles in beaker:	47.1060 g
Sludge + 5.9 mL DI H_2O + boat:	8.3592 g	Dried solids + boat:	2.3770 g
Clean, dry Al weigh boat:	2.2732 g	Clean, dry Al weigh boat:	2.2732 g
Sludge + 5.9 mL DI H_2O:	6.0860 g	Dried solids in boat:	0.1038 g
– 5.9 mL DI H_2O:	5.9000 g		
Sludge (slurry + tars) in boat:	0.1860 g	Sludge (slurry + tars) in boat:	0.1860 g
		– Dried solids in boat:	0.1038 g
Dried solids + funnel + filter paper:	62.9370 g	Semivolatiles in boat:	0.0822 g
Size 0 funnel + 1.2 μm filter paper:	62.5737 g		
Dried, filtered solids in funnel:	0.3633 g	Total Semivolatiles Yield:	47.5985 g = 57.31%
		Total Solids Yield:	0.5809 g = 30.72%
		Total Volatiles Yield:	0.2264 g = 11.97%
		Total Losses:	0.7888
		% Losses:	1.60 %
		Conversion:	69.28 %

Observations: Filtrate has a pale yellow color similar to that of ginger ale. The filtrate has a heavy phenolic, creosote odor reminiscent of barbeque that is a bit overdone. Tar is black and has a very high viscosity; the consistency and rheology seem equivalent to that of warm asphalt.

Hydrothermal Run Number: 5TB3 **Date:** 8/16/2009

Nominal weight loading:	1 : 25	Initial pressure in bomb after He charge:	108.8 psia
Wet bagasse mass:	1.5021 g	Maximum pressure recorded in bomb:	10936.1 psia
Bagasse moisture:	5.20 %	Final bomb pressure before GC analysis:	266.7 psia
Dry bagasse mass:	1.4240 g	Bomb temperature before GC analysis:	21.0 °C
DI H_2O mass:	35.4 g	Density of liquid product:	0.9990 g cm^{-3}
DI H_2O pH:	5.49	Volume of liquid product:	35.3207 cm^3
Total H_2O mass:	35.4781 g	Volume of solid product:	0.0761 cm^3
Run temperature:	500 °C	Volume of gas product:	31.6521 cm^3
Nominal run duration:	5 min	Moles of gas product (less initial He):	0.0174 mol

Unfiltered liquids + beaker:	65.2537 g	Dried solids + beaker:	30.6137 g
Clean, dry beaker:	30.5889 g	Clean, dry beaker:	30.5889 g
Unfiltered liquids:	34.6648 g	Dried solids in beaker:	0.0248 g
(2) Wet Kimwipes (cap + threads):	1.0935 g	Unfiltered liquids from beaker:	34.6648 g
(2) Dry, unused Kimwipe(s)	0.9190 g	Dried solids from beaker:	0.0248 g
Semivolatiles inside cap:	0.1745 g	Semivolatiles in beaker:	34.6400 g
Sludge + 11.8 mL DI H_2O + boat:	14.6148 g	Dried solids + boat:	2.3439 g
Clean, dry Al weigh boat:	2.2799 g	Clean, dry Al weigh boat:	2.2799 g
Sludge + 11.8 mL DI H_2O:	12.3349 g	Dried solids in boat:	0.0640 g
– 11.8 mL DI H_2O:	11.8000 g		
Sludge (slurry + tars) in boat:	0.5349 g	Sludge (slurry + tars) in boat:	0.5349 g
		– Dried solids in boat:	0.0640 g
Dried solids + funnel + filter paper:	66.1949 g	Semivolatiles in boat:	0.4709 g
Size 0 funnel + 1.2 μm filter paper:	66.1139 g		
Dried, filtered solids in funnel:	0.0810 g		

Total Semivolatiles Yield:	35.2854 g	=	52.93%
Total Solids Yield:	0.1698 g	=	11.92%
Total Volatiles Yield:	0.5006 g	=	35.15%
Total Losses:	0.9463 g		
% Losses:	2.56 %		
Conversion:	88.08 %		

Observations: Semi-volatiles had a pungent gasoline aroma; solids are black and tarry but not excessively viscous, the rheology is akin to that of toothpaste squeezed from a tube; tars are smearable and fluid-like, filtrate has a very faint cream vanilla hue and has the exact redolence of the light naphtha fraction present in gasoline; a fine suspension of black particles is floating on the top layer and a similar layer exists on the beaker bottom and an equal number of particles appear to rise to the surface and sink to the bottom; a layer of bubbles exists on the beaker floor

Hydrothermal Run Number: 5TB4 **Date:** 8/22/2009

Nominal weight loading:	1 : 25	Initial pressure in bomb after He charge:	62.5 psia
Wet bagasse mass:	1.5065 g	Maximum pressure recorded in bomb:	10675.5 psia
Bagasse moisture:	5.20 %	Final bomb pressure before GC analysis:	280.8 psia
Dry bagasse mass:	1.4282 g	Bomb temperature before GC analysis:	65.0 °C
DI H_2O mass:	35.4 g	Density of liquid product:	0.9991 g cm^{-3}
DI H_2O pH:	5.75	Volume of liquid product:	36.0050 cm^3
Total H_2O mass:	35.4783 g	Volume of solid product:	0.1039 cm^3
Run temperature:	500 °C	Volume of gas product:	30.9401 cm^3
Nominal run duration:	5 min	Moles of gas product (less initial He):	0.0176 mol

Unfiltered liquids + beaker:	63.4502 g	Dried solids + beaker:	28.6975 g
Clean, dry beaker:	28.6631 g	Clean, dry beaker:	28.6631 g
Unfiltered liquids:	34.7871 g	Dried solids in beaker:	0.0344 g
(2) Wet Kimwipes (cap + threads):	1.6628 g	Unfiltered liquids from beaker:	34.7871 g
(2) Dry, unused Kimwipe(s)	0.9105 g	Dried solids from beaker:	0.0344 g
Semivolatiles inside cap:	0.7523 g	Semivolatiles in beaker:	34.7527 g
Sludge + 0.0 mL DI H_2O + boat:	2.7368 g	Dried solids + boat:	2.2692 g
Clean, dry Al weigh boat:	2.1908 g	Clean, dry Al weigh boat:	2.1908 g
Sludge + 0.0 mL DI H_2O:	0.5460 g	Dried solids in boat:	0.0784 g
– 0.0 mL DI H_2O:	0.0000 g		
Sludge (slurry + tars) in boat:	0.5460 g	Sludge (slurry + tars) in boat:	0.5460 g
		– Dried solids in boat:	0.0784 g
Dried solids + funnel + filter paper:	62.4469 g	Semivolatiles in boat:	0.4676 g
Size 0 funnel + 1.2 μm filter paper:	62.3281 g		
Dried, filtered solids in funnel:	0.1188 g	Total Semivolatiles Yield:	35.9726 g = 48.36%
		Total Solids Yield:	0.2316 g = 16.22%
		Total Volatiles Yield:	0.5059 g = 35.42%
		Total Losses:	0.1964 g
		% Losses:	0.53 %
		Conversion:	83.78 %

Observations: Semi-volatiles had a pungent gasoline aroma; solids are black and tarry but not excessively viscous, the rheology is akin to that of toothpaste squeezed from a tube; tars are smearable and fluid-like, filtrate has a very faint cream vanilla hue and has the exact redolence of the light naphtha fraction present in gasoline

Hydrothermal Run Number: 5TB5 **Date:** 9/3/2009

Nominal weight loading:	1 : 25	Initial pressure in bomb after He charge:	65.5 psia
Wet bagasse mass:	1.5018 g	Maximum pressure recorded in bomb:	10253.9 psia
Bagasse moisture:	5.20 %	Final bomb pressure before GC analysis:	239.6 psia
Dry bagasse mass:	1.4237 g	Bomb temperature before GC analysis:	25.6 °C
DI H_2O Mass:	35.4 g	Density of liquid product:	0.9995 g cm^{-3}
DI H_2O pH:	5.50	Volume of liquid product:	35.8785 cm^3
Total H_2O mass:	35.4781 g	Volume of solid product:	0.1180 cm^3
Run temperature:	500 °C	Volume of gas product:	31.0525 cm^3
Nominal run duration:	5 min	Moles of gas product (less initial He):	0.0168 mol

Unfiltered liquids + beaker:	64.0651 g	Dried solids + beaker:	29.8444 g
Clean, dry beaker:	29.8114 g	Clean, dry beaker:	29.8114 g
Unfiltered liquids:	34.2537 g	Dried solids in beaker:	0.0330 g
(1) Wet Kimwipe(s) (cap + threads):	1.0667 g	Unfiltered liquids from beaker:	34.2537 g
(1) Dry, unused Kimwipe(s)	0.4519 g	Dried solids from beaker:	0.0330 g
Semivolatiles inside cap:	0.6148 g	Semivolatiles in beaker:	34.2207 g
Sludge + 5.9 mL DI H_2O + boat:	9.2803 g	Dried solids + boat:	2.3552 g
Clean, dry Al weigh boat:	2.1938 g	Clean, dry Al weigh boat:	2.1938 g
Sludge + 5.9 mL DI H_2O:	7.0865 g	Dried solids in boat:	0.1614 g
– 5.9 mL DI H_2O:	5.9000 g		
Sludge (slurry + tars) in boat:	1.1865 g	Sludge (slurry + tars) in boat:	1.1865 g
		– Dried solids in boat:	0.1614 g
Dried solids + funnel + filter paper:	62.6440 g	Semivolatiles in boat:	1.0251 g
Size 0 funnel + 1.2 μm filter paper:	62.5753 g		
Dried, filtered solids in funnel:	0.0687 g	Total Semivolatiles Yield:	35.8606 g = 46.39%
		Total Solids Yield:	0.2631 g = 18.48%
		Total Volatiles Yield:	0.5002 g = 35.13%
		Total Losses:	0.2779 g
		% Losses:	0.75 %
		Conversion:	81.52 %

NB: Run 5TB5 is also designated separately as 5RT05 and 5WB2 because this is the standard, baseline run at 500 °C and 4 wt % biomass loading for 5 min.

Hydrothermal Run Number: 5TB6 **Date:** 9/5/2009

Nominal weight loading:	1 : 25	Initial pressure in bomb after He charge:	83.6 psia
Wet bagasse mass:	1.5069 g	Maximum pressure recorded in bomb:	10756.0 psia
Bagasse moisture:	5.20 %	Final bomb pressure before GC analysis:	253.7 psia
Dry bagasse mass:	1.4286 g	Bomb temperature before GC analysis:	29.4 °C
DI H_2O mass:	35.4 g	Density of liquid product:	0.9990 g cm^{-3}
DI H_2O pH:	5.35	Volume of liquid product:	35.6575 cm^3
Total H_2O mass:	35.4783 g	Volume of solid product:	0.1133 cm^3
Run temperature:	500 °C	Volume of gas product:	31.2782 cm^3
Nominal run duration:	5 min	Moles of gas product (less initial He):	0.0168 mol

Unfiltered liquids + beaker:	64.9164 g	Dried solids + beaker:	30.6778 g
Clean, dry beaker:	30.6311 g	Clean, dry beaker:	30.6311 g
Unfiltered liquids:	34.2853 g	Dried solids in beaker:	0.0467 g
(2) Wet Kimwipe(s) (cap + threads):	1.3596 g	Unfiltered liquids from beaker:	34.2853 g
(2) Dry, unused Kimwipe(s)	0.9086 g	Dried solids from beaker:	0.0467 g
Semivolatiles inside cap:	0.4510 g	Semivolatiles in beaker:	34.2386 g
Sludge + 5.9 mL DI H_2O + boat:	9.1467 g	Dried solids + boat:	2.3145 g
Clean, dry Al weigh boat:	2.1875 g	Clean, dry Al weigh boat:	2.1875 g
Sludge + 5.9 mL DI H_2O:	6.9592 g	Dried solids in boat:	0.1270 g
– 5.9 mL DI H_2O:	5.9000 g		
Sludge (slurry + tars) in boat:	1.0592 g	Sludge (slurry + tars) in boat:	1.0592 g
		– Dried solids in boat:	0.1270 g
Dried solids + funnel + filter paper:	59.2093 g	Semivolatiles in boat:	0.9322 g
Size 0 funnel + 1.2 μm filter paper:	59.1303 g		
Dried, filtered solids in funnel:	0.0790 g	Total Semivolatiles Yield:	35.6218 g = 47.48%
		Total Solids Yield:	0.2527 g = 17.69%
		Total Volatiles Yield:	0.4976 g = 34.83%
		Total Losses:	0.5348 g
		% Losses:	1.45 %
		Conversion:	82.31 %

Hydrothermal Run Number: 6TB1 **Date:** 8/31/2009

Nominal weight loading:	1 : 25	Initial pressure in bomb after He charge:	52.4 psia
Wet bagasse mass:	1.2552 g	Maximum pressure recorded in bomb:	11784.4 psia
Bagasse moisture:	5.20 %	Final bomb pressure before GC analysis:	251.7 psia
Dry bagasse mass:	1.1900 g	Bomb temperature before GC analysis:	23.3 °C
DI H_2O mass:	29.5 g	Density of liquid product:	0.9990 g cm^{-3}
DI H_2O pH:	5.35	Volume of liquid product:	29.2297 cm^3
Total H_2O mass:	29.5652 g	Volume of solid product:	0.0763 cm^3
Run temperature:	600 °C	Volume of gas product:	37.7430 cm^3
Nominal run duration:	5 min	Moles of gas product (less initial He):	0.0235 mol

Unfiltered liquids + beaker:	57.4506 g	Dried solids + beaker:	28.6730 g
Clean, dry beaker:	28.6626 g	Clean, dry beaker:	28.6626 g
Unfiltered liquids:	28.7880 g	Dried solids in beaker:	0.0104 g
(2) Wet Kimwipe(s) (cap + threads):	0.9091 g	Unfiltered liquids from beaker:	28.7880 g
(2) Dry, unused Kimwipe(s)	0.8986 g	Dried solids from beaker:	0.0104 g
Semivolatiles inside cap:	0.0105 g	Semivolatiles in beaker:	28.7776 g
Sludge + 5.9 mL DI H_2O + boat:	8.6704 g	Dried solids + boat:	2.3580 g
Clean, dry Al weigh boat:	2.2604 g	Clean, dry Al weigh boat:	2.2604 g
Sludge + 5.9 mL DI H_2O:	6.4100 g	Dried solids in boat:	0.0976 g
– 5.9 mL DI H_2O:	5.9000 g		
Sludge (slurry + tars) in boat:	0.5100 g	Sludge (slurry + tars) in boat:	0.5100 g
		– Dried solids in boat:	0.0976 g
Dried solids + funnel + filter paper:	62.3867 g	Semivolatiles in boat:	0.4124 g
Size 0 funnel + 1.2 μm filter paper:	62.3246 g		
Dried, filtered solids in funnel:	0.0621 g		

Total Semivolatiles Yield:	29.2005 g	=	34.92%
Total Solids Yield:	0.1701 g	=	14.29%
Total Volatiles Yield:	0.6043 g	=	50.78%
Total Losses:	0.7803 g		
% Losses:	2.54 %		
Conversion:	85.71 %		

Observations: Unfiltered semivolatiles have a distinct cresol odor; similar to run at 500 °C some solids rise to the top and and float while other particles in the top layer sink to the bottom

Hydrothermal Run Number: 5RT01 **Date:** 8/24/2009

Nominal weight loading:	1 : 25	Initial pressure in bomb after He charge:	66.5 psia
Wet bagasse mass:	1.5028 g	Maximum pressure recorded in bomb:	10766.0 psia
Bagasse moisture:	5.20 %	Final bomb pressure before GC analysis:	221.5 psia
Dry bagasse mass:	1.4247 g	Bomb temperature before GC analysis:	24.4 °C
DI H_2O Mass:	35.4 g	Density of liquid product:	0.9991 g cm^{-3}
DI H_2O pH:	5.62	Volume of liquid product:	35.6265 cm^3
Total H_2O mass:	35.4781 g	Volume of solid product:	0.1334 cm^3
Run temperature:	500 °C	Volume of gas product:	31.2891 cm^3
Nominal run duration:	1 min	Moles of gas product (less initial He):	0.0154 mol

Unfiltered liquids + beaker:	64.5614 g	Dried solids + beaker:	29.8767 g
Clean, dry beaker:	29.8107 g	Clean, dry beaker:	29.8107 g
Unfiltered liquids:	34.7507 g	Dried solids in beaker:	0.0660 g
(2) Wet Kimwipes (cap + threads):	1.7659 g	Unfiltered liquids from beaker:	34.7507 g
(2) Dry, unused Kimwipe(s)	0.9872 g	Dried solids from beaker:	0.0660 g
Semivolatiles inside cap:	0.7787 g	Semivolatiles in beaker:	34.6847 g
Sludge + 5.9 mL DI H_2O + boat:	8.4327 g	Dried solids + boat:	2.4017 g
Clean, dry Al weigh boat:	2.2545 g	Clean, dry Al weigh boat:	2.2545 g
Sludge + 5.9 mL DI H_2O:	6.1782 g	Dried solids in boat:	0.1472 g
– 5.9 mL DI H_2O:	5.9000 g		
Sludge (slurry + tars) in boat:	0.2782 g	Sludge (slurry + tars) in boat:	0.2782 g
		– Dried solids in boat:	0.1472 g
Dried solids + funnel + filter paper:	59.2107 g	Semivolatiles in boat:	0.1310 g
Size 0 funnel + 1.2 μm filter paper:	59.1264 g		
Dried, filtered solids in funnel:	0.0843 g	Total Semivolatiles Yield:	35.5944 g = 47.30%
		Total Solids Yield:	0.2975 g = 20.88%
		Total Volatiles Yield:	0.4534 g = 31.82%
		Total Losses:	0.5575 g
		% Losses:	1.51 %
		Conversion:	79.12 %

Hydrothermal Run Number: 5RT05 **Date:** 9/3/2009

Nominal weight loading:	1 : 25	Initial pressure in bomb after He charge:	65.5 psia
Wet bagasse mass:	1.5018 g	Maximum pressure recorded in bomb:	10253.9 psia
Bagasse moisture:	5.20 %	Final bomb pressure before GC analysis:	239.6 psia
Dry bagasse mass:	1.4237 g	Bomb temperature before GC analysis:	25.6 °C
DI H_2O Mass:	35.4 g	Density of liquid product:	0.9995 g cm^{-3}
DI H_2O pH:	5.50	Volume of liquid product:	35.8785 cm^3
Total H_2O mass:	35.4781 g	Volume of solid product:	0.1180 cm^3
Run temperature:	500 °C	Volume of gas product:	31.0525 cm^3
Nominal run duration:	5 min	Moles of gas product (less initial He):	0.0168 mol

Unfiltered liquids + beaker:	64.0651 g	Dried solids + beaker:	29.8444 g
Clean, dry beaker:	29.8114 g	Clean, dry beaker:	29.8114 g
Unfiltered liquids:	34.2537 g	Dried solids in beaker:	0.0330 g
(1) Wet Kimwipe(s) (cap + threads):	1.0667 g	Unfiltered liquids from beaker:	34.2537 g
(1) Dry, unused Kimwipe(s)	0.4519 g	Dried solids from beaker:	0.0330 g
Semivolatiles inside cap:	0.6148 g	Semivolatiles in beaker:	34.2207 g
Sludge + 5.9 mL DI H_2O + boat:	9.2803 g	Dried solids + boat:	2.3552 g
Clean, dry Al weigh boat:	2.1938 g	Clean, dry Al weigh boat:	2.1938 g
Sludge + 5.9 mL DI H_2O:	7.0865 g	Dried solids in boat:	0.1614 g
– 5.9 mL DI H_2O:	5.9000 g		
Sludge (slurry + tars) in boat:	1.1865 g	Sludge (slurry + tars) in boat:	1.1865 g
		– Dried solids in boat:	0.1614 g
Dried solids + funnel + filter paper:	62.6440 g	Semivolatiles in boat:	1.0251 g
Size 0 funnel + 1.2 μm filter paper:	62.5753 g		
Dried, filtered solids in funnel:	0.0687 g	Total Semivolatiles Yield:	35.8606 g = 46.39%
		Total Solids Yield:	0.2631 g = 18.48%
		Total Volatiles Yield:	0.5002 g = 35.13%
		Total Losses:	0.2779 g
		% Losses:	0.75 %
		Conversion:	81.52 %

NB: Run 5RT05 is also designated separately as 5TB5 and 5WB2 because this is the standard, baseline run at 500 °C and 4 wt % biomass loading for 5 min.

Hydrothermal Run Number: **5RT10** Date: **8/24/2009**

Nominal weight loading:	1 : 25	Initial pressure in bomb after He charge:	66.5012 psia
Wet bagasse mass:	1.5006 g	Maximum pressure recorded in bomb:	11061.9 psia
Bagasse moisture:	5.20 %	Final bomb pressure before GC analysis:	253.7 psia
Dry bagasse mass:	1.4226 g	Bomb temperature before GC analysis:	23.3 °C
DI H_2O mass:	35.4 g	Density of liquid product:	0.9992 g cm^{-3}
DI H_2O pH:	5.62	Volume of liquid product:	35.5540 cm^3
Total H_2O mass:	35.4780 g	Volume of solid product:	0.1083 cm^3
Run temperature:	500 °C	Volume of gas product:	31.3867 cm^3
Nominal run duration:	10 min	Moles of gas product (less initial He):	0.0184 mol

Unfiltered liquids + beaker:	65.4613 g	Dried solids + beaker:	30.6158 g
Clean, dry beaker:	30.5881 g	Clean, dry beaker:	30.5881 g
Unfiltered liquids:	34.8732 g	Dried solids in beaker:	0.0277 g
(2) Wet Kimwipes (cap + threads):	1.0479 g	Unfiltered liquids from beaker:	34.8732 g
(2) Dry, unused Kimwipe(s)	0.9156 g	Dried solids from beaker:	0.0277 g
Semivolatiles inside cap:	0.1323 g	Semivolatiles in beaker:	34.8455 g
Sludge + 5.9 mL DI H_2O + boat:	8.7750 g	Dried solids + boat:	2.3272 g
Clean, dry Al weigh boat:	2.1978 g	Clean, dry Al weigh boat:	2.1978 g
Sludge + 5.9 mL DI H_2O:	6.5772 g	Dried solids in boat:	0.1294 g
– 5.9 mL DI H_2O:	5.9000 g		
Sludge (slurry + tars) in boat:	0.6772 g	Sludge (slurry + tars) in boat:	0.6772 g
		– Dried solids in boat:	0.1294 g
Dried solids + funnel + filter paper:	59.2107 g	Semivolatiles in boat:	0.5478 g
Size 0 funnel + 1.2 μm filter paper:	59.1264 g		
Dried, filtered solids in funnel:	0.0843 g	Total Semivolatiles Yield:	35.5256 g = 46.71%
		Total Solids Yield:	0.2414 g = 16.97%
		Total Volatiles Yield:	0.5167 g = 36.32%
		Total Losses:	0.6169 g
		% Losses:	1.67 %
		Conversion:	83.03 %

Observations: Solid residues collected in beaker have a dark chartreuse brown appearance; green coloration readily apparent when residue was dissolved in methanol

Hydrothermal Run Number: 5RT30 **Date:** 9/24/2009

Nominal weight loading:	1 : 25	Initial pressure in bomb after He charge:	59.5 psia
Wet bagasse mass:	1.4999 g	Maximum pressure recorded in bomb:	10213.6 psia
Bagasse moisture:	5.20 %	Internal bomb pressure after run:	249.6 psia
Dry bagasse mass:	1.4219 g	Bomb temperature before GC test:	28.2 °C
DI H_2O mass:	35.4 g	Density of liquid product:	0.9992 g cm^{-3}
DI H_2O pH:	5.88	Volume of liquid product:	30.9402 cm^3
Total H_2O mass:	35.4780 g	Volume of solid product:	0.0841 cm^3
Run temperature:	500 °C	Volume of gas product:	36.0248 cm^3
Nominal run duration:	30 min	Moles of gas product (less initial He):	0.0213 mol

Unfiltered liquids + beaker:	59.2279 g	Dried solids + beaker:	29.3112 g
Clean, dry beaker:	29.2632 g	Clean, dry beaker:	29.2632 g
Unfiltered liquids:	29.9647 g	Dried solids in beaker:	0.0480 g
(2) Wet Kimwipe(s) (cap + threads):	1.0050 g	Unfiltered liquids from beaker:	29.9647 g
(2) Dry, unused Kimwipe(s)	0.9282 g	Dried solids from beaker:	0.0480 g
Semivolatiles inside cap:	0.0768 g	Semivolatiles in beaker:	29.9167 g
Sludge + 5.9 mL DI H_2O + boat:	9.1968 g	Dried solids + boat:	2.3749 g
Clean, dry Al weigh boat:	2.2911 g	Clean, dry Al weigh boat:	2.2911 g
Sludge + 5.9 mL DI H_2O:	6.9057 g	Dried solids in boat:	0.0838 g
– 5.9 mL DI H_2O:	5.9000 g		
Sludge (slurry + tars) in boat:	1.0057 g	Sludge (slurry + tars) in boat:	1.0057 g
		– Dried solids in boat:	0.0838 g
Dried solids + funnel + filter paper:	62.4569 g	Semivolatiles in boat:	0.9219 g
Size 0 funnel + 1.2 μm filter paper:	62.4012 g		
Dried, filtered solids in funnel:	0.0557 g	Total Semivolatiles Yield:	30.9154 g = 46.29%
		Total Solids Yield:	0.1875 g = 13.19%
		Total Volatiles Yield:	0.5762 g = 40.53%
		Total Losses:	5.2208 g
		% Losses:	14.15 %
		Conversion:	86.81 %

Observations: Solid residues collected in beaker have a dark chartreuse brown appearance; green coloration readily apparent when residue was dissolved in methanol; Hastelloy solid has a mainly Prussian blue discoloration with an odd patch of metallic silver surface remaining on the surface transverse to the cylindrical axis

Hydrothermal Run Number: 5RT60 **Date:** 9/21/2009

Nominal weight loading:	1 : 25	Initial pressure in bomb after He charge:	77.6 psia
Wet bagasse mass:	1.4973 g	Maximum pressure recorded in bomb:	9446.8 psia
Bagasse moisture:	5.20 %	Internal bomb pressure after run:	265.7 psia
Dry bagasse mass:	1.4195 g	Bomb temperature before GC test:	23.8 °C
DI H_2O mass:	35.4 g	Density of liquid product:	0.9992 g cm^{-3}
DI H_2O pH:	5.69	Volume of liquid product:	28.3974 cm^3
Total H_2O mass:	47.3700 g	Volume of solid product:	0.0562 cm^3
Run temperature:	500 °C	Volume of gas product:	38.5953 cm^3
Nominal run duration:	60 min	Moles of gas product (less initial He):	0.0241 mol

Unfiltered liquids + beaker:	55.7809 g	Dried solids + beaker:	28.7062 g
Clean, dry beaker:	28.6625 g	Clean, dry beaker:	28.6625 g
Unfiltered liquids:	27.1184 g	Dried solids in beaker:	0.0437 g
(2) Wet Kimwipe(s) (cap + threads):	1.0106 g	Unfiltered liquids from beaker:	27.1184 g
(2) Dry, unused Kimwipe(s)	0.9417 g	Dried solids from beaker:	0.0437 g
Semivolatiles inside cap:	0.0689 g	Semivolatiles in beaker:	27.0747 g
Sludge + 5.9 mL DI H_2O + boat:	9.4991 g	Dried solids + boat:	2.3680 g
Clean, dry Al weigh boat:	2.2987 g	Clean, dry Al weigh boat:	2.2987 g
Sludge + 5.9 mL DI H_2O:	7.2004 g	Dried solids in boat:	0.0693 g
– 5.9 mL DI H_2O:	5.9000 g		
Sludge (slurry + tars) in boat:	1.3004 g	Sludge (slurry + tars) in boat:	1.3004 g
		– Dried solids in boat:	0.0693 g
Dried solids + funnel + filter paper:	59.3380 g	Semivolatiles in boat:	1.2311 g
Size 0 funnel + 1.2 μm filter paper:	59.3256 g		
Dried, filtered solids in funnel:	0.0124 g		

Total Semivolatiles Yield:	28.3747 g	=	43.79%
Total Solids Yield:	0.1254 g	=	8.83%
Total Volatiles Yield:	0.6724 g	=	47.37%
Total Losses:	7.7248 g		
% Losses:	20.94 %		
Conversion:	91.17 %		

Observations: Solid residues collected in beaker have a dark chartreuse brown appearance; green coloration readily apparent when residue was dissolved in methanol; Hastelloy solid has a mainly Prussian blue discoloration with an odd patch of metallic silver surface remaining on the surface transverse to the cylindrical axis

Hydrothermal Run Number: 5WA1 **Date:** 8/18/2009

Nominal weight loading:	1 : 37.5	Initial pressure in bomb after He charge:	75.6 psia
Wet bagasse mass:	0.9956 g	Maximum pressure recorded in bomb:	9962.7 psia
Bagasse moisture:	5.20 %	Final bomb pressure before GC analysis:	200.3 psia
Dry bagasse mass:	0.9439 g	Bomb temperature before GC analysis:	29.7 °C
DI H_2O mass:	35.4 g	Density of liquid product:	0.9986 g cm^{-3}
DI H_2O pH:	5.65	Volume of liquid product:	35.3965 cm^3
Total H_2O mass:	35.4517 g	Volume of solid product:	0.0769 cm^3
Run temperature:	500 °C	Volume of gas product:	31.5756 cm^3
Nominal run duration:	5 min	Moles of gas product (less initial He):	0.0127 mol

Unfiltered liquids + beaker:	62.3287 g	Dried solids + beaker:	28.6918 g
Clean, dry beaker:	28.6626 g	Clean, dry beaker:	28.6626 g
Unfiltered liquids:	33.6661 g	Dried solids in beaker:	0.0292 g
(3) Wet Kimwipes (cap + threads):	2.2990 g	Unfiltered liquids from beaker:	33.6661 g
(3) Dry, unused Kimwipe(s)	1.4764 g	Dried solids from beaker:	0.0292 g
Semivolatiles inside cap:	0.8226 g	Semivolatiles in beaker:	33.6369 g
Sludge + 5.9 mL DI H_2O + boat:	9.1349 g	Dried solids + boat:	2.3475 g
Clean, dry Al weigh boat:	2.2929 g	Clean, dry Al weigh boat:	2.2929 g
Sludge + 5.9 mL DI H_2O:	6.8420 g	Dried solids in boat:	0.0546 g
– 5.9 mL DI H_2O:	5.9000 g		
Sludge (slurry + tars) in boat:	0.9420 g	Sludge (slurry + tars) in boat:	0.9420 g
		– Dried solids in boat:	0.0546 g
Dried solids + funnel + filter paper:	62.6647 g	Semivolatiles in boat:	0.8874 g
Size 0 funnel + 1.2 μm filter paper:	62.5770 g		
Dried, filtered solids in funnel:	0.0877 g	Total Semivolatiles Yield:	35.3469 g = 43.45%
		Total Solids Yield:	0.1715 g = 18.17%
		Total Volatiles Yield:	0.3623 g = 38.38%
		Total Losses:	0.5149 g
		% Losses:	1.41 %
		Conversion:	81.83 %

Hydrothermal Run Number: 5WB2 **Date:** 9/3/2009

Nominal weight loading:	1 : 25	Initial pressure in bomb after He charge:	65.5 psia
Wet bagasse mass:	1.5018 g	Maximum pressure recorded in bomb:	10253.9 psia
Bagasse moisture:	5.20 %	Final bomb pressure before GC analysis:	239.6 psia
Dry bagasse mass:	1.4237 g	Bomb temperature before GC analysis:	25.6 °C
DI H_2O Mass:	35.4 g	Density of liquid product:	0.9995 g cm^{-3}
DI H_2O pH:	5.50	Volume of liquid product:	35.8785 cm^3
Total H_2O mass:	35.4781 g	Volume of solid product:	0.1180 cm^3
Run temperature:	500 °C	Volume of gas product:	31.0525 cm^3
Nominal run duration:	5 min	Moles of gas product (less initial He):	0.0168 mol

Unfiltered liquids + beaker:	64.0651 g	Dried solids + beaker:	29.8444 g
Clean, dry beaker:	29.8114 g	Clean, dry beaker:	29.8114 g
Unfiltered liquids:	34.2537 g	Dried solids in beaker:	0.0330 g
(1) Wet Kimwipe(s) (cap + threads):	1.0667 g	Unfiltered liquids from beaker:	34.2537 g
(1) Dry, unused Kimwipe(s)	0.4519 g	Dried solids from beaker:	0.0330 g
Semivolatiles inside cap:	0.6148 g	Semivolatiles in beaker:	34.2207 g
Sludge + 5.9 mL DI H_2O + boat:	9.2803 g	Dried solids + boat:	2.3552 g
Clean, dry Al weigh boat:	2.1938 g	Clean, dry Al weigh boat:	2.1938 g
Sludge + 5.9 mL DI H_2O:	7.0865 g	Dried solids in boat:	0.1614 g
– 5.9 mL DI H_2O:	5.9000 g		
Sludge (slurry + tars) in boat:	1.1865 g	Sludge (slurry + tars) in boat:	1.1865 g
		– Dried solids in boat:	0.1614 g
Dried solids + funnel + filter paper:	62.6440 g	Semivolatiles in boat:	1.0251 g
Size 0 funnel + 1.2 μm filter paper:	62.5753 g		
Dried, filtered solids in funnel:	0.0687 g	Total Semivolatiles Yield:	35.8606 g = 46.39%
		Total Solids Yield:	0.2631 g = 18.48%
		Total Volatiles Yield:	0.5002 g = 35.13%
		Total Losses:	0.2779 g
		% Losses:	0.75 %
		Conversion:	81.52 %

NB: Run 5WB2 is also designated separately as 5TB5 and 5RT05 because this is the standard, baseline run at 500 °C and 4 wt % biomass loading for 5 min.

Hydrothermal Run Number: 5WC2 **Date:** 8/17/2009

Nominal weight loading:	1 : 12.5	Initial pressure in bomb after He charge:	73.5 psia
Wet bagasse mass:	3.0085 g	Maximum pressure recorded in bomb:	11338.6 psia
Bagasse moisture:	5.20 %	Final bomb pressure before GC analysis:	355.3 psia
Dry bagasse mass:	2.8521 g	Bomb temperature before GC analysis:	29.7 °C
DI H_2O mass:	35.4 g	Density of liquid product:	0.9997 g cm^{-3}
DI H_2O pH:	5.32	Volume of liquid product:	36.4478 cm^3
Total H_2O mass:	35.5564 g	Volume of solid product:	0.3119 cm^3
Run temperature:	500 °C	Volume of gas product:	30.2892 cm^3
Nominal run duration:	5 min	Moles of gas product (less initial He):	0.0256 mol

Unfiltered liquids + beaker:	64.0419 g	Dried solids + beaker:	29.3472 g
Clean, dry beaker:	29.2957 g	Clean, dry beaker:	29.2957 g
Unfiltered liquids:	34.7462 g	Dried solids in beaker:	0.0515 g
(2) Wet Kimwipes (cap + threads):	0.9840 g	Unfiltered liquids from beaker:	34.7462 g
(2) Dry, unused Kimwipe(s)	0.8002 g	Dried solids from beaker:	0.0515 g
Semivolatiles inside cap:	0.1838 g	Semivolatiles in beaker:	34.6947 g
Sludge + 5.9 mL DI H_2O + boat:	10.1131 g	Dried solids + boat:	2.6547 g
Clean, dry Al weigh boat:	2.2613 g	Clean, dry Al weigh boat:	2.2613 g
Sludge + 5.9 mL DI H_2O:	7.8518 g	Dried solids in boat:	0.3934 g
– 5.9 mL DI H_2O:	5.9000 g		
Sludge (slurry + tars) in boat:	1.9518 g	Sludge (slurry + tars) in boat:	1.9518 g
		– Dried solids in boat:	0.3934 g
Dried solids + funnel + filter paper:	60.2903 g	Semivolatiles in boat:	1.5584 g
Size 0 funnel + 1.2 μm filter paper:	60.0396 g		
Dried, filtered solids in funnel:	0.2507 g	Total Semivolatiles Yield:	36.4369 g = 41.24%
		Total Solids Yield:	0.6956 g = 24.39%
		Total Volatiles Yield:	0.9803 g = 34.37%
		Total Losses:	0.2957 g
		% Losses:	0.77 %
		Conversion:	75.61 %

Hydrothermal Run Number: 5SBA1 **Date:** 8/19/2009

Nominal weight loading:	1:25	Initial pressure in bomb after He charge:	68.5 psia
Wet 18/25 mesh bagasse mass:	1.5001 g	Maximum pressure recorded in bomb:	10650.3 psia
18/25 mesh bagasse moisture:	7.06 %	Final bomb pressure before GC analysis:	250.7 psia
Dry 18/25 mesh bagasse mass:	1.3943 g	Bomb temperature before GC analysis:	27.8 °C
DI H_2O mass:	35.4000 g	Density of liquid product:	0.9993 g cm^{-3}
DI H_2O pH:	5.54	Volume of liquid product:	36.0477 cm^3
Total H_2O mass:	35.5058 g	Volume of solid product:	0.0989 cm^3
Run temperature:	500 °C	Volume of gas product:	30.9023 cm^3
Nominal run duration:	5 min	Moles of gas product (less initial He):	0.0173 mol

Unfiltered liquids + beaker:	64.3058 g	Dried solids + beaker:	29.3090 g
Clean, dry beaker:	29.2946 g	Clean, dry beaker:	29.2946 g
Unfiltered liquids:	35.0112 g	Dried solids in beaker:	0.0144 g
(2) Wet Kimwipes (cap + threads):	1.7563 g	Unfiltered liquids from beaker:	35.0112 g
(2) Dry, unused Kimwipe(s)	1.0492 g	Dried solids from beaker:	0.0144 g
Semivolatiles inside cap:	0.7071 g	Semivolatiles in beaker:	34.9968 g
Sludge + 5.9 mL DI H_2O + boat:	8.6243 g	Dried solids + boat:	2.4057 g
Clean, dry Al weigh boat:	2.3108 g	Clean, dry Al weigh boat:	2.3108 g
Sludge + 5.9 mL DI H_2O:	6.3135 g	Dried solids in boat:	0.0949 g
– 5.9 mL DI H_2O:	5.9000 g		
Sludge (slurry + tars) in boat:	0.4135 g	Sludge (slurry + tars) in boat:	0.4135 g
		– Dried solids in boat:	0.0949 g
Dried solids + funnel + filter paper:	62.4377 g	Semivolatiles in boat:	0.3186 g
Size 0 funnel + 1.2 μm filter paper:	62.3264 g		
Dried, filtered solids in funnel:	0.1113 g	Total Semivolatiles Yield:	36.0225 g = 48.35%
		Total Solids Yield:	0.2206 g = 15.82%
		Total Volatiles Yield:	0.4995 g = 35.83%
		Total Losses:	0.1575 g
		% Losses:	0.43 %
		Conversion:	84.18 %

Hydrothermal Run Number: 5SBB1 **Date:** 8/21/2009

Nominal weight loading:	1 : 25	Initial pressure in bomb after He charge:	72.5 psia
Wet 45/60 mesh bagasse mass:	1.5005 g	Maximum pressure recorded in bomb:	10539.6 psia
45/60 mesh bagasse moisture:	5.71	Final bomb pressure before GC analysis:	252.7 psia
Dry 45/60 mesh bagasse mass:	1.4149 g	Bomb temperature before GC analysis:	24.4 °C
DI H_2O mass:	35.4 g	Density of liquid product:	0.9993 g cm^{-3}
DI H_2O pH:	5.77	Volume of liquid product:	35.9651 cm^3
Total H_2O mass:	35.4856 g	Volume of solid product:	0.0984 cm^3
Run temperature:	500 °C	Volume of gas product:	30.9855 cm^3
Nominal run duration:	5 min	Moles of gas product (less initial He):	0.0176 mol

Unfiltered liquids + beaker:	64.6122 g	Dried solids + beaker:	29.8343 g
Clean, dry beaker:	29.8121 g	Clean, dry beaker:	29.8121 g
Unfiltered liquids:	34.8001 g	Dried solids in beaker:	0.0222 g
(2) Wet Kimwipes (cap + threads):	1.4172 g	Unfiltered liquids from beaker:	34.8001 g
(2) Dry, unused Kimwipe(s)	0.9643 g	Dried solids from beaker:	0.0222 g
Semivolatiles inside cap:	0.4529 g	Semivolatiles in beaker:	34.7779 g
Sludge + 5.9 mL DI H_2O + boat:	8.9891 g	Dried solids + boat:	2.3800 g
Clean, dry Al weigh boat:	2.2705 g	Clean, dry Al weigh boat:	2.2705 g
Sludge + 5.9 mL DI H_2O:	6.7186 g	Dried solids in boat:	0.1095 g
– 5.9 mL DI H_2O:	5.9000 g		
Sludge (slurry + tars) in boat:	0.8186 g	Sludge (slurry + tars) in boat:	0.8186 g
		– Dried solids in boat:	0.1095 g
Dried solids + funnel + filter paper:	60.1271 g	Semivolatiles in boat:	0.7091 g
Size 0 funnel + 1.2 μm filter paper:	60.0394 g		
Dried, filtered solids in funnel:	0.0877 g	Total Semivolatiles Yield:	35.9399 g = 49.21%
		Total Solids Yield:	0.2194 g = 15.51%
		Total Volatiles Yield:	0.4993 g = 35.29%
		Total Losses:	0.2419 g
		% Losses:	0.66 %
		Conversion:	84.49 %

Hydrothermal Run Number: 5SBC1 **Date:** 8/25/2009

Nominal weight loading:	1 : 25	Initial pressure in bomb after He charge:	76.6 psia
Wet 140/230 mesh bagasse mass:	1.5011 g	Maximum pressure recorded in bomb:	10151.2 psia
140/230 mesh bagasse moisture:	6.30 %	Final bomb pressure before GC analysis:	227.5 psia
Dry 140/230 mesh bagasse mass:	1.4065	Bomb temperature before GC analysis:	24.4 °C
DI H_2O mass:	35.4 g	Density of liquid product:	0.9991 g cm^{-3}
DI H_2O pH:	5.74	Volume of liquid product:	35.7167 cm^3
Total H_2O mass:	35.4946 g	Volume of solid product:	0.1562 cm^3
Run temperature:	500 °C	Volume of gas product:	31.1761 cm^3
Nominal run duration:	5 min	Moles of gas product (less initial He):	0.0153 mol

Unfiltered liquids + beaker:	64.4919 g	Dried solids + beaker:	29.6999 g
Clean, dry beaker:	29.6690 g	Clean, dry beaker:	29.6690 g
Unfiltered liquids:	34.8229 g	Dried solids in beaker:	0.0309 g
(0) Wet Kimwipes (cap + threads):	0.0000 g	Unfiltered liquids from beaker:	34.8229 g
(0) Dry, unused Kimwipe(s)	0.0000 g	Dried solids from beaker:	0.0309 g
Semivolatiles inside cap:	0.0000 g	Semivolatiles in beaker:	34.7920 g
Sludge + 5.9 mL DI H_2O + boat:	9.1581 g	Dried solids + boat:	2.3655 g
Clean, dry Al weigh boat:	2.1970 g	Clean, dry Al weigh boat:	2.1970 g
Sludge + 5.9 mL DI H_2O:	6.9611 g	Dried solids in boat:	0.1685 g
– 5.9 mL DI H_2O:	5.9000 g		
Sludge (slurry + tars) in boat:	1.0611 g	Sludge (slurry + tars) in boat:	1.0611 g
		– Dried solids in boat:	0.1685 g
Dried solids + funnel + filter paper:	62.7284 g	Semivolatiles in boat:	0.8926 g
Size 0 funnel + 1.2 μm filter paper:	62.5795 g		
Dried, filtered solids in funnel:	0.1489 g	Total Semivolatiles Yield:	35.6846 g = 43.65%
		Total Solids Yield:	0.3483 g = 24.76%
		Total Volatiles Yield:	0.4443 g = 31.59%
		Total Losses:	0.4239 g
		% Losses:	1.15 %
		Conversion:	75.24 %

Hydrothermal Run Number: 5CB1 **Date:** 8/21/2009

Nominal weight loading:	1 : 25	Initial pressure in bomb after He charge:	62.5 psia
Wet cellulose mass:	1.5050 g	Maximum pressure recorded in bomb:	10489.3 psia
Cellulose moisture:	4.55 %	Final bomb pressure before GC analysis:	270.8 psia
Dry cellulose mass:	1.4366 g	Bomb temperature before GC analysis:	30.0 °C
DI H_2O mass:	35.4 g	Density of liquid product:	0.9984 g cm^{-3}
DI H_2O pH:	5.78	Volume of liquid product:	36.1749 cm^3
Total H_2O mass	35.4684 g	Volume of solid product:	0.0427 cm^3
Run temperature:	500 °C	Volume of gas product:	30.8314 cm^3
Nominal run duration:	5 min	Moles of gas product (less initial He):	0.0192 mol

Unfiltered liquids + beaker:	65.7792 g	Dried solids + beaker:	30.5922 g
Clean, dry beaker:	30.5897 g	Clean, dry beaker:	30.5897 g
Unfiltered liquids:	35.1895 g	Dried solids in beaker:	0.0025 g
(2) Wet Kimwipes (cap + threads):	1.6391 g	Unfiltered liquids from beaker:	35.1895 g
(2) Dry, unused Kimwipe(s)	0.9163 g	Dried solids from beaker:	0.0025 g
Semivolatiles inside cap:	0.7228 g	Semivolatiles in beaker:	35.1870 g
Sludge + 5.9 mL DI H_2O + boat:	8.4078 g	Dried solids + boat:	2.3006 g
Clean, dry Al weigh boat:	2.2590 g	Clean, dry Al weigh boat:	2.2590 g
Sludge + 5.9 mL DI H_2O:	6.1488 g	Dried solids in boat:	0.0416 g
– 5.9 mL DI H_2O:	5.9000 g		
Sludge (slurry + tars) in boat:	0.2488 g	Sludge (slurry + tars) in boat:	0.2488 g
		– Dried solids in boat:	0.0416 g
Dried solids + funnel + filter paper:	66.1616 g	Semivolatiles in boat:	0.2072 g
Size 0 funnel + 1.2 μm filter paper:	66.1105 g		
Dried, filtered solids in funnel:	0.0511 g	Total Semivolatiles Yield:	36.1170 g = 54.48%
		Total Solids Yield:	0.0952 g = 6.63%
		Total Volatiles Yield:	0.5587 g = 38.89%
		Total Losses:	0.1341 g
		% Losses:	0.36 %
		Conversion:	93.37 %

Observations: Unfiltered liquid is an emulsion with dark brown oil droplets dispersed throughout a brownish orange liquid; filtrate has a pale yellow color with slightly more coloration than that of bagasse filtrate, strong gasoline odor; filtered solids appear oily and have a brownish vermillion hue

Hydrothermal Run Number: 5XB1 **Date:** 8/21/2009

Nominal weight loading:	1 : 25	Initial pressure in bomb after He charge:	76.6 psia
Wet xylan mass:	1.5820 g	Maximum pressure recorded in bomb:	10567.8 psia
Xylan moisture:	9.50 %	Final bomb pressure before GC analysis:	247.6 psia
Dry xylan mass:	1.4317 g	Bomb temperature before GC analysis:	21.1 °C
DI H_2O mass:	35.4 g	Density of liquid product:	1.0000 g cm^{-3}
DI H_2O pH:	5.50	Volume of liquid product:	36.1498 cm^3
Total H_2O mass	35.5503 g	Volume of solid product:	0.0708 cm^3
Run temperature:	500 °C	Volume of gas product:	30.8284 cm^3
Nominal run duration:	5 min	Moles of gas product (less initial He):	0.0170 mol

Unfiltered liquids + beaker:	65.1444 g	Dried solids + beaker:	29.8169 g
Clean, dry beaker:	29.8100 g	Clean, dry beaker:	29.8100 g
Unfiltered liquids:	35.3344 g	Dried solids in beaker:	0.0069 g
(2) Wet Kimwipes (cap + threads):	1.3218 g	Unfiltered liquids from beaker:	35.3344 g
(2) Dry, unused Kimwipe(s)	0.9163 g	Dried solids from beaker:	0.0069 g
Semivolatiles inside cap:	0.4055 g	Semivolatiles in beaker:	35.3275 g
Sludge + 5.9 mL DI H_2O + boat:	8.6800 g	Dried solids + boat:	2.3632 g
Clean, dry Al weigh boat:	2.2679 g	Clean, dry Al weigh boat:	2.2679 g
Sludge + 5.9 mL DI H_2O:	6.4121 g	Dried solids in boat:	0.0953 g
– 5.9 mL DI H_2O:	5.9000 g		
Sludge (slurry + tars) in boat:	0.5121 g	Sludge (slurry + tars) in boat:	0.5121 g
		– Dried solids in boat:	0.0953 g
Dried solids + funnel + filter paper:	60.0973 g	Semivolatiles in boat:	0.4168 g
Size 0 funnel + 1.2 μm filter paper:	60.0417 g		
Dried, filtered solids in funnel:	0.0556 g	Total Semivolatiles Yield:	36.1498 g = 43.67%
		Total Solids Yield:	0.1578 g = 11.02%
		Total Volatiles Yield:	0.6487 g = 45.31%
		Total Losses:	0.0257 g
		% Losses:	0.07 %
		Conversion:	88.98 %

Observations: Unfiltered semi-volatiles are muddy brown in color with distinctive oil beads floating on the surface; solid residue turned a reddish brown (burnt sienna) color when dissolved in methanol; filtrate had a light yellow color somewhat stronger than that of the cellulose-derived liquids

Hydrothermal Run Number: 5LB1 **Date:** 8/25/2009

Nominal weight loading:	1 : 25	Initial pressure in bomb after He charge:	71.5 psia
Wet lignin mass:	1.5720 g	Maximum pressure recorded in bomb:	10190.5 psia
Lignin moisture:	10.80 %	Final bomb pressure before GC analysis:	246.6 psia
Dry lignin mass:	1.4022 g	Bomb temperature before GC analysis:	29.4 °C
DI H_2O mass:	35.4 g	Density of liquid product:	1.0090 g cm^{-3}
DI H_2O pH:	5.54	Volume of liquid product:	35.8337 cm^3
Total H_2O mass:	35.5698 g	Volume of solid product:	0.1461 cm^3
Run temperature:	500 °C	Volume of gas product:	31.0692 cm^3
Nominal run duration:	5 min	Moles of gas product (less initial He):	0.0168 mol

Unfiltered liquids + beaker:	64.2441 g	Dried solids + beaker:	30.6348 g
Clean, dry beaker:	30.6305 g	Clean, dry beaker:	30.6305 g
Unfiltered liquids:	33.6136 g	Dried solids in beaker:	0.0043 g
(2) Wet Kimwipes (cap + threads):	1.7212 g	Unfiltered liquids from beaker:	33.6136 g
(2) Dry, unused Kimwipe(s)	0.8948 g	Dried solids from beaker:	0.0043 g
Semivolatiles inside cap:	0.8264 g	Semivolatiles in beaker:	33.6093 g
Sludge + 0.0 mL DI H_2O + boat:	4.2709 g	Dried solids + boat:	2.5504 g
Clean, dry Al weigh boat:	2.3077 g	Clean, dry Al weigh boat:	2.3077 g
Sludge + 0.0 mL DI H_2O:	1.9632 g	Dried solids in boat:	0.2427 g
– 0.0 mL DI H_2O:	0.0000 g		
Sludge (slurry + tars) in boat:	1.9632 g	Sludge (slurry + tars) in boat:	1.9632 g
		– Dried solids in boat:	0.2427 g
Dried solids + funnel + filter paper:	63.9759 g	Semivolatiles in boat:	1.7205 g
Size 0 funnel + 1.2 μm filter paper:	63.8972 g		
Dried, filtered solids in funnel:	0.0787 g	Total Semivolatiles Yield:	36.1562 g = 34.13%
		Total Solids Yield:	0.3257 g = 23.23%
		Total Volatiles Yield:	0.5980 g = 42.65%
		Total Losses:	-0.1079 g
		% Losses:	-0.29 %
		Conversion:	76.77 %

Observations: Very distinctive Kraft lignin smell common at paper pulp mills employing bleaching operations; unfiltered semi-volatiles are very turbid and have a medium caramel color; lots of solids recovered from bomb which appeared black but upon treatment with solvent appeared dark green; tars were oozy and black but not viscous; filtrate formed an unusual thin, black crusty layer on the interior walls of the bomb unlike any other run

Hydrothermal Run Number: Li/MgO **Date:** 9/8/2009

Nominal weight loading:	1 : 25	Initial pressure in bomb after He charge:	59.5 psia
Wet bagasse mass:	1.5012 g	Maximum pressure recorded in bomb:	10579.9 psia
Bagasse moisture:	5.20 %	Internal bomb pressure after run:	256.7 psia
Dry bagasse mass:	1.4232 g	Bomb temperature before GC test:	27.3 °C
DI H_2O mass:	35.4 g	Density of liquid product:	1.0057 g cm^{-3}
DI H_2O pH:	6.10	Volume of liquid product:	36.1711 cm^3
Total H_2O mass:	35.4780 g	Volume of solid product:	0.0514 cm^3
Run temperature:	500 °C	Volume of gas product:	30.8264 cm^3
Nominal run duration:	5 min	Moles of gas product (less initial He):	0.0184 mol
Li/MgO catalyst mass:	0.2990 g		

Unfiltered liquids + beaker:	64.7377 g	Dried solids + beaker:	29.8138 g
Clean, dry beaker:	29.6684 g	Clean, dry beaker:	29.6684 g
Unfiltered liquids:	35.0693 g	Dried solids in beaker:	0.1454 g
(2) Wet Kimwipe(s) (cap + threads):	1.4297 g	Unfiltered liquids from beaker:	35.0693 g
(2) Dry, unused Kimwipe(s)	0.9143 g	Dried solids from beaker:	0.1454 g
Semivolatiles inside cap:	0.5154 g	Semivolatiles in beaker:	34.9239 g
Sludge + 5.9 mL DI H_2O + boat:	9.1927 g	Dried solids + boat:	2.3547 g
Clean, dry Al weigh boat:	2.2852 g	Clean, dry Al weigh boat:	2.2852 g
Sludge + 5.9 mL DI H_2O:	6.9075 g	Dried solids in boat:	0.0695 g
– 5.9 mL DI H_2O:	5.9000 g		
Sludge (slurry + tars) in boat:	1.0075 g	Sludge (slurry + tars) in boat:	1.0075 g
		– Dried solids in boat:	0.0695 g
Dried solids + funnel + filter paper:	66.3129 g	Semivolatiles in boat:	0.9380 g
Size 0 funnel + 1.2 μm filter paper:	66.1141 g		
Dried, filtered solids in funnel:	0.1988 g	Total Semivolatiles Yield:	36.3773 g = 55.18%
		Total Solids Yield:	0.1147 g = 8.06%
		Total Volatiles Yield:	0.5232 g = 36.76%
		Total Losses:	-0.1140 g
		% Losses:	-0.31 %
		Conversion:	91.94 %

Observations: Unfiltered liquid has a dark brown, oily sheen on top; liquid color has a rose brown tint. Filtered liquid has a rose color similar to a light blush. Plastic formation was noticed in weigh boat after addition of water to remove residual solids in bomb.

Hydrothermal Run Number: MnO_2 (1) **Date:** 9/2/2009

Nominal weight loading:	1 : 25	Initial pressure in bomb after He charge:	68.5 psia
Wet bagasse mass:	1.4973 g	Maximum pressure recorded in bomb:	10190.5 psia
Bagasse moisture:	5.20 %	Internal bomb pressure after run:	201 psia
Dry bagasse mass:	1.4195 g	Bomb temperature before GC test:	26 °C
DI H_2O mass:	35.4 g	Density of liquid product:	1.0008 g cm^{-3}
DI H_2O pH:	5.61	Volume of liquid product:	35.9924 cm^3
Total H_2O mass:	35.4778 g	Volume of solid product:	0.0517 cm^3
Run temperature:	500 °C	Volume of gas product:	31.0048 cm^3
Nominal run duration:	5 min	Moles of gas product (less initial He):	0.0133 mol
MnO_2 catalyst mass:	0.3976 g		

Unfiltered liquids + beaker:	64.7971 g	Dried solids + beaker:	29.7366 g
Clean, dry beaker:	29.6685 g	Clean, dry beaker:	29.6685 g
Unfiltered liquids:	35.1286 g	Dried solids in beaker:	0.0681 g
(2) Wet Kimwipe(s) (cap + threads):	1.3950 g	Unfiltered liquids from beaker:	35.1286 g
(2) Dry, unused Kimwipe(s)	0.9132 g	Dried solids from beaker:	0.0681 g
Semivolatiles inside cap:	0.4818 g	Semivolatiles in beaker:	35.0605 g
Sludge + 5.9 mL DI H_2O + boat:	8.8449 g	Dried solids + boat:	2.4660 g
Clean, dry Al weigh boat:	2.2328 g	Clean, dry Al weigh boat:	2.2328 g
Sludge + 5.9 mL DI H_2O:	6.6121 g	Dried solids in boat:	0.2332 g
– 5.9 mL DI H_2O:	5.9000 g		
Sludge (slurry + tars) in boat:	0.7121 g	Sludge (slurry + tars) in boat:	0.7121 g
		– Dried solids in boat:	0.2332 g
Dried solids + funnel + filter paper:	66.3212 g	Semivolatiles in boat:	0.4789 g
Size 0 funnel + 1.2 μm filter paper:	66.1095 g		
Dried, filtered solids in funnel:	0.2117 g	Total Semivolatiles Yield:	36.0212 g = 64.30%
		Total Solids Yield:	0.1154 g = 8.13%
		Total Volatiles Yield:	0.3913 g = 27.57%
		Total Losses:	0.3694 g
		% Losses:	1.00 %
		Conversion:	91.87 %

Observations: Unfiltered liquid has a darker appearance than normal and consists of oil emulsion droplets that coalesced to form a viscous top layer (the oil droplets are almost in a state of suspended animation, moving only when the entire layer of film shifts position); solids are a dirty brown color (likely the MnO_2); odor strongly reminiscent of light naphtha petroleum fractions; filtrate color has a deep blue-violet color (possible presence of Mn(V)?)

Hydrothermal Run Number: MnO_2 (2) **Date:** 9/6/2009

Nominal weight loading:	1 : 25	Initial pressure in bomb after He charge:	72.5 psia
Bagasse Mass:	1.5074 g	Maximum pressure recorded in bomb:	10595.0 psia
Bagasse moisture:	5.20 %	Internal bomb pressure after run:	206 psia
Dry bagasse mass:	1.4291 g	Bomb temperature before GC test:	27.8 °C
DI H_2O mass:	35.4 g	Density of liquid product:	1.0004 g cm^{-3}
DI H_2O pH:	5.81	Volume of liquid product:	35.9526 cm^3
Total H_2O mass:	35.4783 g	Volume of solid product:	0.0681 cm^3
Run temperature:	500 °C	Volume of gas product:	31.0283 cm^3
Nominal run duration:	5 min	Moles of gas product (less initial He):	0.0134 mol
MnO_2 catalyst mass:	0.3976 g		

Unfiltered liquids + beaker:	63.3141 g	Dried solids + beaker:	28.7399 g
Clean, dry beaker:	28.6624 g	Clean, dry beaker:	28.6624 g
Unfiltered liquids:	34.6517 g	Dried solids in beaker:	0.0775 g
(2) Wet Kimwipe(s) (cap + threads):	0.9190 g	Unfiltered liquids from beaker:	34.6517 g
(2) Dry, unused Kimwipe(s)	0.8924 g	Dried solids from beaker:	0.0775 g
Semivolatiles inside cap:	0.0266 g	Semivolatiles in beaker:	34.5742 g
Sludge + 5.9 mL DI H_2O + boat:	9.8006 g	Dried solids + boat:	2.5344 g
Clean, dry Al weigh boat:	2.2387 g	Clean, dry Al weigh boat:	2.2387 g
Sludge + 5.9 mL DI H_2O:	7.5619 g	Dried solids in boat:	0.2957 g
– 5.9 mL DI H_2O:	5.9000 g		
Sludge (slurry + tars) in boat:	1.6619 g	Sludge (slurry + tars) in boat:	1.6619 g
		– Dried solids in boat:	0.2957 g
Dried solids + funnel + filter paper:	64.0700 g	Semivolatiles in boat:	1.3662 g
Size 0 funnel + 1.2 μm filter paper:	63.8938 g		
Dried, filtered solids in funnel:	0.1762 g		

Total Semivolatiles Yield:	35.9670 g	=	53.47%
Total Solids Yield:	0.1518 g	=	10.62%
Total Volatiles Yield:	0.5132 g	=	35.91%
Total Losses:	0.2754 g		
% Losses:	0.75 %		
Conversion:	89.38 %		

Hydrothermal Run Number: CO (1) **Date:** 9/12/2009

Nominal weight loading:	1 : 25	Initial pressure in bomb after CO charge:	101.7 psia
Wet bagasse mass:	1.5084 g	Maximum pressure recorded in bomb:	10338.4 psia
Bagasse moisture:	5.20 %	Internal bomb pressure after run:	256.7 psia
Dry bagasse mass:	1.4300 g	Bomb temperature before GC test:	28.0 °C
DI H_2O mass:	35.4 g	Moles of CO in bomb initially:	0.0062 mol
DI H_2O pH:	5.79	Density of liquid product:	0.9992 g cm^{-3}
Total H_2O mass:	35.4784 g	Volume of liquid product:	34.8244 cm^3
Run temperature:	500 °C	Volume of solid product:	0.1009 cm^3
Nominal run duration:	5 min	Volume of gas product:	32.1237 cm^3
Headspace volume:	21.79 cm^3	Moles of gas product (less initial CO):	0.0165 mol

Unfiltered liquids + beaker:	63.4820 g	Dried solids + beaker:	29.3130 g
Clean, dry beaker:	29.2636 g	Clean, dry beaker:	29.2636 g
Unfiltered liquids:	34.2184 g	Dried solids in beaker:	0.0494 g
(2) Wet Kimwipe(s) (cap + threads):	0.9817 g	Unfiltered liquids from beaker:	34.2184 g
(2) Dry, unused Kimwipe(s)	0.9274 g	Dried solids from beaker:	0.0494 g
Semivolatiles inside cap:	0.0543 g	Semivolatiles in beaker:	34.1690 g
Sludge + 5.9 mL DI H_2O + boat:	8.8617 g	Dried solids + boat:	2.3885 g
Clean, dry Al weigh boat:	2.3091 g	Clean, dry Al weigh boat:	2.3091 g
Sludge + 5.9 mL DI H_2O:	6.5526 g	Dried solids in boat:	0.0794 g
– 5.9 mL DI H_2O:	5.9000 g		
Sludge (slurry + tars) in boat:	0.6526 g	Sludge (slurry + tars) in boat:	0.6526 g
		– Dried solids in boat:	0.0794 g
Dried solids + funnel + filter paper:	62.4266 g	Semivolatiles in boat:	0.5732 g
Size 0 funnel + 1.2 μm filter paper:	62.3303 g		
Dried, filtered solids in funnel:	0.0963 g	Total Semivolatiles Yield:	34.7965 g = 52.28%
		Total Solids Yield:	0.2251 g = 15.74%
		Total Volatiles Yield:	0.4573 g = 31.98%
		Total Losses:	1.4295 g
		% Losses:	3.87 %
		Conversion:	84.26 %

Observations: Unfiltered liquid has suspension of very fine black particles floating at top; some particles on this layer sink while others on a bottom layer are rising simultaneously; layer of bubbles exists on the beaker floor; filtrate has a light yellow appearance

Hydrothermal Run Number: **$NaBH_4$ (2)** **Date:** **9/9/2009**

Nominal weight loading:	1 : 25	Initial pressure in bomb after He charge:	85.6 psia
Wet bagasse mass:	1.5091 g	Maximum pressure recorded in bomb:	11429.2 psia
Bagasse moisture:	5.20 %	Final bomb pressure before GC analysis:	330 psia
Dry bagasse mass:	1.4307 g	Bomb temperature before GC analysis:	22.2 °C
DI H_2O mass:	35.4 g	Density of liquid product:	1.0021 g cm^{-3}
DI H_2O pH:	5.69	Volume of liquid product:	35.5646 cm^3
Total H_2O mass:	35.4784 g	Volume of solid product:	0.0320 cm^3
Run temperature:	500 °C	Volume of gas product:	31.4524 cm^3
Nominal run duration:	5 min	Moles of gas product (less initial He):	0.0241 mol
$NaBH_4$ mass:	0.1000 g		

Unfiltered liquids + beaker:	64.8944 g	Dried solids + beaker:	30.6023 g
Clean, dry beaker:	30.5889 g	Clean, dry beaker:	30.5889 g
Unfiltered liquids:	34.3055 g	Dried solids in beaker:	0.0134 g
(2) Wet Kimwipes (cap + threads):	0.9995 g	Unfiltered liquids from beaker:	34.3055 g
(2) Dry, unused Kimwipe(s)	0.9343 g	Dried solids from beaker:	0.0134 g
Semivolatiles inside cap:	0.0652 g	Semivolatiles in beaker:	34.2921 g
Sludge + 0.0 mL DI H_2O + boat:	3.5870 g	Dried solids + boat:	2.3050 g
Clean, dry Al weigh boat:	2.2472 g	Clean, dry Al weigh boat:	2.2472 g
Sludge + 0.0 mL DI H_2O:	1.3398 g	Dried solids in boat:	0.0578 g
– 0.0 mL DI H_2O:	0.0000 g		
Sludge (slurry + tars) in boat:	1.3398 g	Sludge (slurry + tars) in boat:	1.3398 g
		– Dried solids in boat:	0.0578 g
Dried solids + funnel + filter paper:	60.1402 g	Semivolatiles in boat:	1.2820 g
Size 0 funnel + 1.2 μm filter paper:	60.0401 g		
Dried, filtered solids in funnel:	0.1001 g		

Total Semivolatiles Yield:	35.6393 g	=	34.01%
Total Solids Yield:	0.0713 g	=	4.98%
Total Volatiles Yield:	0.8728 g	=	61.01%
Total Losses:	0.3257 g		
% Losses:	0.88 %		
Conversion:	95.02 %		

Observations: Brownish oil floating on surface of unfiltered liquid with some sporadic bubbling; filtrate has a pale almond color

Hydrothermal Run Number: 5TiB1 **Date:** 9/26/2009

Nominal weight loading:	1 : 25	Initial pressure in bomb after He charge:	66.5 psia
Wet bagasse mass:	1.5009 g	Maximum pressure recorded in bomb:	9130.8 psia
Bagasse moisture:	5.20 %	Internal bomb pressure after run:	191.3 psia
Dry bagasse mass:	1.4229 g	Bomb temperature before GC test:	23.9 °C
DI H_2O mass:	35.4 g	Density of liquid product:	0.9994 g cm^{-3}
DI H_2O pH:	5.48	Volume of liquid product:	35.3140 cm^3
Total H_2O mass:	35.4780 g	Volume of solid product:	0.1264 cm^3
Run temperature:	500 °C	Volume of gas product:	31.6086 cm^3
Nominal run duration:	5 min	Moles of gas product (less initial He):	0.0130 mol

Unfiltered liquids + beaker:	62.7845 g	Dried solids + beaker:	28.6865 g
Clean, dry beaker:	28.6628 g	Clean, dry beaker:	28.6628 g
Unfiltered liquids:	34.1217 g	Dried solids in beaker:	0.0237 g
(2) Wet Kimwipe(s) (cap + threads):	1.5437 g	Unfiltered liquids from beaker:	34.1217 g
(2) Dry, unused Kimwipe(s)	0.9066 g	Dried solids from beaker:	0.0237 g
Semivolatiles inside cap:	0.6371 g	Semivolatiles in beaker:	34.0980 g
Sludge + 0.0 mL DI H_2O + boat:	2.9286 g	Dried solids + boat:	2.3709 g
Clean, dry Al weigh boat:	2.2118 g	Clean, dry Al weigh boat:	2.2118 g
Sludge + 0.0 mL DI H_2O:	0.7168 g	Dried solids in boat:	0.1591 g
– 0.0 mL DI H_2O:	0.0000 g		
Sludge (slurry + tars) in boat:	0.7168 g	Sludge (slurry + tars) in boat:	0.7168 g
		– Dried solids in boat:	0.1591 g
Dried solids + funnel + filter paper:	62.4291 g	Semivolatiles in boat:	0.5577 g
Size 0 funnel + 1.2 μm filter paper:	62.3301 g		
Dried, filtered solids in funnel:	0.0990 g	Total Semivolatiles Yield:	35.2928 g = 55.06%
		Total Solids Yield:	0.2818 g = 19.80%
		Total Volatiles Yield:	0.3577 g = 25.14%
		Total Losses:	0.9686 g
		% Losses:	2.62 %
		Conversion:	80.20 %

Observations: Extremely pungent odor similar to hydrogen sulfide rotten egg smell was present when bomb opened

Hydrothermal Run Number: 5DB1 **Date:** 9/6/2009

Nominal weight loading:	1 : 25	Initial pressure in bomb after He charge:	68.5 psia
Bone dry bagasse mass:	1.4291 g	Maximum pressure recorded in bomb:	9253 psia
Bagasse moisture:	0.00 %	Internal bomb pressure after run:	219.5 psia
D_2O Mass:	35.4 g	Bomb temperature before GC test:	35.0 °C
Atomic percent D:	100.0 %	Density of liquid product:	1.1000 g cm^{-3}
Minimum isotopic purity	99.96 %	Volume of liquid product:	32.3912 cm^3
Run temperature:	500 °C	Volume of solid product:	0.1158 cm^3
Nominal run duration:	5 min	Volume of gas product:	34.5420 cm^3
		Moles of gas product (less initial He):	0.0158 mol

Unfiltered liquids + beaker:	65.4525 g	Dried solids + beaker:	30.6645 g
Clean, dry beaker:	30.6305 g	Clean, dry beaker:	30.6305 g
Unfiltered liquids:	34.8220 g	Dried solids in beaker:	0.0340 g
(2) Wet Kimwipe(s) (cap + threads):	0.9562 g	Unfiltered liquids from beaker:	34.8220 g
(2) Dry, unused Kimwipe(s)	0.9417 g	Dried solids from beaker:	0.0340 g
Semivolatiles inside cap:	0.0145 g	Semivolatiles in beaker:	34.7880 g
Sludge + 0.0 mL DI H_2O + boat:	3.1855 g	Dried solids + boat:	2.3577 g
Clean, dry Al weigh boat:	2.2394 g	Clean, dry Al weigh boat:	2.2394 g
Sludge + 0.0 mL DI H_2O:	0.9461 g	Dried solids in boat:	0.1183 g
– 0.0 mL DI H_2O:	0.0000 g		
Sludge (slurry + tars) in boat:	0.9461 g	Sludge (slurry + tars) in boat:	0.9461 g
		– Dried solids in boat:	0.1183 g
Dried solids + funnel + filter paper:	59.2266 g	Semivolatiles in boat:	0.8278 g
Size 0 funnel + 1.2 μm filter paper:	59.1206 g		
Dried , filtered solids in funnel:	0.1060 g	Total Semivolatiles Yield:	35.6303 g = 50.47%
		Total Solids Yield:	0.2583 g = 18.07%
		Total Volatiles Yield:	0.4495 g = 31.46%
		Total Losses:	0.4910 g
		% Losses:	1.33 %
		Conversion:	81.93 %

APPENDIX C. VOLATILES COMPOSITION

The tables provided in Appendix C contain the volatiles composition data for every run presented in this dissertation. The initial two columns have the raw peak area and response factors from the GC analysis. These are followed by two more columns that give the composition of every component on a part per million and a molar basis. The subsequent two columns contain a corrected composition after accounting for any extraneous oxygen or nitrogen in the GC transfer lines. The higher heating values are then provided on a molar and a weight basis. Absolute yields of volatiles are provided on a molar and a weight basis, as well. The yields are also described in terms of the number of moles per gram of dry bagasse and in terms of weight percent. Finally, the carbon yield for each component is provided as an absolute weight.

The tables are organized and labeled according to the single free variable in each run. For instance, 300 ºC refers to the bagasse hydrothermal run conducted at 300 ºC with all other parameters fixed at the baseline operating conditions

300 °C

Analyte	Area [counts·s]	Response Factor	C [ppmv]	C [mol %]	C_{corr} [ppmv]	C_{corr} [mol %]	HHV [kJ mol^{-1}]	HHV [MJ kg^{-1}]	Yield [mmol]	Yield [mmol g^{-1}]	Yield [mg]	% Yield [wt %]	C Yield [mg]
H_2	5027.837	1.29965	6534	5.91	6534	6.61	18.88	9.37	0.182	0.095	0.37	0.34	0.00
O_2	4867.133	0.47633	2318	2.10	0	0.00	0.00	0.00	0.000	0.000	0.00	0.00	0.00
N_2	16316.832	0.57690	9413	8.51	0	0.00	0.00	0.00	0.000	0.000	0.00	0.00	0.00
CO	37710.185	0.42924	16187	14.63	16187	16.36	46.31	1.65	0.451	0.236	12.64	11.86	5.42
CH_4	230.425	1.78440	411	0.37	411	0.42	3.70	0.23	0.011	0.006	0.18	0.17	0.14
CO_2	301761.585	0.24503	73941	66.82	73941	74.75	0.00	0.00	2.061	1.080	90.71	85.10	24.76
C_2H_4	235.940	0.90159	213	0.19	213	0.22	3.03	0.11	0.006	0.003	0.17	0.16	0.14
C_2H_6	57.633	0.91348	53	0.05	53	0.05	0.83	0.03	0.001	0.001	0.04	0.04	0.04
C_3H_6	869.552	0.62518	544	0.49	544	0.55	11.31	0.27	0.015	0.008	0.64	0.60	0.55
C_3H_8	34.268	0.62212	21	0.02	21	0.02	0.48	0.01	0.001	0.000	0.03	0.02	0.02
iso-C_4H_{10}	0.000	0.51546	0	0.00	0	0.00	0.00	0.00	0.000	0.000	0.00	0.00	0.00
1,3-C_4H_6 + 1-C_4H_8	872.066	0.50750	443	0.40	443	0.45	11.76	0.21	0.012	0.006	0.68	0.64	0.59
n-C_4H_{10}	402.498	0.51610	208	0.19	208	0.21	6.04	0.10	0.006	0.003	0.34	0.32	0.28
Other C_4	0.000	0.51546	0	0.00	0	0.00	0.00	0.00	0.000	0.000	0.00	0.00	0.00
iso-C_5H_{12}	45.055	0.48772	22	0.02	22	0.02	0.78	0.01	0.001	0.000	0.04	0.04	0.04
n-C_5H_{12}	217.584	0.53372	116	0.10	116	0.12	4.15	0.06	0.003	0.002	0.23	0.22	0.19
Other C_5	141.259	0.51546	73	0.07	73	0.07	2.51	0.03	0.002	0.001	0.15	0.14	0.12
n-C_6H_{14}	140.313	0.73323	103	0.09	103	0.10	4.36	0.05	0.003	0.002	0.25	0.23	0.21
Other C_6+	103.377	0.51546	53	0.05	53	0.05	2.22	0.03	0.001	0.001	0.13	0.12	0.11
	369033.543		110652	100.00	98921	100.00	116.38	12.16	2.76		106.59	100.00	32.60

400 °C

Analyte	Area [counts·s]	Response Factor	C [ppmv]	C [mol %]	C_{corr} [ppmv]	C_{corr} [mol %]	HHV [kJ mol^{-1}]	HHV [MJ kg^{-1}]	Yield [mmol]	Yield [mmol g^{-1}]	Yield [mg]	% Yield [wt %]	C Yield [mg]
H_2	57612.886	1.29965	74877	22.27	74877	23.24	66.43	32.95	1.623	0.858	3.27	1.50	0.00
O_2	5239.690	0.47633	2496	0.74	0	0.00	0.00	0.00	0.000	0.000	0.00	0.00	0.00
N_2	20019.383	0.57690	11549	3.43	0	0.00	0.00	0.00	0.000	0.000	0.00	0.00	0.00
CO	44923.538	0.42924	19283	5.73	19283	5.98	16.94	0.60	0.418	0.221	11.71	5.36	5.02
CH_4	11993.397	1.78440	21401	6.36	21401	6.64	59.14	3.69	0.464	0.245	7.44	3.41	5.57
CO_2	730324.492	0.24503	178951	53.22	178946	55.54	0.00	0.00	3.878	2.051	170.68	78.15	46.58
C_2H_4	9881.561	0.90159	8909	2.65	8909	2.77	39.01	1.39	0.193	0.102	5.42	2.48	4.64
C_2H_6	3025.662	0.91348	2764	0.82	2764	0.86	13.38	0.44	0.060	0.032	1.80	0.82	1.44
C_3H_6	11119.827	0.62518	6952	2.07	6952	2.16	44.41	1.06	0.151	0.080	6.34	2.90	5.43
C_3H_8	2234.031	0.62212	1390	0.41	1390	0.43	9.58	0.22	0.030	0.016	1.33	0.61	1.09
iso-C_4H_{10}	0.000	0.51546	0	0.00	0	0.00	0.00	0.00	0.000	0.000	0.00	0.00	0.00
1,3-C_4H_6 + 1-C_4H_8	3841.972	0.50750	1950	0.58	1950	0.61	15.91	0.29	0.042	0.022	2.33	1.07	2.03
n-C_4H_{10}	6703.591	0.51610	3460	1.03	3460	1.07	30.91	0.53	0.075	0.040	4.36	2.00	3.60
Other C_4	0.000	0.51546	0	0.00	0	0.00	0.00	0.00	0.000	0.000	0.00	0.00	0.00
iso-C_5H_{12}	774.726	0.48772	378	0.11	378	0.12	4.14	0.06	0.008	0.004	0.59	0.27	0.49
n-C_5H_{12}	2540.848	0.53372	1356	0.40	1356	0.42	14.88	0.21	0.029	0.016	2.12	0.97	1.77
Other C_5	0.000	0.51546	0	0.00	0	0.00	0.00	0.00	0.000	0.000	0.00	0.00	0.00
n-C_6H_{14}	377.725	0.73323	277	0.08	277	0.09	3.61	0.04	0.006	0.003	0.52	0.24	0.43
Other C_6+	516.401	0.51546	266	0.08	266	0.08	3.41	0.04	0.006	0.003	0.50	0.23	0.42
	911129.729		336258	100.00	322208	100.00	321.73	41.52	6.98		218.40	100.00	78.50

500 °C Replicate 1

Analyte	Area [counts·s]	Response Factor	C [ppmv]	C [mol %]	C_{corr} [ppmv]	C_{corr} [mol %]	HHV [kJ mol^{-1}]	HHV [MJ kg^{-1}]	Yield [mmol]	Yield [mmol g^{-1}]	Yield [mg]	% Yield [wt %]	C Yield [mg]
H_2	91939.599	1.29965	119489	23.60	119489	23.73	67.83	33.65	4.135	2.904	8.34	1.71	0.00
O_2	1306.774	0.47633	622	0.12	55	0.01	0.00	0.00	0.002	0.001	0.06	0.01	0.00
N_2	3666.675	0.57690	2115	0.42	0	0.00	0.00	0.00	0.000	0.000	0.00	0.00	0.00
CO	14390.105	0.42924	6177	1.22	6177	1.23	3.47	0.12	0.214	0.150	5.99	1.23	2.57
CH_4	62310.662	1.78440	111187	21.96	111187	22.08	196.59	12.25	3.847	2.702	61.72	12.65	46.21
CO_2	821480.041	0.24503	201287	39.76	201286	39.97	0.00	0.00	6.965	4.891	306.53	62.80	83.66
C_2H_4	3737.872	0.90159	3370	0.67	3370	0.67	9.44	0.34	0.117	0.082	3.27	0.67	2.80
C_2H_6	23000.998	0.91348	21011	4.15	21011	4.17	65.09	2.16	0.727	0.511	21.86	4.48	17.47
C_3H_6	10512.603	0.62518	6572	1.30	6572	1.31	26.87	0.64	0.227	0.160	9.57	1.96	8.19
C_3H_8	17478.535	0.62212	10874	2.15	10874	2.16	47.94	1.09	0.376	0.264	16.59	3.40	13.56
iso-C_4H_{10}	2623.999	0.51546	1353	0.27	1353	0.27	7.71	0.13	0.047	0.033	2.72	0.56	2.25
1,3-C_4H_6 + 1-C_4H_8	5900.624	0.50750	2995	0.59	2995	0.59	15.64	0.28	0.104	0.073	5.71	1.17	4.98
n-C_4H_{10}	15806.921	0.51610	8158	1.61	8158	1.62	46.63	0.80	0.282	0.198	16.41	3.36	13.56
Other C_4	0.000	0.51546	0	0.00	0	0.00	0.00	0.00	0.000	0.000	0.00	0.00	0.00
iso-C_5H_{12}	3735.445	0.48772	1822	0.36	1822	0.36	12.76	0.18	0.063	0.044	4.55	0.93	3.79
n-C_5H_{12}	9473.995	0.53372	5057	1.00	5057	1.00	35.51	0.49	0.175	0.123	12.62	2.59	10.51
Other C_5	830.987	0.51546	428	0.08	428	0.09	2.90	0.04	0.015	0.010	1.07	0.22	0.89
n-C_6H_{14}	2358.196	0.73323	1729	0.34	1729	0.34	14.40	0.17	0.060	0.042	5.16	1.06	4.31
Other C_6+	3858.765	0.51546	1989	0.39	1989	0.40	16.28	0.19	0.069	0.048	5.93	1.22	4.96
	1094412.794		506235	100.00	503551	100.00	569.08	52.54	17.42		488.10	100.00	219.70

500 °C Replicate 2

Analyte	Area [counts·s]	Response Factor	C [ppmv]	C [mol %]	C_{corr} [ppmv]	C_{corr} [mol %]	HHV [kJ mol^{-1}]	HHV [MJ kg^{-1}]	Yield [mmol]	Yield [mmol g^{-1}]	Yield [mg]	% Yield [wt %]	C Yield [mg]
H_2	94230.600	1.29965	122467	24.94	122467	25.08	71.68	35.56	4.425	3.098	8.92	1.81	0.00
O_2	659.200	0.47633	314	0.06	0	0.00	0.00	0.00	0.000	0.000	0.00	0.00	0.00
N_2	4127.905	0.57690	2381	0.48	0	0.00	0.00	0.00	0.000	0.000	0.00	0.00	0.00
CO	16219.457	0.42924	6962	1.42	6962	1.43	4.03	0.14	0.252	0.176	7.05	1.43	3.02
CH_4	55571.079	1.78440	99161	20.19	99161	20.31	180.79	11.27	3.583	2.509	57.48	11.63	43.03
CO_2	804927.657	0.24503	197231	40.17	197230	40.39	0.00	0.00	7.126	4.990	313.62	63.48	85.59
C_2H_4	3781.603	0.90159	3409	0.69	3409	0.70	9.85	0.35	0.123	0.086	3.46	0.70	2.96
C_2H_6	20838.522	0.91348	19036	3.88	19036	3.90	60.80	2.02	0.688	0.482	20.68	4.19	16.52
C_3H_6	10694.200	0.62518	6686	1.36	6686	1.37	28.18	0.67	0.242	0.169	10.17	2.06	8.70
C_3H_8	15806.913	0.62212	9834	2.00	9834	2.01	44.71	1.01	0.355	0.249	15.67	3.17	12.80
iso-C_4H_{10}	2260.822	0.51546	1165	0.24	1165	0.24	6.85	0.12	0.042	0.029	2.45	0.50	2.02
1,3-C_4H_6 + 1-C_4H_8	6104.386	0.50750	3098	0.63	3098	0.63	16.68	0.30	0.112	0.078	6.17	1.25	5.38
n-C_4H_{10}	15339.279	0.51610	7917	1.61	7917	1.62	46.66	0.80	0.286	0.200	16.63	3.36	13.74
Other C_4	0.000	0.51546	0	0.00	0	0.00	0.00	0.00	0.000	0.000	0.00	0.00	0.00
iso-C_5H_{12}	3501.385	0.48772	1708	0.35	1708	0.35	12.34	0.17	0.062	0.043	4.45	0.90	3.71
n-C_5H_{12}	9518.598	0.53372	5080	1.03	5080	1.04	36.79	0.51	0.184	0.129	13.24	2.68	11.02
Other C_5	836.034	0.51546	431	0.09	431	0.09	3.01	0.04	0.016	0.011	1.12	0.23	0.94
n-C_6H_{14}	2327.525	0.73323	1707	0.35	1707	0.35	14.66	0.17	0.062	0.043	5.31	1.08	4.44
Other C_6+	4776.993	0.51546	2462	0.50	2462	0.50	20.78	0.24	0.089	0.062	7.67	1.55	6.41
	1071522.159		491049	100.00	488352	100.00	557.82	53.39	17.64		494.07	100.00	220.30

500 °C Replicate 3

Analyte	Area [counts·s]	Response Factor	C [ppmv]	C [mol %]	C_{corr} [ppmv]	C_{corr} [mol %]	HHV [kJ mol^{-1}]	HHV [MJ kg^{-1}]	Yield [mmol]	Yield [mmol g^{-1}]	Yield [mg]	% Yield [wt %]	C Yield [mg]
H_2	95297.581	1.29965	123854	25.97	123853	26.22	74.96	37.18	4.409	3.097	8.89	1.90	0.00
O_2	1223.451	0.47633	583	0.12	0	0.00	0.00	0.00	0.000	0.000	0.00	0.00	0.00
N_2	7100.560	0.57690	4096	0.86	0	0.00	0.00	0.00	0.000	0.000	0.00	0.00	0.00
CO	18751.890	0.42924	8049	1.69	8049	1.70	4.82	0.17	0.287	0.201	8.03	1.72	3.44
CH_4	50890.709	1.78440	90809	19.04	90809	19.23	171.19	10.67	3.233	2.271	51.86	11.10	38.83
CO_2	773808.410	0.24503	189606	39.75	189604	40.14	0.00	0.00	6.749	4.741	297.04	63.60	81.07
C_2H_4	4009.674	0.90159	3615	0.76	3615	0.77	10.80	0.38	0.129	0.090	3.61	0.77	3.09
C_2H_6	19286.555	0.91348	17618	3.69	17618	3.73	58.19	1.94	0.627	0.441	18.86	4.04	15.07
C_3H_6	11096.262	0.62518	6937	1.45	6937	1.47	30.23	0.72	0.247	0.173	10.39	2.22	8.90
C_3H_8	14607.103	0.62212	9087	1.91	9087	1.92	42.72	0.97	0.323	0.227	14.26	3.05	11.66
iso-C_4H_{10}	2063.349	0.51546	1064	0.22	1064	0.23	6.47	0.11	0.038	0.027	2.20	0.47	1.82
1,3-C_4H_6 + 1-C_4H_8	6028.128	0.50750	3059	0.64	3059	0.65	17.03	0.31	0.109	0.076	6.00	1.28	5.23
n-C_4H_{10}	15048.029	0.51610	7766	1.63	7766	1.64	47.33	0.81	0.276	0.194	16.07	3.44	13.28
Other C_4	0.000	0.51546	0	0.00	0	0.00	0.00	0.00	0.000	0.000	0.00	0.00	0.00
iso-C_5H_{12}	3266.128	0.48772	1593	0.33	1593	0.34	11.90	0.16	0.057	0.040	4.09	0.88	3.41
n-C_5H_{12}	9112.715	0.53372	4864	1.02	4864	1.03	36.41	0.50	0.173	0.122	12.49	2.67	10.40
Other C_5	774.756	0.51546	399	0.08	399	0.08	2.88	0.04	0.014	0.010	1.03	0.22	0.85
n-C_6H_{14}	2253.226	0.73323	1652	0.35	1652	0.35	14.67	0.17	0.059	0.041	5.07	1.09	4.24
Other C_6+	4521.647	0.51546	2331	0.49	2331	0.49	20.34	0.24	0.083	0.058	7.15	1.53	5.98
	1039140.172		476983	100.00	472302	100.00	549.95	54.38	16.81		467.03	100.00	207.25

500 °C Replicate 4

Analyte	Area [counts·s]	Response Factor	C [ppmv]	C [mol %]	C_{corr} [ppmv]	C_{corr} [mol %]	HHV [kJ mol^{-1}]	HHV [MJ kg^{-1}]	Yield [mmol]	Yield [mmol g^{-1}]	Yield [mg]	% Yield [wt %]	C Yield [mg]
H_2	96109.767	1.29965	124909	24.14	124909	24.25	69.32	34.39	4.085	2.859	8.23	1.70	0.00
O_2	0.000	0.47633	0	0.00	0	0.00	0.00	0.00	0.000	0.000	0.00	0.00	0.00
N_2	4018.815	0.57690	2318	0.45	0	0.00	0.00	0.00	0.000	0.000	0.00	0.00	0.00
CO	20394.891	0.42924	8754	1.69	8754	1.70	4.81	0.17	0.286	0.200	8.02	1.65	3.44
CH_4	54964.156	1.78440	98078	18.96	98078	19.04	169.55	10.57	3.208	2.245	51.46	10.61	38.53
CO_2	887592.577	0.24503	217487	42.04	217486	42.23	0.00	0.00	7.113	4.979	313.03	64.53	85.43
C_2H_4	4095.829	0.90159	3693	0.71	3693	0.72	10.12	0.36	0.121	0.085	3.39	0.70	2.90
C_2H_6	20806.310	0.91348	19006	3.67	19006	3.69	57.56	1.91	0.622	0.435	18.69	3.85	14.93
C_3H_6	11319.959	0.62518	7077	1.37	7077	1.37	28.28	0.67	0.231	0.162	9.74	2.01	8.34
C_3H_8	15768.249	0.62212	9810	1.90	9810	1.90	42.29	0.96	0.321	0.225	14.15	2.92	11.56
iso-C_4H_{10}	2229.205	0.51546	1149	0.22	1149	0.22	6.41	0.11	0.038	0.026	2.18	0.45	1.81
1,3-C_4H_6 + 1-C_4H_8	6469.772	0.50750	3283	0.63	3283	0.64	16.76	0.30	0.107	0.075	5.92	1.22	5.16
n-C_4H_{10}	15840.076	0.51610	8175	1.58	8175	1.59	45.69	0.79	0.267	0.187	15.54	3.20	12.85
Other C_4	0.000	0.51546	0	0.00	0	0.00	0.00	0.00	0.000	0.000	0.00	0.00	0.00
iso-C_5H_{12}	3724.528	0.48772	1817	0.35	1817	0.35	12.44	0.17	0.059	0.042	4.29	0.88	3.57
n-C_5H_{12}	10524.966	0.53372	5617	1.09	5617	1.09	38.57	0.53	0.184	0.129	13.25	2.73	11.03
Other C_5	966.869	0.51546	498	0.10	498	0.10	3.30	0.05	0.016	0.011	1.18	0.24	0.98
n-C_6H_{14}	3333.941	0.73323	2445	0.47	2445	0.47	19.91	0.23	0.080	0.056	6.89	1.42	5.76
Other C_6+	6295.624	0.51546	3245	0.63	3245	0.63	25.97	0.30	0.106	0.074	9.15	1.89	7.65
	1164455.534		517362	100.00	515042	100.00	550.98	51.52	16.84		485.09	100.00	213.93

600 °C

Analyte	Area [counts·s]	Response Factor	C [ppmv]	C [mol %]	C_{corr} [ppmv]	C_{corr} [mol %]	HHV [kJ mol^{-1}]	HHV [MJ kg^{-1}]	Yield [mmol]	Yield [mmol g^{-1}]	Yield [mg]	% Yield [wt %]	C Yield [mg]
H_2	90559.140	1.29965	117695	22.28	117695	22.50	64.31	31.90	5.285	4.441	10.65	1.78	0.00
O_2	1746.246	0.47633	832	0.16	0	0.00	0.00	0.00	0.000	0.000	0.00	0.00	0.00
N_2	7372.591	0.57690	4253	0.81	0	0.00	0.00	0.00	0.000	0.000	0.00	0.00	0.00
CO	18573.233	0.42924	7972	1.51	7972	1.52	4.31	0.15	0.358	0.301	10.03	1.67	4.30
CH_4	86850.089	1.78440	154975	29.34	154975	29.62	263.75	16.44	6.959	5.848	111.64	18.63	83.59
CO_2	727584.676	0.24503	178280	33.75	178278	34.08	0.00	0.00	8.006	6.728	352.33	58.78	96.16
C_2H_4	2776.694	0.90159	2503	0.47	2503	0.48	6.75	0.24	0.112	0.094	3.15	0.53	2.70
C_2H_6	34179.948	0.91348	31223	5.91	31223	5.97	93.10	3.10	1.402	1.178	42.16	7.03	33.68
C_3H_6	6133.512	0.62518	3835	0.73	3835	0.73	15.09	0.36	0.172	0.145	7.25	1.21	6.20
C_3H_8	24797.328	0.62212	15427	2.92	15427	2.95	65.47	1.48	0.693	0.582	30.55	5.10	24.96
iso-C_4H_{10}	5602.886	0.51546	2888	0.55	2888	0.55	15.85	0.27	0.130	0.109	7.54	1.26	6.23
1,3-C_4H_6 + 1-C_4H_8	3223.937	0.50750	1636	0.31	1636	0.31	8.22	0.15	0.073	0.062	4.05	0.68	3.53
n-C_4H_{10}	7143.377	0.51610	3687	0.70	3687	0.70	20.29	0.35	0.166	0.139	9.62	1.61	7.95
Other C_4	0.000	0.51546	0	0.00	0	0.00	0.00	0.00	0.000	0.000	0.00	0.00	0.00
iso-C_5H_{12}	1237.596	0.48772	604	0.11	604	0.12	4.07	0.06	0.027	0.023	1.96	0.33	1.63
n-C_5H_{12}	2151.351	0.53372	1148	0.22	1148	0.22	7.76	0.11	0.052	0.043	3.72	0.62	3.10
Other C_5	561.672	0.51546	290	0.05	290	0.06	1.89	0.03	0.013	0.011	0.94	0.16	0.78
n-C_6H_{14}	1343.112	0.73323	985	0.19	985	0.19	7.90	0.09	0.044	0.037	3.81	0.64	3.19
Other C_6+	0.000	0.51546	0	0.00	0	0.00	0.00	0.00	0.000	0.000	0.00	0.00	0.00
	1021837.387		528232	100.00	523145	100.00	578.76	54.73	23.49		599.40	100.00	278.00

1 min RT

Analyte	Area [counts·s]	Response Factor	C [ppmv]	C [mol %]	C_{corr} [ppmv]	C_{corr} [mol %]	HHV [kJ mol^{-1}]	HHV [MJ kg^{-1}]	Yield [mmol]	Yield [mmol g^{-1}]	Yield [mg]	% Yield [wt %]	C Yield [mg]
H_2	96294.296	1.29965	125149	27.36	121297	27.13	77.55	38.47	4.181	2.934	8.43	2.00	0.00
O_2	1063.959	0.47633	507	0.11	0	0.00	0.00	0.00	0.000	0.000	0.00	0.00	0.00
N_2	7309.257	0.57690	4217	0.92	0	0.00	0.00	0.00	0.000	0.000	0.00	0.00	0.00
CO	30558.246	0.42924	13117	2.87	13117	2.93	8.30	0.30	0.452	0.317	12.66	3.01	5.43
CH_4	46540.506	1.78440	83047	18.15	83047	18.58	165.38	10.31	2.862	2.009	45.92	10.90	34.38
CO_2	715837.088	0.24503	175402	38.34	173592	38.83	0.00	0.00	5.983	4.200	263.32	62.49	71.86
C_2H_4	5061.111	0.90159	4563	1.00	4563	1.02	14.40	0.51	0.157	0.110	4.41	1.05	3.78
C_2H_6	16165.958	0.91348	14767	3.23	14767	3.30	51.52	1.71	0.509	0.357	15.30	3.63	12.23
C_3H_6	12796.225	0.62518	8000	1.75	8000	1.79	36.83	0.88	0.276	0.194	11.60	2.75	9.94
C_3H_8	12095.916	0.62212	7525	1.64	7525	1.68	37.37	0.85	0.259	0.182	11.44	2.71	9.35
iso-C_4H_{10}	1521.599	0.51546	784	0.17	784	0.18	5.04	0.09	0.027	0.019	1.57	0.37	1.30
1,3-C_4H_6 + 1-C_4H_8	7079.008	0.50750	3593	0.79	3593	0.80	21.13	0.38	0.124	0.087	6.82	1.62	5.95
n-C_4H_{10}	13873.275	0.51610	7160	1.57	7160	1.60	46.10	0.79	0.247	0.173	14.34	3.40	11.86
Other C_4	0.000	0.51546	0	0.00	0	0.00	0.00	0.00	0.000	0.000	0.00	0.00	0.00
iso-C_5H_{12}	2846.044	0.48772	1388	0.30	1388	0.31	10.95	0.15	0.048	0.034	3.45	0.82	2.87
n-C_5H_{12}	8577.735	0.53372	4578	1.00	4578	1.02	36.21	0.50	0.158	0.111	11.38	2.70	9.48
Other C_5	848.384	0.51546	437	0.10	437	0.10	3.33	0.05	0.015	0.011	1.09	0.26	0.91
n-C_6H_{14}	1665.697	0.73323	1221	0.27	1221	0.27	11.46	0.13	0.042	0.030	3.63	0.86	3.03
Other C_6+	3902.225	0.51546	2011	0.44	2011	0.45	18.54	0.22	0.069	0.049	5.97	1.42	5.00
	984036.530		457466	100.00	447081	100.00	544.14	55.34	15.41		421.35	100.00	187.35

5 min RT

Analyte	Area [counts·s]	Response Factor	C [ppmv]	C [mol %]	C_{corr} [ppmv]	C_{corr} [mol %]	HHV [kJ mol^{-1}]	HHV [MJ kg^{-1}]	Yield [mmol]	Yield [mmol g^{-1}]	Yield [mg]	% Yield [wt %]	C Yield [mg]
H_2	95297.581	1.29965	123854	25.97	123853	26.22	74.96	37.18	4.409	3.097	8.89	1.90	0.00
O_2	1223.451	0.47633	583	0.12	0	0.00	0.00	0.00	0.000	0.000	0.00	0.00	0.00
N_2	7100.560	0.57690	4096	0.86	0	0.00	0.00	0.00	0.000	0.000	0.00	0.00	0.00
CO	18751.890	0.42924	8049	1.69	8049	1.70	4.82	0.17	0.287	0.201	8.03	1.72	3.44
CH_4	50890.709	1.78440	90809	19.04	90809	19.23	171.19	10.67	3.233	2.271	51.86	11.10	38.83
CO_2	773808.410	0.24503	189606	39.75	189604	40.14	0.00	0.00	6.749	4.741	297.04	63.60	81.07
C_2H_4	4009.674	0.90159	3615	0.76	3615	0.77	10.80	0.38	0.129	0.090	3.61	0.77	3.09
C_2H_6	19286.555	0.91348	17618	3.69	17618	3.73	58.19	1.94	0.627	0.441	18.86	4.04	15.07
C_3H_6	11096.262	0.62518	6937	1.45	6937	1.47	30.23	0.72	0.247	0.173	10.39	2.22	8.90
C_3H_8	14607.103	0.62212	9087	1.91	9087	1.92	42.72	0.97	0.323	0.227	14.26	3.05	11.66
iso-C_4H_{10}	2063.349	0.51546	1064	0.22	1064	0.23	6.47	0.11	0.038	0.027	2.20	0.47	1.82
1,3-C_4H_6 + 1-C_4H_8	6028.128	0.50750	3059	0.64	3059	0.65	17.03	0.31	0.109	0.076	6.00	1.28	5.23
n-C_4H_{10}	15048.029	0.51610	7766	1.63	7766	1.64	47.33	0.81	0.276	0.194	16.07	3.44	13.28
Other C_4	0.000	0.51546	0	0.00	0	0.00	0.00	0.00	0.000	0.000	0.00	0.00	0.00
iso-C_5H_{12}	3266.128	0.48772	1593	0.33	1593	0.34	11.90	0.16	0.057	0.040	4.09	0.88	3.41
n-C_5H_{12}	9112.715	0.53372	4864	1.02	4864	1.03	36.41	0.50	0.173	0.122	12.49	2.67	10.40
Other C_5	774.756	0.51546	399	0.08	399	0.08	2.88	0.04	0.014	0.010	1.03	0.22	0.85
n-C_6H_{14}	2253.226	0.73323	1652	0.35	1652	0.35	14.67	0.17	0.059	0.041	5.07	1.09	4.24
Other C_6+	4521.647	0.51546	2331	0.49	2331	0.49	20.34	0.24	0.083	0.058	7.15	1.53	5.98
	1039140.172		476983	100.00	472302	100.00	549.95	54.38	16.81		467.03	100.00	207.25

10 min RT

Analyte	Area [counts·s]	Response Factor	C [ppmv]	C [mol %]	C_{corr} [ppmv]	C_{corr} [mol %]	HHV [kJ mol^{-1}]	HHV [MJ kg^{-1}]	Yield [mmol]	Yield [mmol g^{-1}]	Yield [mg]	% Yield [wt %]	C Yield [mg]
H_2	97914.651	1.29965	127255	24.58	127255	24.75	70.75	35.10	4.547	3.196	9.17	1.85	0.00
O_2	1576.779	0.47633	751	0.15	0	0.00	0.00	0.00	0.000	0.000	0.00	0.00	0.00
N_2	4936.396	0.57690	2848	0.55	0	0.00	0.00	0.00	0.000	0.000	0.00	0.00	0.00
CO	15668.426	0.42924	6726	1.30	6726	1.31	3.70	0.13	0.240	0.169	6.73	1.36	2.89
CH_4	69199.309	1.78440	123479	23.85	123479	24.02	213.84	13.33	4.412	3.101	70.78	14.29	52.99
CO_2	767072.411	0.24503	187956	36.30	187954	36.56	0.00	0.00	6.715	4.721	295.54	59.66	80.66
C_2H_4	3356.629	0.90159	3026	0.58	3026	0.59	8.31	0.30	0.108	0.076	3.03	0.61	2.60
C_2H_6	25818.971	0.91348	23585	4.56	23585	4.59	71.56	2.38	0.843	0.592	25.34	5.12	20.24
C_3H_6	9540.986	0.62518	5965	1.15	5965	1.16	23.88	0.57	0.213	0.150	8.97	1.81	7.68
C_3H_8	19841.141	0.62212	12344	2.38	12344	2.40	53.31	1.21	0.441	0.310	19.45	3.93	15.89
iso-C_4H_{10}	3165.073	0.51546	1631	0.32	1631	0.32	9.11	0.16	0.058	0.041	3.39	0.68	2.80
1,3-C_4H_6 + 1-C_4H_8	5550.773	0.50750	2817	0.54	2817	0.55	14.41	0.26	0.101	0.071	5.55	1.12	4.84
n-C_4H_{10}	16360.949	0.51610	8444	1.63	8444	1.64	47.28	0.81	0.302	0.212	17.54	3.54	14.49
Other C_4	0.000	0.51546	0	0.00	0	0.00	0.00	0.00	0.000	0.000	0.00	0.00	0.00
iso-C_5H_{12}	3864.170	0.48772	1885	0.36	1885	0.37	12.93	0.18	0.067	0.047	4.86	0.98	4.04
n-C_5H_{12}	9259.956	0.53372	4942	0.95	4942	0.96	33.99	0.47	0.177	0.124	12.74	2.57	10.60
Other C_5	864.908	0.51546	446	0.09	446	0.09	2.96	0.04	0.016	0.011	1.15	0.23	0.96
n-C_6H_{14}	2346.907	0.73323	1721	0.33	1721	0.33	14.04	0.16	0.061	0.043	5.30	1.07	4.43
Other C_6+	3689.092	0.51546	1902	0.37	1902	0.37	15.24	0.18	0.068	0.048	5.85	1.18	4.90
	1060027.526		517721	100.00	514121	100.00	595.31	55.27	18.37		495.37	100.00	230.01

30 min RT

Analyte	Area [counts·s]	Response Factor	C [ppmv]	C [mol %]	C_{corr} [ppmv]	C_{corr} [mol %]	HHV [kJ mol^{-1}]	HHV [MJ kg^{-1}]	Yield [mmol]	Yield [mmol g^{-1}]	Yield [mg]	% Yield [wt %]	C Yield [mg]
H_2	75768.322	1.29965	98472	21.03	98472	21.25	60.73	30.13	4.517	3.177	9.11	1.58	0.00
O_2	1942.642	0.47633	925	0.20	0	0.00	0.00	0.00	0.000	0.000	0.00	0.00	0.00
N_2	6481.409	0.57690	3739	0.80	0	0.00	0.00	0.00	0.000	0.000	0.00	0.00	0.00
CO	8842.579	0.42924	3796	0.81	3796	0.82	2.32	0.08	0.174	0.122	4.88	0.85	2.09
CH_4	73852.186	1.78440	131781	28.15	131781	28.43	253.16	15.78	6.045	4.251	96.98	16.83	72.61
CO_2	666594.598	0.24503	163336	34.89	163334	35.24	0.00	0.00	7.493	5.269	329.75	57.22	89.99
C_2H_4	2370.302	0.90159	2137	0.46	2137	0.46	6.51	0.23	0.098	0.069	2.75	0.48	2.35
C_2H_6	27749.160	0.91348	25348	5.41	25348	5.47	85.31	2.84	1.163	0.818	34.96	6.07	27.93
C_3H_6	6864.787	0.62518	4292	0.92	4292	0.93	19.06	0.45	0.197	0.138	8.28	1.44	7.09
C_3H_8	22180.994	0.62212	13799	2.95	13799	2.98	66.10	1.50	0.633	0.445	27.91	4.84	22.81
iso-C_4H_{10}	4459.328	0.51546	2299	0.49	2299	0.50	14.24	0.25	0.105	0.074	6.13	1.06	5.07
1,3-C_4H_6 + 1-C_4H_8	4394.907	0.50750	2230	0.48	2230	0.48	12.65	0.23	0.102	0.072	5.64	0.98	4.92
n-C_4H_{10}	14398.425	0.51610	7431	1.59	7431	1.60	46.15	0.79	0.341	0.240	19.81	3.44	16.38
Other C_4	0.000	0.51546	0	0.00	0	0.00	0.00	0.00	0.000	0.000	0.00	0.00	0.00
iso-C_5H_{12}	3536.674	0.48772	1725	0.37	1725	0.37	13.13	0.18	0.079	0.056	5.71	0.99	4.75
n-C_5H_{12}	6883.779	0.53372	3674	0.78	3674	0.79	28.03	0.39	0.169	0.119	12.16	2.11	10.12
Other C_5	900.134	0.51546	464	0.10	464	0.10	3.41	0.05	0.021	0.015	1.54	0.27	1.28
n-C_6H_{14}	3470.755	0.73323	2545	0.54	2545	0.55	23.03	0.27	0.117	0.082	10.06	1.75	8.41
Other C_6+	285.096	0.51546	147	0.03	147	0.03	1.31	0.02	0.007	0.005	0.58	0.10	0.49
	930976.076		468141	100.00	463474	100.00	635.15	53.18	21.26		576.25	100.00	276.29

60 min RT

Analyte	Area [counts·s]	Response Factor	C [ppmv]	C [mol %]	C_{corr} [ppmv]	C_{corr} [mol %]	HHV [kJ mol^{-1}]	HHV [MJ kg^{-1}]	Yield [mmol]	Yield [mmol g^{-1}]	Yield [mg]	% Yield [wt %]	C Yield [mg]
H_2	88872.229	1.29965	115503	17.36	115503	21.05	60.18	29.85	5.073	3.574	10.23	1.53	0.00
O_2	64678.709	0.47633	30808	4.63	6134	1.12	0.00	0.00	0.269	0.190	8.62	1.29	0.00
N_2	159442.774	0.57690	91983	13.83	0	0.00	0.00	0.00	0.000	0.000	0.00	0.00	0.00
CO	29798.044	0.42924	12791	1.92	12791	2.33	6.60	0.24	0.562	0.396	15.73	2.35	6.75
CH_4	75811.663	1.78440	135278	20.33	135278	24.66	219.56	13.69	5.941	4.185	95.31	14.25	71.36
CO_2	868387.314	0.24503	212781	31.98	212736	38.78	0.00	0.00	9.343	6.582	411.19	61.48	112.22
C_2H_4	2276.724	0.90159	2053	0.31	2053	0.37	5.28	0.19	0.090	0.064	2.53	0.38	2.17
C_2H_6	29603.083	0.91348	27042	4.06	27042	4.93	76.89	2.56	1.188	0.837	35.71	5.34	28.53
C_3H_6	6345.811	0.62518	3967	0.60	3967	0.72	14.89	0.35	0.174	0.123	7.33	1.10	6.28
C_3H_8	22863.562	0.62212	14224	2.14	14224	2.59	57.57	1.31	0.625	0.440	27.55	4.12	22.51
iso-C_4H_{10}	5229.735	0.51546	2696	0.41	2696	0.49	14.11	0.24	0.118	0.083	6.88	1.03	5.69
1,3-C_4H_6 + 1-C_4H_8	4056.883	0.50750	2059	0.31	2059	0.38	9.87	0.18	0.090	0.064	4.98	0.74	4.34
n-C_4H_{10}	12165.714	0.51610	6279	0.94	6279	1.14	32.95	0.57	0.276	0.194	16.03	2.40	13.25
Other C_4	0.000	0.51546	0	0.00	0	0.00	0.00	0.00	0.000	0.000	0.00	0.00	0.00
iso-C_5H_{12}	2786.222	0.48772	1359	0.20	1359	0.25	8.74	0.12	0.060	0.042	4.31	0.64	3.58
n-C_5H_{12}	5639.340	0.53372	3010	0.45	3010	0.55	19.40	0.27	0.132	0.093	9.54	1.43	7.94
Other C_5	698.023	0.51546	360	0.05	360	0.07	2.24	0.03	0.016	0.011	1.14	0.17	0.95
n-C_6H_{14}	3364.986	0.73323	2467	0.37	2467	0.45	18.87	0.22	0.108	0.076	9.34	1.40	7.81
Other C_6+	1206.844	0.51546	622	0.09	622	0.11	4.67	0.05	0.027	0.019	2.35	0.35	1.97
	1383227.658		665280	100.00	548579	100.00	551.81	49.86	24.09		668.76	100.00	295.34

2.67 wt % Bagasse Loading

Analyte	Area [counts·s]	Response Factor	C [ppmv]	C [mol %]	C_{corr} [ppmv]	C_{corr} [mol %]	HHV [kJ mol^{-1}]	HHV [MJ kg^{-1}]	Yield [mmol]	Yield [mmol g^{-1}]	Yield [mg]	% Yield [wt %]	C Yield [mg]
H_2	78007.975	1.29965	101383	24.59	101383	25.20	72.04	35.73	3.197	3.386	6.44	1.81	0.00
O_2	4139.908	0.47633	1972	0.48	0	0.00	0.00	0.00	0.000	0.000	0.00	0.00	0.00
N_2	14037.195	0.57690	8098	1.96	0	0.00	0.00	0.00	0.000	0.000	0.00	0.00	0.00
CO	15806.538	0.42924	6785	1.65	6785	1.69	4.77	0.17	0.214	0.227	5.99	1.69	2.57
CH_4	46195.958	1.78440	82432	19.99	82432	20.49	182.44	11.37	2.599	2.753	41.69	11.74	31.22
CO_2	640179.947	0.24503	156863	38.04	156859	38.99	0.00	0.00	4.946	5.240	217.66	61.27	59.40
C_2H_4	4448.939	0.90159	4011	0.97	4011	1.00	14.07	0.50	0.126	0.134	3.55	1.00	3.04
C_2H_6	16046.656	0.91348	14658	3.55	14658	3.64	56.84	1.89	0.462	0.490	13.90	3.91	11.10
C_3H_6	11127.960	0.62518	6957	1.69	6957	1.73	35.60	0.85	0.219	0.232	9.23	2.60	7.90
C_3H_8	12257.081	0.62212	7625	1.85	7625	1.90	42.08	0.95	0.240	0.255	10.60	2.98	8.66
iso-C_4H_{10}	1586.455	0.51546	818	0.20	818	0.20	5.84	0.10	0.026	0.027	1.50	0.42	1.24
1,3-C_4H_6 + 1-C_4H_8	6150.111	0.50750	3121	0.76	3121	0.78	20.40	0.37	0.098	0.104	5.42	1.53	4.73
n-C_4H_{10}	12737.095	0.51610	6574	1.59	6574	1.63	47.04	0.81	0.207	0.220	12.05	3.39	9.96
Other C_4	0.000	0.51546	0	0.00	0	0.00	0.00	0.00	0.000	0.000	0.00	0.00	0.00
iso-C_5H_{12}	2749.782	0.48772	1341	0.33	1341	0.33	11.76	0.16	0.042	0.045	3.05	0.86	2.54
n-C_5H_{12}	8675.153	0.53372	4630	1.12	4630	1.15	40.70	0.56	0.146	0.155	10.53	2.96	8.77
Other C_5	891.318	0.51546	459	0.11	459	0.11	3.89	0.05	0.014	0.015	1.05	0.29	0.87
n-C_6H_{14}	2691.545	0.73323	1974	0.48	1974	0.49	20.58	0.24	0.062	0.066	5.36	1.51	4.48
Other C_6+	5167.839	0.51546	2664	0.65	2664	0.66	27.29	0.32	0.084	0.089	7.24	2.04	6.05
	882897.455		412365	100.00	402291	100.00	585.33	54.09	12.68		355.26	100.00	162.53

4.00 wt % Bagasse Loading

Analyte	Area [counts·s]	Response Factor	C [ppmv]	C [mol %]	C_{corr} [ppmv]	C_{corr} [mol %]	HHV [kJ mol^{-1}]	HHV [MJ kg^{-1}]	Yield [mmol]	Yield [mmol g^{-1}]	Yield [mg]	% Yield [wt %]	C Yield [mg]
H_2	95297.581	1.29965	123854	25.97	123853	26.22	74.96	37.18	4.409	3.097	8.89	1.90	0.00
O_2	1223.451	0.47633	583	0.12	0	0.00	0.00	0.00	0.000	0.000	0.00	0.00	0.00
N_2	7100.560	0.57690	4096	0.86	0	0.00	0.00	0.00	0.000	0.000	0.00	0.00	0.00
CO	18751.890	0.42924	8049	1.69	8049	1.70	4.82	0.17	0.287	0.201	8.03	1.72	3.44
CH_4	50890.709	1.78440	90809	19.04	90809	19.23	171.19	10.67	3.233	2.271	51.86	11.10	38.83
CO_2	773808.410	0.24503	189606	39.75	189604	40.14	0.00	0.00	6.749	4.741	297.04	63.60	81.07
C_2H_4	4009.674	0.90159	3615	0.76	3615	0.77	10.80	0.38	0.129	0.090	3.61	0.77	3.09
C_2H_6	19286.555	0.91348	17618	3.69	17618	3.73	58.19	1.94	0.627	0.441	18.86	4.04	15.07
C_3H_6	11096.262	0.62518	6937	1.45	6937	1.47	30.23	0.72	0.247	0.173	10.39	2.22	8.90
C_3H_8	14607.103	0.62212	9087	1.91	9087	1.92	42.72	0.97	0.323	0.227	14.26	3.05	11.66
iso-C_4H_{10}	2063.349	0.51546	1064	0.22	1064	0.23	6.47	0.11	0.038	0.027	2.20	0.47	1.82
1,3-C_4H_6 + 1-C_4H_8	6028.128	0.50750	3059	0.64	3059	0.65	17.03	0.31	0.109	0.076	6.00	1.28	5.23
n-C_4H_{10}	15048.029	0.51610	7766	1.63	7766	1.64	47.33	0.81	0.276	0.194	16.07	3.44	13.28
Other C_4	0.000	0.51546	0	0.00	0	0.00	0.00	0.00	0.000	0.000	0.00	0.00	0.00
iso-C_5H_{12}	3266.128	0.48772	1593	0.33	1593	0.34	11.90	0.16	0.057	0.040	4.09	0.88	3.41
n-C_5H_{12}	9112.715	0.53372	4864	1.02	4864	1.03	36.41	0.50	0.173	0.122	12.49	2.67	10.40
Other C_5	774.756	0.51546	399	0.08	399	0.08	2.88	0.04	0.014	0.010	1.03	0.22	0.85
n-C_6H_{14}	2253.226	0.73323	1652	0.35	1652	0.35	14.67	0.17	0.059	0.041	5.07	1.09	4.24
Other C_6+	4521.647	0.51546	2331	0.49	2331	0.49	20.34	0.24	0.083	0.058	7.15	1.53	5.98
	1039140.172		476983	100.00	472302	100.00	549.95	54.38	16.81		467.03	100.00	207.25

8.00 wt % Bagasse Loading

Analyte	Area [counts·s]	Response Factor	C [ppmv]	C [mol %]	C_{corr} [ppmv]	C_{corr} [mol %]	HHV [kJ mol^{-1}]	HHV [MJ kg^{-1}]	Yield [mmol]	Yield [mmol g^{-1}]	Yield [mg]	% Yield [wt %]	C Yield [mg]
H_2	95875.814	1.29965	124605	21.60	124605	21.66	61.90	30.71	5.534	1.940	11.16	1.54	0.00
O_2	0.000	0.47633	0	0.00	0	0.00	0.00	0.00	0.000	0.000	0.00	0.00	0.00
N_2	2676.697	0.57690	1544	0.27	0	0.00	0.00	0.00	0.000	0.000	0.00	0.00	0.00
CO	20169.438	0.42924	8658	1.50	8658	1.50	4.26	0.15	0.385	0.135	10.77	1.48	4.62
CH_4	75328.554	1.78440	134416	23.30	134416	23.36	207.99	12.96	5.970	2.093	95.77	13.18	71.71
CO_2	937218.668	0.24503	229647	39.80	229646	39.91	0.00	0.00	10.200	3.576	448.89	61.79	122.51
C_2H_4	2759.465	0.90159	2488	0.43	2488	0.43	6.10	0.22	0.111	0.039	3.10	0.43	2.65
C_2H_6	31378.316	0.91348	28663	4.97	28663	4.98	77.71	2.58	1.273	0.446	38.28	5.27	30.58
C_3H_6	8885.026	0.62518	5555	0.96	5555	0.97	19.87	0.47	0.247	0.087	10.38	1.43	8.89
C_3H_8	22884.949	0.62212	14237	2.47	14237	2.47	54.94	1.25	0.632	0.222	27.88	3.84	22.79
iso-C_4H_{10}	3882.872	0.51546	2001	0.35	2001	0.35	9.99	0.17	0.089	0.031	5.17	0.71	4.27
1,3-C_4H_6 + 1-C_4H_8	5452.073	0.50750	2767	0.48	2767	0.48	12.64	0.23	0.123	0.043	6.77	0.93	5.90
n-C_4H_{10}	18648.934	0.51610	9625	1.67	9625	1.67	48.15	0.83	0.427	0.150	24.85	3.42	20.54
Other C_4	0.000	0.51546	0	0.00	0	0.00	0.00	0.00	0.000	0.000	0.00	0.00	0.00
iso-C_5H_{12}	4987.635	0.48772	2433	0.42	2433	0.42	14.92	0.21	0.108	0.038	7.80	1.07	6.49
n-C_5H_{12}	10437.526	0.53372	5571	0.97	5571	0.97	34.24	0.47	0.247	0.087	17.85	2.46	14.86
Other C_5	801.460	0.51546	413	0.07	413	0.07	2.45	0.03	0.018	0.006	1.32	0.18	1.10
n-C_6H_{14}	2725.827	0.73323	1999	0.35	1999	0.35	14.57	0.17	0.089	0.031	7.65	1.05	6.40
Other C_6+	4506.576	0.51546	2323	0.40	2323	0.40	16.64	0.19	0.103	0.036	8.89	1.22	7.44
	1248619.829		576944	100.00	575399	100.00	586.35	50.65	25.56		726.53	100.00	330.74

18/25 Mesh Size Fraction (0.710 - 1.00 mm)

Analyte	Area [counts·s]	Response Factor	C [ppmv]	C [mol %]	C_{corr} [ppmv]	C_{corr} [mol %]	HHV [kJ mol^{-1}]	HHV [MJ kg^{-1}]	Yield [mmol]	Yield [mmol g^{-1}]	Yield [mg]	% Yield [wt %]	C Yield [mg]
H_2	91077.735	1.29965	118369	24.44	118369	24.67	70.51	34.98	4.274	3.065	8.62	1.76	0.00
O_2	1501.745	0.47633	715	0.15	0	0.00	0.00	0.00	0.000	0.000	0.00	0.00	0.00
N_2	6596.175	0.57690	3805	0.79	0	0.00	0.00	0.00	0.000	0.000	0.00	0.00	0.00
CO	17585.654	0.42924	7548	1.56	7548	1.57	4.45	0.16	0.273	0.195	7.63	1.56	3.27
CH_4	54231.570	1.78440	96771	19.98	96771	20.17	179.54	11.19	3.494	2.506	56.05	11.45	41.97
CO_2	797876.638	0.24503	195504	40.36	195502	40.74	0.00	0.00	7.059	5.063	310.66	63.46	84.78
C_2H_4	3652.042	0.90159	3293	0.68	3293	0.69	9.68	0.35	0.119	0.085	3.34	0.68	2.86
C_2H_6	20213.257	0.91348	18464	3.81	18464	3.85	60.02	2.00	0.667	0.478	20.05	4.09	16.02
C_3H_6	10359.184	0.62518	6476	1.34	6476	1.35	27.78	0.66	0.234	0.168	9.84	2.01	8.43
C_3H_8	15404.439	0.62212	9583	1.98	9583	2.00	44.34	1.01	0.346	0.248	15.26	3.12	12.47
iso-C_4H_{10}	2206.330	0.51546	1137	0.23	1137	0.24	6.81	0.12	0.041	0.029	2.39	0.49	1.97
1,3-C_4H_6 + 1-C_4H_8	5927.322	0.50750	3008	0.62	3008	0.63	16.48	0.30	0.109	0.078	5.98	1.22	5.22
n-C_4H_{10}	15278.106	0.51610	7885	1.63	7885	1.64	47.30	0.81	0.285	0.204	16.55	3.38	13.68
Other C_4	0.000	0.51546	0	0.00	0	0.00	0.00	0.00	0.000	0.000	0.00	0.00	0.00
iso-C_5H_{12}	3494.987	0.48772	1705	0.35	1705	0.36	12.53	0.17	0.062	0.044	4.44	0.91	3.70
n-C_5H_{12}	9626.846	0.53372	5138	1.06	5138	1.07	37.86	0.52	0.186	0.133	13.38	2.73	11.14
Other C_5	782.202	0.51546	403	0.08	403	0.08	2.86	0.04	0.015	0.010	1.05	0.21	0.87
n-C_6H_{14}	2711.329	0.73323	1988	0.41	1988	0.41	17.38	0.20	0.072	0.051	6.19	1.26	5.17
Other C_6+	5073.580	0.51546	2615	0.54	2615	0.54	22.46	0.26	0.094	0.068	8.14	1.66	6.80
	1063599.141		484409	100.00	479886	100.00	560.00	52.76	17.33		489.56	100.00	218.35

45/60 Mesh Size Fraction (0.250 - 0.355 mm)

Analyte	Area [counts·s]	Response Factor	C [ppmv]	C [mol %]	C_{corr} [ppmv]	C_{corr} [mol %]	HHV [kJ mol^{-1}]	HHV [MJ kg^{-1}]	Yield [mmol]	Yield [mmol g^{-1}]	Yield [mg]	% Yield [wt %]	C Yield [mg]
H_2	83610.450	1.29965	108664	27.33	108664	27.54	78.72	39.05	4.837	3.418	9.75	2.06	0.00
O_2	901.743	0.47633	430	0.11	0	0.00	0.00	0.00	0.000	0.000	0.00	0.00	0.00
N_2	4434.697	0.57690	2558	0.64	0	0.00	0.00	0.00	0.000	0.000	0.00	0.00	0.00
CO	18437.783	0.42924	7914	1.99	7914	2.01	5.68	0.20	0.352	0.249	9.87	2.08	4.23
CH_4	43116.098	1.78440	76936	19.35	76936	19.50	173.62	10.82	3.424	2.420	54.94	11.59	41.13
CO_2	628021.343	0.24503	153884	38.71	153883	39.00	0.00	0.00	6.849	4.841	301.44	63.57	82.27
C_2H_4	2915.247	0.90159	2628	0.66	2628	0.67	9.40	0.34	0.117	0.083	3.28	0.69	2.81
C_2H_6	16121.809	0.91348	14727	3.70	14727	3.73	58.22	1.94	0.655	0.463	19.71	4.16	15.75
C_3H_6	8056.779	0.62518	5037	1.27	5037	1.28	26.28	0.62	0.224	0.158	9.43	1.99	8.08
C_3H_8	12269.119	0.62212	7633	1.92	7633	1.93	42.95	0.97	0.340	0.240	14.98	3.16	12.24
iso-C_4H_{10}	1765.562	0.51546	910	0.23	910	0.23	6.62	0.11	0.041	0.029	2.35	0.50	1.95
1,3-C_4H_6 + 1-C_4H_8	4339.999	0.50750	2203	0.55	2203	0.56	14.68	0.27	0.098	0.069	5.40	1.14	4.71
n-C_4H_{10}	11662.355	0.51610	6019	1.51	6019	1.53	43.91	0.76	0.268	0.189	15.57	3.28	12.87
Other C_4	0.000	0.51546	0	0.00	0	0.00	0.00	0.00	0.000	0.000	0.00	0.00	0.00
iso-C_5H_{12}	2520.159	0.48772	1229	0.31	1229	0.31	10.99	0.15	0.055	0.039	3.95	0.83	3.29
n-C_5H_{12}	6809.645	0.53372	3634	0.91	3634	0.92	32.57	0.45	0.162	0.114	11.67	2.46	9.72
Other C_5	538.650	0.51546	278	0.07	278	0.07	2.40	0.03	0.012	0.009	0.89	0.19	0.74
n-C_6H_{14}	1631.887	0.73323	1197	0.30	1197	0.30	12.72	0.15	0.053	0.038	4.59	0.97	3.84
Other C_6+	3210.306	0.51546	1655	0.42	1655	0.42	17.29	0.20	0.074	0.052	6.35	1.34	5.31
	850363.632		397536	100.00	394547	100.00	536.06	56.07	17.56		474.17	100.00	208.92

140/230 Mesh Size Fraction (0.063 - 0.106 mm)

Analyte	Area [counts·s]	Response Factor	C [ppmv]	C [mol %]	C_{corr} [ppmv]	C_{corr} [mol %]	HHV [kJ mol^{-1}]	HHV [MJ kg^{-1}]	Yield [mmol]	Yield [mmol g^{-1}]	Yield [mg]	% Yield [wt %]	C Yield [mg]
H_2	91199.382	1.29965	118527	26.16	118527	26.39	75.43	37.42	4.031	2.866	8.13	1.92	0.00
O_2	1256.846	0.47633	599	0.13	0	0.00	0.00	0.00	0.000	0.000	0.00	0.00	0.00
N_2	5614.745	0.57690	3239	0.72	0	0.00	0.00	0.00	0.000	0.000	0.00	0.00	0.00
CO	17772.473	0.42924	7629	1.68	7629	1.70	4.81	0.17	0.259	0.184	7.27	1.72	3.12
CH_4	48141.202	1.78440	85903	18.96	85903	19.13	170.28	10.61	2.921	2.077	46.86	11.07	35.09
CO_2	736606.195	0.24503	180491	39.84	180489	40.18	0.00	0.00	6.138	4.364	270.12	63.80	73.72
C_2H_4	3785.771	0.90159	3413	0.75	3413	0.76	10.72	0.38	0.116	0.083	3.26	0.77	2.79
C_2H_6	18669.085	0.91348	17054	3.76	17054	3.80	59.23	1.97	0.580	0.412	17.44	4.12	13.93
C_3H_6	10965.840	0.62518	6856	1.51	6856	1.53	31.42	0.75	0.233	0.166	9.81	2.32	8.40
C_3H_8	13910.411	0.62212	8654	1.91	8654	1.93	42.78	0.97	0.294	0.209	12.98	3.07	10.60
iso-C_4H_{10}	1975.762	0.51546	1018	0.22	1018	0.23	6.51	0.11	0.035	0.025	2.01	0.48	1.66
1,3-C_4H_6 + 1-C_4H_8	3747.851	0.50750	1902	0.42	1902	0.42	11.13	0.20	0.065	0.046	3.56	0.84	3.11
n-C_4H_{10}	14082.272	0.51610	7268	1.60	7268	1.62	46.58	0.80	0.247	0.176	14.36	3.39	11.87
Other C_4	0.000	0.51546	0	0.00	0	0.00	0.00	0.00	0.000	0.000	0.00	0.00	0.00
iso-C_5H_{12}	3000.239	0.48772	1463	0.32	1463	0.33	11.49	0.16	0.050	0.035	3.59	0.85	2.99
n-C_5H_{12}	8403.888	0.53372	4485	0.99	4485	1.00	35.31	0.49	0.153	0.108	11.00	2.60	9.16
Other C_5	814.323	0.51546	420	0.09	420	0.09	3.19	0.04	0.014	0.010	1.03	0.24	0.86
n-C_6H_{14}	2520.326	0.73323	1848	0.41	1848	0.41	17.26	0.20	0.063	0.045	5.42	1.28	4.53
Other C_6+	4332.691	0.51546	2233	0.49	2233	0.50	20.49	0.24	0.076	0.054	6.54	1.55	5.47
	986799.303		453002	100.00	449163	100.00	546.63	54.52	15.27		423.38	100.00	187.30

Cellulose

Analyte	Area [counts·s]	Response Factor	C [ppmv]	C [mol %]	C_{corr} [ppmv]	C_{corr} [mol %]	HHV [kJ mol^{-1}]	HHV [MJ kg^{-1}]	Yield [mmol]	Yield [mmol g^{-1}]	Yield [mg]	% Yield [wt %]	C Yield [mg]
H_2	107683.092	1.29965	139950	27.13	139950	27.23	77.85	38.62	5.222	3.635	10.53	1.88	0.00
O_2	875.059	0.47633	417	0.08	0	0.00	0.00	0.00	0.000	0.000	0.00	0.00	0.00
N_2	2732.042	0.57690	1576	0.31	0	0.00	0.00	0.00	0.000	0.000	0.00	0.00	0.00
CO	23561.893	0.42924	10114	1.96	10114	1.97	5.57	0.20	0.377	0.263	10.57	1.89	4.53
CH_4	38608.943	1.78440	68894	13.35	68894	13.41	119.37	7.44	2.570	1.789	41.24	7.38	30.87
CO_2	922798.149	0.24503	226113	43.83	226112	44.00	0.00	0.00	8.436	5.872	371.28	66.45	101.33
C_2H_4	4261.532	0.90159	3842	0.74	3842	0.75	10.55	0.38	0.143	0.100	4.02	0.72	3.44
C_2H_6	21508.324	0.91348	19647	3.81	19647	3.82	59.64	1.98	0.733	0.510	22.04	3.95	17.61
C_3H_6	11845.107	0.62518	7405	1.44	7405	1.44	29.66	0.70	0.276	0.192	11.63	2.08	9.96
C_3H_8	15506.289	0.62212	9647	1.87	9647	1.88	41.68	0.95	0.360	0.251	15.87	2.84	12.97
iso-C_4H_{10}	1884.791	0.51546	972	0.19	972	0.19	5.43	0.09	0.036	0.025	2.11	0.38	1.74
1,3-C_4H_6 + 1-C_4H_8	6929.420	0.50750	3517	0.68	3517	0.68	17.99	0.33	0.131	0.091	7.23	1.29	6.30
n-C_4H_{10}	17542.376	0.51610	9054	1.76	9054	1.76	50.72	0.87	0.338	0.235	19.63	3.51	16.23
Other C_4	376.788	0.51546	194	0.04	194	0.04	1.03	0.02	0.007	0.005	0.42	0.08	0.35
iso-C_5H_{12}	3632.368	0.48772	1772	0.34	1772	0.34	12.16	0.17	0.066	0.046	4.77	0.85	3.97
n-C_5H_{12}	11878.413	0.53372	6340	1.23	6340	1.23	43.63	0.60	0.237	0.165	17.07	3.05	14.21
Other C_5	1104.687	0.51546	569	0.11	569	0.11	3.78	0.05	0.021	0.015	1.53	0.27	1.28
n-C_6H_{14}	3319.523	0.73323	2434	0.47	2434	0.47	19.87	0.23	0.091	0.063	7.83	1.40	6.54
Other C_6+	6613.484	0.51546	3409	0.66	3409	0.66	27.34	0.32	0.127	0.089	10.96	1.96	9.17
	1202662.278		515865	100.00	513872	100.00	526.27	52.95	19.17		558.72	100.00	240.50

Xylan

Analyte	Area [counts·s]	Response Factor	C [ppmv]	C [mol %]	C_{corr} [ppmv]	C_{corr} [mol %]	HHV [kJ mol^{-1}]	HHV [MJ kg^{-1}]	Yield [mmol]	Yield [mmol g^{-1}]	Yield [mg]	% Yield [wt %]	C Yield [mg]
H_2	93053.478	1.29965	120937	26.68	120937	26.75	76.48	37.94	4.555	3.181	9.18	1.95	0.00
O_2	0.000	0.47633	0	0.00	0	0.00	0.00	0.00	0.000	0.000	0.00	0.00	0.00
N_2	2277.907	0.57690	1314	0.29	0	0.00	0.00	0.00	0.000	0.000	0.00	0.00	0.00
CO	28763.869	0.42924	12347	2.72	12347	2.73	7.73	0.28	0.465	0.325	13.02	2.77	5.58
CH_4	45146.623	1.78440	80559	17.77	80559	17.82	158.68	9.89	3.034	2.119	48.67	10.34	36.44
CO_2	752948.169	0.24503	184495	40.70	184494	40.82	0.00	0.00	6.948	4.853	305.79	64.97	83.45
C_2H_4	3544.357	0.90159	3196	0.70	3196	0.71	9.97	0.36	0.120	0.084	3.38	0.72	2.89
C_2H_6	18744.444	0.91348	17123	3.78	17123	3.79	59.09	1.97	0.645	0.450	19.39	4.12	15.49
C_3H_6	10915.700	0.62518	6824	1.51	6824	1.51	31.08	0.74	0.257	0.180	10.81	2.30	9.26
C_3H_8	11966.154	0.62212	7444	1.64	7444	1.65	36.57	0.83	0.280	0.196	12.36	2.63	10.10
iso-C_4H_{10}	1327.521	0.51546	684	0.15	684	0.15	4.35	0.07	0.026	0.018	1.50	0.32	1.24
1,3-C_4H_6 + 1-C_4H_8	5404.032	0.50750	2743	0.60	2743	0.61	15.95	0.29	0.103	0.072	5.69	1.21	4.96
n-C_4H_{10}	12271.113	0.51610	6333	1.40	6333	1.40	40.33	0.69	0.239	0.167	13.86	2.95	11.46
Other C_4	0.000	0.51546	0	0.00	0	0.00	0.00	0.00	0.000	0.000	0.00	0.00	0.00
iso-C_5H_{12}	2753.137	0.48772	1343	0.30	1343	0.30	10.48	0.15	0.051	0.035	3.65	0.78	3.04
n-C_5H_{12}	8519.794	0.53372	4547	1.00	4547	1.01	35.57	0.49	0.171	0.120	12.36	2.63	10.28
Other C_5	722.705	0.51546	373	0.08	373	0.08	2.81	0.04	0.014	0.010	1.01	0.22	0.84
n-C_6H_{14}	1788.150	0.73323	1311	0.29	1311	0.29	12.17	0.14	0.049	0.034	4.26	0.90	3.56
Other C_6+	3427.768	0.51546	1767	0.39	1767	0.39	16.11	0.19	0.067	0.046	5.73	1.22	4.80
	1003574.919		453339	100.00	452025	100.00	517.36	54.06	17.02		470.66	100.00	203.40

Lignin

Analyte	Area [counts·s]	Response Factor	C [ppmv]	C [mol %]	C_{corr} [ppmv]	C_{corr} [mol %]	HHV [kJ mol^{-1}]	HHV [MJ kg^{-1}]	Yield [mmol]	Yield [mmol g^{-1}]	Yield [mg]	% Yield [wt %]	C Yield [mg]
H_2	110431.141	1.29965	143522	29.99	143522	30.13	86.14	42.73	5.064	3.611	10.21	2.49	0.00
O_2	676.852	0.47633	322	0.07	0	0.00	0.00	0.00	0.000	0.000	0.00	0.00	0.00
N_2	3407.340	0.57690	1966	0.41	0	0.00	0.00	0.00	0.000	0.000	0.00	0.00	0.00
CO	2864.322	0.42924	1229	0.26	1229	0.26	0.73	0.03	0.043	0.031	1.22	0.30	0.52
CH_4	69424.196	1.78440	123880	25.89	123880	26.01	231.58	14.44	4.371	3.117	70.12	17.10	52.50
CO_2	689288.057	0.24503	168896	35.29	168895	35.46	0.00	0.00	5.959	4.250	262.25	63.94	71.57
C_2H_4	2306.926	0.90159	2080	0.43	2080	0.44	6.16	0.22	0.073	0.052	2.06	0.50	1.76
C_2H_6	15922.948	0.91348	14545	3.04	14545	3.05	47.64	1.58	0.513	0.366	15.43	3.76	12.33
C_3H_6	4392.330	0.62518	2746	0.57	2746	0.58	11.87	0.28	0.097	0.069	4.08	0.99	3.49
C_3H_8	8028.337	0.62212	4995	1.04	4995	1.05	23.28	0.53	0.176	0.126	7.77	1.89	6.35
iso-C_4H_{10}	648.321	0.51546	334	0.07	334	0.07	2.01	0.03	0.012	0.008	0.69	0.17	0.57
1,3-C_4H_6 + 1-C_4H_8	2360.183	0.50750	1198	0.25	1198	0.25	6.61	0.12	0.042	0.030	2.33	0.57	2.03
n-C_4H_{10}	5701.877	0.51610	2943	0.61	2943	0.62	17.79	0.31	0.104	0.074	6.03	1.47	4.99
Other C_4	0.000	0.51546	0	0.00	0	0.00	0.00	0.00	0.000	0.000	0.00	0.00	0.00
iso-C_5H_{12}	1894.971	0.48772	924	0.19	924	0.19	6.85	0.09	0.033	0.023	2.35	0.57	1.96
n-C_5H_{12}	5262.073	0.53372	2808	0.59	2808	0.59	20.85	0.29	0.099	0.071	7.15	1.74	5.95
Other C_5	1277.036	0.51546	658	0.14	658	0.14	4.71	0.07	0.023	0.017	1.68	0.41	1.39
n-C_6H_{14}	4797.453	0.73323	3518	0.74	3518	0.74	30.98	0.36	0.124	0.089	10.70	2.61	8.94
Other C_6+	3877.152	0.51546	1999	0.42	1999	0.42	17.30	0.20	0.071	0.050	6.08	1.48	5.08
	932561.514		478564	100.00	476274	100.00	514.50	61.27	16.80		410.12	100.00	179.44

Li/MgO Catalyst

Analyte	Area [counts·s]	Response Factor	C [ppmv]	C [mol %]	C_{corr} [ppmv]	C_{corr} [mol %]	HHV [kJ mol^{-1}]	HHV [MJ kg^{-1}]	Yield [mmol]	Yield [mmol g^{-1}]	Yield [mg]	% Yield [wt %]	C Yield [mg]
H_2	96476.205	1.29965	125385	23.05	125385	23.39	66.87	33.17	4.293	3.017	8.65	1.65	0.00
O_2	3212.142	0.47633	1530	0.28	0	0.00	0.00	0.00	0.000	0.000	0.00	0.00	0.00
N_2	11129.462	0.57690	6421	1.18	0	0.00	0.00	0.00	0.000	0.000	0.00	0.00	0.00
CO	11548.458	0.42924	4957	0.91	4957	0.92	2.62	0.09	0.170	0.119	4.75	0.91	2.04
CH_4	65310.671	1.78440	116540	21.42	116540	21.74	193.59	12.07	3.990	2.804	64.02	12.24	47.93
CO_2	880977.237	0.24503	215866	39.69	215863	40.27	0.00	0.00	7.391	5.193	325.29	62.18	88.78
C_2H_4	4679.589	0.90159	4219	0.78	4219	0.79	11.11	0.40	0.144	0.102	4.05	0.77	3.47
C_2H_6	22572.365	0.91348	20619	3.79	20619	3.85	60.01	2.00	0.706	0.496	21.23	4.06	16.96
C_3H_6	15818.272	0.62518	9889	1.82	9889	1.85	37.98	0.90	0.339	0.238	14.25	2.72	12.20
C_3H_8	16271.380	0.62212	10123	1.86	10123	1.89	41.93	0.95	0.347	0.244	15.28	2.92	12.49
iso-C_4H_{10}	2234.179	0.51546	1152	0.21	1152	0.21	6.17	0.11	0.039	0.028	2.29	0.44	1.89
1,3-C_4H_6 + 1-C_4H_8	8130.994	0.50750	4126	0.76	4126	0.77	20.24	0.37	0.141	0.099	7.78	1.49	6.79
n-C_4H_{10}	17191.873	0.51610	8873	1.63	8873	1.66	47.65	0.82	0.304	0.213	17.66	3.38	14.60
Other C_4	0.000	0.51546	0	0.00	0	0.00	0.00	0.00	0.000	0.000	0.00	0.00	0.00
iso-C_5H_{12}	3970.854	0.48772	1937	0.36	1937	0.36	12.75	0.18	0.066	0.047	4.78	0.91	3.98
n-C_5H_{12}	11481.146	0.53372	6128	1.13	6128	1.14	40.43	0.56	0.210	0.147	15.14	2.89	12.60
Other C_5	1081.989	0.51546	558	0.10	558	0.10	3.55	0.05	0.019	0.013	1.38	0.26	1.15
n-C_6H_{14}	3172.013	0.73323	2326	0.43	2326	0.43	18.20	0.21	0.080	0.056	6.86	1.31	5.74
Other C_6+	6395.810	0.51546	3297	0.61	3297	0.62	25.35	0.29	0.113	0.079	9.73	1.86	8.14
	1181654.640		543945	100.00	535991	100.00	588.44	52.16	18.35		523.15	100.00	238.75

MnO_2 Catalyst Replicate 1

Analyte	Area [counts·s]	Response Factor	C [ppmv]	C [mol %]	C_{corr} [ppmv]	C_{corr} [mol %]	HHV [kJ mol^{-1}]	HHV [MJ kg^{-1}]	Yield [mmol]	Yield [mmol g^{-1}]	Yield [mg]	% Yield [wt %]	C Yield [mg]
H_2	92748.661	1.29965	120541	25.03	120541	25.28	72.26	35.85	3.352	2.361	6.76	1.84	0.00
O_2	2404.337	0.47633	1145	0.24	146	0.03	0.00	0.00	0.004	0.003	0.13	0.04	0.00
N_2	6454.575	0.57690	3724	0.77	0	0.00	0.00	0.00	0.000	0.000	0.00	0.00	0.00
CO	23078.859	0.42924	9906	2.06	9906	2.08	5.88	0.21	0.275	0.194	7.72	2.10	3.31
CH_4	53119.755	1.78440	94787	19.68	94787	19.88	177.00	11.03	2.636	1.857	42.28	11.51	31.66
CO_2	781735.447	0.24503	191549	39.78	191547	40.17	0.00	0.00	5.326	3.752	234.39	63.80	63.97
C_2H_4	4358.107	0.90159	3929	0.82	3929	0.82	11.63	0.41	0.109	0.077	3.06	0.83	2.62
C_2H_6	19726.707	0.91348	18020	3.74	18020	3.78	58.95	1.96	0.501	0.353	15.07	4.10	12.04
C_3H_6	13211.383	0.62518	8259	1.72	8259	1.73	35.66	0.85	0.230	0.162	9.66	2.63	8.28
C_3H_8	14901.983	0.62212	9271	1.93	9271	1.94	43.17	0.98	0.258	0.182	11.37	3.09	9.29
iso-C_4H_{10}	2149.333	0.51546	1108	0.23	1108	0.23	6.67	0.11	0.031	0.022	1.79	0.49	1.48
1,3-C_4H_6 + 1-C_4H_8	6763.871	0.50750	3433	0.71	3433	0.72	18.93	0.34	0.095	0.067	5.26	1.43	4.59
n-C_4H_{10}	14297.891	0.51610	7379	1.53	7379	1.55	44.55	0.77	0.205	0.145	11.93	3.25	9.86
Other C_4	0.000	0.51546	0	0.00	0	0.00	0.00	0.00	0.000	0.000	0.00	0.00	0.00
iso-C_5H_{12}	2959.860	0.48772	1444	0.30	1444	0.30	10.68	0.15	0.040	0.028	2.90	0.79	2.41
n-C_5H_{12}	7792.175	0.53372	4159	0.86	4159	0.87	30.84	0.43	0.116	0.081	8.34	2.27	6.94
Other C_5	793.336	0.51546	409	0.08	409	0.09	2.92	0.04	0.011	0.008	0.82	0.22	0.68
n-C_6H_{14}	1923.803	0.73323	1411	0.29	1411	0.30	12.41	0.14	0.039	0.028	3.38	0.92	2.83
Other C_6+	2058.727	0.51546	1061	0.22	1061	0.22	9.17	0.11	0.030	0.021	2.54	0.69	2.13
	1050478.813		481534	100.00	476809	100.00	540.73	53.38	13.26		367.39	100.00	162.07

MnO_2 Catalyst Replicate 2

Analyte	Area [counts·s]	Response Factor	C [ppmv]	C [mol %]	C_{corr} [ppmv]	C_{corr} [mol %]	HHV [kJ mol^{-1}]	HHV [MJ kg^{-1}]	Yield [mmol]	Yield [mmol g^{-1}]	Yield [mg]	% Yield [wt %]	C Yield [mg]
H_2	91182.898	1.29965	118506	24.12	118506	24.35	69.59	34.52	3.252	2.276	6.56	1.70	0.00
O_2	1495.774	0.47633	712	0.15	0	0.00	0.00	0.00	0.000	0.000	0.00	0.00	0.00
N_2	6532.316	0.57690	3768	0.77	0	0.00	0.00	0.00	0.000	0.000	0.00	0.00	0.00
CO	14340.395	0.42924	6155	1.25	6155	1.26	3.58	0.13	0.169	0.118	4.73	1.23	2.03
CH_4	50949.319	1.78440	90914	18.51	90914	18.68	166.29	10.37	2.495	1.746	40.03	10.37	29.97
CO_2	856592.769	0.24503	209891	42.73	209889	43.12	0.00	0.00	5.760	4.031	253.51	65.66	69.19
C_2H_4	4086.038	0.90159	3684	0.75	3684	0.76	10.68	0.38	0.101	0.071	2.84	0.73	2.43
C_2H_6	18525.091	0.91348	16922	3.44	16922	3.48	54.23	1.80	0.464	0.325	13.96	3.62	11.16
C_3H_6	12580.291	0.62518	7865	1.60	7865	1.62	33.26	0.79	0.216	0.151	9.08	2.35	7.78
C_3H_8	13899.372	0.62212	8647	1.76	8647	1.78	39.44	0.89	0.237	0.166	10.46	2.71	8.55
iso-C_4H_{10}	2032.667	0.51546	1048	0.21	1048	0.22	6.18	0.11	0.029	0.020	1.67	0.43	1.38
1,3-C_4H_6 + 1-C_4H_8	6789.255	0.50750	3446	0.70	3446	0.71	18.61	0.34	0.095	0.066	5.21	1.35	4.54
n-C_4H_{10}	14560.090	0.51610	7515	1.53	7515	1.54	44.44	0.76	0.206	0.144	11.99	3.10	9.91
Other C_4	0.000	0.51546	0	0.00	0	0.00	0.00	0.00	0.000	0.000	0.00	0.00	0.00
iso-C_5H_{12}	3275.760	0.48772	1598	0.33	1598	0.33	11.58	0.16	0.044	0.031	3.16	0.82	2.63
n-C_5H_{12}	9292.918	0.53372	4960	1.01	4960	1.02	36.03	0.50	0.136	0.095	9.82	2.54	8.17
Other C_5	904.440	0.51546	466	0.09	466	0.10	3.27	0.05	0.013	0.009	0.92	0.24	0.77
n-C_6H_{14}	2903.511	0.73323	2129	0.43	2129	0.44	18.35	0.21	0.058	0.041	5.03	1.30	4.21
Other C_6+	5849.466	0.51546	3015	0.61	3015	0.62	25.53	0.30	0.083	0.058	7.13	1.85	5.96
	1115792.368		491241	100.00	486758	100.00	541.06	51.31	13.36		386.11	100.00	168.68

CO Reductant

Analyte	Area [counts·s]	Response Factor	C [ppmv]	C [mol %]	C_{corr} [ppmv]	C_{corr} [mol %]	HHV [kJ mol^{-1}]	HHV [MJ kg^{-1}]	Yield [mmol]	Yield [mmol g^{-1}]	Yield [mg]	% Yield [wt %]	C Yield [mg]
H_2	86351.076	1.29965	112226	18.04	112226	19.08	54.54	27.05	3.151	2.204	6.35	1.39	0.00
O_2	15993.772	0.47633	7618	1.22	470	0.08	0.00	0.00	0.013	0.009	0.42	0.09	0.00
N_2	46188.955	0.57690	26646	4.28	0	0.00	0.00	0.00	0.000	0.000	0.00	0.00	0.00
CO	417610.294	0.42924	179255	28.82	179255	30.48	86.24	3.08	5.034	3.520	141.00	30.83	60.46
CH_4	43923.465	1.78440	78377	12.60	78377	13.32	118.64	7.40	2.201	1.539	35.31	7.72	26.44
CO_2	684258.602	0.24503	167664	26.96	167651	28.50	0.00	0.00	4.708	3.292	207.19	45.31	56.55
C_2H_4	3482.055	0.90159	3139	0.50	3139	0.53	7.53	0.27	0.088	0.062	2.47	0.54	2.12
C_2H_6	16157.846	0.91348	14760	2.37	14760	2.51	39.14	1.30	0.414	0.290	12.46	2.73	9.96
C_3H_6	9237.925	0.62518	5775	0.93	5775	0.98	20.21	0.48	0.162	0.113	6.82	1.49	5.84
C_3H_8	12054.215	0.62212	7499	1.21	7499	1.27	28.31	0.64	0.211	0.147	9.29	2.03	7.59
iso-C_4H_{10}	1666.986	0.51546	859	0.14	859	0.15	4.20	0.07	0.024	0.017	1.40	0.31	1.16
1,3-C_4H_6 + 1-C_4H_8	5107.204	0.50750	2592	0.42	2592	0.44	11.59	0.21	0.073	0.051	4.01	0.88	3.50
n-C_4H_{10}	12203.200	0.51610	6298	1.01	6298	1.07	30.82	0.53	0.177	0.124	10.28	2.25	8.50
Other C_4	0.000	0.51546	0	0.00	0	0.00	0.00	0.00	0.000	0.000	0.00	0.00	0.00
iso-C_5H_{12}	2685.425	0.48772	1310	0.21	1310	0.22	7.86	0.11	0.037	0.026	2.65	0.58	2.21
n-C_5H_{12}	7500.939	0.53372	4003	0.64	4003	0.68	24.07	0.33	0.112	0.079	8.11	1.77	6.75
Other C_5	640.722	0.51546	330	0.05	330	0.06	1.91	0.03	0.009	0.006	0.67	0.15	0.56
n-C_6H_{14}	1886.689	0.73323	1383	0.22	1383	0.24	9.87	0.11	0.039	0.027	3.35	0.73	2.80
Other C_6+	4396.608	0.51546	2266	0.36	2266	0.39	15.88	0.18	0.064	0.045	5.48	1.20	4.59
	1371345.979		622003	100.00	588196	100.00	460.80	41.80	16.52		457.28	100.00	199.01

$NaBH_4$ Reductant

Analyte	Area [counts·s]	Response Factor	C [ppmv]	C [mol %]	C_{corr} [ppmv]	C_{corr} [mol %]	HHV [kJ mol^{-1}]	HHV [MJ kg^{-1}]	Yield [mmol]	Yield [mmol g^{-1}]	Yield [mg]	% Yield [wt %]	C Yield [mg]
H_2	122144.472	1.29965	158745	27.04	158745	35.45	101.34	50.27	8.552	5.977	17.24	2.90	0.00
O_2	84307.788	0.47633	40158	6.84	10685	2.39	0.00	0.00	0.576	0.402	18.42	3.10	0.00
N_2	190454.823	0.57690	109873	18.71	0	0.00	0.00	0.00	0.000	0.000	0.00	0.00	0.00
CO	9740.873	0.42924	4181	0.71	4181	0.93	2.64	0.09	0.225	0.157	6.31	1.06	2.71
CH_4	39968.436	1.78440	71319	12.15	71319	15.93	141.82	8.84	3.842	2.685	61.64	10.38	46.15
CO_2	652122.219	0.24503	159790	27.21	159736	35.67	0.00	0.00	8.605	6.015	378.71	63.80	103.36
C_2H_4	2479.594	0.90159	2236	0.38	2236	0.50	7.04	0.25	0.120	0.084	3.38	0.57	2.89
C_2H_6	14153.509	0.91348	12929	2.20	12929	2.89	45.04	1.50	0.696	0.487	20.94	3.53	16.73
C_3H_6	8096.008	0.62518	5061	0.86	5061	1.13	23.27	0.55	0.273	0.191	11.47	1.93	9.83
C_3H_8	10264.119	0.62212	6386	1.09	6386	1.43	31.66	0.72	0.344	0.240	15.17	2.56	12.40
iso-C_4H_{10}	1464.226	0.51546	755	0.13	755	0.17	4.84	0.08	0.041	0.028	2.36	0.40	1.95
1,3-C_4H_6 + 1-C_4H_8	4154.455	0.50750	2108	0.36	2108	0.47	12.38	0.22	0.114	0.079	6.26	1.05	5.46
n-C_4H_{10}	9937.821	0.51610	5129	0.87	5129	1.15	32.97	0.57	0.276	0.193	16.06	2.71	13.27
Other C_4	0.000	0.51546	0	0.00	0	0.00	0.00	0.00	0.000	0.000	0.00	0.00	0.00
iso-C_5H_{12}	2531.227	0.48772	1235	0.21	1235	0.28	9.73	0.13	0.067	0.046	4.80	0.81	3.99
n-C_5H_{12}	6629.050	0.53372	3538	0.60	3538	0.79	27.94	0.39	0.191	0.133	13.75	2.32	11.45
Other C_5	356.467	0.51546	184	0.03	184	0.04	1.40	0.02	0.010	0.007	0.71	0.12	0.59
n-C_6H_{14}	2053.428	0.73323	1506	0.26	1506	0.34	14.11	0.16	0.081	0.057	6.99	1.18	5.85
Other C_6+	3924.481	0.51546	2023	0.34	2023	0.45	18.62	0.22	0.109	0.076	9.39	1.58	7.85
	1164782.995		587155	100.00	447755	100.00	474.81	64.02	24.12		593.60	100.00	244.47

Titanium Bomb

Analyte	Area [counts·s]	Response Factor	C [ppmv]	C [mol %]	C_{corr} [ppmv]	C_{corr} [mol %]	HHV [kJ mol^{-1}]	HHV [MJ kg^{-1}]	Yield [mmol]	Yield [mmol g^{-1}]	Yield [mg]	% Yield [wt %]	C Yield [mg]
H_2	31953.940	1.29965	41529	15.05	41529	15.14	43.28	21.47	3.219	2.262	6.49	1.03	0.00
O_2	555.844	0.47633	265	0.10	0	0.00	0.00	0.00	0.000	0.000	0.00	0.00	0.00
N_2	2527.487	0.57690	1458	0.53	0	0.00	0.00	0.00	0.000	0.000	0.00	0.00	0.00
CO	140988.431	0.42924	60518	21.92	60518	22.06	62.43	2.23	4.691	3.297	131.39	20.93	56.34
CH_4	26627.618	1.78440	47514	17.21	47514	17.32	154.22	9.61	3.683	2.588	59.08	9.41	44.23
CO_2	411699.117	0.24503	100879	36.55	100878	36.78	0.00	0.00	7.819	5.495	344.11	54.81	93.91
C_2H_4	2216.465	0.90159	1998	0.72	1998	0.73	10.28	0.37	0.155	0.109	4.35	0.69	3.72
C_2H_6	7909.006	0.91348	7225	2.62	7225	2.63	41.08	1.37	0.560	0.394	16.84	2.68	13.45
C_3H_6	4309.208	0.62518	2694	0.98	2694	0.98	20.22	0.48	0.209	0.147	8.79	1.40	7.52
C_3H_8	4971.379	0.62212	3093	1.12	3093	1.13	25.03	0.57	0.240	0.168	10.57	1.68	8.64
iso-C_4H_{10}	723.915	0.51546	373	0.14	373	0.14	3.91	0.07	0.029	0.020	1.68	0.27	1.39
1,3-C_4H_6 + 1-C_4H_8	2303.472	0.50750	1169	0.42	1169	0.43	11.21	0.20	0.091	0.064	4.99	0.80	4.35
n-C_4H_{10}	5961.153	0.51610	3077	1.11	3077	1.12	32.29	0.56	0.238	0.168	13.86	2.21	11.46
Other C_4	0.000	0.51546	0	0.00	0	0.00	0.00	0.00	0.000	0.000	0.00	0.00	0.00
iso-C_5H_{12}	1155.633	0.48772	564	0.20	564	0.21	7.25	0.10	0.044	0.031	3.15	0.50	2.62
n-C_5H_{12}	3535.117	0.53372	1887	0.68	1887	0.69	24.32	0.34	0.146	0.103	10.55	1.68	8.78
Other C_5	0.000	0.51546	0	0.00	0	0.00	0.00	0.00	0.000	0.000	0.00	0.00	0.00
n-C_6H_{14}	2436.673	0.73323	1787	0.65	1787	0.65	27.32	0.32	0.138	0.097	11.93	1.90	9.98
Other C_6+	0.000	0.51546	0	0.00	0	0.00	0.00	0.00	0.000	0.000	0.00	0.00	0.00
	649874.458		276028	100.00	274305	100.00	462.84	37.67	21.26		627.77	100.00	266.40

D_2O

Analyte	Area [counts·s]	Response Factor	C [ppmv]	C [mol %]	C_{corr} [ppmv]	C_{corr} [mol %]	HHV [kJ mol^{-1}]	HHV [MJ kg^{-1}]	Yield [mmol]	Yield [mmol g^{-1}]	Yield [mg]	% Yield [wt %]	C Yield [mg]
H_2	90892.650	1.29965	118129	26.61	118129	26.84	76.71	38.05	4.229	2.959	8.53	1.93	0.00
O_2	994.672	0.47633	474	0.11	0	0.00	0.00	0.00	0.000	0.000	0.00	0.00	0.00
N_2	5648.821	0.57690	3259	0.73	0	0.00	0.00	0.00	0.000	0.000	0.00	0.00	0.00
CO	41280.497	0.42924	17719	3.99	17719	4.03	11.39	0.41	0.634	0.444	17.77	4.03	7.62
CH_4	41644.142	1.78440	74310	16.74	74310	16.88	150.30	9.37	2.660	1.861	42.68	9.67	31.95
CO_2	702172.063	0.24503	172053	38.76	172052	39.09	0.00	0.00	6.159	4.310	271.07	61.41	73.98
C_2H_4	4287.567	0.90159	3866	0.87	3866	0.88	12.39	0.44	0.138	0.097	3.88	0.88	3.32
C_2H_6	16768.024	0.91348	15317	3.45	15317	3.48	54.28	1.81	0.548	0.384	16.49	3.74	13.17
C_3H_6	12187.304	0.62518	7619	1.72	7619	1.73	35.63	0.85	0.273	0.191	11.48	2.60	9.83
C_3H_8	11798.798	0.62212	7340	1.65	7340	1.67	37.02	0.84	0.263	0.184	11.59	2.63	9.47
iso-C_4H_{10}	1329.952	0.51546	686	0.15	686	0.16	4.47	0.08	0.025	0.017	1.43	0.32	1.18
1,3-C_4H_6 + 1-C_4H_8	7609.106	0.50750	3862	0.87	3862	0.88	23.07	0.42	0.138	0.097	7.62	1.73	6.64
n-C_4H_{10}	13491.702	0.51610	6963	1.57	6963	1.58	45.53	0.78	0.249	0.174	14.49	3.28	11.98
Other C_4	0.000	0.51546	0	0.00	0	0.00	0.00	0.00	0.000	0.000	0.00	0.00	0.00
iso-C_5H_{12}	2692.020	0.48772	1313	0.30	1313	0.30	10.52	0.15	0.047	0.033	3.39	0.77	2.82
n-C_5H_{12}	10127.984	0.53372	5406	1.22	5406	1.23	43.42	0.60	0.194	0.135	13.96	3.16	11.62
Other C_5	881.713	0.51546	454	0.10	454	0.10	3.52	0.05	0.016	0.011	1.17	0.27	0.98
n-C_6H_{14}	5225.664	0.73323	3832	0.86	3832	0.87	36.51	0.42	0.137	0.096	11.82	2.68	9.89
Other C_6+	2552.383	0.51546	1316	0.30	1316	0.30	12.32	0.14	0.047	0.033	4.06	0.92	3.39
	971585.061		443916	100.00	440182	100.00	557.11	54.40	15.76		441.42	100.00	197.84

APPENDIX D. TEMPORAL VARIATION OF PRESSURE

Figure D1 presented on the following page provides the temporal variation in pressure for 5 sugarcane bagasse hydrothermal conversion trials conducted with different residence times (i.e., 1 min, 5 min, 10 min, 30 min, 60 min). All of the other process parameters in these runs conformed to the standard, baseline conditions (e.g., 500 ºC, 4.00 wt % bagasse loading, unsieved bagasse < 2 mm).

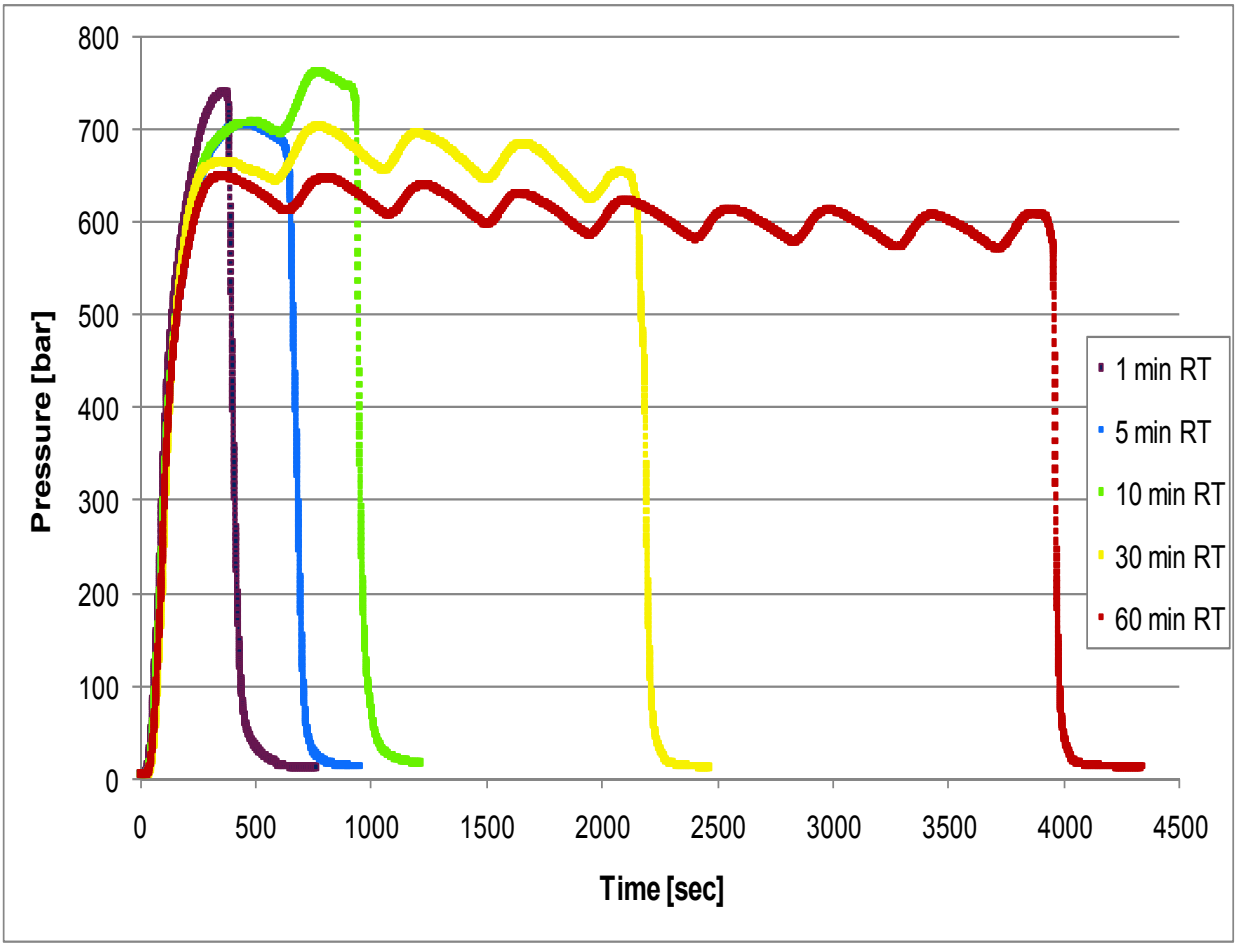

Figure D1. Temporal variation in pressure for 5 different bagasse hydrothermal runs at 500 °C

VITA

John E. White was born in Royal Oak, Michigan in April 1973. He obtained his Bachelor of Science in Engineering in chemical engineering at the University of Michigan in 1996. After graduating, he was employed for 3 years as a research engineer at T/J Technologies, Inc. of Ann Arbor, Michigan, where he engaged in the research and development of high capacitance electrochemical materials. Desiring to further his educational background, he moved to Baltimore, Maryland in 2000 to attend Johns Hopkins University, where he obtained his Masters of Science in Engineering in materials science and engineering in 2003. In 2004, he was hired as an adjunct professor by the Baltimore City Community College, where he taught both general and health chemistry. He began his doctoral studies at Louisiana State University A & M in the fall of 2004 when an opportunity arose to investigate thermochemical conversion of sugarcane bagasse at the Audubon Sugar Institute in Saint Gabriel, Louisiana.